Characterization of heterogeneous diffusion in confined soft matter

Von der Fakultät für Naturwissenschaften

der Technischen Universität Chemnitz

genehmigte Dissertation

zur Erlangung des akademischen Grades

doctor rerum naturalium

(Dr. rer. nat.)

vorgelegt von Lehramtsassessorin Daniela Täuber (geb. März)

geboren am 08.05.1967 in Nürnberg

Bibliographische Beschreibung

Täuber, Daniela
Characterization of heterogeneous diffusion in confined soft matter
Dissertation, Fakultät für Naturwissenschaften
Technische Universität Chemnitz, Oktober 2011

abstract

A new method, probability distribution of diffusivities (time scaled square displacements between succeeding video frames), was developed to analyze single molecule tracking (SMT) experiments. This method was then applied to SMT experiments on ultrathin liquid tetrakis(2-ethylhexoxy)silane (TEHOS) films on Si wafer with 100 nm thermally grown oxide, and on thin semectic liquid crystal films. Spatial maps of diffusivities from SMT experiments on 220 nm thick semectic liquid crystal films reveal structure related dynamics. The SMT experiments on ultrathin TEHOS films were complemented by fluorescence correlation spectroscopy (FCS). The observed strongly heterogeneous single molecule dynamics within those films can be explained by a three-layer model consisting of (i) dye molecules adsorbed to the substrate, (ii) slowly diffusing molecules in the laterally heterogeneous near-surface region of 1 - 2 molecular diameters, and (iii) freely diffusing dye molecules in the upper region of the film. FCS and SMT experiments reveal a strong influence of substrate heterogeneity on SM dynamics. Thereby chemisorption to substrate surface silanols plays an important role. Vertical mean first passage times (mfpt) in those films are below 1 μs. This appears as fast component in FCS autocorrelation curves, which further contain a contribution from lateral diffusion and from adsorption events. Therefore, the FCS curves are approximated by a tri-component function, which contains an exponential term related to the mfpt, the correlation function for translational diffusion and a stretched exponential term for the broad distribution of adsorption events. Lateral diffusion coefficients obtained by FCS on 10 nm thick TEHOS films, thereby, are effective diffusion coefficients from dye transients in the focal area. They strongly depend on the substrate heterogeneity. Variation of the frame times for the acquisition of SMT experiments in steps of 20 ms from 20 ms to 200 ms revealed a strong dependence of the corresponding probability distributions of diffusivities on time, in particular in the range between 20 ms and 100 ms. This points to average dwell times of the dye molecules in at least one type of the heterogeneous regions (e.g. on and above silanol clusters) in the range of few tens of milliseconds.

Furthermore, time series of SM spectra from Nile Red in 25 nm thick poly-n-alkyl-methacrylate (PnAMA) films were studied. In analogy to translational diffusion, spectral diffusion (shifts in energetic positions of SM spectra) can be studied by probability distributions of spectral diffusivities, i.e. time scaled square energetic displacements. Simulations were run and analyzed to study contributions from noise and fitting uncertainty to spectral diffusion. Furthermore the effect of spectral jumps during acquisition of a SM

spectrum was investigated. Probability distributions of spectral diffusivites of Nile Red probing vitreous PnAMA films reveal a two-level system. In contrast, such probability distributions obtained from Nile Red within a 25 nm thick poly-n-butylmethacrylate film around glass transition and in the melt state, display larger spectral jumps. Moreover, for longer alkyl side chains a solvent shift to higher energies is observed, which supports the idea of nanophase separation within those polymers.

key words

heterogeneous diffusion, solid-liquid interface, liquid layering, single molecule detection, fluorescence microscopy, fluorescence correlation spectroscopy, single molecule tracking, simulation, soft matter, TEHOS, smectic-A, 8CB, poly-n-alkyl methacrylate, ultrathin liquid films, thin liquid crystal films, thin polymer films, surface silanols, thermally grown SiO_x, probability distributions of diffusivities, spectral diffusion.

Contents

Contents

List of symbols and abbreviations

$\mathbf{n}$ .... liquid crystal director

η .... (dynamic) viscosity

λ .... wavelength

$\mathbb{N}$ .... set of natural numbers

$\mathbb{R}_0^+$ .... set of real numbers

μ .... mean value of distribution

Φ_F .... fluorescence quantum yield

SiO_x .... silicon oxide with unspecific valences

σ .... standard deviation within distribution

σ_A .... molecular absorption cross section

τ .... time lag

τ^* .... lifetime of excited state

$\tau_{exposure}$ .... exposure time of a SMT video frame

τ_{frame} .... inverse frame rate of a SMT video

τ_{anomal} .... correlation obtained for anomalous diffusion

τ_{rot} .... correlation time for rotational diffusion

τ_D .... correlation time for translational diffusion

τ_{FD} .... correlation time related to freely diffusing molecules

$\tau_{i,dwell}$ .... dwell time within i^{th} layer

τ_R .... correlation time related to adsorption rate

τ_{Tr} .... lifetime of triplet state

a .... radius of the molecule/particle

A, A_i, a_i .... amplitude, amplitude of ith component

A_D .... amplitude of component related to translational diffusion

A_H .... effective *Hamaker* constant

A_R .... amplitude of component related to adsorption rate

A_{fluct} .... amplitude of small fluctuations

A_{FD} .... ratio of freely diffusing molecules

A_{TR} .... ratio of molecules in the triplet state

b .... slip length of a fluid near a wall

c .... concentration

$C(d_{diff})_\tau$ .... (cumulative) probability distribution of d_{diff} at time lag τ

$C(d_{spec})_\tau$ .... (cumulative) probability distribution of d_{spec} at time lag τ

D .... diffusion coefficient

d .... film thickness

$D(\tau)$ .... time dependent short range diffusion coefficient

D_{diff} .... translational diffusion coefficient from $C(d_{diff})_\tau$

d_{diff} .... diffusivity = square displacement/$(2n\tau)$

D_{msd} .... translational diffusion coefficient from distribution of D_{traj}

$D_\parallel$ .... diffusion coefficient parallel to the interface

$D_\perp$ .... diffusion coefficient perpendicular to the interface

D_{ssa} .... translational diffusion coefficient from spot size analysis

D_{rot} .... rotational diffusion coefficient

D_{spec} .... diffusion coefficient for spectral diffusion

d_{spec} .... spectral diffusivity = $\Delta E^2/(2\tau)$

D_{traj} .... translational diffusion coefficient from msd along trajectory

f .... frame rate of SMT video

f_O .... focal length

f_{ij} .... exchange rate from region i to region j

$G(\tau)$ .... normalized autocorrelation function of fluorescence time trace

$G_{D,\text{anomal}}$ .... fitting function of $G(\tau)$ for anomalous lateral diffusion

$G_{D,\text{bi}}$ .... fitting function of $G(\tau)$ for two components of lateral diffusion

G_D .... two-dimensional fitting function of $G(\tau)$ related to lateral diffusion

k, k_{up}, k_{down} .... transition rates

k_B .... Boltzmann constant

k_{nr} .... rate for non-radiative transition

k_r .... rate for radiative transition

M_w .... molecular weight

n .... dimension

N_A .... numerical aperture

N_C .... number of C atoms of polymer side chain

p_i .... equilibrium probability to find the molecule in region i

p_{dock} .... docking probability at an interface

r .... distance, displacement between two positions

R_g .... radius of gyration

R_R .... reaction rate for adsorption of dye molecules at the substrate

r_{pa} .... position accuracy

S_0 .... electronic singlet ground state of dye molecule

S_1, S_2 .... lowest and second lowest excited electronic singlet state of dye molecule

T .... temperature

t .... time

T_1, T_2 .... lowest and second lowest electronic triplet state of dye molecule

T_c .... critical temperature

T_g .... glass transition temperature

v .... velocity

V_{free} .... mean free volume

$V_{\text{RhB}}, V_{\text{R6G}}$ .... molecular volume of RhB and R6G, resp.

w_{xy} .... lateral radius of FCS detection

List of symbols and abbreviations

z	distance between the center of a particle and the solid-liquid interface
5CB	4-n-pentyl-4'-cyanobiphenyl - liquid crystal
8CB	4-n-octyl-4'-cyanobiphenyl - liquid crystal
AFM	atomic force microscope
APD	avalanche photo diode
CCD	charge-coupled device
FCD	focal conic domain
FCS	fluorescence correlation spectroscopy
FWHM	full width at half maximum
LC	liquid crystal
mfpt	mean first passage time
msd	mean square displacement
NMR	nuclear magnetic resonance
no-PDI	non-orienting perylene diimide (N,N'-di-propyl-1,6,7,12-tetra-(4-heptyl-phenoxy)-perylene-3,4,9,10-tetracarboxdiimide) - fluorescent dye
o-PDI	orienting perylene diimide (N,N'-di-hexadecyl-perylene-3,4,9,10-tetracarboxdiimide) - fluorescent dye
OG	Oregon Green 514 - fluorescent dye
OMCTS	octamethylcyclotetrasilane
OTS	octadecyltrichlorosilane
PBMA	poly-n-butyl methacrylate
PDMS	polydimethylsiloxane with trimethyl ends
PDMS-OH	polydimethylsiloxane with hydroxyl ends
PMDMS	polyfunctional poly(methylhydro-dimethyl)siloxane copolymers
PMMA	polymethyl methacrylate
PnAMA	poly-n-alkyl methacrylate
POMA	poly-n-octyl methacrylate
PPMA	poly-n-propyl methacrylate
R6G	Rhodamine 6G - fluorescent dye
RH	relative humidity
RhB	Rhodamine B - fluorescent dye
SM	single molecule
SMT	single molecule tracking
snr	signal to noise ratio
TEHOS	tetrakis(2-ethylhexoxy)silane
TF	terraced film
TIR	total internal reflection

1 Introduction

Diffusion is a widely occurring phenomenon in the world surrounding us. Whether we look at astrophysics, environmentalism, biology, sociology and also in various technical applications diffusion plays a role. Macroscopic diffusion was in general explained, when in 1855 *Adolf Fick* published his now famous second law of diffusion, relating the temporal gradient of solvent concentration to the second derivative of its spatial distribution [Fick55]. Some years earlier, in 1828, *Robert Brown* had studied the motion of pollen grains and various pulverized materials suspended in water with an optical microscope [Brow28]. The origin of this *Brownian Motion* remained unexplained until in 1905 *Albert Einstein* and in 1906 *Marian Smoluchowski* established the theory of thermal motion of colliding particles in a liquid [Eins05, Smol06]. Their theory of kinetic motion of particles has become the foundation for describing diffusion on a microscopic scale.

In recent time the technical improvement led to investigations and technical applications on the nanometer scale. Numbers of biologists study cell division, e.g. [Loos08], or the motion of cells as well as that of proteins and other molecules within cells or cell membranes [Mori07, Petr08]. In the field of bio-mimetics thus obtained insights are used for technical applications [Diez03]. Furthermore, great efforts are made to fabricate various types of *lab on a chip* for fast and cheap analysis, segregation and processing of molecules, with applications in medicine and nanotechnology, e.g. [Manz90, Hu11]. In 2001 the *Royal Society of Chemistry* launched a journal named *Lab on a Chip*, which actually has an impact factor > 6. Another emerging field of research is alternative power generation, where e.g. in solar cells light induced separated charges have to effectively reach the electrodes, which may imply the use of electrolytes [Jia11]. In all those areas of nanometric research and applications, diffusion no longer occurs within large volumes of liquids, but is confined into restricted geometries. Then the diffusing particles or molecules are not only influenced by the properties of the solvent, but also by interactions with the interfaces in their close vicinity. The latter e.g. are the driving force for the self-assembly of coating monolayers used in many applications. However, in most cases the explicit interactions and even more their spatial range are not fully known.

Numerous experimental studies have addressed the changes in diffusion evoked by confining geometries and interactions with interfaces. Amongst them are ensemble methods like nuclear magnetic resonance (NMR) studies, e.g. of diffusion of methane in uni-dimensional channel zeolithes [Kukl96], and of liquid crystal self-diffusion in porous glass [Vilf07], as well as incoherent quasielastic neutron scattering studies, e.g. of liquid crystal in porous glass [Lefo08]. Also optical techniques are used for ensemble measurements, e.g. studies of ensemble fluorescence of dye diffusion in thin polymer films [Hall98], and second harmonic generation and polarized absorption of liquid crystal thin films

on a polyimide substrate [Zakh08], just to name a few recent ones. Further examples may be found in *Diffusion in Condensed Matter*, edited by Heitjans and Kärger, in part II *Interfaces* [Heit05]. However, ensemble methods only allow for investigation of average properties. In contrast single molecule (SM) methods enable for the exploration of local environments and thus complement ensemble methods [Moer03]. Fluorescence correlation spectroscopy (FCS) is widely used in biophysics, e.g. to study surface binding kinetics [Thom83] or the formation and dynamics of lipid domains in membranes [Kahy04]. Furthermore, diffusion in nanopores [Hohl07] and in liquid crystal cells [Kawa08] has also been studied by FCS. The optical detection of single fluorescent molecules [Nguy87, Moer89, Orri90], led to further extension of exploration methods, namely single molecule tracking (SMT) and time series of SM fluorescence spectra as well as of polarization resolved SM fluorescence intensities. A more detailed explanation of SM methods will be given in the following chapters. SMT e.g. has been applied to study diffusion in thin liquid films [Schu03, Honc08], in nanopores [Zürn07] and recently also in thin liquid crystal films [Schu10b, Schu11]. Due to the larger viscosity of polymers, the properties of thin polymer films are mainly studied by time series of SM fluorescence spectra [Hou00] and of polarization resolved SM fluorescence intensities [Scho04].

A common feature of diffusion in confining geometries and at interfaces is the appearance of heterogeneities [Saxt96, Hou00, Schu03, Hac05]. However it is not always straightforward to discriminate, whether the deviations from homogeneous diffusion are caused by a mixture from diffusion within heterogeneous regions or are due to anomalous diffusion behavior. An example for the former is diffusion occurring predominantly in layers with rare exchange between the layers in combination with layer-dependent diffusion coefficients, which was suggested by Schuster et al. to explain the observed anisotropies in SMT experiments in thin liquid films [Schu03]. Whereas anomalous diffusion e.g. is caused by the existence of traps at a membrane [Saxt96], since in that case longer observation times will increase the probability to reach deeper traps [Lube08]. In this context it is important to note that the observed type of diffusion essentially depends on the observation time: Anomalous behavior arises from non-ergodicity, i.e. the probe molecule will not sample all heterogeneous regions within observation time. Then the outcome of an individual measurement varies due to the different composition of regions sampled during observation time. Yet if, due to rare transition rates between the heterogeneous regions, the probe molecule will stay within the same region during observation, the outcome of each individual measurement will be homogeneous diffusion. A large enough set of measurements will then mirror the statistical distribution of heterogeneous regions within the sample (assuming homogeneously distributed probe molecules). Nevertheless, if the observation time is long enough for the probe molecule to sample all regions during an individual measurement (i.e. ergodicity), an effective diffusion coefficient D_{eff} will be observed.

This work was started with the intention to further characterize the anisotropic diffusion observed in the preliminary work on ultrathin liquid films by Schuster et al. [Cich00, Schu02b, Schu02a, Schu03, Schu04]. Manipulation of dye-substrate interactions promised to yield further information on SM dynamics at solid-liquid interfaces.

Moreover, initial SMT experiments on varying time scales, which were conducted within the here reported work, clearly revealed a time-dependence of the obtained D_{msd}. This could not be explained by the previously developed model assuming liquid layering with rare interlayer exchange of SM molecules. Thus, the model for SM dynamics in ultra-thin liquid films had to be revised and improved. Recent theoretical work by Franosch et al. [Kamm08] (demonstrating the time dependence of diffusion on clusters) and by Sokolov et al. [Lube08, Neus09] contributed to the interpretation of the observed time dependence. SMT experiments usually are analyzed by calculating time-averaged mean square displacements (msd) along the detected trajectories [Schm95, Schm96, Schü97]. As was shown by Lubelski, Sokolov and Klafter, distributions of diffusion coefficients D_{traj} obtained from time-averaged single trajectories are relatively broad in case of an anomalous diffusion process, and moreover, the obtained mean values D_{msd} of the distributions D_{traj} depend essentially on the length of the trajectories [Lube08]. The latter was explicitly observed by Schuster et al. in the above mentioned experiments [Schu03], thus hinting to anomalous diffusion. However these D_{msd} were not derived from trajectories of similar lengths, since experimental constraints restrict the gain of long trajectories necessary for good statistics. Thus a thorough comparison of the D_{msd} obtained at different time lags τ as suggested by Lubelski et al. is not feasible.

For this reason, a new analyzing tool for SMT experiments was developed within this work with support [Baue09b] from Michael Bauer and Mario Heidernätsch from the theory group of Günter Radons, TU Chemnitz: Probability distributions of diffusivities d_{diff} are obtained from SMT experiments and analyzed. This tool is based on preliminary work of Schmidt et al. [Schü97] and Bräuchle et al. [Hell04c, Jung08], who used probability distributions and complementary probability distributions of square displacements r^2 of traced molecules, respectively. The diffusivities are time-scaled square displacements r^2 of traced molecules between succeeding frames, i.e. $d_{\mathrm{diff}} = r^2/(4\tau)$, where the time lag τ is the frame time (i.e. the inverse frame rate) of the SMT acquisition or a multiple of it. A detailed explanation of these distributions and their analysis is given in chapter 3. Several publications already made use of this [Täub09a, Tren09b, Schu10b, Schu11]. This new tool now allows for comparison of diffusion coefficients obtained from ensemble averages at different time lags τ. Complementary probability distributions of square displacements were also used by Schwartz et al. [Honc09b]. They time-scaled the diffusivities for enabling direct comparison of the diffusion coefficients as slopes of the distributions plotted in Fig. 4 in [Honc09b]. However, for part (b) of that figure, they do not give the used time intervals, thus they seem not to be aware of the possible dependence of these distributions on the used time interval. Furthermore, spatial distributions of diffusivities can be used to reveal spatial structures, e.g. of thin liquid crystal films [Schu10b], while an analogy of spectral diffusion with spatial diffusion led to the development of analogous tools to study spectral diffusion [Krau11a].

Outline

This work deals with the characterization of heterogeneous diffusion in confined soft matter. In particular, heterogeneous diffusion in thin supported films of soft matter

was investigated via optical single molecule methods. Thereby, the main focus is on the characterization of structure related dynamics in ultrathin liquid films. As was mentioned above, a new tool, probability distributions of diffusivities, was developed for the analysis of SMT experiments on ultrathin liquid films. However, the SMT experiments were restricted to a temporal resolution not faster than fifteen milliseconds. Fluorescence correlation spectroscopy (FCS) enables for the investigation of faster diffusion processes. Hence, FCS was accomplished on ultrathin liquid films to complement the SMT experiments in respect to higher temporal resolution.

In chapter 2 models for structure related dynamics in confined soft matter are outlined, i.e. random walks and mean first passage times, liquid layering at interfaces, characteristics of thin polymer films and thin liquid crystal films, as well as wetting and dewetting at interfaces, and also two models from continuum hydrodynamics describing Brownian motion of hard spheres close to a wall. Furthermore, an overview of single molecule methods for investigation of confined soft matter is given.

Chapter 3 gives the theoretical background of single molecule diffusion dynamics. Here also the new analyzing tools, probability distributions of diffusivities and of spectral diffusivities are explained.

In chapter 4 the experimental setups used within this work are described as well as the materials. Also, a comparison of the tracking software employed within this work is given.

Chapter 5 deals with spectral diffusion. In analogy to translational diffusion, probability distributions of spectral diffusivities $C(d_{\mathrm{spec}})$ are created and analyzed to describe spectral diffusion. In the first part of this chapter simulations are accomplished to demonstrate the use of the $C(d_{\mathrm{spec}})$. Furthermore, implications from spectral jumps during acquisition of a SM spectrum are studied, as well as contributions from noise and fitting uncertainty. In the second part, spectral diffusion of Nile Red molecules embedded in 25 nm thin polymer films is analyzed. The investigation of thin films from three different poly-n-alkyl-methacrylates (PnAMA) (with varied alkyl side chain length) at different temperatures allows for comparison of the probe molecule mobility above and below glass transition temperature. Nile Red in particular is used to probe the local polarity of its environment, which appears to be influenced by the alkyl side chain length of the studied polymers.

Chapter 6 contains investigations of thin liquid tetrakis(2-ethylhexoxy)silane (TEHOS) films. First an overview of reported results on liquid layering from literature is given and compared to experimental results within this work. Then film thinning SMT experiments are described and discussed. Furthermore, the time dependence of diffusion observed by SMT experiments is shown and discussed. In both cases of SMT experiments, conventional analysis by msd along trajectories is complemented by analysis of distributions of diffusivities leading to deeper insights. Then FCS experiments on thin liquid films complementing the SMT studies are described and discussed.

The last chapter 7 deals with substrate induced spatial structures influencing SM diffusion in ultrathin liquid TEHOS films and also in thin liquid crystal 4-n-octyl-4'-cyanobiphenyl (8CB) films. For this, experiments on ultrathin TEHOS films with differ-

ent substrate pre-treatments were conducted. Also, FCS was conducted on ultrathin TEHOS films on micro-structured substrates, which were structured by local laser-induced dehydroxylation of the highly hydroxylated surface. Furthermore, the newly developed method to study probability distributions furthermore is applied to SM diffusion in thin 8CB films. By this, the analysis of SMT experiments via msd along trajectories done by Benjamin Schulz [Schu09] was complemented. Moreover, spatial maps of diffusivities reveal structure related dynamics within those 8CB films.

2 Confined soft matter

As was mentioned in the introduction, diffusion in confined soft matter plays an important role in technical applications and also in bio-medical research. The simplest case of confinement is that in one dimension, e.g. between planar interfaces with solids. Yet there is also an increasing interest into studies of confinement in pores, e.g. [Khok07, Hohl07, Zürn07]. Pores have many promising technical applications in environmentalism, e.g. for filtering gaseous output from industrial plants or for CO_2 storage [Du11]. However, this work concentrates on basic research by mainly investigating thin films of an organic liquid. This is extended by the study of thin polymer films. Finally, the analysis of structure related dynamics is applied to thin liquid crystal films. This chapter thus is organized to first outline some particular features of thin liquid films, then proceeding to polymers and to liquid crystals. Afterwards models of wetting behavior at solid-liquid interfaces are presented together with hydrodynamic models. Furthermore, an overview of single molecule methods applied to study confined soft matter is given.

2.1 Thin films

2.1.1 Liquid layering at interfaces

For about two decades it has been known from ellipsometry studies [Hesl89, Forc93] as well as from X-ray reflectivites [Yu99] that liquids show layering at solid interfaces. Fig. 2.1 (right) shows the electron density profile obtained from ultrathin tetrakis(2-ethylhexoxy)silane (TEHOS) films by X-ray reflectivity according to [Yu99]. In 1993 Forcada and Mate published their investigation on evaporation experiments with ultrathin TEHOS films on Si wafers with native oxide [Forc93]. They showed that the evaporative thinning was not continuous, but oszilated revealing several minima at film thicknesses of about five molecular diameters down to the last remaining molecular layer, see Fig. 2.1 (left). Pervious studies by Heslot et al. [Hesl89] on wetting droplets of TEHOS spread on smooth [111]-Si substrates with native oxide had revealed up to four molecular layers. Recent mechanical investigations of thin TEHOS films on native oxide using an AFM also revealed layering in a region of up to 4-8 nm from the substrate [Pati07].

Thus liquid layering seems to be a widely spread feature at solid-liquid interfaces. However the extend of this layering depends on several conditions as will be discussed in section 6.1. Nevertheless it may also be present in polymers, especially above the glass transition temperature T_g.
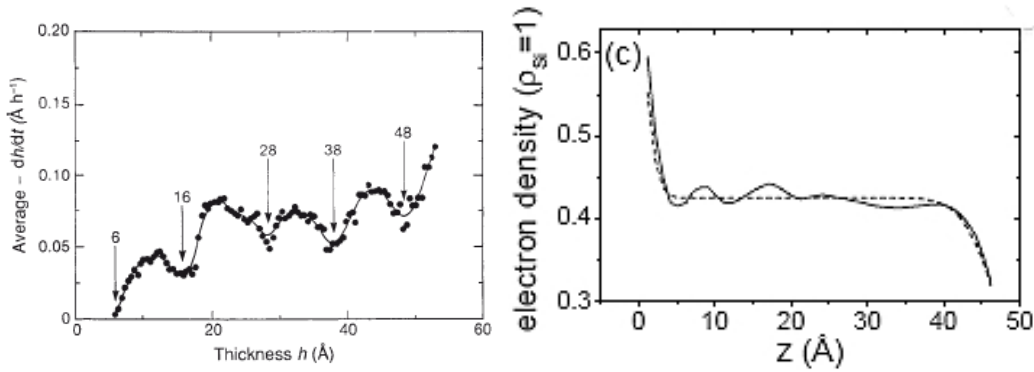
Figure 2.1: (left) Oscillations of evaporation rates depending on film thickness meausred by ellipsometry taken from [Forc93]; (right) electron density varations obtained from X-ray reflectivity taken from [Yu99].

2.1.2 Thin polymer films

In this work the dynamics of amorphous polymers in the vitreous state as well as in the melt are of interest. Thus some short outlines about structure related dynamics will be given here. Mechanic properties as viscosity, shear and relaxation of polymer melts and of solutions of polymers are well obtained from tube models, which were developed by *Doi* and *Edwards* in the late seventies based on considerations from *Rouse* and *Bueche* about chain motions [Sper06]. However tube models still fail to describe polymer dynamics properly. Earlier in the seventies *De Gennes* had developed his theory of reptation of polymer chains, which provides good results for dynamical properties of rubbery polymers. According to the *De Gennes Reptation Theory* the self-diffusion coefficient D of polymer chains in bulk polymer well above glass transition temperature T_g depends on the molecular weight M_w as [Sper06]

$$D \propto M_w^{-2} \,. \tag{2.1}$$

In the vitreous state, far below T_g no translational self-diffusion is expected - although there are some hints at possible lateral displacements due to anisotropies of the films in long term studies on polymethyl methacrylate (PMMA) at 20 K below T_g [Veni99]. Nevertheless, the picture changes when approaching T_g. A parameter for measuring polymer flexibility is the radius of gyration R_g of polymer chains. R_g^2 is defined as the mean square distance away from the center of gravity [Sper06]. Different relationships hold for spheres, rods and random coils. In general R_g^2 is a measure of the stiffness of the respective polymer chain.

Confinement effects

Effects of confinement on the glass transition temperature T_g have been reported from various experiments, see e.g. [Kedd94a] and are widely discussed, e.g. [Genn00]. In thin

films, the direction of the change in T_g depends on the kind of substrate used. Thus e.g. on gold surfaces the T_g of PMMA decreases with decreasing film thickness, while on native SiO_x an increase of T_g is reported [Kedd94b]. Recently improved data analysis from X-ray reflectivity enabled Ahn et al. to prove density enhancement within thin PMMA films at interfaces with Si wafers with native oxide at room temperature, i.e. well below T_g [Ahn09]. By using different polymers and also mixtures of them, they could show that this enhancement depends on one hand on electrostatic interactions (due to polarity) and on the other hand on chemical interactions and H-bonding. In the case of PMMA, H-bonding exists between the ester oxygen and the surface silanols of the Si wafers containing native oxide (after cleaning with piranha solution).

Above T_g in polymer films with strong interactions with the solid surface a slow down of diffusion was observed for films up to 25 R_g thick [Fran96], while the most dramatic decrease occurred below 3 R_g [Lin99]. For PnAMA ranging from alkyl length 1 (PMMA) to 8 (poly-n-octyl methacrylate, POMA) deviations from bulk behavior for T_g and the coefficient of thermal expansion were observed for films thinner than approximately 60 nm [Camp07].

2.1.3 Thin liquid crystal films

Some materials do not show a single transition from solid to liquid, but undergo transitions to one or several mesomorphic phases in between. Since in those meso-phases the materials contain liquid-like as well as solid-like properties, they are named liquid crystals (LC). Although liquid crystals have been known for more than one century now, thorough investigation of their properties only started in the 1960, when the importance of potential applications was realized, while also specific scientific tools for their investigation, like NMR, became available [Genn93, Dunm11]. In liquid crystals usually a liquid-like order exists at least in one direction of space, while some anisotropy is present. Some types of liquid crystals also display a crystalline-like order in one or two directions of space. The direction of the ordering in nematic and smectic-A liquid crystals is described by the liquid crystal director **n**, as is depicted in Fig. 2.2. A significant property of smectic liquid crystals is their reduced compressibility along the director (layer nor-
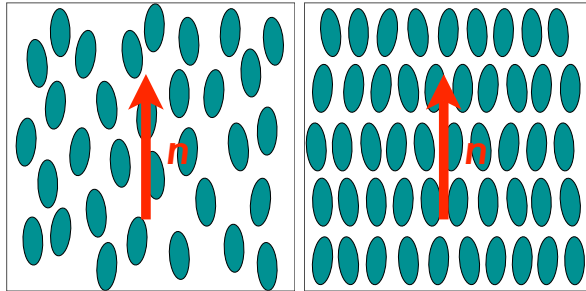

Figure 2.2: (left) Nematic phase, (right) smectic-A phase of a liquid crystal together with the resp. director **n**.

mal) **n**, since compression along **n** or tilt of the layers will lead to a change in the energy density of the smectic liquid crystal [Genn93].

Confinement effects

An important property of liquid crystals is their long range order in combination with liquid-like behavior. Thus they naturally are very sensitive to properties and structure of the surrounding media. This fact e.g. is used in liquid crystal cells, where a brushed polymer surface induces alignment of the liquid crystal molecules [Scha96]. The high sensitivity even allows for quantitative analysis of changes in optical appearance of a supported film of liquid crystal induced by specific binding of biomolecules to surface binding sites [Skai00], which may be used in medical applications. In thin smectic-A liquid crystal films contrary boundary conditions at the liquid crystal-air resp. the liquid crystal-solid interface lead to formation of mesoscopic structures such as focal conic domains (FCD) [Desi06], hemicylinders [Zapp11], coexistence of different film thicknesses [Chak10] or instabilities close to transition temperature [Schl02].

2.2 Wetting and hydrodynamics

Wetting phenomena play a fundamental role in everyday life as well as in technical applications, e.g. sand castles cannot be built out of dry sand [Seem05], there the wetting water film is needed to keep the sand grains together. On the other hand Teflon™ is known to prevent adhesion, which led to many industrial applications. Furthermore, as will be explained below, wetting behavior also is related to nano-hydrodynamics.

2.2.1 Wetting and dewetting
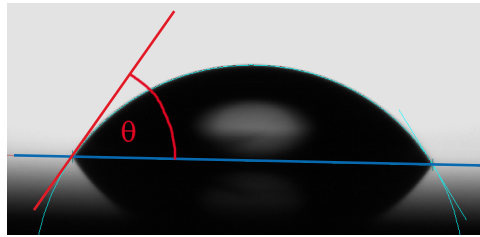
Figure 2.3: Contact angle $\theta = 67°$ of a TEHOS drop on dehydroxylated 100 nm thermally grown silicon oxide.

As was mentioned above, the stability of thin liquid films plays an important role in many technical applications containing solid-liquid interfaces. A quick way to determine the wetting behavior experimentally, is to measure the contact angle θ of the liquid with the substrate, e.g. Fig. 2.3 shows a drop of TEHOS on a dehydroxylated 100 nm thick SiO_x thermally grown on crystalline silicon. The dynamic contact angle $\theta = 67°$ was determined with an OCA20 (*DataPhysics Instruments*, Filderstadt, Germany). For a

contact angle $\theta = 0°$ the liquid wets the solid surface completely, while for $\theta = \pi$ the liquid is non-wetting. In between the behavior of the liquid is termed "partial wetting." In that case the equilibrium contact angle θ is related to a balance of macroscopic forces termed *Young equation*, since it was found by Young in 1805 [Seem05]:

$$\cos\theta = \frac{\sigma_{SV} - \sigma_{SL}}{\sigma_{LV}}\,, \qquad (2.2)$$

where σ_{SV} and σ_{SL} are the solid-vapour and solid-liquid interfacial free energies resp., and σ_{LV} is the liquid-vapour surface tension. Yet *Young*'s eqn. is defined for interfaces *"between semi-infinite media"* and thus *"does not contain specific information about the (long-range) conjoining and disjoining forces acting on a thin liquid film. In order to predict stability conditions for a liquid layer, however, it is necessary to take these forces into account"* [Seem05]. The interaction of these forces can be described as the *"effective interface potential, $\Phi(h)$, [which] contains short-and long-range interactions and is defined as the excess free energy per unit area which is necessary to bring two interacting interfaces from infinity to a certain distance [h] apart"* [Seem05], where h corresponds to the thickness of the liquid layer.

One important part of these interactions are *Van der Waals* forces, which arise from polarization fluctuations in the medium and occur in all materials [Seem05, Isra07]. The *Van der Waals* interaction of two planar surfaces a distance r apart yields [Seem05, Isra07]

$$W(r) = -\frac{A_H}{12\pi r^2}\,, \qquad (2.3)$$

where $W(r)$ is the energy per unit area and A_H is the effective *Hamaker* constant, which depends on the involved materials. It is important to note that the *Van der Waals* forces are long-range forces, which can act on distances up to 100 nm (due to the $1/r^2$-dependence of the potential) [Seem05]. This obviously plays an essential role in confined liquid crystal films, where the use of different thicknesses of oxide layers on silicon wafers led to different liquid crystal structures [Schu09, Schu11].

Recently the influence of surface structure on wetting behavior has been discovered, which also plays an important role in nature, e.g. in plant surface structures [Feng11]. Thus phenomena like super-hydrophobicity and super-hydrophilicity have led to an on-going field of research [Yosh02, Blos03, Yang06].

With respect to the thin liquid films studied in this work, one aim has been to investigate the influence of surface hydropathy on diffusion properties. The here used Si wafers with thermally grown SiO_x are known to be hydrophilic [Belg10], whereas silane monolayers are commonly used to provide hydrophobic surfaces, e.g. [Evme02, Belg10]. However, dewetting of the TEHOS films on octadecyltrichlorosilane (OTS) monolayers [Tren09a] led to the search for a different possibility to study hydrophobic interfaces. Surface hydropathy of silicon oxide is related to the number of OH-terminated Si atoms (i.e. Silanols), which can be modified by temperature treatment, see section 4.2.2 and [Zhur00]. Thus to achieve hydrophilic silicon oxide surfaces, the substrates were boiled for at least 10 h in water, while tempering at 800°C reduced the number of surface

silanols, see section 4.2.2 and [Schu10a]. Moreover, with respect to hydropathy structured SiO_x surfaces were generated by the use of laserinduced dehydroxylation [Hart09] on hydroxylated silicon wafers with 100 nm thermally grown oxide [Schu10a].

2.2.2 Hydrodynamic models

In general, when a liquid flows along a solid surface (i.e. a "wall") it will experience friction at the solid surface. Since (in laminar flow) liquid molecules are able to glide past each other, this will induce a shear in the liquid. The velocity v will be reduced at the solid-liquid interface and will increase with distance z from the wall. In a sufficient distance from the wall the velocity will no longer be affected by the friction. Thus the shear only occurs in the boundary region close to the wall. The shear rate γ is the velocity gradient along z and thus defined by $\gamma = \partial v / \partial z$. Now the question arises, whether the velocity of the fluid under shear will be zero at the interface or whether some kind of gliding exists, which gives the fluid a non-zero velocity directly at the interface. The latter case is termed as slip-boundary condition. The slip length b is defined as the negative distance from the wall, where the shear will have decayed to zero. However, continuos motion of a fluid is a macroscopic view, which breaks down on the molecular level. Nevertheless, the consideration of no-slip or slip boundary condition can often be used to approximate dynamics even on the nanometer scale [Tren09b, Schu10b].

The above mentioned wetting behavior at solid-liquid interfaces plays an important role in nanohydrodynamics, because it determines which hydrodynamic model has to be used [Joly06]. Although there exist experimental deviations, from the theoretical and analytical point of view it is thought that no-slip occurs on wetting surfaces, while on nonwetting surfaces the intrinsic slip lengths do not exceed several tens of nanometers. However, larger slip lengths may be achieved on structured surfaces leading to super-hydrophobicity [Joly06]. In the following two models of hard spheres close to a wall will be outlined, corresponding to no-slip boundary condition [Lin00] and slip boundary condition [Laug05]. The question arises, if the motion of the dye molecules used in this work to probe ultrathin liquid films can be explained by one of these models from continuum hydrodynamics.

Brownian motion of hard spheres close to a no-slip boundary

As mentioned above, the no-slip boundary commonly is thought to occur on wetting surfaces. In particular the no-slip boundary condition should be applied to stable liquid films on solid substrates, since stable films only form, if the liquid wets the solid. Lin et al. report on the direct measurement of constrained Brownian motion of isolated PMMA spheres (diameter 0.93 μm) between two glass walls [Lin00]. They outline a hydrodynamic model to describe that motion: Far from the wall the sphere experiences a drag force $F = -6\pi\eta a v$ (v denotes the velocity of the sphere, η and a are the viscosity of the fluid and the radius of the sphere, resp.). Then the *Stokes-Einstein* relation (eqn. 3.6) describes the diffusion coefficient D. When the sphere is close to a wall the drag force increases and the diffusion is hindered. Due to the linearity of the *Stokes* equations, the

drag force can be separated into motions parallel and perpendicular to the wall. Both components are conventionally represented by correction factors $\lambda_\parallel$ and $\lambda_\perp$ multiplying the drag force in an unbounded liquid [Lin00]. $\lambda_\parallel$ and $\lambda_\perp$ are usually expressed as power series in (a/z), where z is the distance from the center of the sphere with radius a to the wall. Lin et al. give first order approximations for both correction factors. $\lambda_\parallel$ resp. $\lambda_\perp$ appear in the denominator of the *Stokes-Einstein* relation for the diffusion coefficient $D_\parallel$ parallel to the wall, resp. the diffusion coefficient $D_\perp$ perpendicular to the wall. Thus [Lin00]

$$\frac{D_\parallel(z)}{D} \approx 1 - \frac{9}{16}\left(\frac{a}{z}\right) + \mathcal{O}\left(\frac{a}{z}\right)^3, \tag{2.4}$$

and [Lin00]

$$\frac{D_\perp(z)}{D} \approx 1 - \frac{9}{8}\left(\frac{a}{z}\right) + \mathcal{O}\left(\frac{a}{z}\right)^3. \tag{2.5}$$

Actually the higher orders of the *Taylor series* in eqn. 2.4 and 2.5 can only neglected for $a/z \ll 1$. However Lin et al. showed that for $(z/a) > 1.5$ the difference between the first order approximations eqn. 2.4 resp. 2.5 and higher order approximations is $< 1\%$. Furthermore, taking higher orders of the series into account will lead to an even steeper increase of the corresponding diffusion coefficients. This has to be kept in mind, when film thicknesses in the range of the particle size ($a/z \approx 1$) will be considered.

Slip boundary condition for Brownian motion of hard spheres

However, as experimentally accessible lengths scaled down, deviations from the no-slip behavior at wetting boundaries were observed [Laug05]. Lauga and Squires developed a lengthy general expression for a hard sphere undergoing Brownian motion near a partial-slip boundary for incompressible fluids [Laug05]. For small slip length (i.e. $b \ll z$, where z is the experimental length scale) they obtain the following corrections to the above given eqn. 2.4 and 2.5

$$\frac{D_\parallel(z)}{D} = 1 - \frac{9}{16}\left(\frac{a}{z}\right)\left[1 - \frac{b}{z} + \mathcal{O}\left(\frac{b}{z}\right)^2\right] + \mathcal{O}\left(\frac{a}{z}\right)^3, \tag{2.6}$$

and

$$\frac{D_\perp(z)}{D} = 1 - \frac{9}{8}\left(\frac{a}{z}\right)\left[1 - \frac{b}{z} + \mathcal{O}\left(\frac{b}{z}\right)^2\right] + \mathcal{O}\left(\frac{a}{z}\right)^3. \tag{2.7}$$

As can easily be seen, for vanishing slip b the results for a no-slip surface are recovered [Laug05].

2.3 Single molecule methods for investigation of confined soft matter

As was already outlined in the introduction, single molecule (SM) methods are suitable tools to study properties of confined soft matter. In contrast to ensemble methods they

allow for the study of heterogeneous environments, since single molecules probe their local environments. In SM experiments, single dye molecules usually are excited by a laser beam at a certain wavelength. This causes them to fluoresce, which is recorded by a CCD camera or an APD coupled to a microscope. To be able to record fluorescence signals from single dye molecules, they have to be highly diluted within the studied material. The concentrations depend on the particular method, however, typical concentrations range from 10^{-11} mol/l to 10^{-8} mol/l. A short outline of the photophysics of fluorophores is given below. In general SM methods can be classified into two groups (i) SM methods recording fluorescence images of the probe molecules, e.g. single molecule tracking (SMT) experiments, and (ii) SM methods recording SM spectra or fluorescence time traces of the molecules, e.g. [Vall04, Krau11a]. Although fluorescence correlation spectroscopy (FCS) fits into neither category, it is commonly also addressed as SM method. However FCS analyzes the fluorescence fluctuations stemming from highly diluted dye molecules in the focal volume. Thereby the number of simultaneously monitored fluorophores has to be small (< 10) [Schw02]. Nevertheless, in case of large labeled biomolecules in fact single molecules are investigated by FCS.

Another possibility is to categorize SM methods by the type of microscope used for the experiments, which will be done in section 2.3.2.

2.3.1 Photophysics of fluorophores

Here a short outline of the photophysics of fluorophores will be given, following the presentation of the topic by Valeur [Vale05]. Thus for more details see [Vale05], from which also the *Perrin-Jablonski* diagram shown in Fig. 2.4 is taken. This diagram visualizes in a simple way the photophysics of a single dye molecule. *"The singlet electronic states* [of the dye molecule] *are denoted S_0 (fundamental electronic state), S_1, S_2, ... and the triplet states, T_1, T_2, ... Vibrational levels are associated with each electronic state"* [Vale05]. The small spacing of the vibrational levels at room temperature leads to the broad and structureless shape of most absorption and emission spectra. However some aromatic hydrocarbones, e.g. perylenes, exhibit vibronic side bands in their spectra, which is due to the occupation of the resp. energy levels at room temperature and the so called *Franck-Condon factors* that determine the relative intensities of the vibronic bands.

Upon excitation by a photon of suitable wavelength, an electron is shifted from the electronic ground state S_0 of the molecule to an excited state. The molecule then has several possibilities to return into the ground state, the most important ones of which are: (i) internal conversion (IC), i.e. non-radiative transition between two electronic states of the same spin multiplicity; (ii) fluorescence, i.e. the radiative relaxation from the S_1 (in some rare cases also from S_2) to the ground state S_0, whereby the *lifetime* (τ^*) is the characteristic time for the exponential decay of the fluorescence intensity after excitation; (iii) intersystem crossing (ISC) from the S_1 state towards the T_1 state, which occurs on a time scale of 10^{-7} s to 10^{-9} s and may therefore be fast enough to compete with fluorescence de-excitation from the S_1 state; and (iv) phosphorescence, i.e. radiative de-excitation from the T_1 state. Similar to the lifetime τ^* of the S_1 state

also a lifetime τ_{Tr} of the T_1 state can be derived as characteristic time from the radiative and non-radiative decay of this state. Experimentally τ_{Tr} may be derived e.g. by analysis of fluorescence intermittence from single molecules [Voge95] or as characteristic decay time of fluorescence intensity fluctuations from FCS experiments, see section 3.4.3 and [Wide94]. Triplet lifetimes range from 10^{-6} s to 1 s depending on the molecule and the environment (medium, temperature). Thus in SM experiments the de-excitation pathways involving the T_1 state appear as dark intervals, i.e. triplet blinking.
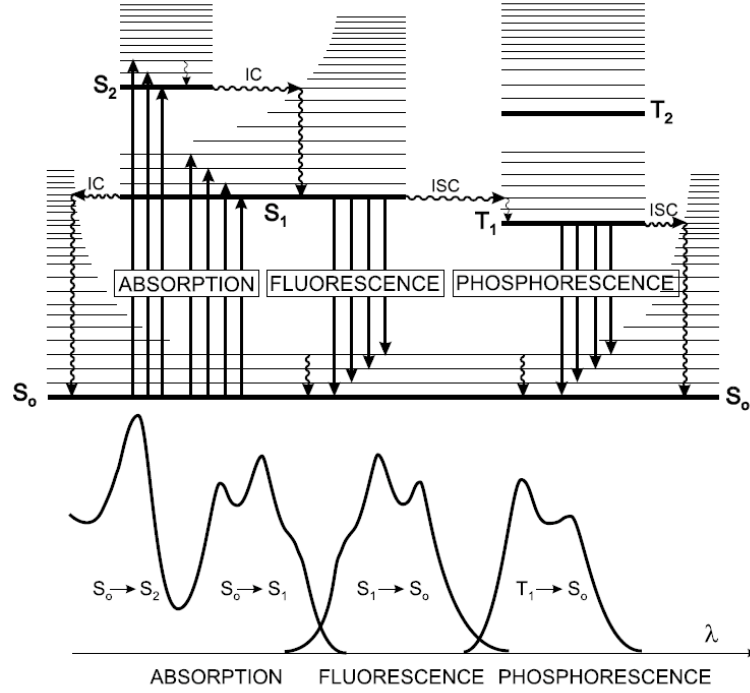

Figure 2.4: *Perrin-Jablonski* diagram and illustration of the relative positions of absorption, fluorescence and phosphorescence spectra, taken from [Vale05].

However, triplet blinking is not the only cause of dark intervals in SM experiments. In Fig. 2.4 only intra-molecular excitation and de-excitation pathways are depicted. Additionally the dye molecule may interact with the surrounding matrix not only by collisions leading to vibrational relaxation, but e.g. by electron transfer or by conformational changes. The latter may also lead to shifts of the fluorescence spectra on observable timescales, i.e. spectral diffusion, see section 3.5 and chapter 5. Besides the blinking dye molecules also will undergo (photo-)bleaching [Gens05, Schu07], i.e. *"a general term for any photochemical process that causes the molecule to eventually change to another form and stop absorbing and/or emitting photons. In practice, at room temperature almost all molecules in aqueous solution photobleach after the emission of $\approx 10^6$ photons"* [Moer03]. A common idea is that photobleaching occurs from a triplet state of the fluorophore, e.g. by photo-oxidation. Thus reduction of the presence of oxygen has

proven to minimize the photobleaching [Desc02, Moer03].

The relation of radiative (k_r) to non-radiative (k_{nr}) de-excitation rates is described by the (fluorescence) quantum yield Φ_F, which is defined as:

$$\Phi_F = \frac{k_r}{k_r + k_{nr}} = k_r \tau^* . \tag{2.8}$$

Thus the quantum yield Φ_F gives the ratio of the number of emitted photons to the number of absorbed photons. Consequently, dye molecules suitable for SM experiments are required to have a high Φ_F, preferentially close to 1.

Another important quantity concerning the excitation of dye molecules is their absorption cross section σ_A, i.e. the effective area of a molecule which is able to capture a photon from the incident laser beam. In solution, i.e. for freely rotating molecules an effective cross section can be evaluated, which is proportional to the total frequency width of the absorption and thus temperature dependent [Moer03]. However the actual σ_A depends on the orientation of the dye molecule in respect to the incident laser beam. In particular for high absorption probability the optical transition dipole of the dye molecule has to be oriented parallel to the electromagnetic field vector. Since this transition dipole is different for different transitions (e.g. $S_1 \rightarrow S_0$ resp. $T_1 \rightarrow T_0$), polarization selected excitation and detection can be used to determine the kind of transition causing the observed fluorescence bands [Cham74]. Furthermore restricting the rotation of the dye molecule can be used to selectively excite specific subselections of dye molecules in a sample and/or to gain information on the structure and dynamics of the surrounding matrix [Schu11], see section 7.2.

2.3.2 Single molecule methods

From an experimental point of view, the various single molecule methods for studying confined soft matter can be grouped according to the type of microscope setup. The conventional optical microscope is a wide field microscope, where a certain region on the sample is imaged simultaneously. Other to this, confocal microscopes only record the fluorescence signal from a tiny spot focussed on the sample. Yet also spatial information may be obtained by scanning the focal spot over a larger region on the sample. Both types of microscopes were used within this work. For the sake of completeness, also near field microscopy will be mentioned briefly.

Near field microscopy

In contrast to the conventional far-field techniques, near field microscopy works below the diffraction limit of light (which is $\approx \lambda/2$). For this an aperture with a diameter much smaller than the diffraction limit is used, e.g. a fractured and metal-coated end of an optical fiber [Moer03] or a nano-fabricated tip. *"If the radiation that propagates through this small hole is detected in close proximity of this aperture, that is within an axial distance on the order of the aperture diameter (far below the optical wavelength), the spot size detected will be that of the sub-wavelength aperture"* [Moer03]. With the use

of scanning technologies the tip can be scanned along the sample surface at a distance of a few nanometers. According to Moerner et al. the advantages of scanning near filed microscopy (SNOM) are (i) lower background due to the reduced sample volume, (ii) immediate orientation information, and (iii) additional topographic information. However the drawbacks are weak intensities and the restriction to almost planar sample surfaces due to the need of the very small working distance [Moer03].

SM methods using wide field microscopes

The fortune of a wide field microscope is the possibility to simultaneously monitor an extended region of the sample. Typical lateral extensions of wide field images are 10-40 μm. Thus, translational diffusion of small molecules in medium viscous material can be monitored by recording images series (where a single wide field image commonly is addressed as *frame*). SMT experiments then trace the fluorescence images of single molecules along the time series of frames [Schm96, Schu03, Zürn07, Schu10b]. For more details see section 3.3 in the following chapter. From SMT experiments information related to translational diffusion can be obtained, e.g. type of diffusion, diffusion coefficients, statistics of adsorption events, and with the use of temperature variation also activation energies for diffusive processes [Honc08]. Advanced applications make use of spectral separation, e.g. to study aggregation of differently labeled biomolecules via *Förster* resonance energy transfer (FRET) [Stei09].

   Further SM methods using wide field microscopy rely on recording fluorescence time traces from fixed regions of the sample. In that case translational diffusion is not desirable (if homogeneous illumination and detection over the investigated region can be assured, a combination with SMT may be possible). The single molecules therefore have to be immobilized at certain positions of the sample, which can be done by the use of highly viscous media, e.g. polymers, or by positioning the dyes on a solid substrate within air. In principle such investigations can also be conducted with a confocal microscope. However there one molecule has to be studied per acquisition, while the extended area simultaneously recorded in a wide field microscope allows to obtain a suitable amount of data for good statistics within a single image series (i.e. video sequence). One such application is to study blinking statistics of single molecules [Schu05]. An advanced method here makes use of polarization splitting, i.e. the fluorescence image is split into two simultaneously recorded images with perpendicular polarization. By crosscorrelating thus obtained fluorescence traces from matching positions in both images, information on rotational behavior of the dyes can be derived [Scho04]. One drawback of wide-field microscopy, however, is the temporal resolution, which in respect to fast processes is restricted to frame times τ_{frame} of few milliseconds only.

SM methods using confocal microscopes

SM methods using confocal microscopes are numerous. Here the fluorescence recording is restricted to the focal volume of the laser beam, which typically is in the range of femtoliters [Schw02]. This can further be reduced by using two-photon excitation [Berl95].

A very common use of confocal microscopy is the above already mentioned fluorescence correlation spectroscopy, for more details see section 3.4. This is in particular widely used in Biophysics. Apart from the simple application using one excitation beam and one detection channel in recent years more sophisticated setups have been developed. E.g. Enderlein et al. developed a two-focus system, by which diffusion coefficients of Rhodamines in water could be determined with high accuracy, thus correcting the previously established value [Dert07]. Furthermore similar to that of wide field microscopes the detection can be separated into several channels for polarization resolved measurements and/or spectral separation of different species. This in particular allows for applications using *Förster* resonance energy transfer. FCS in particular is suitable to study fast processes which require a temporal resolution in the range of ns up to tens of ms.

Other methods employing confocal microscopes e.g. are single photon counting methods, which allow for the determination of fluorescence lifetimes of the tracer molecules. Thus, by using a dye molecule displaying two geometrical conformations with distinguishable lifetimes, Vallée et al. probed the free volume in polymer matrices [Vall04]. As mentioned above, also spectra and time series of spectra from single dye molecules can be recorded using a confocal microscope. This e.g. allows for studying conformational dynamics of dye molecules, as long as the involved geometrical changes affect the electronic configuration of the fluorophore and thus its spectral position [Kowe09, Krau11a]. This in turn may be used for the evaluation of physical properties of the surrounding matrix [Hou00, Kim06]. The dynamics of SM spectra have been named *spectral diffusion*. Here in this work the analysis of such spectral diffusion is accomplished via probability distributions of spectral diffusivities [Krau11a]. For more details see section 3.5 and chapter 5.

In recent time several super-resolution techniques have been developed, most of which are based on scanning confocal microscopy, see e.g. [Hell04b, Blow08, Dert10]. Some of them simply use two types of dye molecules to label their probe molecules together with two-color excitation and detection to measure distances in the nanometer range. Others do not work on the single molecule level, but obtain the high resolution by selectively bleaching the fluorophores outside a small spot, e.g. stimulated emission depletion (STED) uses two-colored excitation and a sophisticated diffraction pattern to obtain fluorescence from a nanometric central region only [Dyba03].

3 Single molecule dynamics in confined soft matter

3.1 Random walks and mean first passage times

Single particle diffusion very often is analyzed and/or simulated via random walk models [Schu02b, Kirs07], e.g. in two dimensions a random walker takes steps of a certain step length and with a selected angle during a distinct time interval. Usually the angle and either the step length or the time interval are randomized, while the other component is fixed. These models are widely used for simulations [Schu02b, Heid09a]. Thus the simulation program developed by Heidernätsch, which is used in this work in section 4.3.2 is based on constant time steps, where particles take steps with randomly distributed angles and a step length randomly chosen from a Gaussian distribution. The variance of the latter equals a diffusion coefficient which is set before running the simulation. Furthermore a dynamic exchange between layers containing different diffusion coefficients can be simulated as well, then exchange rates between those layers have to be set [Heid09a].

In many cases of investigation, heterogeneous or even anomalous diffusion is observed [Saxt96, Hac05]. Then very often besides the dynamic exchange described above, also hindering obstacles have to be implemented into the paths of random walks. Furthermore, random walks on clusters and percolation theory [Höfl06] are used to study diffusion phenomena. Altogether this is a wide field of theoretical research, see e.g. [Kamm08, Neus09].

3.1.1 Mean first passage times

Subjects as different as biochemical reactions and pathways of animals foraging strategies can be described by random walk models [Shle07]. One has to know the probability of arriving at each of the reaction steps/sites to characterize the walk. Nevertheless the question, how many random steps it will take the walker to reach a certain site for the first time, cannot be answered easily. Instead of this "first passage problem" it often is easier to calculate mean first passage times (mfpt) to an arbitrary site [Shle07]. In case of the ultrathin liquid crystal films studied in this work, it is interesting to know the average time it will take a dye molecule to re-adsorb at the solid-liquid interface again. This problem can be described by a random walk with a reflecting boundary (at the liquid-air interface) and an adsorbing boundary at the solid-liquid interface. For the latter different docking probabilities p_{dock} may be considered. In general there exist analytical solutions for this kind of problem, e.g. McKenzie et al. study mfpt of animal
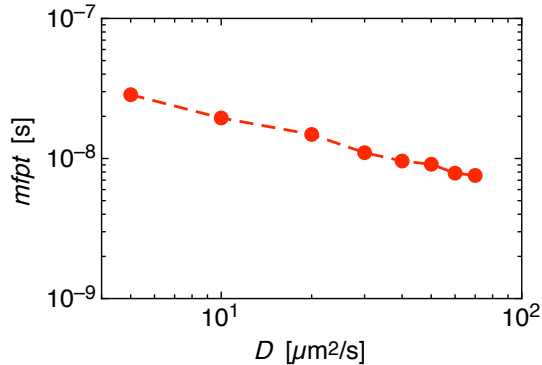
Figure 3.1: mfpt for 5 μm^2/s $\leq D \leq$ 70 μm^2/s, film thickness $d = 10$ nm and docking probability at the solid-liquid interface $p_{dock} = 1$.

movement [McKe09]. They reformulate the unbiased random walk using the spatial displacement ϵ and the time interval τ. Then the mfpt $T(x)$ of a location x is given by [McKe09]:

$$T(x) = \tau + \frac{1}{2}T(x - \epsilon) + \frac{1}{2}T(x + \epsilon), \tag{3.1}$$

since the walker located at x has equal probability of jumping a step ϵ to the left or right. Using Taylor series expansion and applying the diffusion approximation $D = \lim_{\epsilon, \tau \to 0} \frac{\epsilon^2}{2\tau}$ they obtain the differential equation [McKe09]:

$$D\frac{\partial^2}{\partial x^2}T(x) + 1 = 0. \tag{3.2}$$

McKenzie et al. then use this diffusion equation to study a random walk with starting position 0 and end position L. Thereby a reflecting boundary is given at the starting position 0, while at the end position L the walker is adsorbed. Applying a *Neumann* condition $\frac{\partial}{\partial x}T(x) = 0$ yields the reflecting boundary, while a *Dirichlet* boundary condition $T(x_L) = 0$ is used for the adsorbing boundary at L. Then eqn. 3.2 has the solution [McKe09]:

$$T(x) = \tau + \frac{1}{2D}(2Lx - x^2). \tag{3.3}$$

Nevertheless the question about the mfpt of a particle starting at the adsorbing boundary and re-adsorbing to the boundary, cannot be solved by this eqn. 3.3, since in the above described model the particle will not even start, because a *Dirichlet* boundary condition $T(x = 0) = 0$ has to be applied for the adsorbing boundary at $x = 0$.

Therefore, the question of mfpt within ultrathin liquid films here was addressed by a one-dimensional random walk simulation[1], which calculated the mfpt using a Gaussian distributed random variable with mean zero and variance $2D\tau$. The starting position was set to the adsorbing boundary. Yet in the initial step the adsorbing boundary condition

---

[1] M. Heidernätsch provided the simulation program

was replaced by a reflecting boundary condition to get the walkers started. By this a semi-Gaussian distribution of the N walkers next to the absorbing wall was created. Simulations were run for a number of 50000 walkers and a time step of 10^{-11} s. Diffusion coefficients were varied in the range of 5 to 70 $\mu m^2/s$ with film thickness $d = 10$ nm and $p_{dock} = 1$, see Fig. 3.1. As can be seen, for the studied range of diffusion coefficients, the mfpt for a 10 nm thick film is well below 10^{-7} s when $p_{dock} = 1$ is assumed. This result will be of interest in section 6.4 in combination with the analysis of results from FCS experiments.

3.2 Diffusion equations

As stated in the introduction, diffusion is a very widely observed phenomenon. In textbooks considerations often start with concentration gradients in inhomogeneous mixtures of particles [Atki06]. Then the diffusion equation, i.e. *Fick's second law* of diffusion:

$$\frac{\partial c(\mathbf{r}, t)}{\partial t} = D \frac{\partial^2 c(\mathbf{r}, t)}{\partial \mathbf{r}^2} ,$$

(3.4)

with diffusion coefficient D and concentration c, follows from *Fick's first law of diffusion* relating the particle flux J with the spatial change ($\mathbf{r}$ is the vector spanning the spatial dimensions) in concentration:

$$\mathbf{J} = -D \frac{\partial c(\mathbf{r}, t)}{\partial \mathbf{r}} .$$

(3.5)

In general the diffusion coefficient D is neither constant over space nor over time, but it rather is given as a time and space dependent diffusion tensor $\mathbf{D}(t, \mathbf{r})$. Nevertheless diffusion coefficients can be considered for many cases, where physical properties spread according to *Fick's second law*, eqn. 3.4. In the following two well known equations will be given, relating macroscopic diffusion coefficients to properties of the involved particles and solvents.

3.2.1 *Stokes-Einstein* relation for translational diffusion

Translational diffusion of a particle in a liquid can be estimated macroscopically using the *Stokes-Einstein* relation [Bril91]

$$D = \frac{k_B T}{6 \pi \eta a} ,$$

(3.6)

where k_B and T are the *Boltzmann* constant and absolute temperature resp., a is the hydrodynamic radius of the particle and η is the viscosity of the fluid (for common liquids $\eta \propto 1/T$). This equation relates the translational diffusion coefficient D to the *translational Stokes friction* $\gamma_{\text{trans}} = 6 \pi \eta a$ of a sphere with radius a in low viscosity liquids. Thereby a no-slip boundary condition is applied at the interface of the sphere with the liquid.

3.2.2 *Debye-Einstein* **relation for rotational diffusion**

Similar to the *Stokes-Einstein* relation, which relates translational diffusion to macroscopic properties of a liquid, also rotational diffusion can be related to such properties. Thus on a macroscopic scale rotational diffusion can be estimated by the *Debye-Einstein* relation [Bril91]

$$D_{\rm rot} = \frac{k_B T}{8\pi\eta a^3} \,. \tag{3.7}$$

By this equation the *rotational Stokes friction* $\gamma_{\rm rot} = 8\pi\eta a^3$ of a sphere with radius a in low viscosity liquids is related to the rotational diffusion coefficient $D_{\rm rot}$. Also here a no-slip boundary condition holds at the interface of the sphere with the liquid.

In this work diffusion in confined soft matter is studied by the use of fluorescing probe molecules. Although the used single dye molecules have sizes in the range of 1 nm, the above equations can be used to approximate the respective macroscopic diffusion coefficients. However, deviations are expected due to solvent interactions, see e.g. [Jena79] and Table 4.1 in section 4.2.1. Nevertheless the order of magnitude is obtained quite reliably. Furthermore the translational self-diffusion coefficient obtained from bulk TEHOS by NMR experiments is only slightly larger than the diffusion coefficient calculated for R6G using the *Stokes-Einstein* relation eqn. 3.6, see section 4.2.3. This is due to the almost similar size of R6G and TEHOS molecules together with the reaction reluctant property of TEHOS.

3.2.3 *Einstein Smoluchowski* **equation**

Since in this work diffusion is studied on a microscopic scale, i.e. motion of single dye molecules, a relation between single particle motion and macroscopic diffusion coefficients is needed. In 1905 and in 1906 Einstein and Smoluchowski related one-dimensional particle motion with a macroscopic diffusion coefficient. Be λ_x the square root of the arithmetic mean of the squares of all displacements of particles along the x-axis during the time interval τ, then according to Einstein [Eins05] it is related to the macroscopic diffusion coefficient D by:

$$\lambda_x = \sqrt{\bar{x^2}} = \sqrt{2D\tau} \,, \tag{3.8}$$

where $\bar{x^2}$ is the arithmetic mean of all square displacements in the direction of x. *Einstein* also gives the three dimensional case to be equal to $\lambda_x\sqrt{3}$ [Eins05]. In a generalization to n dimensions $\lambda_{\mathbf{r}}^2$ is the sum over the $\bar{r_i^2}$, i.e. the msd obtained in the i-th dimension. Hence, in case of uncorrelated motion in different dimensions, the generalization of eqn. 3.8 is given by:

$$\lambda_{\mathbf{r}}^2 = \sum_{i=1}^{n} \bar{r_i^2} = 2\sum_{i=1}^{n} D_i\tau \,, \tag{3.9}$$

with diffusion coefficient D_i in the i-th dimension. In case of free isotropic diffusion, all D_i have the same value D, leading to

$$D = \frac{\lambda_{\mathbf{r}}^2}{2n\tau} \,. \tag{3.10}$$

The definition of λ_x given by Einstein [Eins05] corresponds to the mean square displacement (msd) averaged over a large sum of diffusing particles. Therefore, eqn. 3.8 relates the macroscopic diffusion coefficient to an ensemble average. In contrast Smoluchowski considered the motion of one particle in a surrounding medium. Then the length of the observation plays a crucial role [Smol06]. Thus the diffusion coefficient can only be derived from the time average of square displacements along a particle trajectory, if the observation time is much larger than the length of the individual time steps. *Smoluchowski* considered a particle moving in three dimensions, but the equation easily can be generalized for n dimensions, leading to

$$D = \lim_{\tau \to \infty} \frac{\mathrm{msd}(\tau)}{2n\tau} \,, \tag{3.11}$$

where D is the macroscopic diffusion coefficient, $\mathrm{msd}(\tau)$ now is the time averaged square displacement along a trajectory, and τ denotes the time lag of the observation. This equation is commonly addressed as *Einstein-Smoluchowski* equation for n dimensions.

Nevertheless one has to keep in mind that both *Einstein* and *Smoluchowski* considered free Brownian motion in an ergodic system. When the ergodicity is broken, the ensemble average is no longer equal to the time average, i.e. eqn. 3.10 and eqn. 3.11 no longer yield the same diffusion coefficient [Lube08].

3.2.4 *Langevin* **equation and** *Fokker-Planck* **equation**

Since the work of *Einstein* and *Smoluchowski* leading to the above equation more than a century has passed now. As the field of statistical physics evolved also new approaches and mathematical tools have been developed. On the level of a single moving particle (or a random walker) *Langevin* equations can be applied to describe the motion, i.e. a stochastic force is added to the newtonian equation of motion. A *Langevin* equation for Brownian motion is given in [Risk96]:

$$\frac{\partial v}{\partial t} + \gamma v = \Gamma(t) = \sqrt{k_B T}\, \zeta(t) \,, \tag{3.12}$$

where γ is the damping coefficient and $\Gamma(t)$ is the fluctuation force per unit mass, which is called the *Langevin* force. $\zeta(t)$ is white noise, i.e. it is a Gaussian variable with zero mean and unity variance which is uncorrelated in time ($\langle \zeta(t)\zeta(t') \rangle = \delta(t - t')$).

However, often the picture of a physical quantity undergoing transitions with random processes is preferred. Then *Fokker-Planck* equations provide a powerful tool to describe the evolution of the physical quantity [Risk96]. In case of Brownian motion not the motion of a single particle, but the evolution of the ensemble can be described by a *Fokker-Planck* equation. From the transition probability density obtained by solving the equation, statistical quantities (e.g. the i-th moments of the probability density distribution) can be derived. Thus on one hand a complete mathematical description of the evolution of the physical system is given, while on the other hand physical quantities, as the macroscopic diffusion coefficient, will be obtained due to their relation to

the moments of the probability distribution. This approach is applied in the following sections 3.3.7 and 3.5.2, where diffusion coefficients are derived from probability distributions of diffusivities, i.e. scaled square displacements. A general form of the *Fokker-Planck* equation for n variables (e.g. n dimensions) is given in [Risk96]:

$$\frac{\partial p(\mathbf{x},t)}{\partial t} = \left[-\sum_{i=1}^{n} \frac{\partial}{\partial x_i} D_i^{(1)}(\mathbf{x}) + \sum_{i,j=1}^{n} \frac{\partial^2}{\partial x_i \partial x_j} D_{ij}^{(2)}(\mathbf{x}) \right] p(\mathbf{x},t) \,. \qquad (3.13)$$

The drift vector $D_i^{(1)}$ and the diffusion tensor $D_{ij}^{(2)}$ generally depend on the n variables (i.e. n components of $\mathbf{x}$), and $p(\mathbf{x},t)$ accordingly is the distribution function of the n variables. In case of 2 dimensions and zero drift, eqn. 3.13 simplifies to

$$\frac{\partial p(\mathbf{x},t)}{\partial t} = \sum_{i,j=1}^{2} \frac{\partial^2}{\partial x_i \partial x_j} D_{ij}^{(2)}(\mathbf{x}) p(\mathbf{x},t) \,. \qquad (3.14)$$

In case of a constant diffusion tensor this is *Fick's second law*. In general, the diffusion tensor may also be time dependent. For this work an interesting case is layered diffusion, i.e. the diffusion in z is independent from x, but D_x depends on z. Postnikov and Sokolov developed a model for lateral diffusion in that case [Post11], which will be described in section 3.3.9.

3.3 Single molecule tracking (SMT)

The development of lasers as light sources and even more important the improvement of detection sensitivity due to the use of electron multiplying devices enabled the detection of single fluorescent molecules [Nguy87, Moer89, Orri90]. Highly sensitive CCD cameras now provide video sequences of single molecules at frame rates up to ≈ 600 frames per second (fps), while they still yield acceptable signal to noise ratios (snr). For tracking single emitting molecules at a wide field microscope a reasonable number of pixels on the CCD chip has to be used simultaneously, e.g. 50 pixel x 50 pixel. This reduces the speed to ≈ 100 fps. Thus diffusing particles with up to ≈ 10 $\mu\mathrm{m}^2/\mathrm{s}$ may be tracked with sufficient quality. Nevertheless this method strongly depends on singling of emitters, therefore dye molecules have to be highly diluted in the surrounding matrix, i.e. in approximately nanomolar concentration. The *Rayleigh* criterion applied to visible light, yields a possible resolution in the range of 200 to 300 nm ($\hat{=}\lambda/2$). Although several methods have been developed to improve the optical resolution of static or rather slowly moving structures, e.g. stimulated emission depletion imaging (STED) [Hell04a, Blow08], this still is not possible for wide field microscopy. Therefore, the singling of emitters is the crucial feature which enables position accuracies in the range of few nanometers. Of course this also requires ultraclean sample processing to avoid destruction of the accuracy by fluorescing dirt.

Within the obtained video sequences spots representing single molecules are searched and combined into trajectories. For the later several algorithms have been developed.

In this work most video sequences were analyzed using the software package *tracking.sh*, which originally was developed by Schuster et al. [Schu02b, Schu03]. For this, *tracking.sh* was modified, e.g. see section 3.3.2 as well as supplemented with additional features, e.g. see section 3.3.7. Parallel to this work Heidernätsch in close cooperation developed the program *DSAA*, which combines a simulation tool with tracking programs and further data analysis [Heid09a]. Further details and a comparison of results using the different tracking programs are given in section 4.3.

A conventional way to obtain diffusion coefficients form SMT experiments is to calculate mean square displacements (msd) along detected trajectories [Qian91, Saxt97b, Schu03, Zürn07, Arci08, Schu10b].

3.3.1 Position accuracy

Although the *Rayleigh* criterion determines the optical resolution of the microscope, in SM experiments the position of the emitting molecule can be determined one order of magnitude better. Since the dye molecule is more than two orders of magnitude smaller than the wavelength of the emitted light, it can be considered as point like emitter. Hence in the microscope image a diffraction limited spot (i.e. an *Airy* disk), is produced, which depends on the optics and geometry of the setup and can be described by the point spread function of the setup. The radial intensity distribution is a first order Bessel function and can be approximated by a two-dimensional Gaussian [Zhan07].

Nevertheless the quality of fit (from fitting a two-dimensional Gaussian to the detected spots) strongly depends on the signal to noise ratio (snr). The detection noise using CCD chips depends on readout noise from digitalization of the analog signal, i.e. clock induced charge, and on background fluctuations: Diffuse stray light from the environment and the reflection of excitation light have to be reduced by a careful design of the setup and the use of adequate filters. Nevertheless so called *dark counts* occur within the pixels of the CCD chip due to thermal excitation of electrons. This can be reduced by cooling the chip. Furthermore the position accuracy r_{pa} depends on the number of pixels illuminated by a single immobile emitter. However, increasing the number of illuminated pixels geometrically, will only improve r_{pa}, if at the same time the snr is kept constant, which can only be achieved by a longer acquisition time. Thus for a given setup geometry r_{pa} is inversely proportional to the snr [Bobr86, Kubi00]. Within SMT experiments the position accuracy yields a threshold for detecting mobile molecules.

Determination of position accuracy from msd

Due to the restricted position accuracy r_{pa}, the msd of immobile molecules is constant over time with a non-zero constant, $\mathrm{msd}(\tau) = \Delta y \neq 0$, if the trajectory is long enough to give good averaging statistics. Fig. 3.2 (a) shows an example containing three immobile (–) and two slowly moving trajectories ($\cdots$) from an acquisition with frame rate $\tau_{\mathrm{frame}} = 1$ s. The msd from the immobile trajectories fluctuates around a constant value Δy. These fluctuations are mainly caused by the graining of the detected spots due to the pixel size of the CCD and by low statistics (averages over small data sets only). They
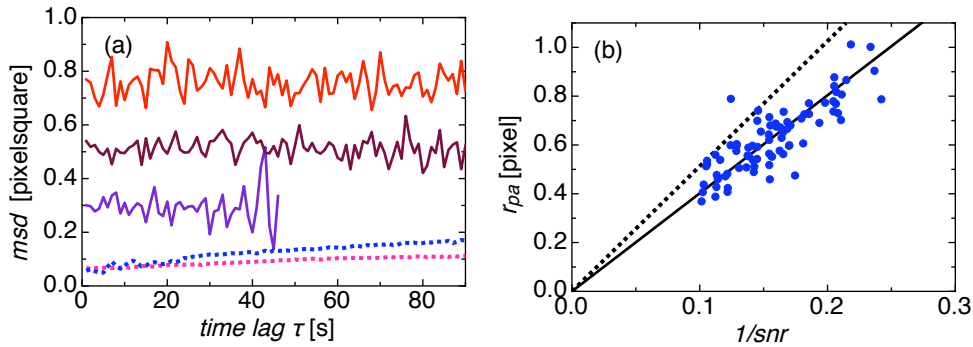
Figure 3.2: (a) msd plots of several trajectories from (–) immobile molecules and ($\cdots$) slowly moving molecules, (b) r_{pa} over the inverse snr for all immobile trajectories detected in one SMT acquisition, (–) mean slope, ($\cdots$) mean slope + 2 standard deviations.

will increase for the largest time lags τ over a trajectory (the msd for these τ is built from few displacements only), as can be seen for the short purple trajectory. The two dotted trajectories are much longer than the other three, hence their msd display smaller fluctuations. For all five trajectories $\Delta y \approx \mathrm{msd}(\tau = 0) \neq 0$, can be derived from a linear fit to the msd. The position accuracy can be derived from the Δy by $r_{\mathrm{pa}} = \sqrt{\Delta y}$ According to Kubitscheck [Kubi00] r_{pa} is inversely proportional to the snr. Thus, the snr is higher for those trajectories with smaller Δy. The snr differs for different trajectories, in particular it is lower for fast diffusing molecules than for immobile ones. Therefore, r_{pa} obtained for an average snr from immobile and slowly moving molecules (as was initially implemented in *tracking.sh*) is a rather rough estimate for the discrimination between mobile and immobile molecules. Hence, *tracking.sh* was modified to derive the Δy form all detected trajectories which are assigned to immobile or slow molecules. Then the squareroot of Δy (i.e. the r_{pa}) is multiplied by the snr obtained for the resp. trajectory. Fig. 3.2 (b) shows a plot of r_{pa} over the corresponding noise to signal ratio (1/snr) for all slow and immobile trajectories detected in one SMT acquisition. Afterwards the mean values of those products (i.e. the slopes in the plot) and their standard deviations are determined. Thus r_{pa} as a function of the snr is obtained and further applied during analysis within *tracking.sh*.

3.3.2 Correction factor for geometrical averaging

Heidernätsch developed a simulation tool for two-dimensional SMT, which provides simulated video sequences similar to those acquired by CCD cameras on experiments [Heid09a]. As mentioned above, the simulation program is part of his *DSAA*-package. A comparison of the diffusion coefficient set for a simulation of homogeneous diffusion with the value obtained from analysis of the simulated video sequence revealed a mismatch, i.e. the latter value was only 2/3 of the initially set diffusion coefficient [Heid09a]. As was previously shown by Montiel et al. [Mont06], as well as by Savin and Doyle [Savi05], this mismatch is due to the geometrical averaging over the path of the molecule during

camera exposure. The detected spots in the video frames usually are fitted by two-dimensional Gaussians, as was described above, see section 3.3.1. This yields the mean position of the diffusing molecule during exposure. Within tracking procedures those mean positions are connected into a trajectory. Then the distance between succeeding positions is calculated. Depending on the exposure time, this procedure yields a smaller value than the real diffusion coefficient [Savi05, Mont06]. Montiel et al. give an approximation in case $\tau_{\text{exposure}} \approx \tau_{frame}$:

$$\frac{D_{apparent}}{D} = 1 - \frac{\tau_{\text{exposure}}}{3\tau_{frame}}, \tag{3.15}$$

where τ_{exposure} is the exposure time of a single frame and τ_{frame} is the frame time, i.e. the time between to starts of exposure (inverse frame rate). Even frame transfer cameras need some few milliseconds where the obtained signal is shifted from the exposed part of the chip to the dark part. Therefore, the frame time is always larger than the exposure time. Nevertheless within typical SMT experiments $\tau_{\text{exposure}} \approx \tau_{frame}$. Hence eqn. 3.15 can be approximated by $D_{apparent}/D \approx 2/3$, i.e. the ratio observed from simulations by Heidernätsch. Therefore, the SMT data shown in this work here were corrected either with $D_{apparent}/D = 2/3$ or with eqn. 3.15.

3.3.3 Types of diffusion
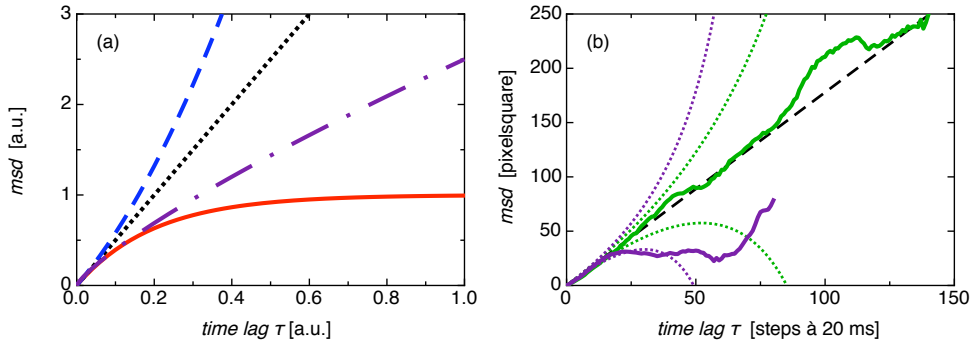
Figure 3.3: (a) msd plots of ($\cdots$) normal diffusion, (—) diffusion in a cage, ($-\cdot$) subdiffusion and (- -) superdiffusion, (b) Experimental trajectories of finite length (light green) 142 steps à 20 ms, (purple) 82 steps, ($\cdots$) limits of corresponding 95% confidence region for the case of homogeneous diffusion; (- -) normal diffusion with coefficient $D_{\text{traj}} \approx 0.6$ μm^2/s obtained for each trajectory from analysis by weighted msd according to Saxton [Saxt97a].

Depending on the physical constraints, the msd along a particle trajectory will exhibit a certain dependence on time. However, the relation between msd and time can be expressed by the following equation (apart from diffusion restricted to a cage):

$$\text{msd} \propto \tau^{\alpha} \qquad \text{where} \qquad 0 < \alpha < 2. \tag{3.16}$$

When the motion of a particle is caused by an external force it will follow a ballistic trajectory, thus $\alpha = 2$. If the motion is caused by a stochastic force, e.g. thermal fluctuations, or if a large enough stochastic force is added to an external force, the motion will be diffusive. Depending on the timescale of observation there will be crossover regions [Li10, Puse11]. The duration of the ballistic motion can be estimated to be the time $\tau_p = m/(6\pi\eta a)$, where m and a are the particles' mass and radius resp., whereas η is the dynamic viscosity of the liquid [Puse11]. For a silica sphere with diameter 1 μm in water $\tau_p \approx 0.1$ μs [Puse11]. In contrast, for a single dye molecule like RhB m is nine orders of magnitude smaller, while a is only three orders of magnitude smaller ($a_{\mathrm{RhB}} \approx 0.67$ nm, see section 6.2.3) yielding $\tau_p \approx 0.1$ ps in water.

Furthermore there are several types of diffusive motion depending on the physical constraints of the motion. Thus we will observe normal diffusion if the motion is caused by a stochastic force only, i.e. no external force acting on the particles. Then in eqn. 3.16 the exponent $\alpha = 1$ and the msd plot is of linear shape (dotted line in Fig. 3.3 a). If also an external force acts on the particles, we will observe superdiffusion (dashed line in Fig. 3.3 a) and $1 < \alpha \leq 2$. Then for short time lags, the diffusive behavior of the motion will dominate, while due to the τ^2 dependence, on long time scales the ballistic motion will take over [Qian91].

If diffusion is restricted to a cage, initially, i.e. for small time lags τ, the msd plot has a linear shape, while it approaches a constant value for larger τ, as can be seen in Fig. 3.3 (a) solid line. If diffusion is hindered by some obstacles or traps, we observe subdiffusion with $0 < \alpha \leq 1$ [Saxt96], see Fig. 3.3 (a) dash-dotted line. In the presence of obstacles, diffusion is anomalous at short times and normal at long times with an intermediate crossover region [Saxt96]. Also a power-law distribution of traps will cause anomalous diffusion, since the probability for the particle to find an even deeper trap gets higher for longer waiting time. In the latter case the system is non-ergodic. Then ensemble averages will differ from time averages along single trajectories [Lube08]. On amorphous substrates the surface potentials may be continuously distributed within some few orders of magnitude, causing a power-law distribution of adsorption times in the corresponding time regime. For example, the silanols on the thermally grown SiO_x used in this work vary in density and in orientation, see section 4.2.2. Thus hydrogen bonds formed with the dye molecules vary in geometry and therefore also in interaction energy. However, the width of the corresponding surface potential distribution is limited. Thus on sufficiently long timescales the dye molecule will sample all traps within the area of observation, i.e. the system becomes ergodic on long time scales. Then homogeneous diffusion with an effective diffusion coefficients is observed.

3.3.4 Interface potentials for adsorption events

For the just mentioned adsorption sites for dyes at the substrate several potentials may play a role, which will be detailed below. However, to calculate the effect on the length of adsorption duration, the average collision rate for the dyes with the surface has to be known. This rate can be calculated for gas molecules at known pressure and temperature, e.g. for N_2 at atmospheric pressure and 25°C it is ≈ 5 ns^{-1} [Atki06]. In liquids the rate

will be much larger due to the higher density. Yet, it is difficult to determine the collision rate with the solid interface, since there density oscillations may occur [Klei98, Yu99, Jabb07], which strongly depend on the type of surface interactions [Evme06]. For this reason, determination of adsorption lengths cannot be achieved from calculations without further knowledge of e.g. the temperature dependence. However, the linear dependence of the collision rate on temperature may be used to relate interface potentials to diffusion measurements by temperature variation [Honc08, Honc09a]. The following types of interactions will contribute to interface potentials at the solid-liquid interface:

Hydrogen bonding: Typical hydrogen bonds have a strength of $\approx 20 \, \text{kJ/mol}$ [Atki06]. Depending on bonding geometry and on the involved types of atoms the bond length will vary and thus also the potential strength. The range of the latter is between $\approx 10 \, \text{to} \, 40 \, \text{kJ/mol}$ ($\approx 10 \, \text{to} \, 40 \, \text{meV}$ for a single bond). On the thermally grown SiO_x, the bond lengths will vary in particular due to geometrical constraints caused by the amorphous structure of the substrate. Furthermore, some dye molecules (e.g. Rhodamines) may exhibit twofold hydrogen bonding, leading to further variation of interface potentials [Honc08].

Electrostatic interactions: The SiO_x grown on n-doped Si wafers is slightly negatively charged. Yet the distribution of e.g. dangling bonds within the SiO_x will induce an interface potential modulation on a molecular scale.

Van der Waals **interactions:** Polarization fluctuations are known to influence the wetting behavior of liquids on solids [Seem01, Seem05]. As was detailed in section 2.2.1, the *Van der Waals* interaction between two planar surfaces has a square dependence on the distance and thus may act on distances up to 100 nm. The potential furthermore depends on the effective *Hamaker* constant A_H, see eqn. 2.3, which may be calculated for specific combinations of materials, see e.g. [Tren09a]. However, to determine adsorption lengths of dye molecules, not only the vertical modulation of the potential for the system solid-liquid-air has to be known. The dye molecules themselves will induce modulations on the local potential structure.

3.3.5 Finite length of observation

The above detailed interface potentials will lead to an almost continuos distribution of potentials of adsorption sites and thus to anomalous diffusion on corresponding timescales. Yet, it may be desirable to obtain effective diffusion coefficients at longer observation times, where the system is ergodic and thus exhibits homogeneous diffusion. However, in contrast to theoretical derivations and numerical simulations, experimental investigations are quite often constrained by limitation of the observable area and by limited time of observation. In particular, with single molecule (SM) studies observation is limited by bleaching and blinking of the dye molecules. Tracking experiments are further restricted due to the limited residence time of the dye molecule within the observed area. Fig. 3.3 (b) shows msd plots of two experimental trajectories with different observation length. At the simplest level one would like to know whether the underlying diffusion process

was homogeneous or not. Qian et al. used the statistical variance to select for homogeneous diffusion [Qian91]. For a trajectory with a time step length (time lag between succeeding steps) τ, a total number of steps L and a diffusion coefficient D the variance of the square displacement at the time lag $m\tau$ is given by

$$\text{Variance}(m\tau) = (4Dm\tau)^2(2m^2 + 1)/3l(L - m + 1), \quad m \in \mathbb{N}. \tag{3.17}$$

Then the standard deviation σ yields a probability for the given trajectory to stem from homogeneous diffusion. In Fig. 3.3 (b) for both trajectories the $\pm 2\sigma$ dotted lines are plotted, which (under the assumption of Gaussian distribution) enclose the area of 95% probability for homogeneous diffusion. Thus in case of each trajectory, there is a 95% probability that the trajectory would lie in the area enclosed by the respective two dotted lines when the motion was caused by homogeneous diffusion. As can be seen, the longer (green) trajectory lies in the respective area, while the shorter (purple) one does not and therefore probably does not stem from homogeneous motion. Unfortunately this estimate does not rule out that a heterogeneous motion would lead to a trajectory lying within the boundaries. Thus the longer (green) trajectory as well can stem from heterogeneous diffusion. Nevertheless, this method may be used to test a large enough set of trajectories on homogeneous diffusion: If more than 5% of the trajectories lie outside of the area of 95% confidence, the trajectories within the data set will not stem solely from homogeneous diffusion.

For homogeneous diffusion Saxton developed a method to cope with finite trajectory length, by using weighted mean square displacements [Saxt97a]. For short, Saxton used the inverse of the variance calculated by Quian et al., see eqn. 3.17 to weight the corresponding msd values for each time lag. This leads to an enhanced significance of the first few msd values. Details are also given in [Schu02b], since Schuster used this method to calculate diffusion coefficients along tracked molecule trajectories within his SMT software package *tracking.sh*, which was used with some modifications and supplements in this work to analyze SMT data. However, the diffusion coefficient ascribed to the trajectories by this method is a short range diffusion coefficient corresponding to the first few time lags, as can be seen from the short trajectory (purple) in Fig. 3.3 (b).

Saxton further developed a method to derive an average diffusion coefficient D_{msd} from distributions of diffusion coefficients D_{traj} obtained for a set of trajectories, e.g. from investigation of one sample by SMT [Saxt97a, Schu02b] by fitting the distributions with the following function:

$$F_L(D_{\text{traj}}) = \frac{N}{D_{\text{msd}}\Gamma(N)} \left(\frac{ND_{\text{traj}}}{D_{\text{msd}}}\right)^{N-1} \exp\left(-\frac{ND_{\text{traj}}}{D_{\text{msd}}}\right), \tag{3.18}$$

where Γ is the Gamma-function, L is the step-length of the trajectories, $N = L/\epsilon_{\text{eff}}$ is the effective number of uncorrelated segments, and ϵ_{eff} denotes the effective index distance, which is 2.6 for uncorrelated segments in accordance to the above described weighting [Schu02b]. An example is shown in Fig. 3.4 (a), where a distribution of D_{traj} from experimental trajectories with length $L \geq 50$ is plotted together with $F_{50}(D)$ for $D_{\text{msd}} = 0.32\ \mu\text{m}^2/\text{s}$ (—) resp. $0.54\ \mu\text{m}^2/\text{s}$ ($\cdots$). As can be easily seen, $F(D)$ broadens for
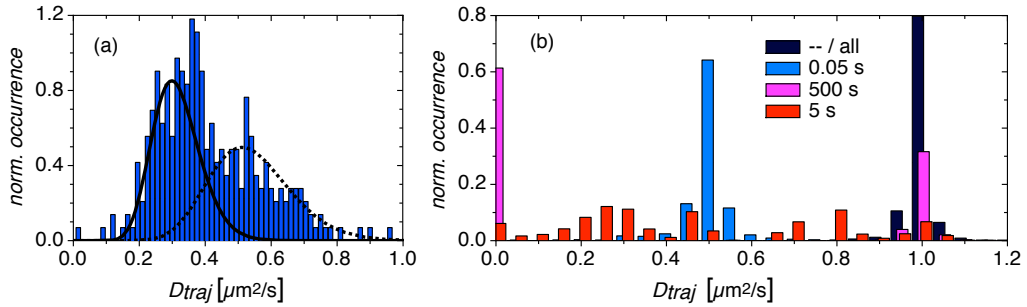
Figure 3.4: (a) Distribution of diffusion coefficients D_{traj} together with fits of D_{msd} according to eqn. 3.18: (——) $D_{\text{msd}} = 0.31$ $\mu\text{m}^2/\text{s}$, ($\cdots$) $D_{\text{msd}} = 0.54$ $\mu\text{m}^2/\text{s}$; (b) distribution of D_{traj} obtained from a simulated two-layer system with various mean dwell times according to [Heid09a].

larger values of D_{msd}. This suggests that a broad distribution of D_{traj} may be regarded as a sum of two or more components. But this interpretation of a broad distribution of D_{traj} is only valid, if there is no exchange between those components during the relevant interval of observation, as will be explained in the following section. This has to be checked carefully, since in general a broad distribution of thus obtained diffusion coefficients along trajectories may hint to anomalous diffusion [Lube08].

3.3.6 Implications of heterogeneities on distributions of diffusion coefficients

If distributions of D_{msd} deviate from the shape given by eqn. 3.18, then the underlying diffusion will be heterogeneous. Nevertheless one has to be careful to interpret such distributions, e.g. as stemming from a set of different diffusion coefficients due to liquid layering [Schu03], even more since the example given by Schuster et al. mixes trajectories of different time lengths and thus observation times. According to Lubelski, Sokolov and Klafter such broad distributions are a hint to ergodicity breaking, where ensemble averages no longer are similar to time averages [Lube08]. Then ensemble averages obtained for different time lags should deviate from each other, which theoretically can be used to describe the system [Baue09b]. For this purpose the SMT software package *tracking.sh* was supplemented to yield distributions of diffusivities (scaled square displacements). The analysis of which is described in the following section.

Nevertheless heterogeneous diffusion can be treated as a sum of several components, as long as there is no exchange between the components during observation time [Heid09a]. Fig. 3.4 (b) shows distributions of D_{traj} obtained from simulations of a two-layer system with diffusion coefficients $D_1 = 0.01$ $\mu\text{m}^2/\text{s}$ and $D_2 = 1$ $\mu\text{m}^2/\text{s}$ for three different mean dwell times (τ_{dwell}, average time, for which a dye molecules stays in the corresponding layer), which were conducted by Heidernätsch [Heid09a]. The rates for interlayer transition were kept symmetric (and thus also the mean dwell times). For comparison the distribution corresponding to diffusion with D_2 within a single layer is also shown. The simulation step width 0.02 s ($\simeq \tau_{\text{frame}}$ in the experiment) and the simulation duration

of 60 s ($\tau_{\text{observation}}$) were kept constant in all cases. Hence all trajectories had a similar length of $n = 60/0.02 = 3000$ steps. The D_{traj} were obtained by using weighted msd along the detected trajectories, as was explained above. Table 3.1 sums up the results.

Table 3.1: Distributions of D_{traj} from simulations of a two-layer system with different mean dwell times τ_{dwell} according to [Heid09a]:

# layers	τ_{dwell} [s]	$\tau_{\text{observation}}$ [s]	step width [s]	comment on distribution
1	− / all	60	0.02	single, around D
2	0.05	60	0.02	single, around $D_{average}$
2	5	60	0.02	broad, unspecific
2	500	60	0.02	separated, around D_1 and D_2

As is expected due to the finite observation length, the single layer simulation with $D_2 = 1 \ \mu m^2/s$ leads to a small distribution of the D_{traj} around 1 $\mu m^2/s$. For the two layer simulation three typical cases can be observed:

$\tau_{\text{dwell}} \ll \tau_{\text{observation}}$ yields a single distribution around the average value $D_{average} = 0.5 \ \mu m^2/s$ of D_1 and D_2. In the here shown case the mean dwell time (0.05 s) is three orders of magnitude shorter than the overall observation time, see Fig. 3.4 (b, cyan).

$\tau_{\text{dwell}} > \tau_{\text{observation}}$ leads to two separate distributions around D_1 and D_2 resp., see Fig. 3.4 (b, magenta). In that case ($\tau_{dwell} = 500$ s) a two-component fit using eqn. 3.18 for each component will render the real diffusion coefficients D_1 and D_2.

$\tau_{\text{dwell}} \approx \tau_{\text{observation}}$ generates a broad distribution of D_{traj}, see Fig. 3.4 (b, red). Then fitting with eqn. 3.18 or with its extension to multiple components, will render arbitrary diffusion coefficients. Nevertheless, from this type of distribution some information may be obtained: The diffusion coefficients derived from analysis of such distributions via multi-component fits using eqn. 3.18 are smaller than the largest component of the involved diffusion process and larger than the smallest component.

In the above given examples, the step width ($\simeq \tau_{\text{frame}}$) was kept constant. Yet, it may be varied as well. However, variation of τ_{frame} in the experiment will also increase the observation time, because a sufficient number of time steps is necessary to analyze detected trajectories. In principle, it would be possible to obtain trajectories of equal observation length from acquisitions at different τ_{frame}. But then the amount of data obtained at the acquisition for the shorter τ_{frame} will be very large and thus difficult to handle.

3.3.7 Probability distributions of diffusivities

As was explained, analysis of trajectories using msd has several constraints. In particular, by averaging over all displacements of a given step length τ information may get lost, which could be helpful to understand the process causing the motion. A useful alternative approach therefore is to analyze distributions of displacements or of square displacements at fixed τ in terms of probabilities [Hell04c]. In general this method will no longer yield the macroscopic diffusion coefficient of a system, since this is achieved only in the long time limit according to eqn. 3.11. However, short range diffusion coefficients $D(\tau)$ can be determined, which monitor the behavior of the system within τ. Furthermore, by comparing probability distributions of scaled square displacements (diffusivities d_{diff}) for different time lags, the time evolution of the system can be determined. This issue has been published in [Baue09b]:

M. Bauer, M. Heidernätsch, D. Täuber, C. von Borczyskowski and G. Radons. Investigations of heterogeneous diffusion based on the probability density of scaled squared displacements observed from single molecules in ultra-thin liquid films. *Diffusion Fundamentals Journal*, Vol. 11, p. 104(14), 2009.

Although the diffusion in ultrathin liquid films is three-dimensional, we can only observe two dimensional diffusion due to the projection into a plane perpendicular to the microscope's direction of observation. Nevertheless we should use a three-dimensional *Fokker-Planck* equation to describe the diffusion, because the diffusion is known to be heterogeneous in z-direction (perpendicular to the solid-liquid interface of the sample) [Schu04]. Unfortunately there is no practicable way to analyze this type of diffusion unless some simplifications can be made, e.g. in section 3.3.9 a linear dependence of the diffusion coefficient $D_{xy}(z)$ on z is assumed. But as will be shown later in this work, the experimental data do not support this model. Therefore, the two-dimensional *Fokker-Planck* equation will be used here to analyze certain "snapshots" of the system, i.e. distributions of the lateral diffusion coefficients at different time lags, and for different film thicknesses (i.e. Δz). By comparison of the results, conclusions about the three-dimensional system can be made. A suitable way thus is to use short range diffusion coefficients obtained from probability distributions of diffusivities as will be explained in this section here.

The two-dimensional *Fokker-Planck* equation for drift-free diffusion is given in eqn. 3.14. Assuming constant diffusion coefficients (which is not really valid here, but is used for approximation) and replacing the parameter t for time by the time lag τ, the probability distribution can be written as [Kirs07]:

$$p(x, y, \tau)\partial x \partial y = \frac{1}{\sqrt{4\pi D\tau}} \exp\left(-\frac{x^2 + y^2}{4D\tau} \right) \partial x \partial y \,. \tag{3.19}$$

Unless spatial heterogeneities are present, the diffusion can be assumed to be homogeneous in the xy-plane. Then the cartesian coordinates can be replaced by spherical ones, with $r^2 = x^2 + y^2$. Integration over the angle yields the dependence on distance

r [Kirs07]:

$$p(r,\tau)\partial r = \frac{1}{4D\tau}\exp\left(-\frac{r^2}{4D\tau}\right)r\partial r,.\qquad(3.20)$$

Substitution of r^2 by u with $\frac{\partial r}{\partial u} = \frac{1}{2r}$, and taking into account that $r = \pm\sqrt{u}$ leads to [Kirs07]:

$$p(u,\tau)\partial u = \frac{1}{4D\tau}\exp\left(-\frac{u}{4D\tau}\right)\partial u.\qquad(3.21)$$

Cumulative probability distributions

Now integration from 0 to R^2 yields the cumulative probability distribution [Kirs07]:

$$P(R^2,\tau) = 1 - \exp\left(-\frac{R^2}{4D\tau}\right).\qquad(3.22)$$

The complementary cumulative probability distribution $C(R^2,\tau) = 1 - P(R^2,\tau)$ [Hell04c] then simply is an exponential decay and thus more easily accessible for fitting experimental data. $C(R^2,\tau)$ is the probability that a molecule starting at the origin at $\tau = 0$ will by the time τ exceed the circle of radius R:

$$C(R^2,\tau) = \exp\left(-\frac{R^2}{4D\tau}\right).\qquad(3.23)$$

Scaling

As was explained before, time scaling of the square displacements used with the probability distributions enables to easily follow a probable temporal evolution within the system. Thus the *Einstein* eqn. 3.10 is used for $n = 2$ to scale the observable, i.e. the square displacements r^2, giving the new scaled observable, the diffusivity d_{diff}:

$$d_{\mathrm{diff}} = \frac{r^2}{4\tau}.\qquad(3.24)$$

Insertion into eqn. 3.23 gives:

$$C(d_{\mathrm{diff}})_\tau = \exp\left(-\frac{d_{\mathrm{diff}}}{D}\right),\qquad(3.25)$$

where the probability $C(d_{\mathrm{diff}})_\tau$ no longer explicitly depends on τ and thus is denoted with subscript τ. In case several independent diffusion processes contribute to the distribution of diffusivities eqn. 3.25 can be modified into a multi-component term:

$$C(d_{\mathrm{diff}})_\tau = \sum_i a_i \exp\left(-\frac{d_{\mathrm{diff}}}{D_i}\right)\qquad with \qquad \sum_i a_i = 1.\qquad(3.26)$$

For example, the simulated two-layer diffusion described in section 3.3.6 with observation time smaller than the dwell time τ_{dwell} can be analyzed properly by a two-component

term. However, the application of eqn. 3.26 to the case when the $\tau_{i,\mathrm{dwell}}$ are in the range of the observation time, will not yield the physical diffusion coefficients, but short range diffusion coefficients $D_i(\tau)$ describing the behavior of the system during time lag τ. Nevertheless a comparison of the derived $D_i(\tau)$ for different time lags τ will show the temporal evolution of the system and thus provide insight into the contributing physical processes.

3.3.8 Spotsize analysis

Schuster et al. developed a method to calculate diffusion coefficients from the size of the smeared out spots in single CCD frames [Schu02a]. For this the average size A_0 of the spots of immobile molecules is determined by two-dimensional Gaussian approximation. Then the diffusion coefficient can be calculated via

$$D = \frac{A - A_0}{c\tau} \, , \qquad (3.27)$$

where A is the spotsize of the diffusing molecule, τ is the exposure time, and c is a constant, which gives the average deviation of the shape of the spots from an ellipse. Schuster et al. used simulations to determine $c = 1/3$. Nevertheless they found a rather broad distribution for the diffusion coefficients obtained from single spotsizes within their simulation. The distribution narrowed considerably, when averages over five frames along detected trajectories were used. The latter was then applied to experimentally obtained trajectories from a thin TEHOS film on a glass substrate, which rendered an average diffusion coefficient $D_{\mathrm{ssa}} = 1.3 \pm 0.1$ $\mu\mathrm{m}^2/\mathrm{s}$. For comparison, the diffusion coefficient obtained by msd analysis was given by $D_{\mathrm{msd}} = 1.1 \pm 0.1$ $\mu\mathrm{m}^2/\mathrm{s}$ [Schu02a]. Since the determination of diffusion coefficients by spotsize analysis does not suffer from constraints of tracking procedures due to connection of geometrically averaged positions (see section 3.3.2), and the given D_{msd} was not corrected for the latter, the D_{ssa} should have been 1.5 times the given D_{msd}. However, it is only slightly larger. A small error within calculation of the D_{ssa} certainly is due to the use of the frame time (inverse frame rate) instead of the real exposure time, which was not known exactly. Typical frame transfer times are ≈ 1.5 ms for this kind of CCD chip, but it depends also on the used region of the full chip. Nevertheless an exposure time of 23.5 ms instead of 25 ms will increase D_{ssa} by 6% to 1.4 $\mu\mathrm{m}^2/\mathrm{s}$, which still is smaller than 1.5 times the D_{msd}. The more recent camera software *Andor Solis*™ for the *Andor*™ cameras also provides exposure times. Thus by using modern software for data acquisition, diffusion coefficients may be calculated by the described spotsize analysis using the proper time lag. Yet, also the other contributions to the deviation of the D_{ssa} from 1.5 times the D_{msd} have to be considered.

So far there is another constraint on using the above described spotsize analysis with diffusion in ultrathin TEHOS films: As will be shown later in this work, the diffusion in such films is strongly heterogeneous. Thus the considerations explained in section 3.3.6 have to be taken into account. The calculation of D_{msd} using weighted msd according to section 3.3.5 counts mainly on the first few time lags yielding short range diffusion

coefficients [Saxt97a]. The observation time can be approximated by the effective segment length to 2.6 times the inverse frame rate [Schu02b]. Whereas the observation time for the D_{ssa} is 5 times τ_{exposure}. As will be described in section 6.3 slower diffusion coefficients are expected for longer observation times, which may also account for the slow value obtained for D_{ssa} after averaging over five frames. Nevertheless distributions of time scaled single spotsizes may be used similar to the distribution of diffusivities d_{diff} to analyze the diffusion. However, they have a stronger dependence on imaging quality and statistical properties, e.g. the average geometrical position of immobilized dye molecules in respect to the direction of detection, than the latter.

3.3.9 Model of lateral diffusion in layered films

Postnikov and Sokolov recently developed a model for lateral diffusion in ultrathin layered films [Post11], which will be outlined here. The model corresponds to a particle performing diffusion in two dimensions, where the properties of the vertical diffusion (which here shall be denoted z-direction) do not depend on x, but the diffusion coefficient in x does depend on z and thus is denoted $D_x(z)$. The probability density $p(x,z,t)$ then is described by the *Fokker-Planck* equation corresponding to anisotropic diffusion:

$$\frac{\partial p}{\partial t} = D_x(z)\frac{\partial^2 p}{\partial x^2} + D_z\frac{\partial^2 p}{\partial z^2}. \tag{3.28}$$

Due to the conditions of the diffusion in the two variables, the solution of the physical problem has to factorize: $p(x,z,t) = p_x(x,t)p_z(z,t)$, the derivation for this is given in [Post11]. Since the diffusion in z does not depend on x, the probability density $p_z(z,t)$ is described by:

$$\frac{\partial p_z}{\partial t} = D_z\frac{\partial^2 p_z}{\partial z^2}, \tag{3.29}$$

while the probability density $p_x(x,t)$ is described by an equation containing a time-dependent diffusion coefficient $D(t)$:

$$\frac{\partial p_x}{\partial t} = D(t)\frac{\partial^2 p_x}{\partial x^2}, \tag{3.30}$$

with

$$D(t) = \int_0^d D_x(z)p_z(z,t)dz, \tag{3.31}$$

where d denotes the thickness of the film. Now Postnikov and Sokolov introduce a new variable $\tau_z = \int_0^t D(t)dt$ which reduces eqn. 3.30 to the simple diffusion equation:

$$\frac{\partial p_x}{\partial \tau_z} = \frac{\partial^2 p_x}{\partial x^2}. \tag{3.32}$$

From this Postnikov and Sokolov conclude that $p_x(x,t)$ is Gaussian, and that the msd of the lateral diffusion (in x-direction) equals $2\tau_z$.

They then give two examples, one for a thick film (infinite d) and one for finite d, both with the assumption of a linear dependence $D_x(z) = kz$. In the latter case the msd shows an initial superdiffusion $\langle x^2 \rangle \propto t^{1.5}$ and an asymptotic normal diffusion, see Fig. 1 in [Post11]. Nevertheless for the msd obtained within this work, this kind of behavior was not generally observed, see e.g. Fig. 3.3 (b) in section 3.3.3.

Although Sokolov and Postnikov used a two-dimensional model, it should be applicable also for the three-dimensional diffusion studied in this work. Then $p_x(x,t)$ has to be replaced by $p_{xy}(x,y,t)$ with two independent lateral dimensions x and y. A modification of eqn. 3.32 for two dimensions therefore has the following form:

$$\frac{\partial p_{xy}}{\partial \tau} = \frac{\partial^2 p_{xy}}{\partial x^2} + \frac{\partial^2 p_{xy}}{\partial y^2}. \tag{3.33}$$

Then p_{xy} still is Gaussian, while its msd equals 4τ.

3.4 Fluorescence correlation spectroscopy (FCS)

Fluorescence correlation spectroscopy (FCS) is a powerful tool to study processes involving fluorescence intensity fluctuations on the level of few (in some cases even single) molecules. Improved single photon counting detector technologies (avalanche diodes) and the use of two detection channels moved time resolutions into the picosecond range [Schw02]. With FCS time traces of the fluorescence signal from a tiny focal region on the sample are recorded and autocorrelated (or in case of two detection channels crosscorrelated). From the autocorrelation characteristic times for the physical processes causing the fluctuations can be derived. The normalized autocorrelation function is defined as [Schw02]:

$$G(\tau) = \frac{\langle \delta F(t) \delta F(t+\tau) \rangle}{\langle F(t) \rangle^2} \qquad \text{with} \qquad \delta F(t) = F(t) - \langle F(t) \rangle, \tag{3.34}$$

where $F(t)$ is the fluorescence signal at time t, τ is the time lag, and the fluctuations $\delta F(t)$ are defined as the deviations from the temporal average of the signal. If the excitation power and the effective Volume V_{eff} can be considered as constant, the fluctuations depend only on changes in local concentration $c(\mathbf{r}, \tau)$ of the dye, as well as on fluctuations of the molecular absorption cross section σ_A and fluctuations of the quantum yield Φ_F. With the overall detection efficiency κ, the spatial distribution of excitation energy $I_{ex}(\mathbf{r})$, and the optical transfer function $S(\mathbf{r})$ of the setup geometry (determines the spatial collection efficiency of the setup), the variations may be written [Schw02]:

$$\delta F(\tau) = \kappa \int_V I_{ex}(\mathbf{r}) S(\mathbf{r}) \delta(\sigma_A \Phi_F c(\mathbf{r}, \tau)) \mathrm{d}V. \tag{3.35}$$

In general the detected intensity fluctuations stem from several physical processes, which range from antibunching (statistics of fluorescence emission) over rotational diffusion and triplet state blinking to lateral diffusion, see Fig. 3.5 left. As long as the characteristic
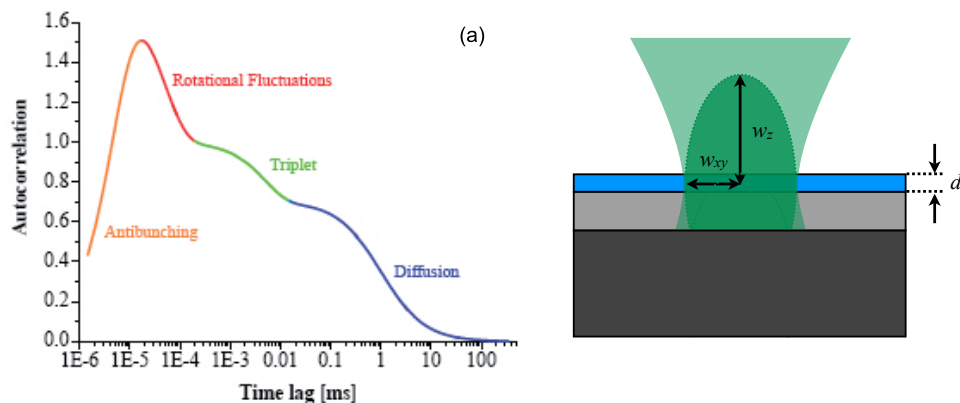
Figure 3.5: (left) Timescales of various processes monitored by autocorrelation analysis taken from [Schw02]; (right) FCS detection profile in case of a thin liquid film with thickness d on a silicon wafer with thermally grown oxide, $2w_{xy}$ and $2w_z$ are the lateral focus width and the focus depth, resp.

times of the involved processes deviate from each other by some orders of magnitude, the parts of the autocorrelation function related to the different processes can be separated. The relative amplitudes of the different parts are related to the number of dye molecules taking part in the respective process and to the magnitude of their emission [Schw02]. Nevertheless, it has to be taken into account that fluorescence intensities (and thus their fluctuations as well) originating from the same species of dye molecules may differ due to geometrical conditions for the respective process. E.g. adsorbed molecules at the solid-liquid interface may have a higher fluorescence signal than freely diffusing ones, when the optical transition dipole of the former is oriented parallel to the field vector of the exciting light beam. Whereas their fluorescence may also be quenched due to unfavorable configuration. Thus correlations related to ad-/desorption kinetics may have a strongly varying amplitude and therefore can show up pronouncedly in the autocorrelation curve as well as be hidden by other processes, or occur with any amplitude in between those extremes.

To obtain characteristic times for the involved processes, the nature of the process and the geometry of the excitation/detection volume has to be taken into account. Usually the excitation beam is considered to have a two-dimensional Gaussian profile, which is a sufficient approximation of the diffracted light beam described by the *Airy* function [Zhan07]. Thereby the width $2w_{xy}$ of the profile is determined by the $1/e$-decay of the intensity. In the direction of light propagation the focal depth of the objective determines the height ($= 2w_z$, see Fig. 3.5 right) of the detection volume for bulk liquids. However, with ultrathin liquid films the height is restricted to the film thickness d.

47

3.4.1 Translational diffusion

Irrespectively of the specific setup the following relation between the characteristic time related to translational diffusion τ_D and the diffusion coefficient D is valid [Elso74, Schw02]:

$$D = \frac{w_{xy}^2}{4\tau_D}. \tag{3.36}$$

Since in our case, the film thickness d is much smaller than w_z, the two-dimensional approximation of the normalized autocorrelation function for lateral diffusion has to be used, which is given by [Arag76]:

$$G_D(\tau) = \frac{1}{1 + \tau/\tau_D}. \tag{3.37}$$

Otherwise a correction for diffusion in z-direction has to be implemented, see [Arag76].

The above given eqn. holds for homogeneous diffusion. However, in many cases the translational diffusion is not homogeneous. Instead the mean square displacement (see section 3.3.3) is not proportional to the time t, but to t^α with $0 < \alpha < 1$. Then eqn. 3.37 is modified accordingly [Schw02] to

$$G_{D,\mathrm{anomal}}(\tau) = \frac{1}{1 + (\tau/\tau_\mathrm{anomal})^\alpha}. \tag{3.38}$$

The phenomenon of anomalous diffusion is still not completely understood in respect to FCS measurements. Thus physical insight obtained from fits to anomalous diffusion behavior may be restricted to the case, where the microscopic origin of the parameters α and τ_anomal is known [Hac05]. Furthermore no conventional diffusion coefficient can be defined in this case [Schw02].

Sometimes it is reasonable to expect two discriminable translational diffusion coefficients. Then instead of using eqn. 3.38 for anomalous diffusion, the following two-component term may be used [Hac05]:

$$G_{D,\mathrm{bi}}(\tau) = A\frac{1}{1 + \tau/\tau_{D1}} + (1 - A)\frac{1}{1 + \tau/\tau_{D2}}. \tag{3.39}$$

3.4.2 Rotational diffusion

In solution dye molecules can freely rotate. Since their excitation as well as the detection of their fluorescence emission depends on the angle of the optical transition dipole with the incident electromagnetic field, the rotational dynamics appears as fluorescence fluctuations in the FCS signal. This effect occurs already for circular polarized incident light, but is enhanced for linear polarized light. The autocorrelation function $G'(\tau)$ then has to be modified by adding an exponential term [Wide99, Schw02]

$$G(\tau) = (1 + A_R \exp(-\tau/\tau_\mathrm{rot}))\,G'(\tau)\,, \tag{3.40}$$

where τ_rot is the characteristic time for rotational diffusion and the amplitude A_R depends on the geometry of the experiment including the polarization of the exciting light.

3.4.3 Triplet blinking and other fluorescence intermittencies

Another cause of fluorescence fluctuations is triplet blinking, i.e. the excited dye molecule turns via intersystem crossing (ISC) into the triplet state, see section 2.3.1. In the triplet state the molecule does not fluoresce but stays dark. Therefore, the triplet lifetime τ_{Tr} appears as dark intervals in the fluorescence signal leading to correlation times in the corresponding time regime, as is depicted in Fig. 3.5 left. As long as the other involved processes occur on a different time scale, the respective parts of the correlation function can be separated. In that case an additional term appears in the correlation function, leading to [Cher09]

$$G(\tau) = \left(1 + \frac{A_{Tr}}{1 - A_{Tr}} \exp(-\tau/\tau_{Tr}) \right) G'(\tau) \,, \tag{3.41}$$

where A_{Tr} is the fraction of dye molecules in the triplet state. Since all the dye molecules used within this work have a quantum yield close to one, A_{Tr} is very small. Therefore, this term is also very small and can be neglected.

Besides triplet blinking other causes of fluorescence intermittency may exist, e.g. reversible electron transfer with the surrounding matrix or spectral shifts in combination with changes of fluorescence intensity due to conformational changes, see [Kowe09, Krau11a]. If the contribution to fluorescence fluctuations from such a process is large enough and if the process occurs on time scales separable from the other processes contributing to $G(\tau)$ a similar expression as eqn. 3.41 with the respective $A_{process}$ and $\tau_{process}$ may be used.

3.4.4 Reaction kinetics

At solid-liquid interfaces also ad-/desorption events take place. When a dye molecule adsorbs to the surface, its rotation will be hindered. This in general leads to a change in fluorescence intensity. However, the signal will be enhanced if the optical transition dipole of the dye is situated parallel to the field vector of the incident light, whereas the dye molecules will not be excited if their dipole is oriented perpendicular to the field vector. Thompson and Axelrod studied surface binding kinetics by total internal reflection (TIR) fluorescence microscopy with FCS [Thom83]. When the lateral observation area can be considered large in comparison to the vertical one and to molecular size, the shape of the fluorescence correlation function $G(\tau)$ is determined by a reaction rate R_R for surface binding and a bulk diffusion rate R_B

$$R_R = \frac{k}{\beta} \qquad \text{and} \qquad R_B = D \left/ \left(\frac{\beta \langle C \rangle}{\langle A \rangle} \right)^2 \right. \tag{3.42}$$

where k is the desorption rate and β is defined as the average fraction of binding sites that remain free at equilibrium. D is the bulk diffusion coefficient, while $\langle A \rangle$ and $\langle C \rangle$ are the thermodynamic ensemble average concentrations of freely diffusing molecules and surface bound molecules, respectively. Using these rates Axelrod and Thompson

give an extended expression for the autocorrelation function $G(\tau)$ related to sorption kinetics [Thom83]

$$G(\tau) = \frac{G(0)}{v_-^{1/2} - v_+^{1/2}} \left\{ v_-^{1/2} w \left[-i(v_+ R_R \tau)^{1/2} \right] - v_+^{1/2} w \left[-i(v_- R_R \tau)^{1/2} \right] \right\}, \qquad (3.43)$$

where

$$v_\pm^{1/2} = \frac{1}{2}(R_R/R_B)^{1/2}[-1 \pm (1 - 4R_B/R_R)^{1/2}],$$

and

$$w(i\eta) = e^{\eta^2} \mathrm{erfc}(\eta) \qquad (\eta \text{ complex}).$$

The value at time zero thereby is

$$G(0) = \frac{1}{Z}\left[\frac{1}{\gamma(1-\beta)} - 1 \right], \qquad (3.44)$$

where Z is the total number of binding sites within the observation area and γ is the fraction of molecules that are fluorescent labeled (which in case of observation of single dye molecules of course is equal to 1). This relation for the amplitude $G(0)$ of the normalized correlation function is related to the particular TIR setup used by Axelrod and Thompson, where predominantly adsorption kinetics is monitored and fluctuations from transient molecules can be neglected. erfc is the complementary error function, which commonly is defined as [Bron08]

$$\mathrm{erfc}(z) = 1 - \mathrm{erf}(z) = 1 - \frac{2}{\sqrt{\pi}} \int_0^z e^{-u^2} du. \qquad (3.45)$$

However, due to its complexity this general correlation function for binding kinetics given in eqn. 3.43 is not suitable for fitting routines. Yet according to Thompson and Axelrod eqn. 3.43 in the limiting cases of $R_B \ll R_R$ (bulk diffusion limit) and $R_R \ll R_B$ (reaction limit) simplifies to

$$G_{\mathrm{diff}}(\tau) \approx \exp(-R_B\tau)\,\mathrm{erfc}(\sqrt{R_B\tau}) \qquad (R_B \ll R_R) \qquad (3.46)$$

$$G_{react}(\tau) \approx \exp(-R_R\tau) \qquad\qquad (R_R \ll R_B). \qquad (3.47)$$

More general equations treating reaction kinetics at interfaces are also given by Lieto et al. [Liet03], but they require the knowledge and the variation of dye concentrations, which hardly is possible here, since the used dyes are only weakly soluble in TEHOS.

With the TIR illumination used by Thompson and Axelrod, the excitation of fluorophores decays exponentially in z-direction restricting the detection to the solid-liquid interface and its vicinity. In case of the ultrathin films studied in this work the detection similarly is reduced to a small vertical region (i.e. the film thickness d, see Fig. 3.5 right) in comparison to the lateral extension (which typically is about 0.6 μm). Therefore, the considerations of Thompson and Axelrod give a useful approximation for analyzing FCS experiments on ultrathin liquid films. In the experiment dye concentrations were in the

range of 10^{-6} mol/l to 10^{-8} mol/l, i.e. the dyes are highly diluted. Thus most binding sites will remain free and β therefore should not be much smaller than 1. Furthermore the (charged resp. polar) dye molecules have a higher preference to adsorb to the surface (preferentially at surface silanols, see section 4.2.2) than to remain in the unpolar liquid. Thus k is small, leading to a small R_R. On the other hand $D \approx 50 \ \mu m^2/s$ for R6G and similarly sized dyes in bulk TEHOS, see section 4.2.3. Yet as mentioned above, $\langle C \rangle$ is larger than $\langle A \rangle$, reducing the bulk diffusion rate R_B. However, the small film thickness d leads to mean first passage times for freely diffusing dye molecule in the range of 0.1 μs, see section 3.1.1. Since the rate for freely diffusing molecules is the inverse of this mean first passage time, it is quite large. Therefore, due to the effect of the confinement eqn. 3.47 can give an approximation within the analysis of FCS experiments on ultrathin liquid films.

3.5 Spectral diffusion

Parts of this section have contributed to the following publication [Krau11a]:

S. Krause, P.F. Aramendía, D. Täuber, C. von Borczyskowski. Freezing single molecule dynamics on interfaces and in polymers. *Phys. Chem. Chem. Phys.*, Vol. 13, p. 1754-1761, 2011.
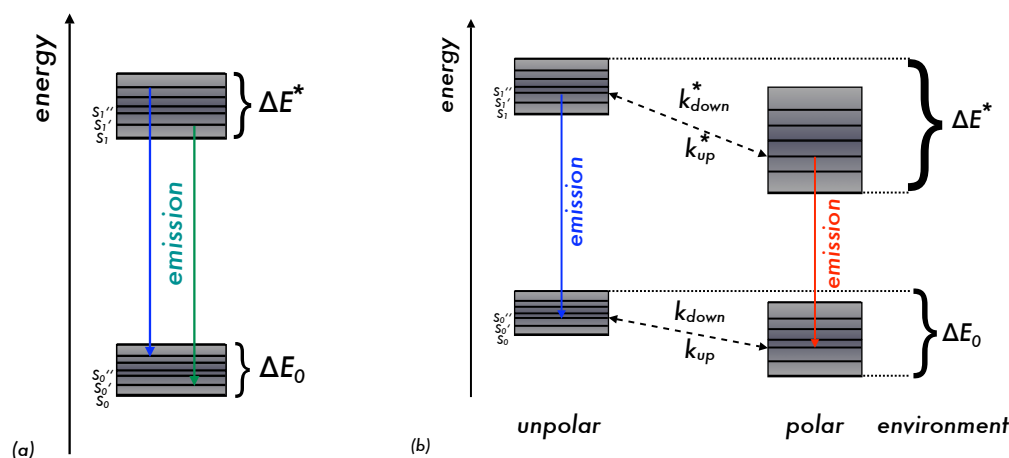
Figure 3.6: (a) Respective energy levels of fluorescent molecule due to interactions with the surrounding matrix; de-excitation via fluorescence is depicted by colored arrows to visualize the change in transition energy. In contrast to Fig. 2.4 for simplicity only the resp. S_0 and S_1 states are shown; (b) additional changes in the respective energy levels due to internal charge transfer configuration of Nile Red.

The here used fluorescent dyes contain a chromophor, i.e. an extended π orbital system over part of the molecule which can be excited from its energetic ground state by

absorption of a photon of suitable wavelength, see section 2.3.1. Thereby, the π orbital system may rearrange into a different geometry containing a higher energy. The excited molecule will return to the ground state again after some time. The average time for this decay is denoted lifetime τ^* of the excited state, which is typically in the range of nanoseconds. The energy of the photon is determined by the energetic difference between the ground state and the excited state [Vale05].

When the dye molecule is embedded in a matrix, the energies of both ground and excited states are slightly changed due to interaction with the matrix, e.g. by *Van der Waals* interactions. Because of the different geometry of the charge distribution in the respective π orbitals, the interaction with the matrix usually differs for the ground and for the excited state [Vale05], thus leading to changes in fluorescent wavelengths as well, see Fig. 3.6 (a). The largest observable shift (ΔE_{max}) in emission wavelength thereby depends on the potential-landscape (see Fig. 3.7) of both ground and excited states. The range of the energetic change of fluorescence is influenced by the change in the energy of the ground state ΔE_0 as well as the excited state ΔE^* (see Fig. 3.6). Consequently fluorescent dyes often show a solvent shift upon changing the dielectricity of the solvent, i.e. the absorption and emission peaks are shifted to different wavelengths. In ensemble measurements in a heterogeneous matrix the interaction with the surrounding matrix leads to an inhomogeneous broadening of the line widths of the absorption and emission spectra.
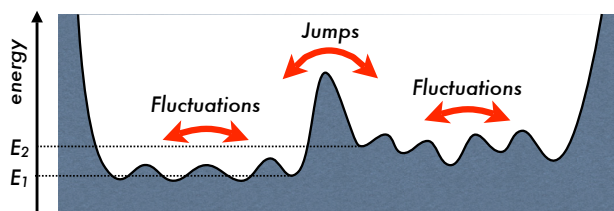
Figure 3.7: Potential landscape of the electronic state of a dye molecule (either S_0 or S_1). Overcoming the large barrier results in spectral jumps. The fluctuations (smaller, densely distributed jumps) induced by the potential landscape in the right part have a larger amplitude (energetic range) than those from the left part, caused e.g. by stronger coupling to the matrix.

On the other hand, single molecule (SM) emission spectra directly show the properties of their local environments. If fluctuations of the surrounding matrix occur on suitable time scales, e.g. in highly viscous fluids or even in the vitreous state of amorphous polymers, these fluctuations will induce fluctuations of the energies of the electronic states of the dye, which can be seen in time series of SM spectra, as shown in Fig. 3.8. This commonly is denoted as spectral diffusion [Boir99, Baie08, Krau11a]. In certain cases these small spectral fluctuations are accompanied by some larger spectral jumps. These jumps occur, when a barrier in the potential landscape of the dyes electronic state, which leads to a larger spectral shift, is overcome, see Fig. 3.7. In the time series shown in Fig. 3.8 this happened after 38 s. Here the energy barrier is due to transitions between a locally excited and an internal charge transfer conformation [Guid10] of the
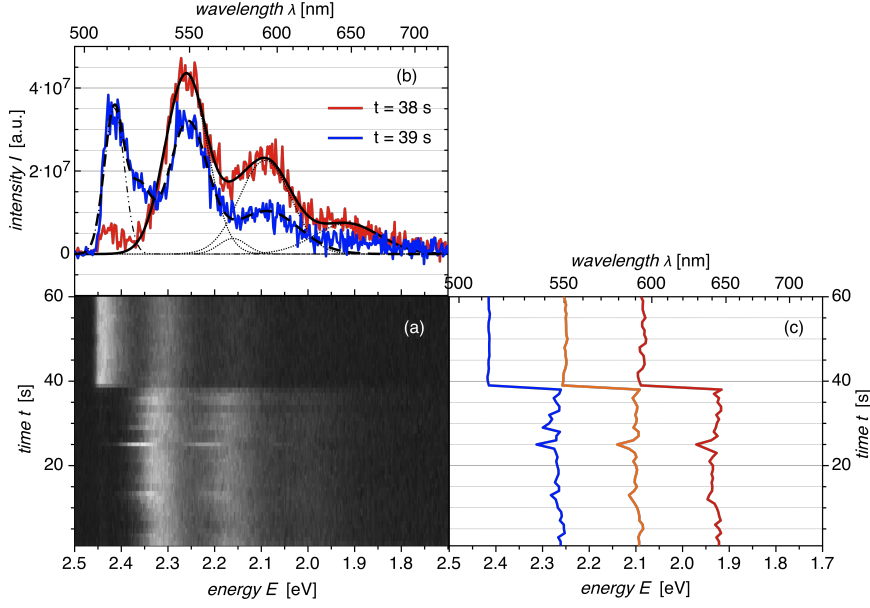
Figure 3.8: (bottom left) Time series of SM emission spectra, (right) corresponding peak positions, (top) SM spectra at 38 s and at 39 s, obtained from Nile Red in a 25 nm thin PBMA film at 323 K, (—) and (- -) fits with three Gaussians, resp., faint lines show single components.

fluorescent dye Nile Red. See Fig. 4.3 (d) and (e) for the respective structure formulas. Since the internal charge transfer state of Nile Red has a larger dipole moment than the locally excited state [Kaws08], this conformation is favored in polar environments. Due to the larger dipole moment also the interaction with the surrounding matrix is stronger, which leads to larger spectral fluctuations, as depicted in Fig. 3.6 (b) as well as in the right part of the potential landscape shown in Fig. 3.7. This also can be seen in the first 38 s of the time series in Fig. 3.8 in comparison to the smaller amplitude of fluctuations after the spectral jump.

The frequency of those spectral jumps depends on the transition rates in both directions. Thereby the transitions usually either occur in the ground state (transition rate k_{down} resp. k_{up} depicted in Fig. 3.6 b) or in the excited states (transition rates k^*_{down} and k^*_{up} in the same figure). The ratio of the respective rates is *Boltzmann* distributed, see eqn. 3.48.

$$\frac{k_{up}}{k_{down}} = e^{-\frac{\Delta E}{k_B T}} \,, \tag{3.48}$$

where $\Delta E = E_2 - E_1$ is the energy difference between the resp. minima next to the barrier, see Fig. 3.7. Thus the ratio of the transition rates depends on the difference between the two energy levels and on temperature. Furthermore, the rates themselves depend on the temperature. Higher temperatures will increase the probability for the system to overcome the barrier and thus increase the transition rates. They also are influenced by the structure of the surrounding matrix, e.g. in a glassy polymer conformational changes may be restricted to the size of the free volume, thus limiting the possibility of spectral

jumps due to conformational changes of the dye molecule, see [Vall04]. Furthermore, the detection of spectral jumps depends on the spectral resolution of the setup (which for the here used setup is about 0.4 nm) and on the temporal resolution. Spectral jumps with a higher frequency than the acquisition rate of the time series will result in intermediate spectra showing no spectral diffusion at all. At intermediate rates (and small differences between the related transition energies), a dense distribution of spectral jumps will be visible, which here is addressed as "fluctuations" (e.g. in Fig. 3.7). Spectral jumps with larger energetic differences will be observed less frequently, because the larger energetic difference implies also a larger difference between the related electronic states of the molecule, which according to eqn. 3.48 leads to a smaller transition rate.

The energetic positions of SM spectra are often determined from the positions of their peaks. These usually are obtained from multi-Gaussian fits to the spectra, as can be seen in Fig. 3.8 (top).

3.5.1 Analogy to translational diffusion

The accumulation time of the SM spectra, typically 0.5 s to 2 s, determines the temporal resolution for the spectral fluctuations. Within this temporal resolution the fluctuating energy levels appear almost continuously distributed around some mean values (besides some few larger jumps). Thus the spectral fluctuations can be treated in analogy to translational diffusion. Yet, the range of the spectral fluctuations is limited by the maximal possible range of shifts in the energy levels of the dye, see ΔE_{max} in Fig. 3.6 (a). The latter also corresponds to the height differences in the potential landscape depicted in Fig. 3.7. For this reason, the appropriate analogy is translational diffusion in a cell, see Fig. 3.3 (a) for the corresponding plot of the msd. However, due to blinking and bleaching of the dyes, the SM time series are not long enough to use the calculation of msd for evaluation of spectral diffusion coefficients. Yet in section 3.3.7 a method was developed to obtain short range diffusion coefficients $D(\tau)$ for translational diffusion within fixed time lags τ. This is a matter of choice, if the behavior of an anomalous or heterogeneous system at short time scales is of interest, which cannot be achieved by the determination of long range diffusion coefficients. As explained above, spectral diffusion is by its nature restricted and therefore no long range diffusion coefficients can be determined. However, the short range diffusion coefficients derived from the probability distributions as detailed below, will render useful information about the behavior of the system dye-matrix.

Additionally the temporal evolution of the spectral diffusion can be investigated. By changing the acquisition time (i.e. time lag τ), the time dependence of the system in the range of the studied time lags can be seen: If for two time lags $\tau_1 < \tau_2$ the related diffusion coefficients are equal, i.e. $D(\tau_1) = D(\tau_2)$, the system is likely to behave homogeneous within $[\tau_1, \tau_2]$. This is similar to the initially linear dependence of the msd on time for diffusion in a cage, see the corresponding plot in Fig. 3.3 (a). Otherwise for the studied time lags the system is outside of the homogeneous regime.

Since spectral diffusion describes energetic displacements during time, and energy is a one dimensional observable, we here have to use the equations for diffusion in one

dimension instead of those for two-dimensional diffusion used in section 3.3.7.

3.5.2 Probability distributions of spectral diffusivities

The *Fokker-Planck*-Equation for one-dimensional Brownian motion with (linear) drift coefficient $S(x)$ and diffusion coefficient $D(x)$ is given by [Risk96]

$$\frac{\partial}{\partial \tau} p(x,\tau) = \left(-\frac{\partial}{\partial x} S(x) + \frac{1}{2} \frac{\partial^2}{\partial x^2} D(x) \right) p(x,\tau). \tag{3.49}$$

For zero drift and a constant diffusion coefficient $D(x) = D$ the distribution of the transition probability density $p(x,\tau)$ can be expressed as [Kirs07]

$$p(x,\tau)\partial x = \frac{1}{\sqrt{4\pi D\tau}} \exp\left(-\frac{x^2}{4D\tau} \right) \partial x. \tag{3.50}$$

Now the probability distribution of the squared displacement $u = x^2$, with $u \in [0,\infty]$, is obtained by taking into account that it is the sum of $p(\sqrt{u},\tau)dx$ and $p(-\sqrt{u},\tau)dx$, while $\frac{\partial x}{\partial u} = \frac{1}{2\sqrt{u}}$ [Kirs07]

$$p(u,\tau)\partial u = \frac{1}{\sqrt{4\pi D\tau u}} \exp\left(-\frac{u}{4D\tau} \right) \partial u. \tag{3.51}$$

Cumulative probability distributions

Integration of eqn 3.51 with boundaries 0 and ΔE^2 yields the probability $P(\Delta E^2, \tau)$ to obtain a value $x^2 \le \Delta E^2$ for a given time interval τ [Kirs07] (for definition of erfc resp. erf see eqn. 3.45)

$$P(\Delta E^2, \tau) = \int\limits_0^{\Delta E^2} p(u,\tau)\partial u = \mathrm{erf}\left(\sqrt{\frac{\Delta E^2}{4D\tau}} \right). \tag{3.52}$$

For consistency with the two dimensional case, the complementary cumulative probability $C(\Delta E^2, \tau)$ is used, which is therefore given by

$$C(\Delta E^2, \tau) = 1 - P(\Delta E^2, \tau) = 1 - \mathrm{erf}\left(\sqrt{\frac{\Delta E^2}{4D\tau}} \right) = \mathrm{erfc}\left(\sqrt{\frac{\Delta E^2}{4D\tau}} \right). \tag{3.53}$$

Similarly to the two dimensional case the *Einstein* equation 3.10 for one dimension is used to obtain scaled square displacements, i.e. spectral diffusivities d_{spec}

$$d_{\mathrm{spec}} = \frac{\Delta E^2}{2\tau}. \tag{3.54}$$

In the experiment the spectral diffusivities d_{spec} result from spectral diffusion during the acquisition time τ. Using the integration variable $s = d_{\text{spec}}$ and $\frac{\partial u}{\partial s} = 2\tau$, the probability distribution in eqn 3.51 can be transformed to

$$p(s, \tau)\partial s = \frac{1}{\sqrt{4\pi D 2\tau^2 s}} \exp\left(-\frac{s}{2D}\right) 2\tau \partial s \,, \tag{3.55}$$

where $p(s, \tau)$ no longer explicitly depends on τ and thus will be denoted as $p(s)_\tau$. Integration now yields the probability distribution function

$$P(d_{\text{spec}})_\tau = \int\limits_0^{d_{\text{spec}}} p(s)_\tau \partial s = \text{erf}\left(\sqrt{\frac{d_{\text{spec}}}{2D}}\right) \,. \tag{3.56}$$

The complementary probability distribution for spectral diffusion therefore is

$$C(d_{\text{spec}})_\tau = 1 - \text{erf}\left(\sqrt{\frac{d_{\text{spec}}}{2D}}\right) \,. \tag{3.57}$$

In case if two independent physical processes contribute to the distribution of spectral diffusion eqn 3.57 can be modified by adding a second term, with $a \in [0, 1]$

$$C(d_{\text{spec}})_\tau = 1 - a\,\text{erf}\left(\sqrt{\frac{d_{\text{spec}}}{2D_1}}\right) - (1 - a)\,\text{erf}\left(\sqrt{\frac{d_{\text{spec}}}{2D_2}}\right) \,. \tag{3.58}$$

A multi-componet probability distribution of spectral diffusivities is expressed by

$$C(d_{\text{spec}})_\tau = 1 - \sum_i a_i\,\text{erf}\left(\sqrt{\frac{d_{\text{spec}}}{2D_i}}\right) \quad \text{where} \quad \sum_i a_i = 1 \,. \tag{3.59}$$

4 Experimental setups, materials and tracking programs

In this chapter the two microscopy setups used for optical investigation and the setup for laser-induced dehydroxylation will be described. At this point also the writing of the structures is explained. This is followed by a description of the used materials together with the cleaning procedure of the substrates and the sample preparation methods. In particular the hydroxylation and dehydroxylation of the thermal silica substrates is detailed. The last part describes and compares the used tracking program packages *tracking.sh* and *DSAA*.

4.1 Experimental setups

4.1.1 Wide field microscope

Wide field microscopy has the advance to simultaneously monitor a larger region on the sample. With the homebuilt setup used here (see Fig. 4.1 a) the illuminated spot is about 30 μm in diameter. Video sequences were recorded from an ≈ 16 μm x 16 μm area within the illuminated region. The light source for excitation is an argon-krypton ion laser (*Coherent* Innova 70C Spectrum), where the wavelength at 514 nm was used. To avoid vibrations induced by the laser, the excitation light was coupled into the setup by a single mode fiber (*Thorlabs*). An electro optical modulator (EOM) (*ConOptics* ADP 370) was used for power stabilization. The incident power on the sample was in the range of 100 W/cm^2 to 400 W/cm^2, depending on the used dye and the frame rate of the video sequence, which ranged from 50 fps to 1 fps (i.e. frame times τ_{frame} of 20 ms to 1 s). A bandpass (515NB3, *Omega Optical*, FWHM = 3 nm) removed possible Raman lines from the excitation beam. An achromatic dispersion lens ($f = 45$ mm) after a pinhole widened the excitation beam to the desired size on the sample. The objective (*Zeiss* Epiplan Neofluar, 100x, $N_A = 0.9$) was used in epi-illumination. Therefore a dichroic mirror (525 DRLP, *Omega Optical*) was needed to separate the detection from the excitation. Since dichroic mirrors do not preserve the polarization of the reflected light, a $\lambda/2$ waveplate was used in addition to a $\lambda/4$ waveplate to obtain circular polarization on the sample. For freely diffusing and thus fast rotating dye molecules this would not be necessary, but in case of surface diffusion, molecules may be restricted in rotation. Circular polarized excitation ensures that all dye molecules with optical transition dipoles in the plane parallel to the substrate will be excited equally. Another achromatic lens ($f = 250$ mm) was used to focus the detected fluorescence light onto the CCD chip of the camera. Within this work two different CCD cameras
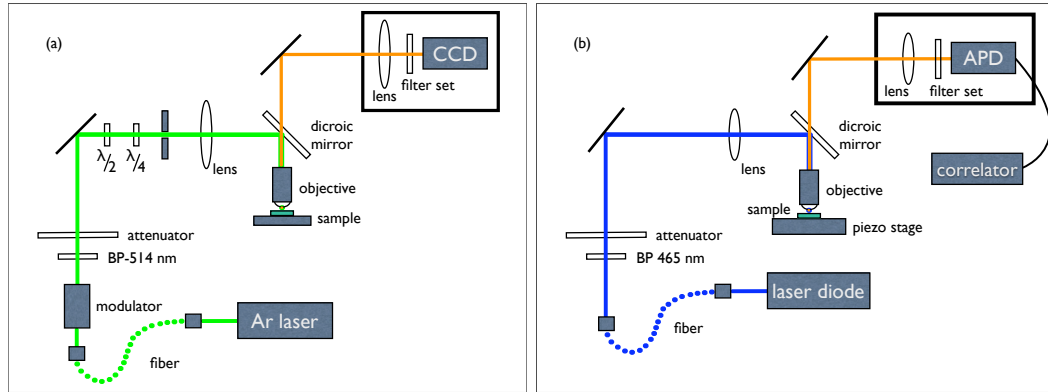
Figure 4.1: (a) Wide field microscope setup, (b) confocal microscope setup.

were used: A Pentamax -512EFT, Gen IV Intensifier, *Princeton Instruments* and an *Andor* iXon DU-885K. A long pass filter (ALP 530, *Omega Optical*) filtered residual excitation light from the detected fluorescence light. Both cameras are equipped with frame transfer options. By this, the signal distribution from the exposed part of the chip is shifted to an equally sized dark chip, which then is read out while the other chip can be used for new acquisition. This reduces dark times during readout to the shift time. However, the dark time for the Pentamax camera is not known, and could only be estimated from information on the implemented CCD chip to be about 1.5 ms. In contrast, the *Andor Solis*™ software provides information about actual dark times of the *Andor* camera.

4.1.2 Confocal microscope for fluorescence correlation spectroscopy (FCS)

With FCS the fluorescence intensity is collected from a single spot on the sample and traced over time. Therefore a confocal microscope setup is used, where the illuminated/detected spot on the sample typically has a diameter of 0.6 μm to 0.8 μm (radial 1/e decay). The most common application of FCS is in biophysics where cells or macroscopic molecules are traced within liquid volumes of several micrometer or even millimeter height. There the use of a pinhole to remove fluorescence contributions from regions outside the focal volume is necessary. In contrast, with the investigation of thin films in this work the film thickness was always smaller than the height of the vertical focus length, which is approximately 1 μm. This renders the use of a pinhole obsolete. For this reason, in the homebuilt setup used here (see Fig. 4.1 b, [Schm10]), the fluorescence light was formed into a parallel beam by the objective and focussed onto the APD (*Picoquant* MPD, PDM Series, temporal resolution < 50 ps), where the entrance pinhole of the APD ($\varnothing = 20$ μm) was used to remove scattered and diffusive light.

The used light source was a pulsed laser diode (*Picoquant* LDH-P-C470) with 465 nm wavelength at the frequency of 40 MHz. A single mode fiber coupled the light to the setup, where a bandpass (*Omega Optical* 3rd Millenium, 465±5 nm) was used to remove

side bands of the excitation light. The parallel beam was focussed onto the sample by an objective (*Zeiss* EC Epiplan Neofluar, 100x, $N_A = 0.9$). Thereby the focal spot can be adjusted automatically [Schm10]. The lateral radius of the focal spot w_{xy} was determined to be 350 ± 50 nm [Schu09, Schm10]. The detected fluorescence light was separated from the excitation beam by a dichroic mirror (*AHF Analysetechnik AG*, 470 nm) and filtered by an additional long pass (*Omega Optical* 480ALP, 480 nm). The autocorrelation was done either by a correlator (*ALV Laser Vertriebsgesellschaft m.b.H.* ALV5000 Multiple Tau Digital Correlator, with temporal resolution 0.2 μm) or based on a single module counting card (*Becker & Hickl* SPC-630) using the program *spcm*. A piezo scan stage (*Physik Instrumente (PI)*, P-517.3CL) was used for lateral positioning and vertical focussing on the sample. It was controlled by a homewritten program (in LabVIEW™, [Schm10]) using a counting card (*Sheldon Instruments* SI-C6xDSP-PCI) together with an analog module (SI-MOD68xx).

4.1.3 Setup for laser-induced dehydroxylation
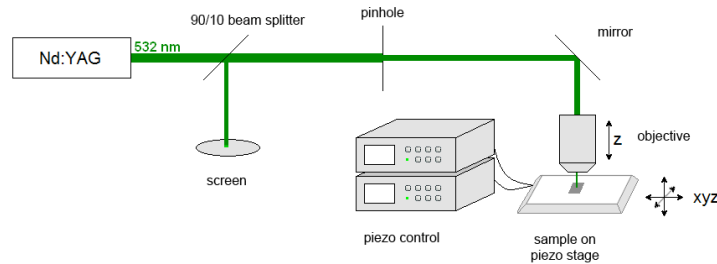
Figure 4.2: Setup for laser-induced dehydroxylation, taken from [Schu10a].

The setup used for laser-induced dehydroxylation (see Fig. 4.2) was built by Sebastian Schubert [Schu10a] according to descriptions in literature [Balg06, Hart09]. By this method the absorption of photons within the underlying silicon layer beneath the thermal oxide generates hot electrons, which relax via inelastic phonon scattering into the valence band. Thereby the energy uptake of the crystal structure generates a local temperature increase, which leads to thermal dehydroxylation of the substrate surface [Hart09, Schu10a]. The laser power has to be tuned such that the substrate does not melt, while temperatures above 800°C have to be reached to irreversibly remove surface silanols. Melting of the substrate can be seen immediately due to the increase in light scattering [Schu10a]. After processing it can be checked at an optical microscope with sufficient magnification, e.g. Zeiss LSM 500, as well as by AFM measurements.

The light source, a frequency duplicated Nd:YAG-Laser (Millenia Pro, *Spectra Physics*) provides light at 532 nm with a power ranging from 0.23 W to 10 W. The objective is a (Planachromat 12.5x/0.25, *Zeiss*) and thus has a magnification of 12.5 and $N_A = 0.25$. By this the lateral spot diameter in the focus is 2.7 μm. The structures were written by scanning the sample in x- and y-direction using a piezo stage (Tritor 101 CAP, *piezosys-*

tem jena) with an integrated universal serial interface card (EDA 4, *piezosystem jena*), which was controlled using the demo-version of EDA 2/3/4/5 Version 1.1610.98.[1] Since this setup does not provide an image of the sample, the focus was set on the sample with the aid of a screen. 77% of the power output reached the sample surface. Thus at an power output of 1 W, the power density of the focussed beam on the sample is 14.5 MW/cm^2 [Schu10a].

4.2 Materials

4.2.1 Fluorescent dyes for SM studies
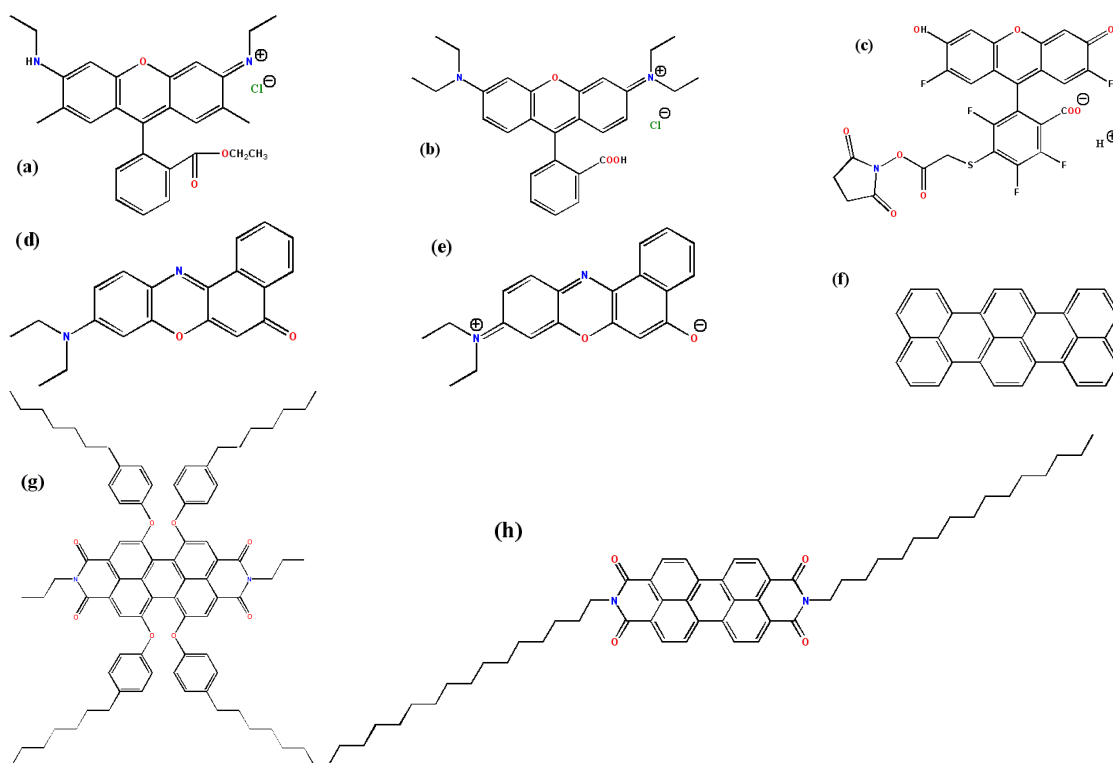
Figure 4.3: Chemical structures of dyes used in this work (a) Rhodamine 6G, (b) Rhodamine B, (c) Oregon Green, (d,e) Nile Red, (f) Terrylene, (g) no-PDI and (h) o-PDI; not to scale.

Single dye molecules can be used with optical microscopy techniques to probe soft matter on a local scale. By use of an appropriate laser wavelength the dye molecule is excited from its electronic ground state (S_0) to a higher energetic state, as was detailed in section 2.3.1; while the additional explanations in section 3.5 (see Fig 3.6) also take interactions with the surrounding matrix into account. From the higher energetic states it can relax by a set of radiative and non-radiative pathways [Vale05]. The ratio

---

[1]Robert Schmidt, TU Chemnitz, kindly implemented the program.

of which determines the quantum yield Φ_F of the dye, i.e. the ratio of emitted photons to absorbed photons, see eqn. 2.8. Dyes used in SM studies typically have high quantum yields. Furthermore, a high photostability is needed: Due to photo-activation the dye molecule can reversibly (i.e. blinking, photophysical bleaching) [Cich07, Schu07] or irreversibly (photochemical bleaching) [Zond04, Schu07] turn into a non-fluorescing state. For both processes the (lowest) electronic triplet state T_1 of the molecule plays a role, although there are also other possibilities for blinking, e.g. reversible electron transfer to the surrounding matrix. Usually the conversion from electronic singlet to triplet states is forbidden, due to different multiplicities of electron spins. But overlap of the electron wave functions allows the intersystem crossing to some extend [Vale05]. The triplet decay rate for highly photostable dyes is in the range of several kHz to MHz [Wide94] and therefore the triplet lifetime may play a role in fluorescence correlation spectroscopy [Schw02]. In this work several dyes where used, the structure formulas of which are shown in Fig. 4.3. Short descriptions of the dyes are given below.

Xanthenes

Rhodamines as well as Oregon Green (OG) are xanthene derivatives, shown in Fig. 4.3 (a) -(c). Rhodamine 6G (R6G) and Rhodamine B (RhB) are widely used for bio-labeling as well as for other SM studies. Both dyes are known to form aggregates in aqueous solution, but those usually are non-fluorescent [Lópe82, Mial91, Mont00]. In case of Rhodamine B in TEHOS, bulk excitation spectra revealed two fluorescent components with a shift of 23 nm in absorption and 12 nm in emission [Schu10a]. Thus further investigations were conducted using R6G, which showed only one fluorescent component [Schu10a]. R6G is cationic, while RhB exists in a zwitterionic and in a cationic from, depending on the degree of deprotonation. However the observed spectral shifts for the two observed components of RhB in the bulk experiments in TEHOS are too large to be explained by partial protolysis. For further considerations see [Schu10a] and references therein. The rhodamines were obtained from *Radiant Dyes*, Germany, while OG was purchased from *Invitrogen*, Germany.

The triplet lifetimes for RhB in ethylene glycol and R6G in distilled water are 6.0 μs and 2 μs, respectively, as given by Menzel et al. [Menz98] and Widengren et al. [Wide94]. Jena et al. measured rotational diffusion correlation times of RhB and R6G in different alcohols, DMSO (dimethylsulfoxide) and formamide by subnanosecond transient-dichrosim experiments. They also calculated molecular volumes of the dyes from *Van der Waals* increments ($V_{R6G} = 414\,\text{Å}^3$, $V_{RhB} = 414\,\text{Å}^3$ and estimated their ellipticity and a geometrical factor determining the deviation from elliptic shape (both Rhodamines are considered as oblate ellipsoids with ellipticity=2). Using these parameters they conducted comparative calculations according to the *Debye-Einstein* relation eqn. 3.7, see [Jena79]. Their results are given in Table 4.1 together with the viscosities of the solvents.

Due to its carboxylic group, Oregon Green is anionic at $pH > 6$. Below this value the neutral form coexists. Since the anion has a far higher quantum yield, mainly this component is detected within SM studies [Gill04].

Table 4.1: Experimentally obtained rotational diffusion times of RhB and R6G in different solvents compared to calculations using the *Debye-Einstein* relation eqn. 3.7 according to Jena et al. [Jena79].

Solvent	τ_{rot}(R6G) [ps]	τ_{rot}(RhB) [ps]	η [mPa s]
Ethanol	310±20	260±20	1.2
calculation (Ethanol)	150	142	1.2
Propanol	490±30	460±30	2.2
DMSO	480±30	–	2.2
calculation (Propanol & DMSO)	275	–	2.2
formamide	600±40	–	4.0
pentanol	1090±60	–	4.0
calculation (formamide & pentanol)	500	–	4.0
Decanol	3400±2500	3050±250	13.5
calculation (Decanol)	1690	1595	13.5
Ethylene glycol	3000±200	2800±200	19.5
calculation (Ethylene glycol)	2440	2305	19.5

Perylenes and terrylene

Perylenes have a slightly smaller quantum yield than the xanthenes. Consequently their triplet lifetime is somewhat longer: Lang et al. give two values for triplet lifetimes of a perylene-diimide in hexadecene to be 20 μs and 290 μs [Lang05] (ascribed to a splitting into different T_1 sublevels). A fourfold branched and thus spherical shaped perylene diimide (no-PDI: N,N'-di-propyl-1,6,7,12-tetra-(4-heptyl-phenoxy)-perylene-3,4,9,10-tetra-carboxdiimide),[2] see Fig. 4.3 (h), was used within TEHOS films as a neutral and thus less interacting dye in comparison to the rhodamines. No-PDI was also used within liquid crystal films, because it did not align with the liquid crystal structure. Another perylene diimide (o-PDI: N,N'-di-hexadecyl-perylene-3,4,9,10-tetracarboxdiimide)[2] with C_{16} chains substituted at the two nitrogen atoms, see Fig. 4.3 (g), was designed to align with the nematic liquid crystal director in 8CB, and proved to do so [Schu10b]. Spectroscopic studies revealed some degree of aggregation of o-PDI which is consistent with reports on a similar perylene diimide with C_{18} chains [Stru00]. For further comparisons an unsubstituted terrylene was used, see Fig. 4.3 (f). It has a sufficiently high quantum yield and was used due to its smaller shape and probably less interactions with the substrate. Triplet lifetimes of the terrylene are reported to be 300 μs and 12 ms in a crystal of p-terphenyl at 1.5 K [Voge95], while at room temperature an upper limit is given to be 18±2 μs [Kulz99]. The terrylene was purchased from *PAH Research Institute*, Greifenberg, Germany.

---

[2]no-PDI and o-PDI were synthesized by Harald Graaf, TU Chemnitz.

Nile Red

Nile Red is known to exhibit a large solvochromatic shift in the UV-visible region, which is ascribed to the existence of an internal charge transfer process. Nevertheless there is an ongoing discussion about the strength of the change in dipole moments between the ground and the excited state and the corresponding geometries [Dutt91, Ghon00, Kaws08], which also led to some theoretical investigations [Guid10]. Chemical structures for the locally excited state as well as for the planar internal charge transfer state, as stated in [Guid10], are shown in Fig. 4.3 (d) and (e), respectively. Alternatively a twisted internal charge transfer state is discussed in literature [Ghon00]. There the charge separation is enhanced due to twisting of the diethylamino group. Nevertheless the latter is less supported by recent calculations [Guid10]. However, due to its sensibility to solvent polarity Nile Red has been used in SM studies to probe local environments e.g. of polymers [Hou00, Hou02, Kim06]. In this work it was used to probe the properties of thin polymer films via the analysis of spectral diffusion of SM spectra. Nile Red was obtained from *Bio Chemika (Sigma for Fluorescence)*.

4.2.2 Silica substrates

Silica exists in crystalline (e.g. quartz) and in amorphous form. Here in this work n-doped silicon wafers (specific resistance 1...8 Ωcm), with 100 nm thermally grown oxide layers were used as substrates (*Center for Microtechnologies, ZFM*, TU Chemnitz). The crystalline Si wafers were cut in 100-direction and were polished afterwards. Then they were oxidized by a dry O_2 process, i.e. within an oxygen flux at 1000°C under addition of few % HCl (to avoid defects [Shir76]). Afterwards the wafers were covered by a removable protection film and cut into pieces of 10 mm x 20 mm. In that way fabricated oxides are amorphous. Nevertheless, there exists a residual order as was shown by X-ray diffraction [Tats04]. This can be explained by the growth process: According to a model suggested in 1965 by Deal and Grove, the O_2 molecules diffuse through the growing SiO_2 layer and react at the $Si - SiO_2$ interface [Tats05]. There the oxygen atoms are incorporated into the silicon crystal mainly by breaking the Si bonds perpendicular to the surface, resulting in an elongation of the previous crystal structure in that direction under addition of some static disorder [Tats04]. By this the silicon atoms remain sufficiently ordered to scatter X-rays at the lowest-order reflection of the new, expanded lattice [Munk04]. Density relaxation of fumed silica on (100) silicon occurs at approximately 1000°C [Tani90]. Thus considerable changes in oxide structure are expected to occur at this temperature. For this reason, slight modifications of the substrate surface, as will be described in the following, should be restricted to lower temperatures.

For investigation of structure formation in thin liquid crystal films also n-doped Si wafer with native oxide were used (*Center for Microtechnologies, ZFM*, TU Chemnitz). Their specific resistance was 1...8 Ωcm) and they similarly were cut in (100) orientation and polished.

Silanols on silica surfaces - modification by substrate pre-treatment.
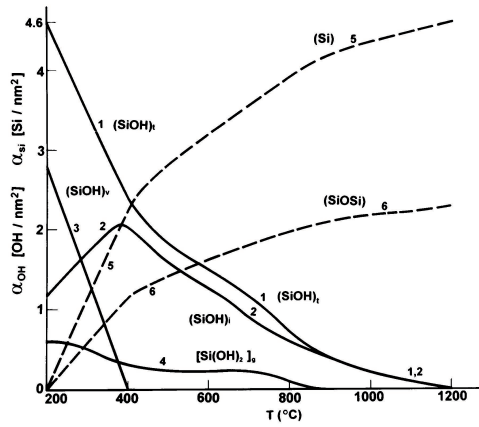
Figure 4.4: Surface silanol number densities depending on annealing temperature (in vacuo) taken from Zhuralev: (1) average concentration of total surface silanol groups, (2) average concentration of free isolated silanol groups, for more details see text and [Zhur00]; reprinted with permission.

Depending on the fabrication conditions silica surfaces display different amounts of surface silanoles, i.e. OH groups bound to surface Si atoms. Moreover, at ambient conditions, freshly cut Si surfaces are immediately oxidized, leading to a native oxide layer of 1.5 nm to 4 nm thickness, which depending on the environmental conditions also contains a certain amount of surface silanoles. Furthermore, water molecules may adsorb onto the silica surface via H-bonding to the oxygen atoms of the silanoles. However, the surface silanoles affect the interface properties of silicon/silica surfaces used in technical applications, e.g. field effect transistors. For this reason early attempts to specify the amount and types of silanoles were made, using site selective adsorbates, see e.g. Armistead et al. [Armi69]. Later, when IR spectroscopy was established, the types of silanoles were characterized due to their different bond lengths leading to characteristic vibrations and thus IR emission lines. However, advanced knowledge was needed to discern also between surface silanoles and internal OH groups within the silica. Eventually the number of possible surface silanol groups was determined to be ≈ 4.5 per nm^2 [Iler79]. In 2000 Zhuravlev summarized the results in a review article [Zhur00], from which Fig. 4.4 was taken, showing the temperature dependence of the silanol density specified for the different types of silanoles. Depending on the surface structure and environmental conditions, there are

vincinal (bridged) silanoles which are interconnected by H-bonding, see Fig. 4.5 (a) including an additional water layer of up to six molecules thickness and (b). The water layer is fully removed at 200°C [Zhur00], while the vincinal silanoles occur up to 400°C, see Fig. 4.4 curve (3).

geminal (paired) silanoles i.e. a surface silicon atom is connected to two hydroxyl groups.

These silanoles are more stable. They exist to a certain amount up to 800°C, see curve (4) in Fig. 4.4 (c).

isolated silanoles i.e. the distance to neighboring silanoles is too large to form H-bonds, and there is only one hydroxyl group per surface Si atom, see Fig. 4.5 (d). Isolated silanoles are most stable. During tempering (in vacuo) their number initially increases up to 400°C, see curve (2) in Fig. 4.4. This is caused by the removal of hydroxyl groups from vincinal and geminal silanoles, leaving isolated silanoles at that position. Isolated silanoles can be found on silica surfaces for temperatures up to 1200°C. However their number decreases with increasing temperature.

siloxane bridges contain no hydroxyl groups, see Fig. 4.5 (e). They are very stable. Silica tempered at 1000°C mainly is terminated by siloxane bridges (curve (5) in Fig. 4.4 gives the number density of surface Si atoms free from silanoles, i.e. twice the number of siloxane bridges, which is depicted in curve (6)).

Of course also geminal silanoles can build H-bonds with other geminal silanoles and/or with vincinal ones.
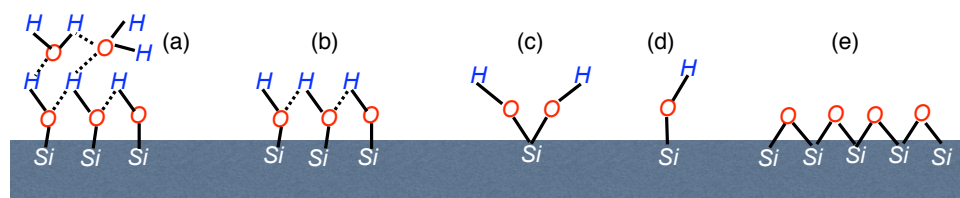
Figure 4.5: Types of surface termination on silica surfaces (a) vincinal silanoles with additional water layer, (b) vincinal silanoles only, (c) geminal silanoles, (d) isolated silanole, (e) siloxane bridges.

While Zhuravlev studied various types of silica gels and porous glasses, Dugas and Chevalier investigated the surface hydroxylation on fumed and thermal silica [Duga03]. They find that the surface hydroxyl density of thermally grown silica resembles that of silica gel tempered at 1000°C. Furthermore by boiling the dehdroxylated substrate for 4 h in water, the surface density of silanoles could be almost fully recovered for fumed silica, while it stayed low (i.e. less than half of the amount of surface silicon atoms) for thermally grown silica, which had been fabricated at 1000°C. Treatment in piranha solution yielded similar results for thermally grown silica.

According to Iler, fluorescent dyes preferentially adsorb to surface silanols [Iler79, Graa07]. This was used by Schubert to compare the local silanol distribution for thermally grown silica substrates after three types of substrate pre-treatment [Schu10a]. The pre-treatments consisted in (i) tempering at 800°C for 0.5 h in air, (ii) etching in prianha solution for 1 h at 70°C in ultrasonic bath, and (iii) boiling in water for 20 h. For this study confocal images were taken on substrates covered by a thin layer of R6G. Those images show a heterogeneous distribution of fluorescence intensity on a sub-micrometer scale. The images were then analyzed using WSxM 5.0 [Horc07], in particular by the

tools provided within the *flooding* menu. For this the mean intensity and the corresponding standard deviation very evaluated for each image. The intensity threshold then was set to the mean intensity reduced by one standard deviation. Thus 65% of the obtained intensity values were selected for the evaluation. After smoothing with a Gaussian, the local intensity distribution showed interconnected "islands" (i.e. clusters, see [Horc07, Gome92]) of varying size and shape. From this distribution then cluster size and coverage were determined (using a cluster threshold size of 0.05 μm^2) [Schu10a]. The results are printed in Table 4.2.

Table 4.2: Local silanole distribution on differently treated thermal SiO$_x$ according to [Schu10a].

pre-treatment	tempered	piranha	boiled in water
investigated area [μm^2]	110	110	81
# of clusters in area	36	85	22
coverage [%]	46.4	49.4	53.5
average cluster size [μm^2]	1.42	0.64	1.97
nearest neighbor distance [μm]	1.75	0.64	0.66

Although these results cannot give absolute values for silanol cluster size and coverage (due to the lack of a normalization procedure), they reveal interesting features of the local silanole distribution. Furthermore they verify the observation of Dugas and Chevalier [Duga03] that the degree of hydroxylation of thermal SiO$_x$ can only be modified to a small extend, since the coverage ranged from 46.4% for the dehydroxylated (tempered) substrate to 53.5% for the hydroxylated substrate (boiled in water) only. Apart from these global aspects, it is interesting to note the differences obtained by the hydroxylation processes using prianha resp. water. The larger average size of fewer clusters observed after hydroxylation in boiling water supports the idea that hydroxylation primarily occurs at the edges of existing silanole clusters [Schu10a], where the bond strength of siloxane bridges is weakened due to the neighboring silanole [Zhur00]. In contrast etching in piranha solution primarily creates new and thus small silanole clusters [Schu10a]. Yet the growth of these new clusters is restricted by the ongoing etching process. An interesting question not yet studied therefore is, whether previous etching has an influence on the silanol distribution obtained by hydroxylation in boiling water.

Silanol gliding of dyes via H-bonding

Honciuc et al. investigated surfactant diffusion (fluorescently labeled palmitic acid) at the solid-liquid interface of hexane on fused silica substrates [Honc08]. From temperature dependent measurements they found a two-fould activation energy of diffusion. Their suggestion is that the process with the lower activation energy is caused by a kind of silanol gliding of the palmitic acid molecules: The acid group binds to surface silanols

via double-H-bonding. On silanol clusters it may break the H-bonds successively to bind to a neighboring silanol. Since only one H-bond has to be loosed at a time, the activation energy is lower as for diffusion activation by simultaneously breaking two H-bonds [Honc08].

The dye molecules used within the SMT and FCS experiments in this work (R6G, RhB, OG, o-PDI and no-PDI) all possess at least two amino groups or single oxygen ends (i.e. ketone groups), see section 4.2.1. This also enables for successive H-bonding on silanol clusters.

Surface roughness measured by AFM

Polished Si wafers typically have a surface roughness below 0.2 nm [Yu99]. The surface of SiO_x thermally grown on a Si wafer has a slightly higher value of ≈ 0.3 nm. In this work here such Si wafers with 100 nm thermally grown oxide underwent a radical cleaning procedure to remove residual dirt before use in SM experiments. Details are given in the following subsection. To determine the roughness of the substrates, AFM measurements were conducted in nonconductive mode using an AFM from *Anfatec Instruments*, Oelsnitz.[3] Fig. 4.6 (left) shows an AFM-height image from a substrate treated for 1 h in piranha solution. The evaluation of the roughness by the widely used software *WSxM 5.0* [Horc07] via a fourier transformation yielded an average roughness of 0.6 nm for this substrate.[4]
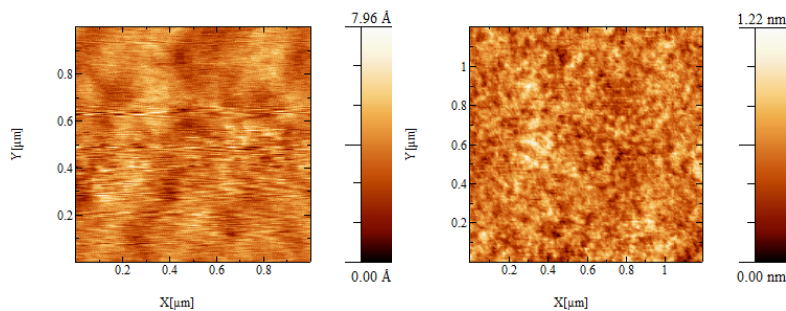
Figure 4.6: AFM height images of Si wafer with 100 nm thermally grown oxide (left) cleaned for 1 h in piranha solution (right) additionally tempered for 0.5 h at 800°C in air.[3,4]

As was explained above, to obtain dehydroxylated surfaces the substrates were additionally tempered at 800°C in air. This leads to an increase of the oxide thickness by some tens of nanometers. However, the oxide mainly grows at the interface with the crystalline Si. Thus besides the modification of the silanol density no particular change on the substrate surface is expected. AFM measurements on a substrate tempered for

---

[3]David Poster, then TU Chemnitz, kindly conducted the AFM measurements

[4]Ines Trenkmann, TU Chemnitz, kindly provided the images and determined the average roughness using *WSxM 5.0* [Horc07].

0.5 h at 800°C yielded an average roughness of 0.2 nm, the corresponding AFM-height image is shown in Fig. 4.6 (right).[3,4]

Substrate cleaning

As was already mentioned, the substrates used for SM experiments had to undergo a strict cleaning procedure. For this they first were rinsed thoroughly by the alternating use of acetone and ethanol (both technical grade). Then they were placed for 10 min in a mixture of ethanol and acetone (both *Merck* spectroscopic grade) at 50°C in ultrasonic bath. Afterwards they were rinsed with de-ionized water (*Milli-Q*, specific resistance < 18.2 MΩcm, TOC < 4 ppm), and dried within nitrogen flux. Then they were etched for 0.5 h - 2 h at 70°C in piranha solution, i.e. a 1:1 mixture of H_2O_2 (*Merck*, 30%) and H_2SO_4 (*Merck*, 96%) in an ultrasonic bath. Finally they were again rinsed with de-ionized water and dried by nitrogen flux. The purity of the substrates was checked at a wide field microscope.

Laser-induced dehydroxylation
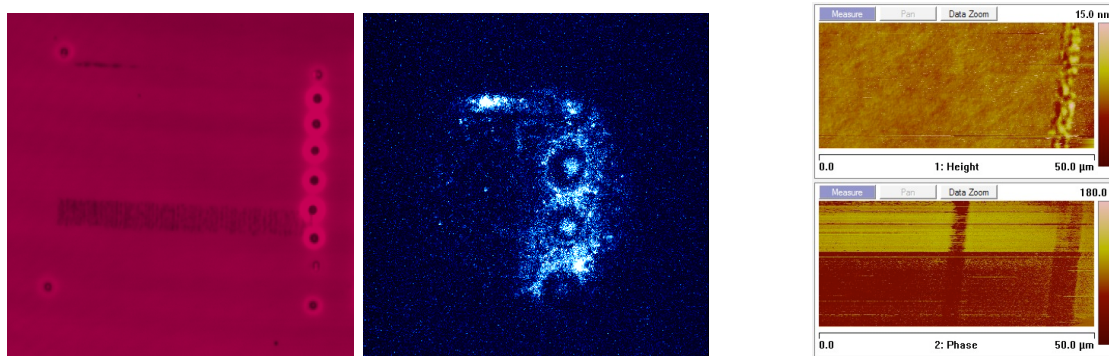
Figure 4.7: Image of written structure in reflected light of 514 nm wavelength: (left) complete square structure taken at a *Zeiss* LSM 500, (middle) top right corner of the same structure coated by a 10 nm thick TEHOS film doped with R6G, taken at the above described wide field microscope; (right) AFM height (top) and phase (bottom) images of a different laser-written structure taken from [Schu10a].

Before laser-induced dehydroxylation, cleaned Si substrates with 100 nm thermally grown oxide were boiled for at least 10 h in water to obtain a highly hydroxylated surface. Lines were then written over 100 μm in $x-$ direction with a periodicity of 3 Hz, a total of 30 periods per line and a triangle voltage with symmetric peak position. By writing 20 lines with a spacing of 0.5 μm in $y-$ direction a dehydroxylated area of 100 μm x 20 μm was generated. Structures consisted of alternating dehydroxylated 5 stripes of 20 μm with untreated ones forming a total width of 100 μm. Since the dehydroxylated structures cannot be seen at an optical microscope [Schu10a], the start and the end (both at the $x = 0$) of the dehydroxylated stripes were marked by melted

holes (at higher laser power), as well as the four corners of the total square structure. Additionally melted lines were written at the position $y = 0$ resp. 100 μm.

Fig. 4.7 shows images of such structures: The left image was taken in reflected light at a *Zeiss* LSM 500. The dark stripe was written by higher laser power, which resulted in melting of the substrate. Furthermore the holes indicating the starts and ends of the stripes can be seen. Fig. 4.7 (middle) shows the top right corner of the same structure. However there it had been covered by an approximately 10 nm thick TEHOS film, which was doped with R6G in nanomolar concentration. This image was taken at the above described homebuilt wide field microscope in reflection with frame time $\tau_{\mathrm{frame}} = 100$ ms (for this the longpass filter had been removed). Also there the limiting melted holes and top line can be seen. Fig. 4.7 (right) shows AFM images[5] of two lines written by Sebastian Schubert with the same setup. The melted line at the right can be seen in the height image (top) and in the phase image (bottom). However the dehydroxylated line in the middle only appears in the phase image [Schu10a]. This is due to the different interaction with the AFM tip in respect to the surrounding substrate surface. The absence of a height modification is a clear indication that no melting of the substrate occurred at that line.

4.2.3 Ultrathin liquid TEHOS films

Tetrakis(2-ethylhexoxy)-silane (TEHOS) is an organic liquid with feasible properties for optical SM studies. The chemical structure is shown in Fig. 4.8 (a). The molecular formula is $C_{32}H_{68}O_4Si$. TEHOS was obtained from *ABCR GmbH*, Germany, with grade 97%. Its molar mass is 544.965 g/mol. Abott et al. determined the viscosity to be 6.8 mPas (25°C) [Abbo61]. There are several values given in literature for surface tension: 32 mN/m [Mo06], 25.38 mN/m [Alag99] and 25.9 mN/m [Tren09a]. Since thin TEHOS films showed dewetting on Si wafers covered with OTS monolayers, Trenkmann also determined the polar fraction of the surface tension as 1.0 mN/m and the disperse fraction as 24.9 mN/m [Tren09a].
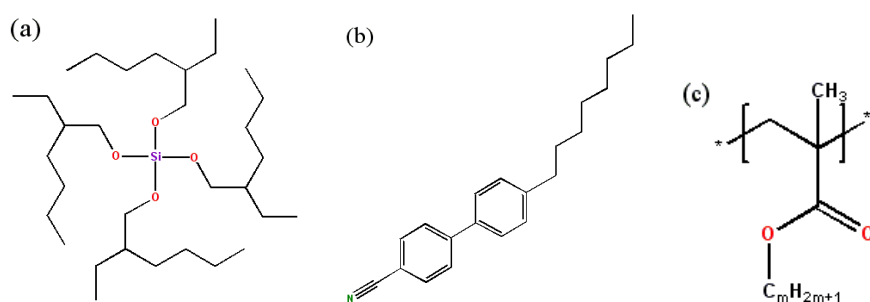
Figure 4.8: Chemical structures of investigated materials (a) TEHOS, (b) 8CB, (c) poly-n-alkyl-methacrylates with m=1: PMMA, m=3: PPMA and m=4: PBMA (not to scale).

---

[5]The AFM measurements were kindly conducted by Thomas Baumgärtel. AFM images were taken from [Schu10a].

Due to the long and branched alkyl chains the molecule conformation is quite flexible, also intercalation of alkyl chains for neighboring molecules may occur. Thus the spacing of molecular layering at solid-liquid interfaces is reported to be 10.3 ± 2.7 Å determined by AFM measurements and X-ray reflectometry [Pati07, Yu99]. In the interfacial layer at silica surfaces, the molecules will expose their oxygen groups towards the silica in favor of forming hydrogen bonds. Therefore all their alkyl chains are oriented to the same side opposite to the silica. Thus the height of the interfacial TEHOS layer is only ≈ 0.7 nm in contrast to otherwise ≈ 13 nm, which was obtained from ellipsometry measurements [Vill96]. The self-diffusion coefficient of bulk TEHOS has been determined by pulsed field gradient NMR to be 78 $\mu m^2/s$ [Vali07]. Recent FCS measurements using two-photon excitation yielded approximately 70 $\mu m^2/s$ for diffusion of the dye Coumarin 153 in bulk TEHOS [Pati07], while approximately 55 $\mu m^2/s$ were reported for Alexa 488 (a Rhodamine derivative) in bulk TEHOS [Grab07]. The *Stokes-Einstein* relation 3.6 with $\eta = 6.8$ mPas and a hydrodynamic radius $a = 0.45$ nm yields $D \approx 70$ $\mu m^2/s$ at 25°C. This hydrodynamic radius is quite small compared to the reported interlayer spacings noted above. Yet the *Stokes-Einstein* relation considers a no-slip boundary at the surface of a hard sphere particle. This certainly is not the case with TEHOS. In particular its long alkyl chains are able for intermolecular entanglement and thus also can glide along each other leading to slip boundary condition and a comparatively small hydrodynamic radius for the use with the *Stokes-Einstein* relation.

Sample preparation

The substrates were cleaned thoroughly by the procedure described above. Then they were dip-coated into solutions of TEHOS in hexane (*Merck*, spectroscopic grade) using a commercial dip-coater (KSV instruments). They remained for 20 s in the solution and then were withdrawn at a speed of 5 mm/s. Film thickness was controlled by changing the concentration of TEHOS in hexane, e.g. a solution of 0.3% TEHOS led to a film with 10 ± 1 nm thickness. Investigation of the samples was started after a waiting time of at least 30 min, to have the hexane evaporate off completely.

Determination of film thickness

The film thickness of ultrathin liquid TEHOS films was measured using a variable angle spectroscopic ellipsometer (VASE™, *J.A. Woollam Co., Inc.*, covering the spectral range from 0.73 to 5 eV)[6] at the angles of 65°, 70° and 75°. The *Cauchy* eqation 6.1 for the wavelength dependence of the dispersion was used for fitting the film thickness of TEHOS. For more details see section 6.1.2. The *Cauchy* parameters for TEHOS had been determined as $A_n = 1.4633$ and $B_n = 0.0039$ using the small wavelength region of 2.1 ± 0.1 eV for the fit.[7] The film thickness was then determined from a three-layer fit to the measurements, which consisted of the thick Si substrate, a SiO_x layer and a thin TEHOS layer. Due to quite similar refraction indices of TEHOS and SiO_x, the layer

---

[6]Prof. Dr. Dr. h.c. D.R.T. Zahn, TU Chemnitz, kindly allowed the use of the instrument.
[7]Daniel Lehman, TU Chemnitz, kindly determined the *Cauchy* parameters for TEHOS.

thickness of the latter had to be determined beforehand. This was done by using a blank substrate from the same wafer (which underwent the same cleaning procedure, as the substrate used for the TEHOS film).

For comparison X-ray reflectivity was used on one sample to determine the thickness of the TEHOS film.[8] The ellipsometry and X-ray reflectometry measurements were conducted on the same day, starting with the ellipsometry measurement. The obtained values for the film thickness by X-ray reflectometry were 3.4 ± 0.1 nm resp. 2.6 ± 0.6 nm. The difference in the results produced by the two methods was probably due to the area of the film which was examined. In case of X-ray reflectometry the value is an average over the whole sample, and the error gives the variation in thickness over the sample, including the edges which will show rather strong derivations due to the dipping procedure (spare edge where the sample was held by the tweezers). In contrast, the ellipsometry measurements are conducted using an elliptical spot with 3 mm (short) axis on the sample perpendicular to the optical axis. Thus the edges of the substrate can be excluded from the measurements.

4.2.4 Thin films of poly-n-alkyl-methacrylates

Due to its wide range of application, PMMA has been investigated extensively. Thus multiple physical constants and relations are provided by literature. Kirste et al. investigated vitreous PMMA of several molecular weights M_w by neutron scattering. They derived a relation between M_w and the radius of gyration R_g [Kirs75]:

$$R_g^2 = 0.096 M_w^{0.98} \tag{4.1}$$

where R_g is the average value corresponding to the distribution of molecular weights in the polymer. This relation also implies that in the vitreous state all features of unperturbed coils are present. Investigations of poly-n-alkyl-methacrylates with varying side chain length reveal increasing chain stiffness for increasing n-alkyl side chain length [Hero86].

Table 4.3: Physical Data of used polymers PMMA, PPMA and PBMA.

Polymer	M_w [g/mol]	T_g [K][9]	R_g [Å]	V_{free} [nm^2][10]
PMMA	350,000	388	161[11]	0.105
PPMA	150,000	308		
PBMA	337,000	298		0.132

---

[8]Mirko Kehr, TU Chemnitz, kindly conducted the X-ray measurement and data analysis.
[9]given by the manufacturer.
[10]mean hole volume at room temperature according to [Vall04].
[11]calculated by eqn 4.1.

Rogers et al. studied the influence of side chain length within poly-n-alkyl-methacrylates on glass transition and on free volume in the liquid state. They ascribed the decrease of T_g with increasing side chain length to a corresponding increase of free volume, which they calculated to be about 15% of the respective specific volume of the polymers [Roge57]. Decades of polymeric research led to more elaborate understanding of structure and transitions. For lower side chain length poly-n-alkyl-methacrylates ($N_C < 6$, where N_C is the number of the C atoms of the side chains) it was confirmed that a cooperative α relaxation starts 10 - 20 K above T_g, i.e. certain numbers of polymer chains start to move cooperatively [Bein01]. Furthermore the idea of nanophase separation evolved: In case of the poly-n-alkyl-methacrylates this results from preferred separation of the polar backbone from the unpolar alkyl side chains. This effect was confirmed by X-ray scattering experiments for side chain $N_C \geq 3$. Furthermore nanophase separation explains the coexistence of two glass transition temperatures for all higher members ($N_C \geq 3$) of the poly-n-alkyl methacrylate series, where the lower T_g stems from the alkyl part of the side chains [Bein01].

Sample preparation

Samples of 25 nm as well as of 200 nm thick PMMA, PPMA resp. PBMA were prepared by spin-coating from a solution in toluene onto Si substrates with 100 nm thermally grown oxide. The film thickness was controlled by changing the concentration of the polymer in toluene. Nile Red had been added to the solution before spin-coating in nanomolar concentration. Afterwards the samples were kept at 50°C and 10^{-5}mbar for at least 10 h to ensure complete evaporation of the solvent.

4.2.5 Thin liquid crystal 8CB films

The series of alkyl-cyanobiphenyls (nCB) have been thoroughly studied in recent years [Schl02, Zihe03, Jin05, Vilf07, Lefo08]. Much work was done on pentyl-cyanobiphenyl (5CB), which is nematic at room temperature and thus easier to handle and to model than the here used octyl-cyanobiphenyl. In this work the analysis of experiments[12] done on thin films of 4-n-octyl-4'-cyanobiphenyl (8CB) by Benjamin Schulz [Schu09] was complemented by analysis of diffusivities, which also contributed to two publications [Schu10b, Schu11]. 8CB was obtained from *Synthon Chemicals*, Wolfen, Germany. At room temperature 8CB is in the smectic-A phase [Bell92], see Table 4.4 for the transition temperatures of bulk 8CB. In thin films the phase transitions are likely to be shifted in temperature, as was reported for confinement in silica aerogel [Bell92]. The chemical structure of an 8CB molecule is given in Fig. 4.8 (b). The rod-like 8CB molecules contain a polar section, the cyanobiphenyl part, while the alkyl part is unpolar. Therefore the molecules align pairwise with their cyanobiphenyl groups face to face, while their alkyl groups stick out in opposite directions. Thus a smectic-A layer consists of a bilayer of oppositely oriented 8CB molecules, which leads to a layer thickness of 3.2 nm [Xu00].

---

[12]Benjamin Schulz conducted sample preparation and experiments as well as the analysis of SMT experiments by msd and the analysis of FCS experiments [Schu09].

Table 4.4: Phase transition temperatures of bulk liquid crystal 8CB [Bell92].

transition	crystalline/smectic-A	smectic-A/nematic	nematic/isotropic
T [°C]	21.5	33.7	40.5

The diffusion within 8CB in the smectic-A phase is known to be anisotropic. NMR experiments reveal a self-diffusion coefficient in the range of 28 $\mu m^2/s$ for diffusion parallel to the liquid crystal director **n**, and 13 $\mu m^2/s$ for diffusion perpendicular to **n** [Dvin06].

As was already mentioned in section 2.1.3, liquid crystals (LC) are very sensitive to interface properties. In particular in thin smectic-A films, contrary boundary conditions at the interfaces lead to frustration and thus to the appearance of mesoscopic structures, such as focal conic domains (FCD) [Four90] and hemicylinders [Mich06, Zapp11]. The alignment of the smectic-A 8CB molecules at the interface with air is homeotropic [Desi06], i.e. the liquid crystal director **n** (the layer normal) is perpendicular to the interface. In contrary, for Si wafers with native oxide the anchoring of 8CB molecules is reported to be planar [Jin05]. However at the edge of spreading 8CB droplets, terraced structures with characteristic spacing have been observed [Xu00], which imply homeotropic alignment of the 8CB molecules for ultrathin films in that case. For Si wafers with 100 nm thermally grown oxide up to now no studies of anchoring conditions are known. Yet also in that case planar anchoring of the 8CB molecules is expected.

Sample preparation

Samples of 4 to 220 nm thick 8CB films on Si wafers with two types of oxide were prepared[12] by spincoating from a solution of 8CB in toluene, as described in [Schu09, Schu10b]. One type of Si wafers contained only native oxide, whereas the other contained 100 nm thermally grown SiO_x. For part of the investigations the samples were heated up to 35°C into the nematic phase for 0.5 h and then cooled down again, as was described in [Schu11]. 8CB films with different thickness were prepared. The film thickness was controlled by the concentraction of 8CB in toluene. Either no-PDI or o-PDI was added in nanomolar concentration before spincoating.

4.3 Comparison of used tracking software packages *tracking.sh* and *DSAA*

To obtain single molecule trajectories from video sequences taken at a wide field microscope sophisticated tracking programs are needed. First the background intensity has to be dealt with. Then the fluorescence intensity images, i.e. "spots," from the single dye molecules have to be detected in each frame and traced along the video sequence, while miss-assignments have to be avoided. Since the single dye molecules are two or-

ders of magnitude smaller than the fluorescence wavelength, they can be considered as point-like emitters. Therefore the spots in a video frame are images of the point spread function of the setup, which are smeared out by the diffusion during exposure of the frame. Furthermore the detected SM trajectories have to be analyzed, in particular diffusion coefficients D_{traj} along the trajectories and distributions of diffusivities have to be obtained together with some further distributions of interesting quantities, e.g. lengths of adsorption events and signal to noise ratios.

Within this work two different program packages were used: The program package *tracking.sh* was developed by Cichos and Schuster [Schu02b] and was modified within this work, e.g. to obtain diffusivities. The other package *DSAA* was developed by Mario Heidernätsch in close cooperation[13] [Heid09a, Heid09b]. The latter package also contains a simulation tool with which video sequences of diffusing molecules can be modeled. This simulation tool includes modeling diffusion with vertical layers containing different user-specified diffusion coefficients and interlayer exchange rates.

In the following first an overview of the main features of both packages will be given. Then distributions of diffusivities obtained from tracking simulated video sequences (created by *DSAA*) by both packages are compared and discussed. Finally the comparison is extended to experimentally obtained videos.

4.3.1 Main features

Denoising and spot detection

Denoising of the acquired video images (removal of background intensity, i.e. noise) is accomplished differently by the two different programs. While *tracking.sh* simply calculates an average background for the full image throughout the whole video sequence, which then is subtracted from the intensities for each pixel, *DSAA* allows for local background evaluation on a user-defined-size window around local intensity maxima by the use of up to two common background filters [Heid09a]. The latter is superior and in particular suitable for inhomogeneous background distribution.

With *tracking.sh* the spots are then found as sets of connected pixels with intensities above a threshold level. The center position of each spot is derived by fitting the intensity distribution within the interconnected area to a two-dimensional Gaussian. The widths of the two Gaussians are stored with the center position, giving the area of the spot. *DSAA* provides two ways for detecting the SM spots, a "blob-detector" which will not be described here, since it was not used, and a "spot-detector" which checks for local intensity maxima in a user-defined-size window. There the center position coordinates are derived from the brightness weighted centroid of the pixels in the window region around the local intensity maximum [Heid09a].

Furthermore the outcome of denoising and spot detection for a selected set of filters

---

[13]A cooperation with the theory group KSND of Prof. Dr. G. Radons, TU Chemnitz, existed within the project P4 *Diffusion and trapping in confined liquid films and at interfaces* of DFG-FOR 877 *From local constraints to macroscopic transport*, and is extended to the new P4 *Driven diffusion in nanoscaled systems* in the second funding period.

and detection parameters by *DSAA* can be immediately visualized and reconsidered before progressing to the tracking section of the package.

Tracking the spots
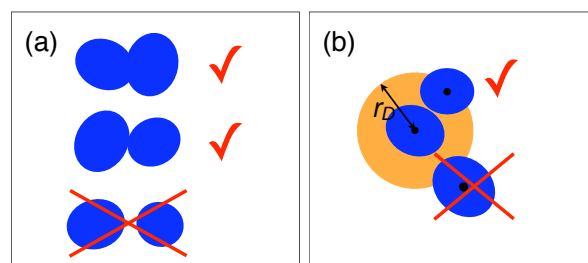
Figure 4.9: Criteria for linking spots in succeeding frames used by (a) *tracking.sh*: Overlapping or touching spots, (b) *DSAA*: Distance between center positions is smaller than r_D.

The program *tracking.sh* tracks the spots, by searching in succeeding video frames for the closest neighbor to the previous position of the spot. For combining two succeeding spots the criterion has to be fulfilled that the two spots are overlapping or at least touching each other, see Fig. 4.9 (a). This increases the reliability of the tracking procedure, but it also has a drawback: Fast moving molecules with respect to the CCD exposure time will yield large smeared out spots with faint outer regions. Therefore the area of the spots may not be fully recognized by *tracking.sh*. Thus the probability for detecting diffusing molecules decreases with increasing diffusion coefficients leading to an underestimation of the diffusion within the investigated sample, as will be seen in the following section on analysis of simulated videos. *tracking.sh* also provides a way to cope with short fluorescence intensity intermittencies "blinking" which occur due to photophysical processes of the dye molecules [Cich07]: Up to two succeeding frames may be skipped. As long as the third frame contains a spot fulfilling the tracking criterions, its position and dimensions will be combined into the trajectory.

A short description of the tracking method developed by Mario Heidernätsch in close cooperation has been published in [Heid09b]:

M. Heidernätsch, M. Bauer, D. Täuber, G. Radons and C. von Borczyskowski. An advanced method of tracking temporarily invisible particles in video imaging. *Diffusion Fundamentals Journal*, Vol. 11, p. 111(2), 2009.

This tracking method is based on an algorithm developed by Sbalzarini and Koumoutsakos [Sbal05], which is improved to handle also short fluorescence intermittencies. In *DSAA* both tracking algorithms, the newly developed one and the one developed by Sbalzarini et al. are implemented. Both algorithms obtain the trajectories by an optimization procedure, which calculates the optimal pairing of the whole set of spots detected in succeeding frames via a cost function. Heidernätsch additionally implemented a user-defined memory length, which is used to calculate the optimized spot linking for

the corresponding number of succeeding frames in one step, i.e. not only two frames are considered at one time, but three or four succeeding frames. Thus short blinking events no longer lead to trajectory ending. Both algorithms need a user-defined estimate of the diffusion coefficient D. This value then is used to define a circle with radius r_D around each spot within which the algorithms search for matching spots in the succeeding frame, see Fig. 4.9 (b).

Distributions of diffusivities and msd analysis

Both tracking packages use the method of weighted mean square displacements (msd) developed by Saxton [Saxt97a] to obtain diffusion coefficients D_{traj} along detected trajectories. Distributions of D_{traj} are provided for subsets of the detected trajectories. These subsets are selected according to a user-defined minimum trajectory length and additionally by an area criterion, i.e. the lateral area covered by the center positions of the diffusing molecule has to exceed a user-defined number of pixels. The latter was implemented to sort out immobile molecules and peculiar trajectories. However the user-defined parameter for the area selection can be set to zero, actually turning off the criterion.

During this work the dependence of the obtained diffusion coefficients D_{traj} on the used exposure time was realized, see section 6.3. Thus in cooperation with the theory group of Prof. Dr. G. Radons, TU-Chemnitz,[13] an additional tool was developed: Probability distributions of diffusivities, see section 3.3.7. These probability distributions provide access to larger data sets thus yielding better statistics than the distributions of D_{traj}. Furthermore by those distributions the observation time is set to the frame time (inverse frame rate) and so access is provided to the actual temporal resolution of the experiment, which up to then was obscured by the need for a larger minimum trajectory length within msd analysis. Diffusivities d_{diff} are time-scaled square displacements (see section 3.3.7). Thus they are obtained from tracing spots in succeeding frames. This feature was implemented into both tracking packages. Thereby within *DSAA* the memory length has to be set to the minimum (succeeding frames only) to avoid contributions from blinking events, where the diffusivities then would be obtained by scaling with the then larger time step, which due to the time dependence of the diffusion process is not feasible. Within *tracking.sh* blinking events are excluded for this reason.

4.3.2 Analysis of simulated video sequences

To test the tracking programs *tracking.sh* and *DSAA* simulations where created with *DSAA*. For simplicity homogeneous diffusion with a single diffusion coefficient was simulated first. The simulated frame rate was 50 fps. Fig. 4.10 shows the obtained probability distributions of d_{diff} together with mono-exponential fits for (a,c) $D = 2.5 \ \mu\mathrm{m}^2/\mathrm{s}$ and (b) $D = 5 \ \mu\mathrm{m}^2/\mathrm{s}$. The solid line denotes the diffusion coefficient used within the simulation. For tracking using *DSAA* the estimated diffusion was set to $D = 5 \ \mu\mathrm{m}^2/\mathrm{s}$, which for (a) resp. (b) exceeded resp. matched the simulated value. As can be seen, the diffusion coefficient obtained from fitting $(\cdots)$ the probability distributions derived by *DSAA*

($\bullet$) in both cases exceeds the simulated value, yielding (a) $D_{\mathrm{diff}} = 3.0 \; \mu\mathrm{m}^2/\mathrm{s}$ and (b) $D_{\mathrm{diff}} = 5.7 \; \mu\mathrm{m}^2/\mathrm{s}$.

In contrast, probability distributions of d_{diff} obtained by *tracking.sh* ($\blacklozenge$) underestimated the simulated diffusion coefficient. Furthermore those distributions show a kink. Mono-exponential fits (- -) to the initial straight part yielded (a) $D_{\mathrm{diff}} = 2.0 \; \mu\mathrm{m}^2/\mathrm{s}$ and (b) $D_{\mathrm{diff}} = 3.8 \; \mu\mathrm{m}^2/\mathrm{s}$, which is about two thirds resp. three quarters of the simulated value. As was explained above, *tracking.sh* only links two spots in succeeding frames, if the areas covered by them overlap or at least touch each other (Fig. 4.9 a). However the edges of the smeared out spots from diffusing molecules may be very faint, eventually their intensity drops below the detection threshold. This issue gets more severe for faster diffusing molecules. Therefore not all trajectories from fast diffusing molecules will be detected by *tracking.sh* leading to the observed kink in the probability distribution. This was further investigated by changing the size of the spots used within the simulation. Previously (Fig. 4.10 a and b) the simulations had been created using a diameter of 0.3 μm for immobile spots. In Fig. 4.10 (c) the diameter of immobile spots was changed in 0.1 μm steps from 0.2 μm to 0.5 μm. Again the black line denotes the simulated diffusion coefficient. As can be seen, the result obtained by *tracking.sh* considerably improves with increasing spot size (the dashed line again corresponds to $D_{\mathrm{diff}} = 2.0 \; \mu\mathrm{m}^2/\mathrm{s}$). For an immobile spot diameter $= 0.5 \; \mu$m a mono-exponential fit to the obtained probability distribution renders $D_{\mathrm{diff}} = 2.4 \; \mu\mathrm{m}^2/\mathrm{s}$, which is close to the simulated value $D = 2.5 \; \mu\mathrm{m}^2/\mathrm{s}$. The simulations created with varied spot sizes also were analyzed using *DSAA*. Here no influence of the spot size on the result was expected, since the tracking algorithm does not use the spot size but only the center positions (Fig. 4.9 b). The obtained distributions matched this expectation and therefore are not shown here. Although the estimate of 0.3 μm for the diameter of immobile spots was derived from comparisons with experimental videos, the experimentally occurring spot sizes may not fully be recovered by the simulations. Changes of the signal to noise ratio from 2 up to 8 within the simulations did not show noticeable effects on tracking performance with both tracking packages.
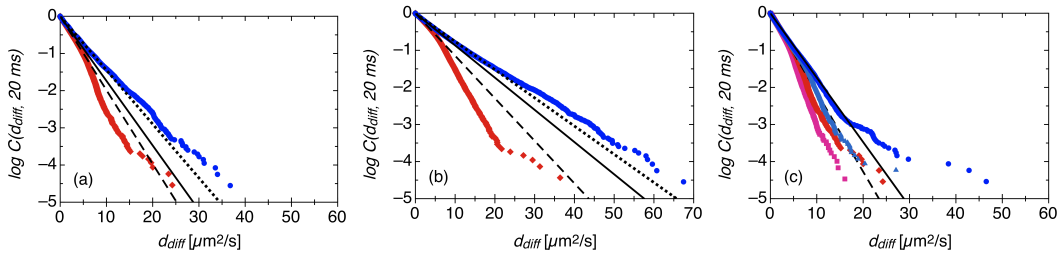
Figure 4.10: Probability distributions of d_{diff} from analysis of simulated video sequences and mono-exponential fits (a) simulated $D = 2.5 \; \mu\mathrm{m}^2/\mathrm{s}$, (b) simulated $D = 5 \; \mu\mathrm{m}^2/\mathrm{s}$, (a,b) ($\blacklozenge$ and - -) *tracking.sh* data resp. fit, ($\bullet$ and $\cdots$) *DSSA* data resp. fit, (—) simulated value; (c) simulated $D = 2.5 \; \mu\mathrm{m}^2/\mathrm{s}$ with varied spot size ($\blacksquare$) 0.2 μm, ($\blacklozenge$) 0.3 μm, ($\blacktriangle$) 0.4 μm, and ($\bullet$) 0.5 μm analyzed by *tracking.sh*.

Up to here simple homogeneous diffusion was used to test the tracking programs. However within the experiment, diffusion coefficients will vary by one or two orders of magnitude. Therefore further simulations were created using a two-layer system with layer-dependent diffusion coefficients.

Two-layer simulations
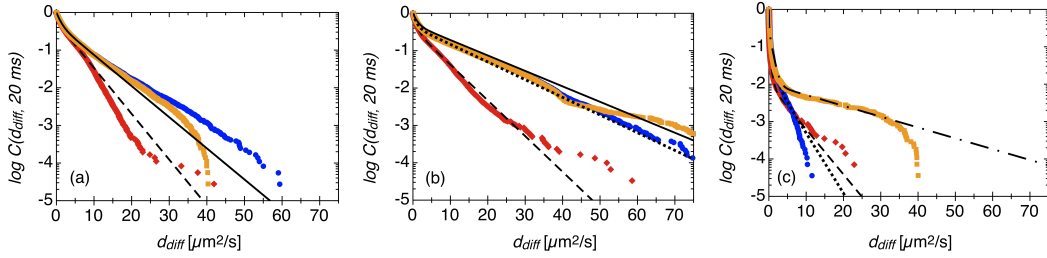
Figure 4.11: Probability distributions of d_{diff} from analysis of (a,b) simulated video sequences and bi-exponential fits using two-layer simulations with $D_1 = 1$ μm^2/s and (a) $D_2 = 5$ μm^2/s, (b) $D_2 = 10$ μm^2/s, (c) experimentally obtained video; (a,b,c) ($\blacklozenge$ and - -) *tracking.sh* data resp. fit, ($\bullet$ and $\cdots$) *DSSA* algorithm Heidernätsch data resp. fit, ($\blacksquare$ and - ·) *DSSA* algorithm Sbalzarini data resp. fit, (—) simulated values.

In the following the performance of both tracking packages was further tested using two-layer simulations with different diffusion coefficients $D_1 \neq D_2$ and symmetric exchange rates between the layers. The diameter of immobile spots again was set to 0.3 μm and the frame rate to 50 fps. This time both algorithms available with *DSAA* were compared. As can be seen in Fig. 4.11 (a and b) only slight differences appear when comparing those algorithms. The Sbalzarini algorithm in both cases yields slightly higher values, in particular D_2 is recovered very well. The results from fitting the probability distributions of d_{diff} using eqn. 3.26 for two components are given in Table 4.5. In contrast to both *DSAA* algorithms the values obtained using *tracking.sh* deviate about 20% for the smaller D_1, while the faster component D_2 is even more poorly reproduced.

Summing up the results obtained from analyzing simulated videos, it can be said that the *DSAA* algorithms show a better performance than the *tracking.sh* in matching the simulated diffusion coefficients. However the former show a dependence on the estimated diffusion coefficient used for the tracking. On the other hand, the performance of *tracking.sh* strongly depends on the size of the spots, which may not be reproduced well by the simulated videos. Nevertheless *tracking.sh* shows a strong tendency to underestimate the diffusion coefficients. In the following section both tracking packages will be applied to experimentally obtained videos.

Table 4.5: Parameters from fits to probability distributions of d_{diff} obtained from analysis of bi-layer simulation.

tracking algorithm	A_1	$D_{\text{diff},1}$ [μm^2/s]	A_2	$D_{\text{diff},2}$ [μm^2/s]
simulated values	0.5	1	0.5	5
tracking.sh	0.45	0.8	0.55	3.6
DSAA Heidernätsch	0.49	0.9	0.51	5.2
DSAA Sbalzarini	0.48	0.9	0.52	5.0
simulated values	0.5	1	0.5	10
tracking.sh	0.62	0.8	0.38	4.5
DSAA Heidernätsch	0.56	0.9	0.44	9.2
DSAA Sbalzarini	0.6	1.1	0.4	10.0

4.3.3 Analysis of experimentally obtained video sequences

The tracking program packages where further applied to the same experimentally obtained video sequence, where the frame rate again was 50 fps. Fig. 4.5 (c) shows probability distributions of d_{diff} obtained by analysis using the different algorithms together with three-exponential fits according to eqn. 3.26 for three components. The *DSAA*-Heidernätsch algorithm was used setting $D = 1\ \mu$m^2/s, while for the *DSAA*-Sbalzarini algorithm D was set to 5 μm^2/s again. The results from the fits are shown in Table 4.6, while Fig. 4.12 shows corresponding plots of the detected trajectories for *tracking.sh* (left) and *DSAA*-Sbalzarini (right).

Table 4.6: Diffusion coefficients $D_{\text{diff},i}$ [μm^2/s] from fits to probability distributions of d_{diff} from analysis of experimentally obtained video.

tracking algorithm	set D	$D_{\text{diff},0}$	$D_{\text{diff},1}$	$D_{\text{diff},2}$
tracking.sh	—	0.08	0.3	2.4
DSAA Heidernätsch	1	0.09	0.7	2.7
DSAA Sbalzarini	5	0.06	0.8	15

Setting $D = 1\ \mu$m^2/s for *DSAA* yielded quite similar results for both *DSAA* algorithms as obtained by the application of *tracking.sh* (the results using the Sbalzarini algorithm with $D = 1\ \mu$m^2/s are not shown here). However when D was set to 5 μm^2/s, the results deviated considerably, yielding a fast component $D_{\text{diff},2} = 15\ \mu$m^2/s. This certainly is due to false linking, as can be seen in Fig. 4.12 (right), where the detected trajectories are plotted. The star-like shapes are an indication for false linking, i.e. spots originating from different dye molecules are linked into one trajectory. These stars occur far more often with *DSAA* (not all are marked). In that case the false-linking is quite obvious. However for smaller diffusion coefficients it may not be discerned by looking at the
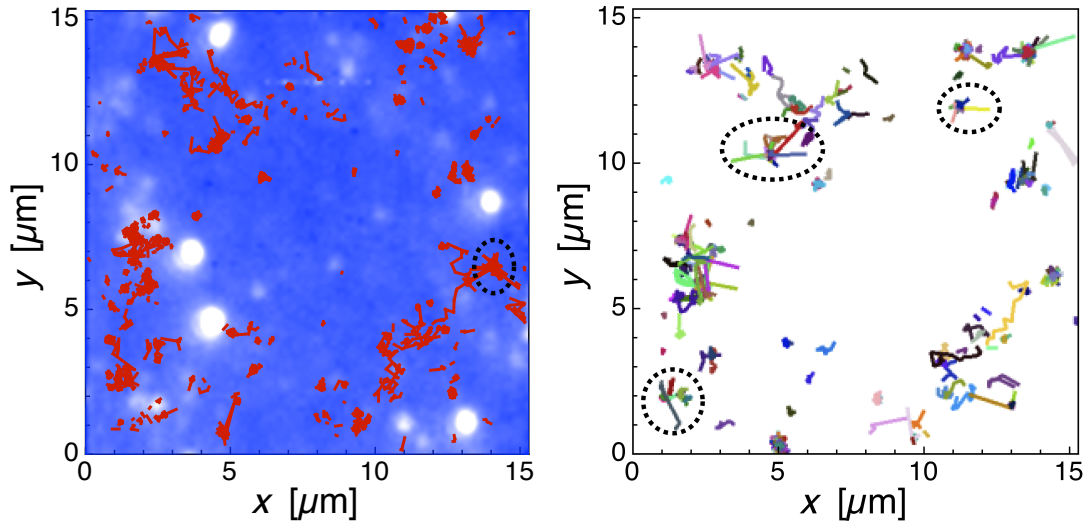
Figure 4.12: Plot of detected trajectories from an experimentally obtained video with frame rate 50 fps analyzed by (left) *tracking.sh* (plotted on spatial intensity distribution integrated over all frames), and (right) *DSSA*-Sbalzarini with estimated D set to 5 μm^2/s; dotted circles highlight star-like shapes indicating false linking.

plotted trajectories. Thus there is a definite need for a good estimate of the diffusion coefficient to obtain proper results from application of the *DSAA* algorithms. Yet in the experiments on diffusion in thin liquid films several different diffusion coefficients are present, which differ by two orders of magnitude at least, as can be seen from the analysis with *tracking.sh* (and from FCS experiments, see section 6.4). Therefore it is not possible to define a proper diffusion coefficient for the use of *DSAA*. For this reason the application of the *DSAA* package should be restricted to experiments, where the range of the diffusion coefficients is well known and restricted to one order of magnitude.

4.3.4 Conclusion

The comparison of the tracking program packages *DSAA* and *tracking.sh* showed that the former is superior on the analysis of experiments with known diffusion coefficients. However, when it is not possible to estimate the diffusion coefficient, or when there are several diffusion coefficients differing by some orders of magnitude, the results obtained by applications of *DSAA* are not reliable. On the other hand *tracking.sh* underestimates the diffusion coefficients. This issue gets more severe for fast diffusion in respect to the frame rate of the video sequence, since then the single diffusing molecules are imaged by large smeared out spots with faint outer regions. For this reason *tracking.sh* can only yield lower limits for the real diffusion coefficients.

5 Spectral diffusion

As was already stated in section 2.3 on single molecule methods, the properties of highly viscous matter, such as polymers in their glassy state, are not accessible by experimental methods investigating translational diffusion. However, they can be studied using either polarization resolved microscopy to gain information by rotation dynamics of tracer molecules [Ruit97, Scho04, Kowe09, Adhi11], or by analyzing fluorescence spectra obtained from single tracer molecules at a confocal microscope [Hou02, Kim06]. An advanced method of the latter is to analyze time traces of such SM spectra for spectral diffusion, i.e. the changes in peak positions and shape of the SM spectra are monitored over time [Kowe09, Krau11b]. Within this work a new way of statistical analysis of such spectral diffusion was developed: Probability distributions are created from spectral diffusivities d_{spec}, i.e. time scaled square displacements of peak positions between succeeding spectra, see section 3.5. This method has already been published in [Krau11a]:

S. Krause, P.F. Aramendía, D. Täuber and C. von Borczyskowski. Freezing single molecule dynamics on interfaces and in polymers. *Phys. Chem. Chem. Phys.*, Vol. 13, pp. 1754–1761, 2011.

Since this method is new, first some simulations are presented in the following section 5.1. In particular they show how spectral diffusion originating from a two-level system (i.e. a fluorophore with two spectral positions) is described by such cumulative probability distributions of spectral diffusivities and how these distributions are influenced by changes in physical quantities (e.g. the jump rate). Furthermore, the energy difference between the two spectral positions can be derived from such probability distributions. Usually the jumps between the spectral positions are accompanied by smaller fluctuations around the main peak positions. These fluctuations contain some experimental noise and contributions from fitting uncertainty, but they additionally monitor true physical fluctuations, e.g. small changes due to the interactions of the fluorophore with the surrounding matrix, which lead to slight height modulations in the potential landscape of the dye, see Fig. 3.7 in section 3.5. As was detailed in the just mentioned section 3.5, short range spectral diffusion coefficients D_{spec} can be derived from the probability distributions of spectral diffusivities. The D_{spec} provide a new means to characterize the strength of spectral diffusions and thus yield information on the system dye-matrix.

Fluorescence emission from single molecules is weak. For this reason a considerable accumulation time (typically 0.5 or 1 s) is needed to obtain a reasonable signal to noise ratio for SM spectra. However, spectral jumps may occur on a much faster time scale. When the fluorophore jumps from one spectral position to another during integration

time, the recorded spectrum will be a mixture of the spectra corresponding to both positions. The effect of such mixings on the recorded spectra and on the probability distributions of d_{spec} will be investigated in section 5.1.2.

In the experimental section 5.2 the new tool will be applied to study spectral diffusion within thin poly-n-alkyl-methacrylate films. Polymers are widely used e.g. as spacers and insulators in technical applications. For this the physical properties, e.g. glass transition temperature and polarity have to be known. However, there is an ongoing discussion on how these properties may change close to interfaces with solids, which just recently led to lively discussions in the focussed sessions CPP 13 and CPP 16: *Confinement of Polymers in Nanoscopic Layers - How Much do Properties Change? I* resp. *II* at the annual spring meeting of the german physics society (DPG) in Dresden [Nunn11]. Here in this work first results were obtained by applying the analysis of probability distributions of d_{spec} to SM spectra obtained from Nile Red molecules in 25 nm polymer films. Further experiments on thicker polymer films are currently under investigation[1] for comparing the properties. Yet these first results already show that analysis of probability distributions of d_{spec} is a promising to tool, which may be able to contribute to the solution of this issue.

5.1 Simulations

5.1.1 Evaluation of spectral jumps and small fluctuations from probability distributions of d_{spec}

Two-level systems with varied range of small fluctuations
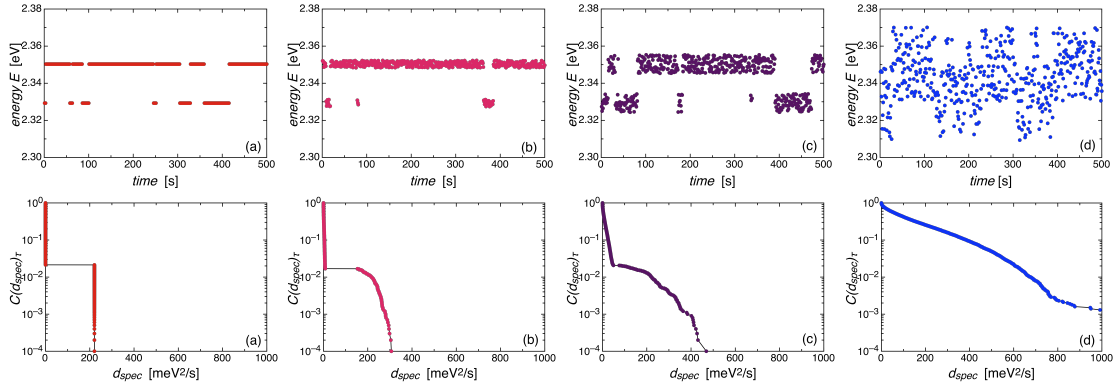
Figure 5.1: Simulated time traces of spectral jumps and fluctuations (top) and respective probability distributions of diffusivities (bottom) for (a) no, (b,c) small and (d) large fluctuations. The energetic difference for the jumps is 21 meV, $k_{up} = 0.039$ per step, $k_{down} = 0.015$ per step.

---

[1]Beatriz Aráoz, Universidad de Buenos Aires, currently is analyzing the SM spectra from these experiments

Depending on the particular system dye-matrix, the ratio between the ranges of frequent spectral fluctuations and occasional jumps may be different. High frequent spectral fluctuations can only be discriminated from occasionally occurring jumps, if the range of energetic differences of the fluctuations is smaller than the energy gap for the jumps. Fig. 5.1 (top) shows simulated time traces of a two-level system for several relations between the range of fluctuations and the energy gap for the jumps (for better visualization the latter was fixed to 21 meV and only the range of the fluctuations was varied). Thereby the two levels are related to two different transition energies between the involved electronic states of the dye molecule. The respective probability distributions of diffusivities are shown in the bottom row. For these simulations the jump rates were chosen to be similar for all four examples ($k_{\mathrm{up}} = 0.039$ per simulation step, $k_{\mathrm{down}} = 0.015$ per step, resembling higher stabilization of the higher energetic fluorescence, e.g. as with Nile Red in unpolar environments, see section 3.5). As can be seen, with no or with only small fluctuations the energy gap stemming from the jumps is clearly visible in the probability distribution. The "left-hand branch" (i.e. d_{spec} smaller than the energy gap) is generated by the spectral fluctuations. For increasing d_{spec} the gap is followed by a "right-hand branch" (also named "high energetic branch"), which originates from jumps modulated by fluctuations. When the range of the fluctuations gets in the range of this energy gap, the corresponding gap in the probability distribution closes. Eventually even the kink at the transition from the left-hand branch of fluctuations towards the regime of the jumps vanishes. Thus larger conformational changes of the dye molecule can only be observed from spectral diffusion, if the resulting spectral shift is larger than the fluctuations induced by frequent smaller conformational changes, e.g. due to thermally induced interactions with the matrix. However, also noise contributes to the fluctuations and may conceal spectral shifts.

Effect of transition rates on probability distributions
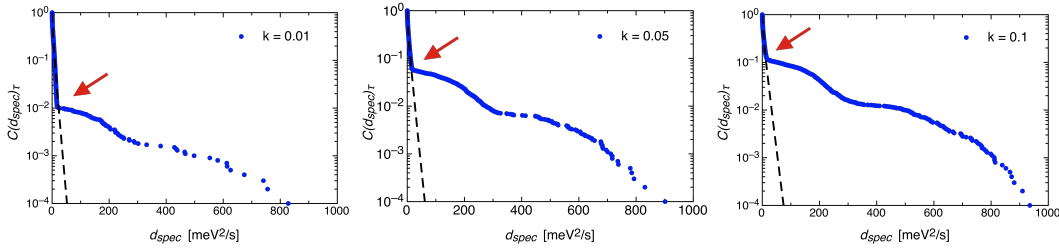
Figure 5.2: Probability distributions of simulated spectral diffusion with different (symmetric) transition rates: $k = 0.01$, $k = 0.05$ and $k = 0.1$ (from left). Red arrows denote the jump probability, (- -) fits to the left-hand branch suing eqn. 3.57. In contrast to Fig. 5.1 a complex distribution of energy levels was used as is described in section 5.1.2.

In the previously shown simulations the jump rates were arbitrarily chosen, in experiment however, the rates are related to the energy gap and to temperature via eqn. 3.48. Yet, since the probability distributions are built from square energy differences, the di-

rection of the jumps cannot be evaluated from those distributions. Nevertheless the total jump rate $k = 2k_{\mathrm{up}}k_{\mathrm{down}}/(k_{\mathrm{up}} + k_{\mathrm{down}})$ can be obtained from the diagrams: The probability value at the starting position of the kink gives the jump rate k, see the arrows in Fig. 5.2. Besides the ratio of the small fluctuations to the jumps, the general shape of the distribution is not influenced by changing the jump rate, as can be seen in Fig. 5.2 for three different jump rates. To clearly demonstrate the similar shape, the simulations shown here where generated using not a simple two-level system but a more complex distribution of energetic positions, including energetic positions from intermediate spectra, see Fig. 5.6 (a) in section 5.1.2. Thus the high energetic branch (i.e. right part of the distribution for d_{spec} larger than the value at the kink) shows a complex structure, as will be detailed in section 5.1.2.

Determination of diffusion coefficients for spectral fluctuations

As mentioned above, the left-hand branches in Fig. 5.2 stem from the fluctuations and were fitted using eqn. 3.57 (dashed lines), rendering a diffusion coefficient $D_{\mathrm{fluct}} = 3$, 4 and 5 meV^2/s for the rates $k = 0.01$, 0.05 and 0.1 resp. (and simulated acquisition time $\tau = 1$ s). Since the fluctuations were simulated as normal distributed random variable on the interval $[-3, 3]$ meV, the expected spectral diffusion coefficient D_{fluct} can be determined by calculating the variance (= first moment) of the distribution, which is defined by

$$\mathrm{Var}(Y) = \left\langle (Y - \bar{Y})^2 \right\rangle = \frac{1}{X_2 - X_1} \int_{X_1}^{X_2} (y - \bar{Y})^2 dy \,, \qquad (5.1)$$

where Y is the normal distributed variable on the interval $[X_1, X_2]$, and $\bar{Y}$ is the mean of the distribution. For the interval $[-3, 3]$ meV eqn. 5.1 yields 3 meV^2, rendering $D = 3$ meV^2/s, since $\tau = 1$ s. The values obtained from the fits are slightly larger than the calculated value from the normal distribution. This is caused by some small jumps (energetic ranges in the range of the fluctuations) due to partly small spacing within the distribution of energy levels used for generating the simulations. As was shown in Fig. 5.1 (d), jumps cannot be discerned from fluctuations, if the corresponding energy gap is of similar range as the fluctuations. Of course this additional contribution gets larger, when the jump rate is increased, thus the values obtained from the fit get slightly larger in Fig. 5.2 from left to right.

Usually it is of interest to evaluate the energy gaps for the spectral jumps. Thus, in the following two paragraphs different methods to obtain the energy gaps from probability distributions of spectral diffusivities are presented, followed by a paragraph on the evaluation of the energy gaps from probability density distributions of spectral displacements.

Determination of largest energy gap from the range of the spectral diffusivities

Here again a two-level simulation was used together with a three-level simulation to demonstrate how the largest energy gap can be evaluated from the probability distribu-
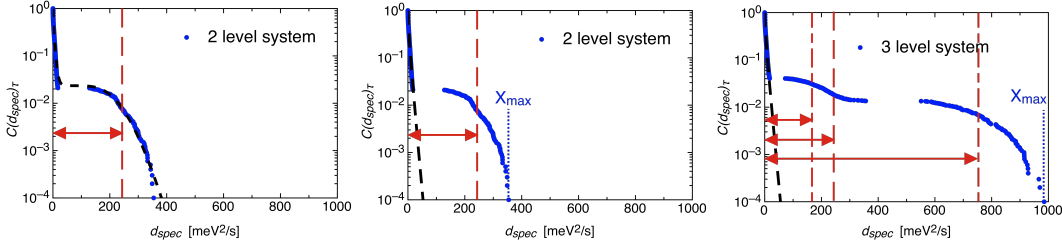
Figure 5.3: Probability distribution of simulated spectral diffusion using a simple two-level (left and middle) and three-level system (right), with (- -) fits to left branch (middle and right) and to the complete distribution (left), respectively. Arrows and vertical dashed lines denote the energy differences of the levels; X_{max} is the largest occurring spectral diffusivity.

tions of spectral diffusivities. In contrary to the complex probability distributions shown in Fig. 5.2 the simulation created from a simple two-level distribution shows no complex structure, see Fig. 5.3 (left and middle). The range A_{fluct} of the added fluctuations again was 3 meV. The vertical dashed line and the horizontal arrow denote the d_{spec} resembling the energy difference between the two levels. It reaches into the middle of the high energy branch of the distribution. This can be understood as an effect of the fluctuations: the smallest steps are those were the maximum possible fluctuation increases the lower energy level and decreases the upper level ($E_2 - E_1 - 2A_{\text{fluct}}$, where the E_i denote the mean energetic position of the respective two energy levels). Since those steps are rare, the slope of the probability distribution is small there, resembling a fast increase in d_{spec}. More frequent are energy steps which contain ΔE in the range of the difference between the two underlying energy levels. The steep end of the right branch of the distribution is limited by the maximum possible energetic shift $E_{max} = E_2 - E_1 + 2A_{\text{fluct}}$. Fig. 5.3 (right) shows the distribution obtained using a simple three-level system (i.e. three different transition energies between the involved electronic states). The corresponding three energy gaps are denoted by horizontal lines and arrows. Again the extension of the high energetic branch is delimited by the fluctuations. Furthermore, knowing A_{fluct} and the largest occurring spectral diffusivity X_{max}, the largest energy gap ΔE between the contributing energy levels can be calculated by

$$(\Delta E + 2A_{\text{fluct}})^2 = 2\tau X_{max} \tag{5.2}$$

using the definition of d_{spec} given in eqn. 3.54. With $A_{\text{fluct}} = 3$ meV this renders 21 meV for the two-level system and 38 meV for the three-level system, which is in accordance with the used energy gaps for creating the distributions. In those simple distributions eqn. 5.2 can be used to calculate A_{fluct}: In both graphs the small fluctuations branch is limited by $d_{\text{spec}} \approx 20$ meV^2/s. Setting $\Delta E = 0$ renders ≈ 6 meV $= 2A_{\text{fluct}}$.

Fitting function to probability distributions of d_{spec} including spectral jumps

Usually experimental data display only rare jumps. Thus fitting the high energetic branch in probability distributions from such data is not possible. Nevertheless in some

occasions jumps will occur frequent enough for further analysis. Clearly the jumps are distributed around some mean value $b \neq 0$, which resembles the energy gap ΔE of the jumps. Eqn 5.3 is motivated by the notation of the normal distribution function or Q-function for normal distributions with mean value $b \neq 0$ and its relation to the error function [Bron08]. Its mathematical derivation is beyond the scope of this work. The definition of d_{spec} according to eqn. 3.54 explains how the energy gap $b = \Delta E$ is implemented into eqn. 5.3, $k \in [0, 1]$ is the jump rate, $b = \Delta E$ must not be negative (i.e. $b \in \mathbb{R}_0^+$; for a defenition of erf see eqn. 3.45).

$$C(d_{\text{spec}})_\tau = (1-k)\left(1 - \text{erf}\left(\sqrt{\frac{d_{\text{spec}}}{2D}}\right)\right) + 0.5k\left(1 - \text{erf}\left(\frac{\sqrt{d_{\text{spec}}} - \sqrt{2b^2/\tau}}{\sqrt{2D}}\right)\right) \quad (5.3)$$

Fig. 5.3 (left) shows a fit to the jumps according to eqn. 5.3. The used values were $k = 0.02$, $b = 21$ meV, and $D = 3.2$ meV^2/s. The jump rate used within the simulation was $k = 0.025$, which is in agreement with the value obtained from the fit. Furthermore, b matches the energy gap of the simulation and the diffusion coefficient is in agreement with the spectral diffusion originating from the added fluctuations with $A_{\text{fluct}} = 3$ meV, as was explained above.

Energy gaps of spectral jumps derived from probability density distribution

In contrary to the determination of the largest energy gap, it is quite difficult to determine the position of the smaller ones. Here the use of the probability density distribution of spectral displacements ΔE may help. Fig. 5.4 shows the corresponding one for the three-level system (which had been used also for creating the probability distribution of d_{spec} in Fig. 5.3 right). In this probability density distribution according to eqn. 3.50 the jumps lead to Gaussian shaped distributions centered at their respective (positive and negative) mean values. Since this probability density distribution is dominated by the peak centered at zero stemming from small fluctuations (including noise), the right part of the

Figure 5.4: Probability density distribution of simulated three-level system, inset: magnification of the distribution of (positive) jumps and corresponding fits.

distribution ($\Delta E > 0$) is magnified in the inset to visualize the side peaks resulting from the jumps (the left part is symmetric to the right part). Single Gaussian fits at the respective positions yielded values of 19 resp. 39 meV. The larger one is in good accordance with the used energy gap of 38.8 eV. Nevertheless it was not possible to conduct a two Gaussian fit on the interval $[0.01, 0.03]$ eV to resolve the two other energy gaps at 17.8 meV resp. 21.0 meV. Thus close proximity of energy gaps cannot be resolved here either, but their mean value can be obtained.

5.1.2 Implications of spectral jumps during acquisition time

Although spectral jumps usually occur on a fast time scale, the obtained spectra within the experiment depend also on the accumulation time (typically 1 s). Thus a spectral jump during the interval of acquisition may lead to an intermediate "mixed" spectrum. The latter is a superposition of the two contributing spectra, whereby their amplitudes were multiplied by the ratio of the corresponding fractions of the accumulation time.

Since the main peak positions from Gaussian fits to the spectra are used for further analysis (see section 3.5), the outcome may severely depend on the contributing fractions for the mixed spectra. If simple mono-Gaussian shape peaks of equal amplitude and small peak distance are mixed, the peak positions of the intermediates will perform a linear transition from one energy level to the other, see Fig. 5.5 (a). But the here obtained Nile Red spectra contain three to four Gaussians. The fits to mixed spectra of those render much more complicated distributions of main peak positions. Thus those mixings should be taken into account within simulations of spectral diffusion. Here, first intermediates from two Gaussian shaped spectra are studied, before superpositions from experimentally obtained spectra will be analyzed.

Intermediates of two single Gaussian shaped spectra

To understand the experimentally obtained distributions of spectral fluctuations and jumps, simulations with different types of superpositions of spectra were conducted. Two spectra s_1 and s_2 were gradually mixed[2] with a mixing ratio m between 0 and 1, rendering intermediate spectra $s_{mix}(m) = (1 - m)s_1 + ms_2 +$ noise. In a first step the simplest case was simulated by mixing two artificial single Gaussian shaped spectra, see Fig. 5.5. All Gaussians had the same line width (FWHM) of 0.1 eV. Proportional random noise (amplitude 0.05x the signal intensity of the spectrum) was added to the calculated intermediate spectra. For the first two simulations the energy gap $\Delta E = 0.02$ eV, which is a realistic value for e.g. spectral diffusion due to conformational changes of a molecule. The other two were simulated with $\Delta E = 0.1$ eV, i.e. a larger gap while the Gaussians are still overlapping. Each ΔE was simulated either with Gaussians of similar amplitudes (i.e. similar intensities of the spectra) as well as with amplitude ratio 2 : 1. As can be seen in the distributions of the obtained main peak positions, Fig. 5.5 (third row) rendered from single Gaussian fits[3] to the intermediate spectra, in all cases the distribution can be regarded as continuos. However, the larger ΔE yields higher probabilities to obtain values close to the peak positions of the two parent spectra s_1 and s_2 than intermediate ones.

Time traces of spectra were then created from each set of intermediate spectra, by sequencing energy levels which were randomly picked from the main peak distributions obtained from fits to the intermediates. Again fluctuations A_{fluct} in the range of 3 meV

---

[2]For this a small program was written using the software package *proFit*™ from *Quantum Soft*, Switzerland.

[3]The *Peaks*-function of *proFit*™ together with *Levenberg-Marquardt* fit algorithm was used for the fits.

were added. From those simulated time traces probability distributions of diffusivities were calculated. Due to the continuous distributions of main peak positions (i.e. energy levels), the thus obtained probability distributions do not show any gaps, but are continuos themselves. The larger energy gap ΔE for the distributions shown in Fig. 5.5 (c) and (d) leads to larger jumps and thus a flattened shape of the transitions in respect to those with smaller ΔE, as can be seen in Fig. 5.5 (bottom) comparing (a) and (b) with (c) and (d). Changing the amplitude ratio of the Gaussian spectra from 1 : 1 to 2 : 1 has only minor effects on the shape of the probability distributions.
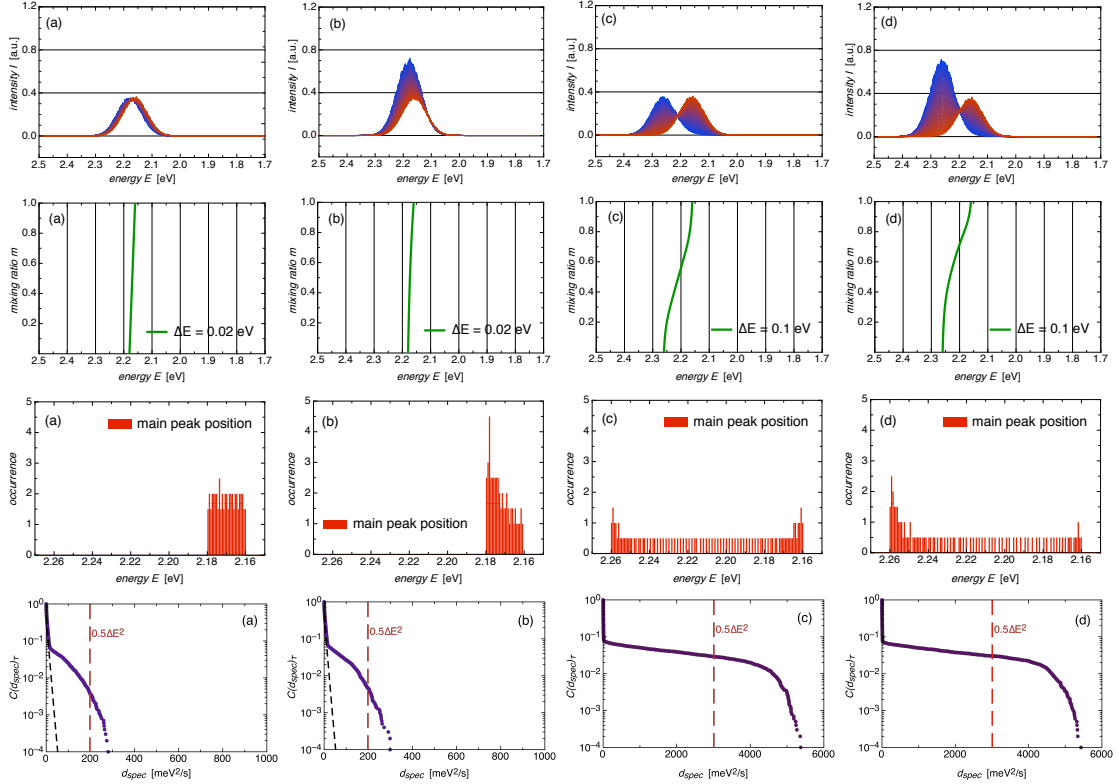
Figure 5.5: Superposition spectra (top), peak position (second row), histograms of main peak positions form fits to those spectra (third row), and probability distributions of simulated spectral diffusion using the main peak distributions, with transition rate 0.05 (bottom) using two single Gaussian spectra with (a) $\Delta E = 0.02$ eV and equal amplitude (i.e. equal intensity), (b) $\Delta E = 0.02$ eV and amplitude ratio 2 : 1, (c) $\Delta E = 0.1$ eV and equal amplitude, (d) $\Delta E = 0.1$ eV and amplitude ratio 2 : 1.

The above simulated time traces resemble fast spectral diffusion, i.e. spectral jumps occur frequently during acquisition time. In that case it can be considered to obtain diffusion coefficients from the probability distributions not only for the fluctuations, but for the jumps as well. However, as can be seen in Fig. 5.5 (bottom row: c and d), these distributions contain three regions: (i) the left-hand branch at small d_{spec} originating from the fluctuations, (ii) a region with smaller slope which stems from the jumps,

and (iii) the high energy branch, which originates from the jumps modulated by the fluctuations. Thus two-component fits using eqn. 3.58 to those distributions should be restricted to parts (i) and (ii). However, in case of the smaller energy gap used for the simulations shown in Fig. 5.5 (a and b), it may be difficult to discern, where region (ii) ends.

Intermediates of two experimentally obtained spectra
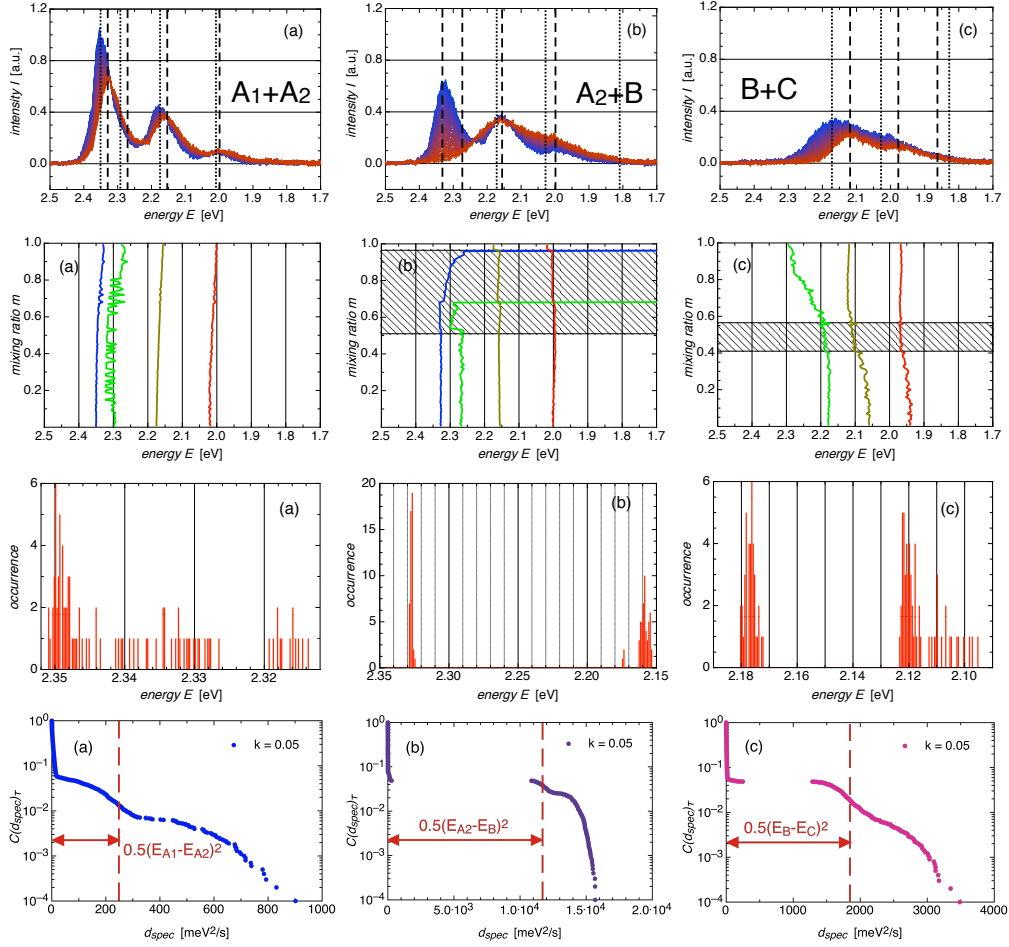
Figure 5.6: Gradually mixed spectra with marked peak positions of the parent spectra: ($\cdots$) types A_1 and B, (- -) types A_2 and C (top), peak positions (second row), histograms of main peak positions (third row), and probability distribution of simulated spectral diffusion (bottom) using gradually mixed spectra types (a) A_1 and A_2, (b) A_2 and B and (c) B and C. The shaded regions highlight mixing ratios m which render problematic main peak positions.

The experimentally obtained Nile Red spectra of Nile Red in 25 nm thin PMMA films on Si-wafers with thermally grown SiO_2 contained three to four peaks, and thus were fitted by a superposition of three to four Gaussians. As could be seen in Fig. 3.8

(top) in section 3.5, different types of spectra were obtained. Thereby four typical types were discerned: Two of them contain main peaks with high intensities at high energies, they were named A_1 and A_2, while the other two typical spectra B and C have weaker intensities and their main peaks appear at lower energies. Thereby the spectra were classified according to their shape and the range of their main peak wavelength. Fig. 5.7 in the experimental section 5.2 shows typical examples of these for types. However, also intermediates of them were observed, e.g. both spectra shown in Fig. 3.8 (top) are intermediates of the types A_1 and A_2.

To study the implications from experimentally obtained intermediates, in a second step the typical spectra shown in Fig. 5.7 were used to create superpositions. Fig. 5.6 (top) shows three examples of mixing: a) similarly shaped spectra type A_1 and A_2; b) differently shaped spectra A_2 and B; and c) similarly shaped spectra B and C. The created series of superposition spectra were fitted using the *Peaks*-function of *proFit*™ with three or four Gaussian peaks and *Levenberg-Marquardt* fit algorithm. The second and third row in Fig. 5.6 show plots of the peak positions and histograms of the obtained main peak positions resp.. The shaded regions in the plots of the peak positions (second row: b and c) denote mixing rates m at which the fits to the resulting intermediate spectra yielded energetic positions outside the energy interval determined by the parent spectra. There the main peaks of the intermediates are a superposition of the main peak of the lower energetic spectrum with the second peak of the higher energetic spectrum.

Since the energetic distance between the types A_1 and A_2 spectra is only 0.02 eV, there is almost a continuous transition of main peak positions on the energy interval spun by the parent spectra, similar to the case of two Gaussians with differing amplitude and $\Delta E = 0.02$ eV shown in Fig. 5.5 (b). Both A-type spectra contain low energetic shoulders at their main peaks (see Fig. 5.7). Thus these peaks were fitted by a superposition of two Gaussians. However, due to the mixing in combination with the added noise the main peaks of the intermediates are not always resolved properly, e.g. rendering positions more than 0.01 eV below the energy level of the main peak of the lower energetic parent spectrum. The absolute deviations in case of intermediates generated from types A_2 and B, resp. from types B and C are of the same order. Yet there the energetic distance between the resp. spectra is much larger. For the shaded areas in Fig. 5.6 the main peaks of the intermediates are a superposition of the main peak of the lower energetic spectrum with the second peak of the higher energetic spectrum, which leads to the observed energy levels outside the energy interval spun by the main peak positions of the two parent spectra.

The obtained peak distributions of the intermediates again were used to create time series of spectra as described before (resembling high transition rates leading to intermediates in almost every interval of acquisition). From those time series the probability distributions of d_{spec} were calculated. As can be see in Fig. 5.6 (bottom), the probability distributions in all three cases contain extensions of their high energy branches towards higher d_{spec}. These are caused by intermediates yielding energetic positions outside the interval spun by the positions of their parent spectra. Furthermore, the probability distribution in (a) is continuous in the region corresponding to the energy gap $E_{A1} - E_{A2}$,

while in (b) and (c) gaps appear in the resp. region. This is due to the narrow energetic distance of the A-type spectra, leading to a continuous transition as was explained above.

5.1.3 Contributions from noise and fitting uncertainty

Experimentally obtained spectra contain some setup noise due to shot noise from the detector and background events on the CCD chip of the spectrometer. The former will contribute to the signal proportionally, while the latter causes noise with a constant amplitude. Additional constant background, mainly due to residual excitation light, can be easily extracted by subtraction of a baseline which was recorded on a blank sample and averaged over twenty spectra. Contributions from photon statistics of the dye should be low, due to the acquisition time of 1 s, whereas contributions from shot noise due to laser modulations usually occur on longer time scales. A typical value for the amplitude of the constant setup noise (background events on the CCD) in the experimentally obtained spectra is 3×10^6, while the signal varied from 5×10^6 to 2×10^8 (arbitrary units). The proportional noise (due to detector shot noise) was estimated to be below 5% of the signal. Furthermore, the uncertainty from fitting contributes to the fluctuations. To estimate the contribution from noise and fitting uncertainty, some simulations were conducted. For this time series of 100 spectra were created from a given spectrum by adding random noise with an amplitude of 3×10^6 and 5% proportional noise. The thus created spectra were fitted with the relevant Gaussian peaks functions. Then main peak fluctuations were analyzed in two ways: first the variance of the 100 main peaks was calculated, and second spectral diffusivities were calculated and analyzed using eqn. 3.57. For the latter, a time lag of 1 s was implemented, which matches the acquisition time from experiment. As was detailed in section 5.1.1, the variance divided by the acquisition time should match the diffusion coefficient D_spec obtained from analysis of the probability distributions of d_spec. Simulations were conducted on three different types of spectra: first a single Gaussian shaped spectrum with amplitude 3×10^7, i.e. 10 times the constant noise was used. The other two used spectra were experimentally obtained spectra types A_2 and C, see Fig. 5.7. Before using them, averages over 10 succeeding stable spectra were calculated to reduce the contribution of noise. The results from the simulations are shown in Table 5.1.

As can be seen, the diffusion coefficients D_spec obtained from the fits to the probability distributions match the calculated variances apart from the evaluations on the main peak of type A_2 spectra. The latter spectra contain a main peak with a lower energy shoulder, see Fig. 5.7. This increases the uncertainty of the fits, which leads to the high value of ≈ 320 meV^2/s for the resp. variance, since shoulders are frequently recognized as main peaks. The probability distribution for those spectra is better fitted with two components using eqn. 3.58 instead of 3.57. Then the larger component $D_{2,spec}$ matches the calculated variance, while the smaller one is of similar range as the D_spec obtained from analysis of type C spectra and thus can be ascribed to genuine variations of values obtained from fits to the main peak position. For comparison also the D_spec obtained from the single component fit using eqn. 3.57 is shown, which is only slightly larger

Table 5.1: Contributions from noise and fitting uncertainty on spectral diffusion.

type of spectrum	peak	variance of peak position [meV^2]	D_{spec} [meV^2/s]	$D_{2,spec}$ [meV^2/s]
gauss	single	0.52	0.55	-
A_2	main	326	5.6	-
A_2	main	326	2.8	323
A_2	second	0.74	0.77	-
C	main	5.9	4.6	-

than the D_{spec} obtained for type C spectra. Thus the evaluation of the contribution from noise and fitting uncertainty using probability distributions of d_{spec} is superior to the estimate obtained from calculating the variance of the recovered peak positions. Furthermore, fluctuations of the second peak (containing no shoulder) of the type A_2 spectra were analyzed as well. The obtained D_{spec} is smaller and comparable to that for the single Gaussian spectrum. The contribution of setup noise and fitting uncertainty to the series of type C spectra is about one order of magnitude larger. This is due to the lower amplitude and the broadening of the peaks in respect to the single Gaussian shaped and the A-type spectra. As a consequence contributions from fitting uncertainty and noise to diffusion coefficients D_{spec} in the range of 2 to 5 meV^2/s are realistic for experimentally obtained spectra of Nile Red. In case of problematic fits caused by the shoulder of the type A spectra, a contribution in the range of 300 meV^2/s is expected. However, even single component fits to the resp. probability distribution of d_{spec} will render the correct order of magnitude for these contributions.

Conclusion

Intermediates generated by similarly shaped spectra with energetic distance in the range of the line widths of their main peaks will render energetic positions almost continuously distributed on the interval spun by their parent spectra. However, shoulders and side peaks of the latter may cause intermediates with main peak positions outside of this energy interval pretending larger spectral diffusion than actually is the case.

5.2 Experiment

Experimental spectra of Nile Red in 25 nm thin polymer films were obtained with a laser scanning confocal setup equipped with a cryostat for temperature modification [Krau09].[4] The recorded spectra were corrected by the calibration curve for the spectrometer as well as for background signal. To reduce bleaching by interactions with oxygen [Schu05], the cryo was held at 10^{-5} mbar. Three different poly-n-alkyl methacrylates were investigated: PMMA, PBMA (both Sigma Aldrich) and PPMA (*Scientific Polymer*). Some specifications are given in Table 4.3. The polymers were dissolved in toluene (*Merck*, spectroscopic grade), doped with Nile Red in nanomolar concentration and spin coated on Si wafers with 100 nm thermally grown oxide (*Center for Microstructures*, Chemnitz), see also section 4.2.4 for the sample preparation. To ensure solvent evaporation, the samples were held at 10^{-5} mbar at 323 K for at least 10 h before the optical investigation[5]. All three 25 nm thin polymer films were investigated

Table 5.2: Numbers of SM time series (numbers of single SM spectra in brackets) obtained for the three 25 nm thin polymer films at different temperatures, together with the corresponding energy ranges for peak positions (given in eV) used to characterize the different types of Nile Red spectra

Polymer	SM series (spectra)	T [K]	T/T_g	A_1	A_2	B	C
PMMA	27 (1229)	295	0.76	[2.45,2.35]	]2.35,2.25]	]2.25,2.15]	]2.15,1.9]
PPMA	13 (501)	296	0.96	[2.45,2.38]	]2.38,2.33]	]2.33,2.17]	]2.17,1.9]
PBMA	13 (634)	294	0.99	[2.45,2.37]	]2.37,2.25]	]2.25,2.15]	]2.15,1.9]
PBMA	27 (1128)	323	1.08	[2.45,2.39]	]2.39,2.32]	]2.32,2.18]	]2.18,1.9]
PPMA	12 (785)	77	0.25	[2.45,2.35]	]2.35,2.25]	]2.25,2.14]	]2.14,1.9]

at room temperature, which in case of PBMA is close to T_g. The sample containing PPMA resp. PBMA additionally was studied at 77 K resp. 323 K. All temperatures were held stable within ±1 degree. To obtain SM spectra from the samples, first a scan was conducted on an area of 100 μm x 100 μm. Then the focus was set on detected spots within the overview image and single SM spectra were acquired, to check whether the fluorescence could be ascribed to Nile Red. If this was the case, series of 60 to 200 succeeding SM spectra were obtained at an acquisition time of 1s per spectrum. Some dye molecules bleached rather quickly, while others were stable. As was explained in sections 4.2.1 and 3.5, Nile Red can undergo an internal charge transfer leading to a shift in the position of the fluorescence maximum. However, also the intensity of the fluorescence changes. Thereby the higher energetic emission exhibits higher intensities. Thus Nile Red molecules in that state (*A*-type spectra, see below) are more likely to

---

[4]The spectra were acquired by Beatriz Aráoz, Universidad de Buenos Aires. We thank Stefan Krause, TU-Chemnitz, for assistance with the setup.

[5]Sample preparation was done by Beatriz Aráoz, Universidad de Buenos Aires, in Chemnitz.

be detected. For this reason the sets of obtained SM series are not free from subjective pre-selections for the higher energetic Nile Red spectra. Furthermore, from some detected spots several series of SM spectra were acquired. Therefore statistical trends on the ratio of the different types of Nile Red spectra within the resp. polymer films have to be treated with care. In Table 5.2 the numbers of SM series obtained from each sample at the resp. temperature is given together with the total amount of valid SM spectra within those series. The Nile Red spectra were classified into four types (see Fig. 5.7) according to their shapes and energetic positions. Thereby an influence of used polymer and temperature on the resp. energetic positions of the different types of Nile Red spectra was observed. Thus in Table 5.2 also the corresponding energy intervals for the resp. peak positions are shown. Due to the used longpass filter for removing excitation light, the spectra were cut at 2.45 eV towards higher energies.

5.2.1 Spectral types and main peak distributions
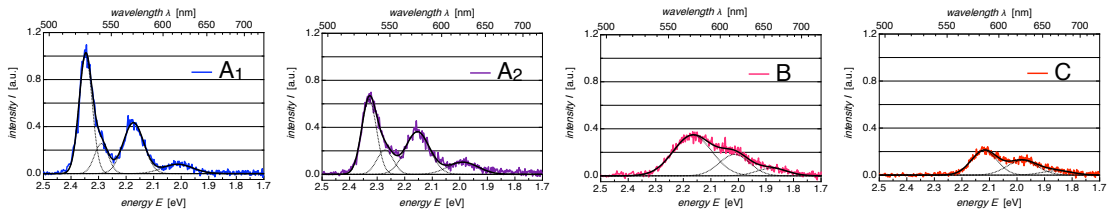
Figure 5.7: Typical examples of SM spectra of Nile Red, obtained from a 25 nm thin PMMA film at 295 K, together with (dotted lines) Gaussian fits to 4 peaks (types A_1 and A_2) and to 3 peaks (types B and C), and their superposition (solid lines).

As was mentioned in the previous section on simulations, the experimentally obtained SM spectra were characterized into four types A_1, A_2, B and C according to their energetic positions and shapes. Fig. 5.7 shows typical examples of those spectral types. The spectra were fitted by three to four Gaussians using the *Peaks*-function of *proFit*™ and *Levenberg-Marquardt* fit algorithm. From those fits, the main peak positions were evaluated.[6] The obtained distributions are shown in Fig. 5.8 for the five combinations of polymer film and temperature. Thereby shifts in positions of the spectral types corresponding to polymer type and temperature can be observed. Thus the energy ranges for the characterization of the spectral types had been determined from the observed main peak distributions. These energy ranges are shown in Table 5.2 together with the numbers of SM series and total numbers of analyzed SM spectra.

---

[6] An *Apple Script*™ program was written for characterizing and analyzing the spectra using the results from the fits.

When comparing the main peak distribution obtained from the PMMA film, Fig. 5.8 (a), with the one from the PBMA film at room temperature, Fig. 5.8 (c), a shift of the A_1 peak towards higher energies is obvious (compare the leftmost peaks of the two distributions). This shift actually is even more pronounced, because the spectra were cut at 2.45 eV by the longpass filter (to remove excitation light). Thus lower values were obtained from the Gaussian fits to those peaks with an accountable cut. Due to the accompanying shoulder at the lower energy side of the first peak, it was not possible to fit only this side for obtaining the real peak position. From the PBMA film almost no B type spectra were obtained. B type spectra (as well as C type) in contrast to the A type spectra usually are broad with no sharp intersections between the different peaks, see Fig. 5.7. Thus the observed spectra with peaks in the range of 2.37 to 2.25 eV can be discerned as type A_2 from their overall shape. Comparing the investigations of the PBMA film at 294 K (close to T_g) to those at 323 K (well above T_g) no significant energy shifts can be seen. The slight variations are within statistical accuracy, in particular since within the experiment at 323 K several SM series were obtained from the same A_1-type dye molecule. In case of the PPMA film the only recorded A_1 type spectra blinked and then bleached within the first ten seconds of the series. Even at 77 K this film showed fast bleaching of type A spectra.
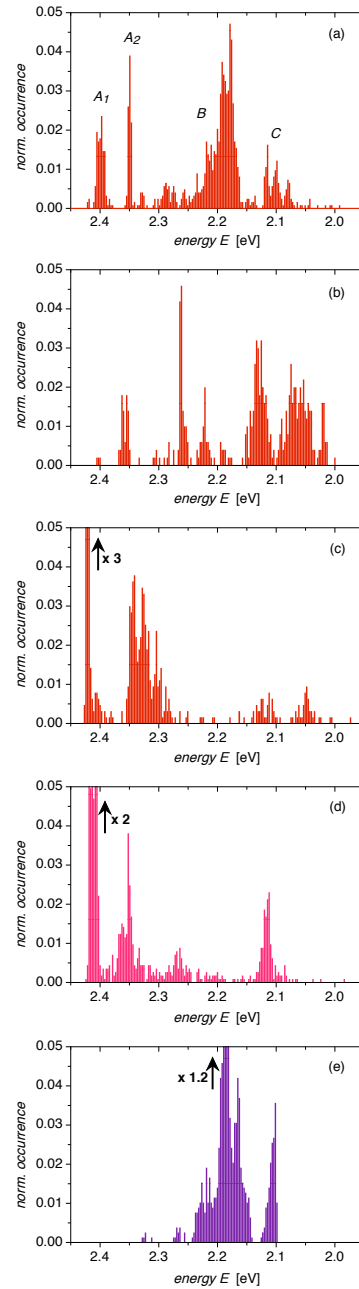
Figure 5.8: Distributions of main peak positions of SM spectra obtained from 25 nm thick films of (a) PMMA at 295 K, (b) PPMA at 296 K, (c) PBMA at 294 K, (d) PBMA at 323 K, and (e) PPMA at 77 K.

Conclusion

In contrast to PMMA for PBMA nanophase separation of polar main chains and alkyl side chains is expected, see section 4.2.4 and [Bein01]. Thus the dye molecules can be surrounded by unpolar alkyl chains alone, leading to the observed solvent shift of A-type molecules in respect to the PMMA film. A further suggestion is that B-type spectra can be assigned to local environments, where the dye molecule "sees" polar and unpolar parts of the polymer. The PBMA film was investigated close to T_g and in its melt state. Thus a higher mobility of dye molecules and polymer chains is expected. Then Nile Red molecules will not stay at the nanophase boundaries, but will be integrated into the resp. regions at their resp. conformation. Thus instead of type B spectra a higher frequency for spectral jumps is expected. This will be investigated in the following section using probability distributions of spectral diffusivities. The lack of A-type molecules within the investigated PPMA film is not understood here. Indeed further experiments on PPMA films using a different charge of PPMA did show A-type spectra. However, these investigations have not been fully analyzed yet.

In the following probability distributions of spectral diffusivities will be analyzed to investigate the dynamics within the 25 nm thick PnAMA films.

5.2.2 Probability distributions of spectral diffusivities
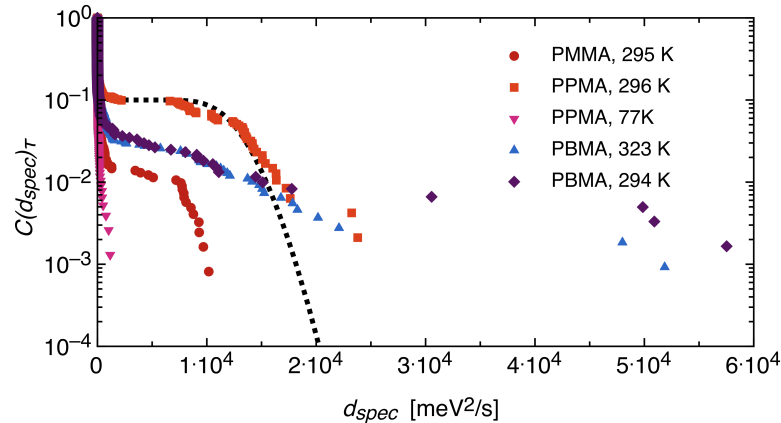
Figure 5.9: Probability distributions of spectral diffusivities of complete data sets (containing all types of spectra) for (•) PMMA at 295 K, (■) PPMA at 296 K, (▼) PPMA at 77 K, (▲) PBMA at 323 K and (♦) PBMA at 294 K; ($\cdots$) fit to PPMA at 296 K using eqn. 5.3.

Spectral jumps

The PPMA film investigated at 77 K did not show any spectral jumps. For all three samples at room temperature and also for PBMA at 323 K spectral jumps were observed, as can be seen in Fig. 5.9 showing probability distributions of spectral diffusivities for

the three polymer films at the resp. temperatures. The spectral diffusivities, i.e. scaled square displacements between succeeding main peak positions, see eqn. 3.54, had been calculated from all series of succeeding SM spectra, i.e. no selection for the different types of spectra was made. The corresponding cumulative probability distributions were then created from all spectral diffusivities obtained for a particular sample at the same temperature.

Interestingly the probability distribution of spectral diffusivities obtained from PMMA as well as that one from PPMA at room temperature is discontinuous in the range between $2 \cdot 10^3$ and $8 \cdot 10^3$ meV^2/s followed by a high energy branch. These distributions resemble the three-level system shown in Fig. 5.3. However, a two-level system with a nearly continuos transition of main peak positions from intermediate spectra will lead to a similar shaped probability distribution. For this reason these two distributions were fitted using eqn. 5.3, yielding a diffusion coefficient for spectral fluctuations $D_{\text{spec}} \approx 40$ meV^2/s and an energy gap of 22 meV resp. $D_{\text{spec}} \approx 100$ meV^2/s and an energy gap of 28 meV for PMMA and PPMA, respectively, see also Table 5.3. These energy gaps are intermediate between typical energy gaps for transitions between the two A type spectra (about 20 meV) and transitions between B and C type spectra (about 50 meV). The range of fluctuations derived from the spectral diffusion coefficients is 12 meV and 20 meV, respectively, and thus well above contributions from noise and fitting uncertainty. For the fits the jump rates had been set to $k = 0.02$ and $k = 0.1$ resp. according to the values seen in Fig. 5.9 (see section 5.1 Fig. 5.2). Since at room temperature both polymers are in the glassy state and at least 30°C below T_g, the mobility of the polymer chains and thus the dye molecules is restricted. Yet the spectral diffusion can be explained by small conformational changes of the dye molecules within existing holes. The average hole size = free volume is known to increase with side chain length [Vall04], which is in accordance with the observed larger energy gap for spectral jumps in case of PPMA. However, the higher D_{spec} and the larger energy gap in that case can also be explained by a solvent shift, since the longer alkyl chains, even leading to nanophase separation, in PPMA will enable for an increasingly unpolar local environment of the dye molecule in respect to PMMA.

In contrast, both probability distributions obtained from the PBMA sample do not resemble a two- or three-level system. In Fig 5.9 some few large jumps can be seen (up to 0.34 eV), exhibiting a gap towards intermediately sized d_{spec}. The jump rate can be determined to $k \approx 0.04$, which is intermediate between the values obtained for PPMA and PMMA. However, in case of PPMA the number of studied molecules was smaller (13 SM series were analyzed), and the PPMA was obtained from a different company. For this reason the higher jump rate obtained for PPMA may be either induced by low statistics, unknown differences from fabrication or the smaller molecular weight (for the latter see Table 4.3). Furthermore, one might expect a higher jump rate at higher temperature, even because PBMA is in its melt state at 323 K. Yet 294 K is only 4 degrees below bulk T_g and also there the number of investigated molecules was smaller than with PBMA at 323 K. Due to the complex structure of the probability distributions, it was not possible to fit them using eqn. 5.3 for the evaluation of average

energy gaps. On the other hand diffusion coefficients D_{spec} obtained from fits using the multi-component function eqn. 3.59 are only valid, if the spectral displacements are Gaussian distributed with mean $\mu = 0$. This is likely to be the case for fluctuations. However, spectral displacements stemming from jumps will rather be distributed with $\mu = \text{b} > 0$ and therefore the second term in eqn. 5.3 has to be used. One could think of a superposition from differently sized energy gaps. However, due to the complexity of the function it is no longer accessible for fits.

Spectral fluctuations

In the following the two largest data sets (PMMA at 295 K and PBMA at 323 K) will be investigated for spectral fluctuations without investigations of spectral jumps. In particular, with PBMA the high energy branch cannot be fitted by the egn. 5.3 for a two-level system. For the investigation of the fluctuations a multicomponent function according to eqn. 3.59 was fitted to the left-hand branches of the probability distributions to determine spectral diffusion coefficients, as can be seen in Fig. 5.10. The local structure in PnAMA is known to be heterogeneous and Nile Red was chosen to probe this local structure due to its sensibility to the polarity of its environment [Hou02, Kim06]. Thus a closer look at the classified spectral types and its comparison for the different data sets can give more detailed information about local structures. Generally both A type spectra are assigned to an unpolar local structure, while the B and C type spectra stem from more polar regions, where the optical transition energy is lowered due to stronger interactions of the dye molecule with its environment [Hou00]. In the latter case matrix fluctuations have a larger effect on the energetic position of the optical transition (see Fig. 3.6, thus leading to a broadening of the respective spectra. This is in agreement with the narrower line widths of the A type spectra in respect to the broadened peaks of B and C types, see Fig. 5.7. However, due to contributions from a lower energy shoulder to the main peaks of A-type spectra, the fitting accuracy is similar for all spectra, as was shown from simulations in section 5.1.3. Form these simulations the contribution from setup noise and fitting uncertainty can be estimated to be in the range of 2 to 5 meV^2/s.
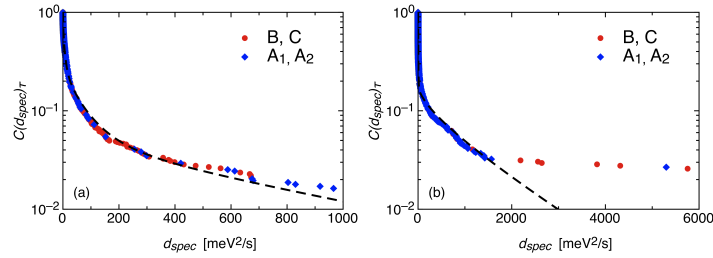
Figure 5.10: Small diffusivity parts of probability distributions of spectral diffusivities highlighting the fluctuations for (a) PMMA at 295 K, (- -) three-component fit, (b) PBMA at 323 K, (- -) two-component fit - using a different scale for d_{spec}; (blue) higher energy subsets, (red) lower energy subsets.

   To study a mutual influence of the interaction with the local matrix, the two largest data sets obtained form the resp. polymer film therefore were split into two subsets according to their spectral positions, i.e. they were sorted into higher energy = "blue" (A_1 and A_2) and lower energy = "red" (B and C) spectra according to the limits for main peak energies given in Table 5.7. The plots of the resp. probability distributions are shown in Fig. 5.10. For both PMMA subsets a freely running fit using the sum of two error functions according to eqn. 3.58 worked quite well. The obtained D_1 values of 2.2 and 3.2 meV^2/s (for blue and red subsets respectively) are in the range given from simulations in section 5.1.3. The obtained D_2 values were 31 meV^2/s and 47 meV^2/s for the blue resp. red subset. A slightly larger D_2 value for the red subset is in agreement with the predicted occurrence of larger fluctuations of Nile Red in more polar matrices.

   In contrary to this the probability distributions stemming from the PBMA film at 323 K could not be fitted well. First of all the obtained values for D_1 (corresponding to noise and fitting uncertainty) from freely running fits were too small in both cases. When fixing $D_1 = 2$ meV^2/s, reasonable values for D_2 in the range of $6 pm 3$ x 10^2 meV^2/s were obtained. However, the uncertainty from these fits is too large to determine differences between the resp. subsets. The higher uncertainty for fitting the PBMA data is no surprise, since that polymer at 323 K is in its liquid state. Therefore the Nile Red molecules are able to explore larger regions of the sample during the acquisition of the spectra. Thus several physical processes contribute to the spectral diffusion: dye rotation, translational diffusion of the dye and rearrangements of the polymer chains interacting with it.

Table 5.3: Results from analysis of probability distributions of d_{spec}

Polymer	T [K]	T/T_g	ΔE [meV]	$D_{2,blue}$ [meV^2/s]	$D_{2,red}$ [meV^2/s]	D_3 [meV^2/s]
PMMA	295	0.76	22	31 ± 1	47 ± 1	(5 ± 1) x 10^2
PPMA	296	0.96	28			≈ 1 x 10^2
PBMA	294	0.99				
PBMA	323	1.08				(6 ± 3) x 10^2

   Since for PMMA in the range of $200\,\text{meV}^2/\text{s} < \text{d}_{\text{spec}} < 400\,\text{meV}^2/\text{s}$ a further almost continuous component can be seen in Fig. 5.10, the fluctuations in that case were additionally fitted by a three-component function according to eqn. 3.59, see (- -) in Fig. 5.10 (a). This rendered $D_3 = (5 \pm 1)$ x10^{2}meV^2/s, i.e. of similar range as the D_2 values obtained for PPMA (from fit to the complete distribution, see above) and for PBMA. For BBMA in Fig. 5.10 (b) an even faster component is visibly, however this already is the transition to the high energy regime of spectral jumps and thus may not be fitted similar to the dense spectral fluctuations). Table 5.3 sums up the results from the fits. As can be seen, a spectral diffusion coefficient of magnitude 10^2 to 10^3 meV^2/s is present in all analyzed probability distributions, and thus is a common property of the spectral

diffusion of Nile Red within the studied polymers at the corresponding temperatures. Yet, as was shown in section 5.1.2, intermediates generated from spectral jumps during acquisition of the SM spectrum, may pretend additional energy gaps in the range of 0.01 to 0.02 eV, and thus contribute to the spectral diffusion in the range of a few 100 meV^2/s (at an acquisition time $\tau = 1\,s$). Thus the observed diffusion coefficient in the order of 10^2 meV^2/s may be related to these mimicked spectral jumps due to incorrect energetic positions attributed to intermediates.

Moreover a single Gaussian distributed component is a rough approximation for the observed spectral fluctuations. Thus the fluctuations are likely to originate from a superposition of several possible small conformational changes, as will be induced by an undulated potential structure similar to that shown in Fig. 3.7 at both sides of the energy barrier.

5.3 Conclusion and outlook

Probability distributions of spectral diffusivities are a promising tool to analyze spectral diffusion. As was shown by simulations, contributions from noise and fitting uncertainty are in the range of 2 to 5 meV^2/s. However, if the SM spectra contain shoulders or side peaks, intermediates originating from spectral jumps during acquisition of a SM spectrum may lead to incorrectly attributed spectral positions in the range of 0.01 eV and thus mimic larger spectral jumps than actually are the case. A spectral diffusion coefficient in the order of 10^2 meV^2/s thus may be generated from these incorrectly evaluated intermediates (for acquisition time $\tau = 1\,s$).

The probability distributions of spectral diffusivities obtained form a 25 nm thick PPMA resp. PMMA film, resemble a two-level system and thus could be fitted with the function combining spectral fluctuations and jumps given in eqn. 5.3. Both polymers at room temperature are in the vitreous state. The slightly larger energy gap obtained for PPMA (28 meV in respect to 22 meV) can be related to the larger free volume due to the longer side chains of PPMA, or to a stabilization of the unpolar state of Nile Red. However, form the investigated PPMA film only very few A-type spectra were obtained in contrast to the investigated PMMA sample. Thus the observed larger energy gap may be simply caused by the larger energetic distance between B and C type spectra in respect to that between A_1 and A_2 types. Since further investigations on a different charge of PPMA yielded higher numbers of A-type spectra, the analysis of these newer experiments may contribute to the clarification of this issue. No large spectral jumps for the polymer films in the vitreous state were observed. This implies that either the free volume is too small for the conformational changes accompanying the internal charge transfer of Nile Red, or that no such changes occur since the Nile Red molecules are immobilized within local environments of distinct polarity.

The sensitivity of this new tool could be manifested at the analysis of fluctuations from selected subsets of the spectral diffusivities achieved from the PMMA film: The spectral diffusion coefficient obtained from the subset experiencing an unpolar environment (A-type spectra) was slightly smaller than the one obtained from the polar subset (31 ± 1

and $47 \pm 1 \ meV^2/s$, resp.). This is in agreement with the expectation of a stronger coupling of the dyes' energetic states to matrix fluctuations for a polar environment.

In contrast to the samples containing PMMA and PPMA the 25 nm thick PBMA film was studied close to the bulk T_g of PBMA (4 K below) and in its melt state. In both experiments large spectral jumps related to internal charge transfer of Nile Red molecules could be observed. However, their number was not large enough for statistical analysis using the probability distributions. Fits to the fluctuations in case of the PBMA film at 323 K using a two-component function for spectral diffusion did not render reliable diffusion coefficients, but only a rough estimate of their range. However, in the melt state of the polymer the dye molecules cannot only undergo conformational changes, but they will rotate and even exhibit translational diffusion, thus exploring different local environments. For this reason a contribution of several physical processes to the spectral diffusion is expected, which may only be separated within the probability distribution, if each one induces Gaussian distributed spectral displacements, leading to a superposition of single Gaussians. Yet this is not necessarily the case.

Furthermore, the obtained main peak distributions from the investigated polymer films support the idea of nanophase separation [Bein01] in case of PBMA, since for the latter the A-type spectra were shifted towards higher energies in respect to those obtained from the PMMA film. This resembles a solvent shift due to stronger stabilization of the spectra within unpolar regions of the PBMA induced by the aggregation of the alkyl side chains.

The analyzed experimental data qualitatively match the predictions from polymer science and previous studies on poly-n-alkyl methacrylates. Nevertheless more experimental investigations are needed to explore the influence of M_w and temperature, as well as of the side chain length. Further theoretical considerations may even lead to quantitative relations between spectral diffusion and physical properties of the investigated polymers.

6 Ultrathin liquid films

6.1 Liquid layering at solid interfaces

In chapter 2 the observation of liquid layering at interfaces with solids has already been mentioned. However, the extent of layering may differ for different materials and environments. In the following a short overview on literature will be given, which shows that the extent of layering primarily depends on the kind of liquid, but it further can be influenced by relative humidity, temperature and surface roughness.

However, the influence of the kind of solid substrate on liquid layering has not been investigated yet. Instead, several studies implicitly presume similar conditions for different substrates, when results from different experimental methods have to be compared, see e.g. Patil et al. [Pati07]. In section 2.2.1 on wetting phenomena the *Van der Waals* interaction between two planar surfaces is given in eqn. 2.3, which includes the material related effective *Hamaker* constant A_H. Due to the $1/r^2$-dependence of the potential the *Van der Waals* forces can act on distances up to 100 nm [Seem05], thus influencing the wetting behavior of thin liquid films. Therefore it is reasonable to expect an influence on layering within these films, too. Trenkmann used an approximation given by Israelachvili [Isra07] to calculate A_H for the systems SiO_x/TEHOS/air and Si/TEHOS/air to be $-0.25e^{-20}$ J and $-22.3e^{-20}$ J, respectively [Tren09a]. Thus the *Van der Waals* potentials are two orders of magnitude weaker in case of substrates with 100 nm oxide layer in respect to those substrates with native oxide, where the contribution from the thin SiO_x layer is negligible compared to the long-range interaction of the silicon.

As will be shown in the experimental part 6.1.2 of this section, experimental results obtained within this work using Si wafers with 100 nm thick thermally grown oxide differ from those reported in literature using Si wafers with native oxide. This hints to an influence of the kind of substrate on the extent of layering. Therefore, the following overview on reports from literature is grouped in respect to the used solid substrates.

6.1.1 Selected reports on liquid layering

Si wafers with native oxide

Villette et al. [Vill96] studied the influence of relative humidity (RH) on wetting behavior of poly(dimethylsiloxanes) with trimethyl (PDMS) or hydroxyl (PDMS-OH) ends, a nonionic siloxane poly(ethylene oxide) surfactant and TEHOS on Si-wafers with a 17 Å thick (native) oxide layer. For rendering hydrophilic surfaces they swept the substrate for 20 min by a flow of oxygen saturated with water, while a hydrophobic surface was obtained by exposure to hexamethyldisilazane for 24 h at room temperature. While

neither PDMS nor PDMS-OH showed any impact of RH on wetting grafted, hydrophobic surfaces, the spreading rate of PDMS on the hydrophilic substrate clearly increased with increasing RH. Simultaneously the drop profile changed in favor to the growth of the first layer at the expense of the others. The nonionic siloxane did not wet any of the surfaces, and TEHOS did not wet grafted hydrophobic surfaces. On hydrophilic substrates TEHOS showed a complex dependence on RH: Up to a RH of about 82% the spreading rate increased, above 85% relative humidity only a monolayer spreaded. The authors ascribe this to a special conformation of the TEHOS molecule in the first layer, which makes it appear hydrophobic towards upper layers.

Further studies revealed the dependence of the layering on surface roughness [Yu99], where the study of electron density variations showed that the layering vanished at an interface length of about 2.4 Å, and on impurities [Yu99, Yu00]. Doerr et al. investigated the dependence on the shape of the liquid molecules. Thus they demonstrated that *Van der Waals* interactions are responsible for the ordering at amorphous substrates like native SiO_2, which implies the dependence on molecular shape [Doer00]. This was also confirmed by the suppression of density oscillations when the molecular weight of PDMS was increased [Evme01]. Similar results were obtained for polyfunctional poly(methylhydro-dimethyl)siloxane copolymers (PMDMS) on Si-wafers with native oxide. X-ray data for both types of molecules revealed a low electron density region in direct vicinity of the surface. Increasing direct interactions of PMDMS by increasing the fraction of MeHSiO groups led to an increase of the amplitude of that density dip, while the further shape of the profile was independent of the fraction of $Si - H$ groups in the PMDMS. On hydrophobic substrates only this first density dip was observed, while there were no further density oscillations [Evme02]. Furthermore, simulations for the liquid-vapor interface [Chac01] predicted that surface layering will appear below about $0.2\,T_c$, where T_c is the critical temperature, even under high surface roughness. This was confirmed by Mo et al. using substrates with surface roughness > 20 Å and TEHOS [Mo06].

Mica substrate

Mukhopadhyay et al. used a surface force apparatus consisting of cylindrically shaped mica sheets together with FCS to study diffusion within confined octamethylcyclotetrasiloxane (OMCTS) using coumarin 153 as fluorescent probe [Mukh02]. At a distance of 0.7 times the ratio of contact they obtained an autocorrelation function, which clearly showed at least four different decay times, which led to diffusion coefficients of 0.1 μm^2/s, 0.7 μm^2/s, 2.9 μm^2/s and 40 μm^2/s.

Quartz cover slip substrates

Fluorescent experiments cannot be done on Si wafers with oxide layers below 50 nm due to fluorescence quenching and interference effects [Bras04]. Thus Patil et al. used quartz cover slip substrates for their FCS measurements in contrast to the use of Si wafers with native oxide for their above mentioned mechanical measurements [Pati07]. Using coumarin 153 as fluorescent probe they found a dependence of their obtained diffusion

coefficient on film thickness (range 14 - 22 nm), when using a single component autocorrelation function. Their data could be fitted well with two diffusing species, rendering $D_{\text{fast}} = 10 \ \mu\text{m}^2/\text{s}$ and $D_{\text{slow}} = 0.2 \ \mu\text{m}^2/\text{s}$. Grabowski et al. conducted temperature dependent FCS measurements on a 15 nm thick TEHOS film on a quartz cover slip (and on a 10 nm thin hexadecene film) using Alexa 488 and R6G as fluorescent probes [Grab07]. Although the data clearly display heterogeneous diffusion, they used a single species autocorrelation function for determining temperature dependent diffusion coefficients. From those they derived diffusion activation energies of 0.2 - 0.3 eV/molecule. The respective bulk values were about three times smaller (0.07 - 0.1 eV/molecule). Also optical investigations of tracer diffusion within ultrathin TEHOS films and percursor layers of wetting TEHOS droplets [Schu03, Schu04] by Schuster et al. were done on quartz cover slips. As mentioned earlier in this work, the results of Schuster et al. were interpreted assuming several liquid layers with rare interlayer exchange. However, the observed broad distributions of diffusion coefficients obtained from msd along trajectories in combination with the power-law distributed adsorption events [Schu03] according to Sokolov et al. [Lube08] are a clear sign for anomalous diffusion and thus may not be interpreted in terms of liquid layering without further evidence.

6.1.2 Experimental
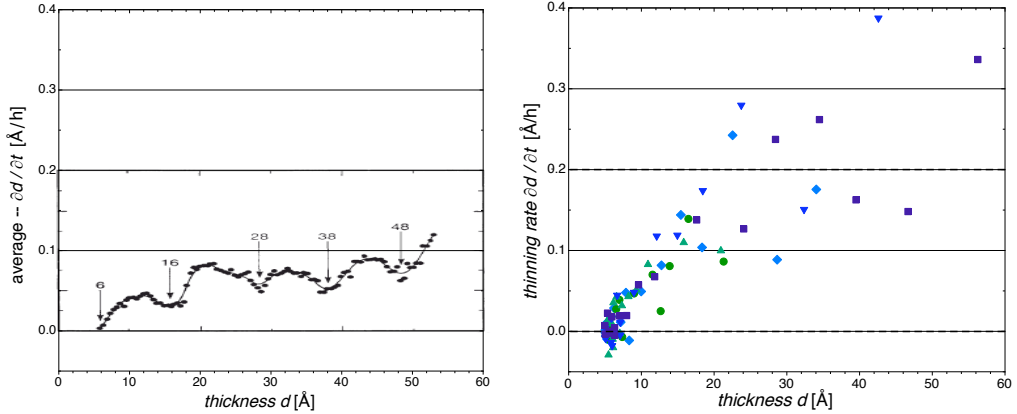
Figure 6.1: Film thinning rates depending on film thickness (left) on Si substrate with native oxide [Forc93]; (right) on Si substrate with 100 nm SiO$_x$, series of measurements on different samples are denoted by different symbols.

Thin films of TEHOS were prepared on Si wafers with 100 nm thermally grown oxide as described in chapter 4.2.3. The film thickness was studied by ellipsometry using a variable angle spectroscopic ellipsometer[1] (VASE™, *J.A. Woollam Co.*, Lincoln, NE, USA) in reflection at the three angles 65°, 70° and 75° over the wavelength range of 0.73 to 5 eV. Several TEHOS films were investigated in long time observations, i.e. measurements

---

[1]The ellipsometer kindly was provided by Prof. Dr. D.R. Zahn, TU-Chemnitz.

on the same sample were repeated after 24 to 72 hours within a period of up to 30 days. The samples were stored under ambient conditions. The obtained ellipsometry angles Ψ and Δ were fitted to a three-layer model using the software WVASE32™. The silicon and the SiO_x layer where modeled using optical constants from the materials library of the program, while for fitting the TEHOS layer the ordinary *Cauchy* equation [Cauc30, Li04] for the wavelength dependent refraction index $n(\lambda)$ was used up to second order:

$$n(\lambda) = A_n + \frac{B_n}{\lambda^2} + \mathcal{O}(4)\,. \tag{6.1}$$

The *Cauchy* coefficients $A_n = 1.4633$ and $B_n = 0.0039$ for TEHOS had been determined by Daniel Lehmann from fits to ellipsometry measurements on an ≈ 100 nm thick TEHOS film in the visible range at 2.1 ± 0.1 eV. Since the refraction index of TEHOS is very similar to that of SiO_x, the thickness of the TEHOS layer could only be determined in dependence of a given thickness of the SiO_x layer. The latter had been determined beforehand from a similarly treated blank substrate (i.e. without TEHOS film) from the same wafer. Nevertheless, this method rendered the thickness of the SiO_x layer within an accuracy of ± 1 nm, thus yielding different offsets for the long time observations of thinning TEHOS films. This offset can be determined from the residual thickness obtained after the evaporation of the TEHOS film, i.e. the obtained thicknesses then centered around this offset within an accuracy of ± 2 nm. For better visualization the series of measurements presented in Fig. 6.1 (right) were therefore corrected for this offset to the value of 6 Å, which matches the smallest film thickness reported by Forcada et al., see Fig. 6.1 (left). This residual film thickness of 6 nm according to Forcada et al. remained stable for weeks. It can be explained by incomplete evaporation leaving a residual monolayer of TEHOS on the sample, where the TEHOS molecules are oriented with their oxygen towards the substrate in favor of hydrogen bond formation [Vill96].

As can easily be seen in Fig. 6.1 by comparing the left and the right diagram, the film thinning behavior observed within this work deviates from the values obtained by Forcada et al. Within this work the ellipsometry measurements were aimed primarily to obtain film thicknesses for samples used within diffusion experiments. Nevertheless, a comparison with film thinning of samples not used for diffusion measurements was conducted to ensure that there was no influence on thinning rates from the use of the samples for diffusion measurements. Due to less thorough investigation, a variation of the obtained thinning rates around the average values obtained by Forcada et al. would have been expected in case of similar thinning rates. Instead, the thinning rates obtained here are considerably higher. For the lowest layer, the evaporation rate is only slightly larger, and a minimum of evaporation may be seen at d about 12 Å pointing to some extend of layering. Yet for thicker films, the deviation of the observed evaporation rate from those reported by Forcada et al. is even more pronounced. In particular, the average thinning rate reaches the value of 0.1 Å/h already at a film thickness of approximately 15 Å, while 0.1 Å/h are reported by Forcada et al. only for a film thickness larger than 50 Å. According to Vilette et al. [Vill96] the interfacial TEHOS layer at silica surfaces is about 7 Å due to orientation of the TEHOS molecules with their oxygen groups towards the silica. Thus a film thickness of 15 Å is intermediate between one and two TEHOS

layers. The observed higher evaporation rates may therefore point to weaker layering, with only one or two observable liquid layers in case of the here used substrates.

However, there may also be a contribution from surface roughness on the observed differences in evaporation rates. AFM measurements of the Si substrates with 100 nm thermally grown SiO_x (after the cleaning procedure of the substrates) yield an average roughness of about 6 Å when analyzed by *WSxM 5.0* [Horc07], see section 4.2.2. Preliminary AFM measurements had yielded smaller values (about 3 Å). This roughness is twice the range where Yu et al. observed decay of the liquid layering, see above and [Yu00]. But Yu et al. had derived the surface roughness from X-ray experiments and not by AFM, which may lead to different values. Furthermore, as was noted above, there is also a temperature dependence on the amount of layering [Mo06]. Therefore a comparative study with similar experimental conditions has to be conducted on both types of substrates to discern whether the substrate material influences liquid layering or whether the here observed differences are due to other conditions, e.g. relative humidity or surface roughness.

6.1.3 Conclusion

The here observed thinning rates are considerably larger than those reported by Forcada et al. on a 4 to 5 nm thick TEHOS film on a Si wafer with native oxide. This difference may point to an influence of the kind of substrate on layering. However, also the surface roughness on substrates containing thick thermal oxide usually is larger than that of polished Si wafers with native oxide. In particular after the here used cleaning procedure by etching in Piranha solution, AFM measurements yielded an average roughness of approximately 6 Å, which is about twice the value (about 2.4 Å) for which Yu et al. report decay of layering. Furthermore, there are literature reports on an influence of temperature and of relative humidity on layering and wetting behavior of TEHOS films on Si wafers with native oxide [Mo06, Vill96]. Thus a comparative study with carefully observed experimental conditions is needed to study a possible influence of the kind of substrate on liquid layering. Nevertheless, the larger evaporation rate in case of the here used TEHOS films points to weaker layering, with only one or two observable liquid layers.

6.2 Film thinning studied by SMT
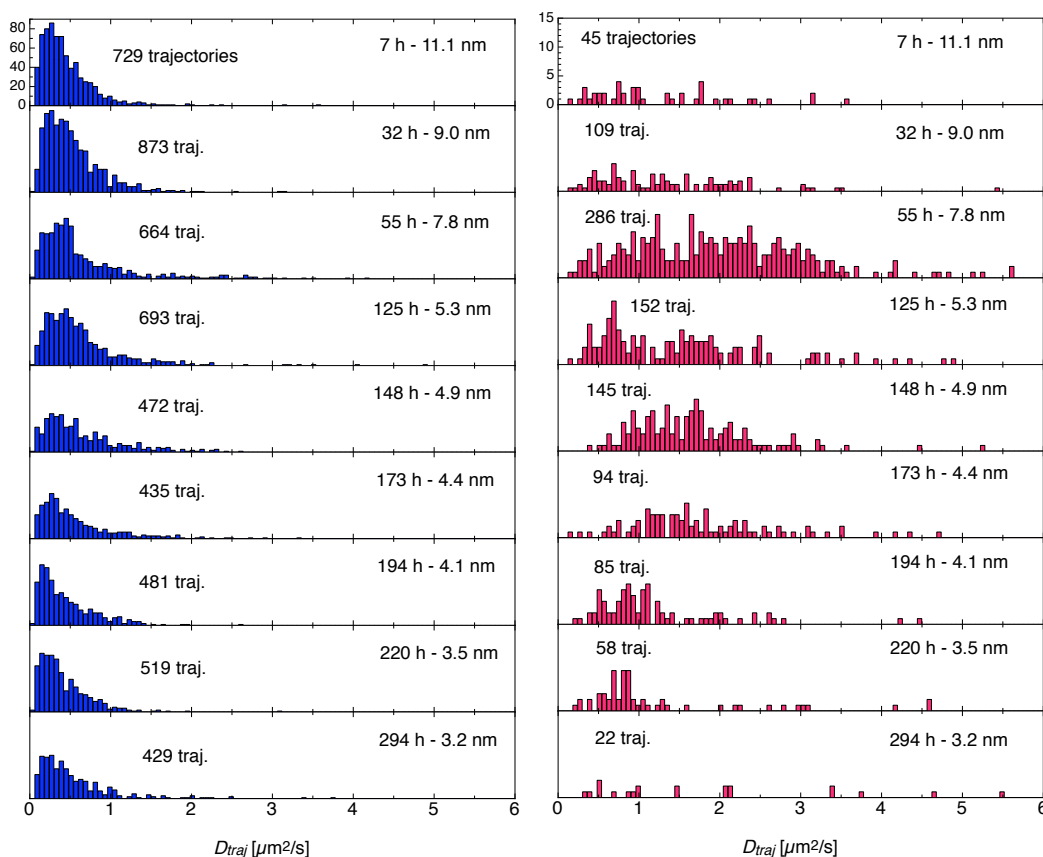
Figure 6.2: Long time observation of RhB in thinning TEHOS film. Distribution of D_{traj} for (left) all detected trajectories with time length ≥ 0.6 s, (right) trajectories exceeding a lateral area of 1.3 $\mu\mathrm{m}^2$ (and time length ≥ 0.3 s).

Part of this section has been published in [Täub09a], [Täub09b] and in [Baue09a]:

D. Täuber, M. Heidernätsch, M. Bauer, G. Radons, J. Schuster and C. von Borczyskowski. Single molecule tracking of the molecular mobility in thinning liquid films on thermally grown SiO_2. *Diffusion Fundamentals Journal*, Vol. 11, p. 107(11), 2009.

D. Täuber, M. Heidernätsch, M. Bauer, G. Radons, J. Schuster and C. von Borczyskowski. Discriminination between static and dynamic heterogeneities in single dye diffusion in ultrathin liquid films. *Diffusion Fundamentals Journal*, Vol. 11, p. 76(2), 2009.

M. Bauer, M. Heidernätsch, D. Täuber, J. Schuster, C. von Borczyskowski and G. Radons. Investigations of static and dynamic heterogeneities in ultra-thin liquid films via scaled squared displacements of single molecule diffusion. *Diffusion Fundamentals Journal*, Vol. 11, p. 70(2), 2009.

However, in these publications the SMT data had not been corrected for geometrical averaging according to section 3.3.2, which has been done now by multiplication with a factor 3/2 according to eqn. 3.15. To gain insight into the effect of the confinement, long time observations were conducted on ultrathin TEHOS films on Si substrates with 100 nm thermally grown SiO_x. The samples had been prepared according to the procedure described in section 4.2.3. RhB was used as probing dye molecule. Due to the evaporation rate of ≈ 0.3 Å/h (see section 6.1.2), the investigated TEHOS film thinned from initially 11.1 ± 1 nm to 3.2 ± 1 nm over a period of 294 h. Video sequences of 5 000 frames each were recorded at the wide field microscope using the *Andor™ iXon DU 885* CCD camera at a frame rate $f = 50$ fps. For each measurement 10 video sequences were acquired resulting in 50 000 frames in total. The software package *tracking.sh* was used to track the fluorescing molecules within the videos and to calculate diffusion coefficients D_{traj} via weighted mean square displacements along the trajectories as well as to obtain probability distributions of diffusivities d_{diff}.

6.2.1 Diffusion coefficients obtained from msd

Fig. 6.2 shows the obtained distributions of D_{traj}. For the left part all trajectories with step length ≥ 30 ($\simeq 0.6$ s total time length) were used. As can be seen, the number of detected trajectories decreases after 125 h. Furthermore, there is an initial slight shift of the median towards larger values, peaking at 125 h ($d = 5.3$ nm), see Fig. 6.3 (circles). Afterwards the median decreases again and the distribution narrows. The right part of Fig. 6.2 shows a different subset of the detected trajectories. Here only those trajectories had been selected, which exceeded a lateral area of 1.3 μm^2, while their time length varies from 0.3 s ($\simeq 15$ frames) to

Figure 6.3: Median D_{msd} of distributions of D_{traj} in Fig. 6.2 left (circles) and right (squares).

29.4 s ($\simeq 1470$ frames). Thus mainly immobile molecules were excluded from the subset, which puts the focus on mobile trajectories. Here the shift of the median values (Fig. 6.3 squares) and the change in the width of the distribution over time is even more pronounced. D_{traj} varies between 0.1 μm^2/s and 6 μm^2/s resulting in broad distributions which, according to Lubelski et al., points towards anomalous diffusion [Lube08]. Hydrodynamic considerations suggest the dependence of the diffusion coefficient on the distance to the solid-liquid interface, see section 2.2.2. Thus causing diffusion heterogeneity by a dynamic exchange between vertical regions of the sample. However, also static heterogeneities due to lateral interface inhomogeneities (e.g. adsorption sites) of the sample may contribute to the observed diffusion heterogeneity [Täub09b, Baue09a].

Furthermore, the observed distribution of D_{traj} depends on the $7 - 294$ h waiting time after sample preparation. Within the first 50 h the distributions of D_{traj} broaden and their medians shift to larger values. The reason for this initial increase of dye mobility

within the thin TEHOS films is not clear. Literature investigations on silanes and gelation experiments [Schu10a] hint to a slow chemical modification of the interface leading to a chemisorbed monolayer of TEHOS [Tren09b], which would shield absorption sides for the dye molecules at the interface. According to observations in our lab this process ends or slows considerably after ≈ 50 h. Then the decrease of mobility due to the narrowing film thickness takes over. Yet, the derivation of diffusion coefficients by msd along trajectories is a strongly averaging method. Hence, no information is available, whether the decrease of mobility is due to a layered structure of the film, where different diffusion coefficients can be ascribed to the layers, or whether the dye molecules simply concentrate in the vicinity of the substrate. In the latter case they would be considerably slowed down in the layer(s) closest to the substrate, while the diffusion in the upper regions of the film still might be bulk-like. Here the investigation of probability distributions of diffusivities d_{diff} provides further insight.

6.2.2 Diffusion coefficients obtained from probability distributions of diffusivities
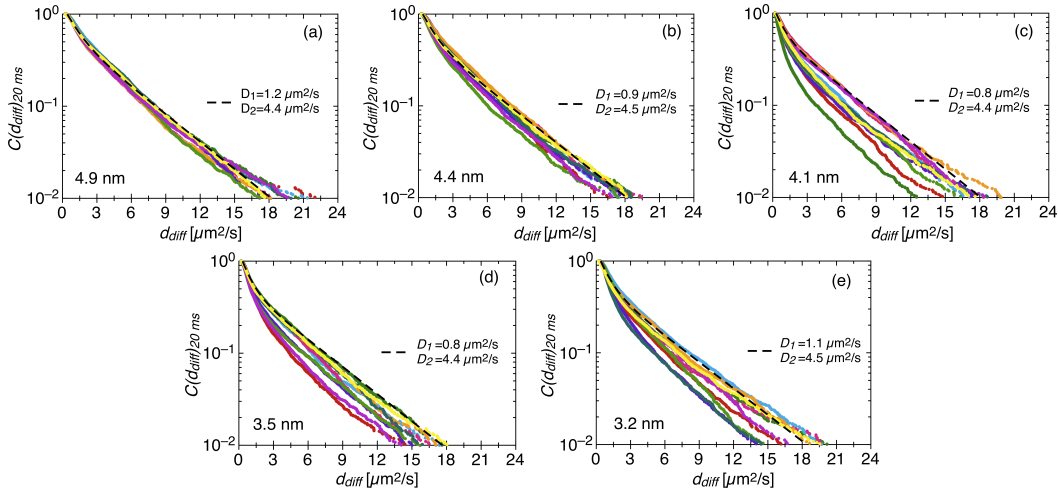
Figure 6.4: Cumulative probability distributions for decreasing film thickness: (a) 4.9 nm, (b) 4.4 nm, (c) 4.1 nm, (d) 3.5 nm, and (e) 3.2 nm. Dashed lines show a bi-exponential fit, for which the values of D_1 and D_2 are noted.

Fig. 6.4 shows probability distributions of d_{diff} for the last five measurements ($d = 4.9$ nm to 3.2 nm), where the corresponding distributions of D_{traj} narrow (see Fig. 6.2) and their median decreases. Due to experimental conditions, the amount of detected immobile molecules varies for each video sequence. Using the complete data sets therefore leads to strong variations in the initial part of the distributions, hampering direct comparisons. Thus data from immobile molecules were excluded before further analysis, using the relation between position accuracy r_{pa} and snr explained in section 3.3.1. To ensure removal of 95% of the immobile d_{diff}, the threshold for $r_{\text{pa}}*$ snr was set to
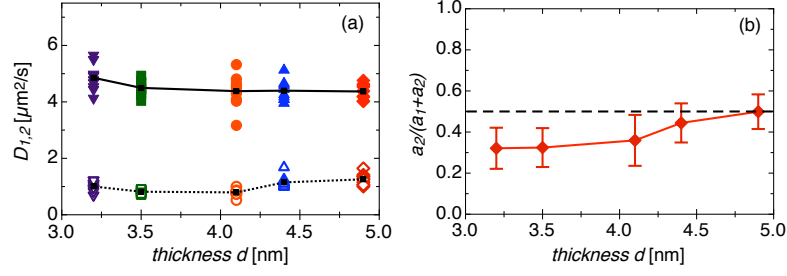
Figure 6.5: (a) Diffusion coefficients D_1 (open symbols) and D_2 (filled symbols) from bi-exponential fits to each distribution $C(d_{\text{diff}})_{\tau=20\text{ms}}$ in Fig. 6.4. Mean values of D_1 as well as of D_2 are connected by lines. (b) Mean values of relative amplitude a_2 for those fits. Error bars denote standard deviations.

the mean value $+ 2$ standard deviations. Thus also some d_{diff} from slowly moving dye molecules were excluded. Therefore, the reduced distributions were fitted with a bi-exponential function according to eqn. 3.26, without the requirement of $a_1 + a_2 = 1$. This results in two diffusion coefficients D_1 and D_2 (determined for $\tau = 20$ ms) revealing a heterogeneity of the system at least at times in the range of 20 ms. Fig. 6.5 (a) shows D_1 and D_2 as a function of film thickness. For each set of recordings the values obtained from the ten video sequences (each one consisting of 5 000 frames) are shown. The lines connect the corresponding mean values. In Fig. 6.5 (b) the relative (mean) amplitudes a_2 are shown as a function of film thickness.

Since immobile molecules were excluded from the $C(d_{\text{diff}})_\tau$, the observation of two diffusion coefficients cannot be explained by the process of ad-/desorption at the interface and an otherwise homogeneous diffusion in the liquid, but the liquid films contain at least two distinguishable physical diffusion coefficients which here are named D_{slow} and D_{fast}. The frame time ($\tau_{\text{frame}} = 20$ ms) is short enough to reveal this heterogeneity. Within longer frame time, the dye would have enough time to sample all regions, thus displaying homogeneous diffusion with an effective diffusion coefficient D_{eff}. However, D_1 cannot be addressed as D_{slow} and D_2 as D_{fast} unless it can be shown that the average dwell times within the corresponding regions are larger than τ_{frame}, see section 3.3.6. The investigations addressing this question will be reported in section 6.3.

Nevertheless, the observed D_1 and D_2 are characteristic compositions of the underlying physical processes within τ_{frame}. D_{fast} could be bulk diffusion, unless there are further confinement effects slowing the diffusion even in the upper region of the film which was lost by evaporation. D_{slow} could either be some kind of surface diffusion, where the molecule may glide on the surface e.g. via silanol bridging [Honc08], or a slowdown of diffusion in the liquid layer(s) close to the solid interface [Schu03]. Both will be addressed here as *near-surface* diffusion. Yet, an interpretation of the slower component D_1 with respect to the near-surface diffusion is not straightforward, since D_1 is directly correlated with the threshold set for immobile molecules. At this fast frame rate ($f = 1/\tau_{\text{frame}} = 50$ fps) it is not possible to distinguish between very slow diffusion and
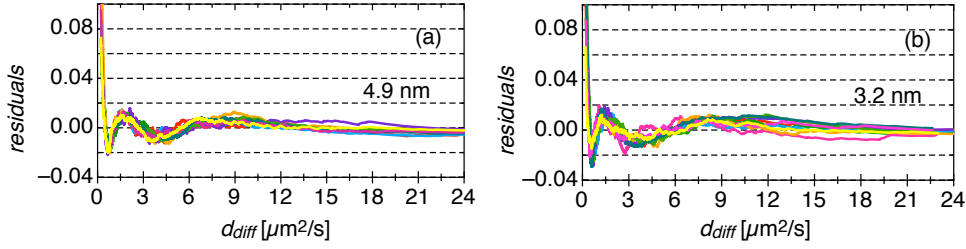
Figure 6.6: Fitting residuals for two comparative sets of bi-exponential fits for (a) 4.9 nm (Fig. 6.4.a), and (b) 3.2 nm (Fig. 6.4.e) thick films.

complete immobility. Thus, by variation of the threshold for mobile molecules due to experimentally caused variations of position accuracy r_{pa} and snr, a varying amount of slowly diffusing molecules will be excluded from the probability distribution, thus causing the fluctuations of D_1 seen in Fig. 6.5 (a).

One important result is the nearly constant average value for $D_2 = (4.5 \pm 0.2)$ $\mu m^2/s$ during film thinning from 4.9 nm to 3.2 nm. The slight increase at 3.2 nm stems from two less quality fits which yielded somewhat unreasonable high values for D_2. But the overall quality of the bi-exponential fits did only slightly deviate from those for 4.9 nm, as can be seen from the corresponding plots of their residuals in Fig.6.6 (a) and (b). Nevertheless, this shows that there is no pronounced difference between the diffusion coefficients D_{fast} in the upper layer of the 3.2 nm thin film and in the upper region present in the 4.9 nm thin film, which was lost during evaporation. According to the molecular size of TEHOS (see section 4.2.3), and assuming liquid layering, the 3.2 nm thick film only contains three complete molecular layers and an incomplete fourth one, whereas at 4.9 nm thickness the film would contain five complete molecular layers. Therefore, there can be only minor changes within the values of the diffusion coefficients of the third to fifth molecular layer, if layering was present in the upper region of TEHOS films on 100 nm SiO_x at all.

The diffusion coefficient of Alexa 488 (a rhodamine derivate) in bulk TEHOS has been reported to be approximately 55 $\mu m^2/s$, see section 4.2.3 and [Grab07]. For the here used RhB a similar bulk diffusion value is expected. However, this is much larger, than the observed value $D_2 = 4.5 \pm 0.5$ $\mu m^2/s$. Therefore, either there is a further confinement effect, which leads to a slower value for $D_{fast} = D_2$, or the mean dwell time in the upper region is considerably slower than τ_{frame} ($= 20$ ms). Also static sample heterogeneity due to heterogeneous distribution of surface silanols at the substrate surface (see section 4.2.2 and 7.1) may cause the appearance of two discernible diffusion coefficients in SMT experiments. This cannot be discriminated from the here reported thinning experiment alone and will be addressed in the following sections and in the following chapter.

Furthermore, as can be seen in Fig. 6.5 (b), the amplitude a_2 of the faster component D_2 decreases with decreasing film thickness, which shows that the concentration of dye molecules tends to become higher within the related region of slowed diffusion. Thus the change in shape of the distributions of D_{traj} of the 5 thinnest films in Fig. 6.2 (a) and (b) is not due to a loss of layers containing faster diffusion coefficients, but due

to a higher probability of finding the molecules in the region of slowed motion. Previous measurements of films with a thickness below 2 nm revealed hardly any trajectory which fulfilled the threshold criteria (area $> 1.3\mu\ m^2/s$) that has been applied for the trajectories used for the distributions shown in Fig. 6.2 (a). This might either be explained by a pronounced slowdown of the diffusion within the two molecular diameters closest to the substrate, or it also could be due to a higher adsorption probability (and thus reduction of mobility) at the solid-liquid interface. The insights gained from the film thinning experiment detailed above point towards an explanation of the diffusion in ultrathin TEHOS on Si substrates with thick thermally grown oxide by a three-layer model, which will be presented in the following.

6.2.3 Three-layer model for SM dynamics at the interface TEHOS/SiO_x
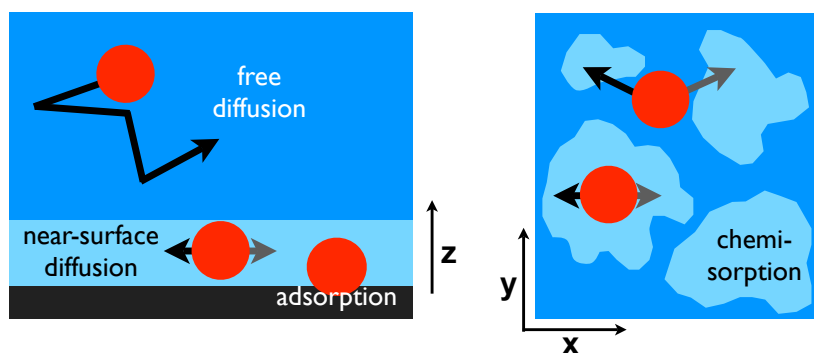
Figure 6.7: (left) Three-layer model for SM dynamics at the interface TEHOS/SiO_x, (black region) SiO_x, (blue+light blue) TEHOS, (right) substrate induced lateral heterogeneity of SM diffusion.

The observations from the above detailed film thinning experiment can be explained by a three-layer model for the SM dynamics at the interface TEHOS/SiO_x as shown in Fig. 6.7 (left). The model consists of

(i) an interfacial layer, where dye molecules are adsorbed at the SiO_x surface and thus are immobilized.

(ii) a near-surface layer, where dye molecules diffuse slowly. This can be a kind of surface gliding via H-bonding at surface silanols as suggested by Honciuc et al. [Honc08] or simply a slowdown of diffusion due to attractive interface potentials, e.g. electrostatic attraction or due to long range *Van der Waals* forces, see section 2.2.1. Yet, this near-surface layer probably is not homogeneous: The amorphous thermally grown SiO_x is covered by irregularly distributed and clustered surface silanols [Iler79, Zhur00, Schu10a], and see section 4.2.2. Hence, the slow near-surface diffusion may be restricted to silanol clusters, while the dye molecules diffuse fast on the interjacent regions of siloxane bridges, see Fig. 6.7 (right). This will further be discussed

in section 7.1. The observed diffusion coefficients D_1 and D_2 from SMT experiments then depend on the relation between the dwell times in the corresponding regions and the frame time.

(iii) a third layer, where dye molecules can diffuse freely. This third layer spans the remaining film thickness. However, this not necessarily equals bulk diffusion. There might be a modulation of the diffusion coefficients depending on the distance to the near-surface layer according to hydrodynamic considerations for a particle at a no-slip or partial-slip boundary, see section 2.2.2 for the corresponding hydrodynamic models. This issue will be evaluated in the following.

The geometrical shape of the rhodamines can be approximated by oblate spheroids, see section 4.2.1 and [Jena79]. Jena et al. obtained a molecular volume $V_{\mathrm{RhB}} = 414\,\text{Å}^3$ for Rhodamine B. To obtain an approximation of the hydrodynamic radius, the molecule will be treated as sphere. This rough approximation yields 6.7 Å for the radius of a RhB molecule. The hydrodynamic radius however, also depends on possible interactions with the surrounding solvent. RhB is a zwitterionic molecule, yet TEHOS is an unpolar solvent with branched alkyl chains shielding the oxygen atoms from interactions. Thus no increase of the hydrodynamic radius due to a solvent shell is expected. Furthermore, RhB dimers usually are non-fluorescent [Schu10a, Lópe82] and thus will not be detected in the SM experiments. The TEHOS molecules are of similar size as the RhB molecules. For bulk TEHOS a self-diffusion coefficient $D = 78\ \mu\mathrm{m}^2/\mathrm{s}$ was obtained from NMR measurements [Vali07]. Using the Stokes-Einstein relation, eqn. 3.6, this renders a hydrodynamic radius for the TEHOS molecules of 4 Å, which is considerably small, since the size of TEHOS molecules is reported to be within 0.6 to 1.4 nm in diameter ($= 2a$), see section 4.2.3. However, the Stokes-Einstein relation considers particles as hard spheres with no-slip boundary at their interface with the solvent. Thus it is a rather rough estimate for the TEHOS molecules, which may intercalate with their alkyl chains and thus also glide past each other (resembling partial slip at intermolecular contact). Setting the above obtained values for TEHOS into relation with a hydrodynamic radius for RhB of 0.67 nm when using the *Stokes-Einstein* relation eqn. 3.6 yields D is approximately 50 $\mu\mathrm{m}^2/\mathrm{s}$. However, also in case of RhB the requirement of no-slip boundary at the surface of a hard sphere particle for the application of the *Stokes-Einstein* relation is only a rough approximation. Yet a hydrodynamic radius of RhB molecules can be estimated to be between the 0.4 nm derived for the TEHOS molecules (using the *Stokes-Einstein* relation), and 1 nm. Therefore, further considerations at first will be made using the experimentally obtained bulk diffusion coefficient of TEHOS together with $a = 0.4$ nm, as well as using $a = 1$ nm and the corresponding $D = 32\ \mu\mathrm{m}^2/\mathrm{s}$ calculated via the *Stokes-Einstein* relation.[2]

Fig. 6.8 (a) shows reduced diffusion coefficients $D_\parallel$ and $D_\perp$ for the diffusion of hard

---

[2]In previous considerations the latter value was used for diffusion of rhodamine molecules in bulk TEHOS [Schu02b, Schu03]. However, this was based on a comparison with the diffusion coefficient of R6G in water obtained from FCS experiments, which meanwhile is known to be erroneous [Dert07]. The corrected value is one third larger, which agrees with $D \approx 50\ \mu\mathrm{m}^2/\mathrm{s}$.

spheres parallel and perpendicular to a wall obtained from the hydrodynamic no-slip boundary model described in section 2.2.2. The red curves were calculated for $a = 0.4$ nm, while the blue ones were obtained setting $a = 1$ nm. $D_\parallel$ (solid lines) was calculated using eqn. 2.4, while for $D_\perp$ (dashed lines) eqn. 2.5 was used. The bulk diffusion coefficients (dotted lines) were obtained from the *Stokes-Einstein* relation using the viscosity of TEHOS $\eta = 6.8$ mPas and were plotted for comparison. As can be seen, the $D_\parallel$ in both cases are already much larger than 4.5 μm^2/s at a distance $z = 2$ nm to the interface. However, the fast component D_2 obtained from the probability distributions of diffusivities in the above reported film thinning experiment is 4.5 ± 0.5 μm^2/s for all investigated film thicknesses. One possibility to explain this discrepancy would be a kind of *solvation shell*, i.e. solvent molecules arrange in a special way around the solute molecule and thus accompany its motion. Usually this is due to strong solvent/solute interactions e.g. hydrogen bonding or counterions shielding a charged particle. Fig. 6.8 (b) shows the corresponding plots of $D_\parallel$ assuming $a = 1.5$ nm (—) and $a = 5$ nm (-··-). Only in the latter case a considerably small diffusion coefficient to meet the observed value of D_2 is obtained. However, the interactions between the charged RhB molecules and the unpolar TEHOS molecules are not likely to be strong enough to cause such a large solvation shell. Furthermore, a partial-slip boundary at the solid/liquid interface would lead to even larger diffusion coefficients $D_\parallel$ and thus cannot be used to solve this issue. The here discussed hydrodynamic models use a no-slip or partial-slip boundary at the solid-liquid interface and a linear dependence of the *Stokes Drag* on the distance z to the interface. As was shown above, these models cannot contribute to the evaluation of a possible slight dependence of the diffusion coefficient D_2 on z within the upper layer.
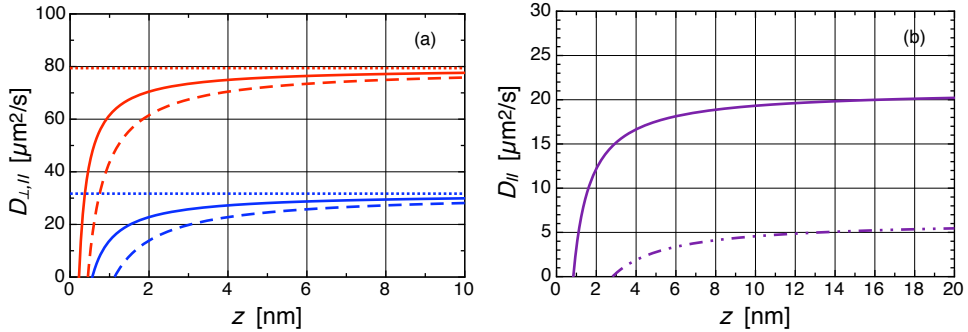
Figure 6.8: Dependence on interface distance z of diffusion coefficients calculated from hydrodynamic no-slip model: (a) $D_\parallel$ (—) and $D_\perp$ (- -) for particle with hydrodynamic radius $a = 0.4$ nm (red) and $a = 1$ nm (blue), bulk diffusion coefficients (···); (b) $D_\parallel$ for $a = 1.5$ nm (—) and $a = 5$ nm (-··-).

Yet there are two general ways to explain the considerable small value of about 5 μm^2/s observed for D_2: On the one hand there might be additional attractive surface forces acting on the dye molecules, e.g. for the charged dyes electrostatic interactions with the SiO$_x$ may be considered. However, also a non-charged dye was used for investigation, yielding similar diffusion coefficients, see the results from SM experiments containing a

perylene diimide (no-PDI) in the next section. Moreover, the long range *Van der Waals* interactions discussed in respect to wetting behavior (see section 2.2.1 and [Seem05]) may also be taken into account for the slowdown of the diffusion within thin films. On the other hand, as was already mentioned previously, the D_2 obtained from the analysis of diffusivities not necessarily have to match the diffusion coefficients for free diffusion in the above detailed three-layer model. If the dwell time of the dye molecules in the upper region of the film is considerably shorter as the frame time τ_{frame} used within the experiment, the observed diffusion coefficients will be effective diffusion coefficients only. Thus the comparatively slow D_2 in respect to the bulk diffusion coefficients are possibly caused by the strong confinement within the ultrathin TEHOS films forcing the dye molecules to enter the near-surface region with high frequency. In that case a time dependence of the probability distributions of d_{diff} should be observed. Explanations of the observed values for D_1 and D_2 may further consider the influence of the lateral substrate heterogeneity. Also then a time dependence related to the dwell times in the corresponding regions is expected. Thus experiments with varied frame rates $f = 1/\tau_{\text{frame}}$ are likely to provide more information on this issue. This will be the subject of the next section.

6.2.4 Conclusion

Probability distributions of diffusivities obtained from SMT at $\tau_{\text{frame}} = 20$ ms with an optical wide field microscope provide a powerful tool to study the heterogeneities of molecular motion in ultrathin ($d \leq 10$ nm) films at solid-liquid interfaces. Film thinning experiments show that no significant slowdown of the diffusion occurs within the distance from five to three molecular diameters from the solid-liquid interface. By this analysis of diffusivities, two discernible diffusion coefficients D_1 and D_2 are obtained, which do not change upon film thinning. Yet, their amplitudes change in favor of the slow component. This points towards an increased dye concentration in the corresponding region of slow motion within the thin TEHOS films. Thus the change of the distributions of diffusion coefficients calculated from weighted mean square displacements along trajectories (D_{traj}) can be explained by the increased presence of probe molecules in the region related to the slow component of diffusion. This finding leads to the suggestion that single dye diffusion in ultrathin TEHOS films on Si substrates with thick thermally grown SiO_x can be explained by a three-layer model containing (i) immobile adsorbed molecules at the interface (ii) a near-surface region with slowly diffusing molecules, and (iii) freely diffusing molecules in the remaining upper regions of the film. However, the lateral extension of the near-surface layer most probably is inhomogeneous, due to the influence from substrate heterogeneity. In particular, the suggested "silanol-gliding" by Honciuc et al. [Honc08], will be restricted to the silanol clusters on the substrate surface. Moreover, this experiment cannot resolve, whether there is still a slight dependence of the diffusion coefficient in the upper layer on the distance z to the substrate, or not. This issue can only be resolved by access to much shorter observation times.

Nevertheless, studies of the time dependence of the probability distributions of diffusivities by variation of τ_{frame} will contribute to the clarification of the question, if the

obtained values for D_1 and D_2 can be ascribed to diffusion in two heterogeneous regions. In case of dwell times τ_{dwell} in the heterogeneous regions in the range of τ_{frame}, a time dependence of D_1 and D_2 will be observed, while the obtained values are intermediates of such heterogeneous diffusion. Thus, the following section will concentrate on such experiments. Yet, there is likely to be also an influence from spatial heterogeneities of the substrate surface (see section 4.2.2) on SM dynamics.This question will be addressed in section 7.1. Furthermore, variations of the dye-substrate interactions are likely to reveal more information about the nature and the magnitude of the slow diffusion in the near surface region. For this reason, differently charged dye molecules were used in the experiments which are reported in the following sections.

6.3 Time dependence of diffusion studied by SMT

In the previous section, studies of a mutable time dependence of diffusion coefficients obtained from SMT experiments were suggested to further clarify the cause of the observed heterogeneous diffusion. Moreover, a time dependence of these diffusion coefficients is expected, since broad distributions of diffusion coefficients obtained from msd along trajectories hint to anomalous diffusion [Lube08] at least in the investigated time regime. As shown in the previous section and in the work of Schuster et al. [Schu03, Schu04], the distributions of D_{traj} obtained from SMT experiments on ultrathin TEHOS films are too broad for homogeneous diffusion. One feature leading to anomalous diffusion are power-law distributed traps [Lube08]. In SMT experiments, this question can be addressed by analyzing adsorption events along single molecule trajectories. For the thin TEHOS films studied in this work adsorption events are power-law distributed at least over two orders of magnitude in time, as can be seen in the next chapter 7 in section 7.1.2, where adsorption events were investigated depending on the substrate pre-treatment. Power-law distributed adsorption events were reported also by Schuster et al. for thin TEHOS films on quartz cover slips. There, the broad distribution of D_{traj} was interpreted to correlate with layer dependent diffusion coefficients, although a dependence of the distribution on trajectory length and thus on observation time was shown [Schu03]. Yet this broad distribution may be explained by the power-law distributed adsorption sites in the investigated time regime, and thus layer dependent diffusion can neither be evidenced nor dismissed by the reported investigations alone.

However, the film thinning experiment described in the previous section suggests the existence of two vertical layers with different diffusion coefficients (and a third immobile component). According to the model of Postnikov et al. [Post11], see section 3.3.9, this generates a time dependence of the lateral diffusion coefficients. This time dependence was observed experimentally, comparing video sequences with frame times of 20 ms and 100 ms. While the D_{traj} obtained from approximately 10 nm thick films with $\tau_{\text{frame}} = 100$ ms ranged between 0.2 μm^2/s and 0.4 μm^2/s, for $\tau_{\text{frame}} = 20$ ms the D_{traj} was found to be ≈ 1 μm^2/s. Previously Schuster et al. had found $D_{\text{traj}} = 1$ μm^2/s for a 4 nm thick film and $D_{\text{msd}} = 1.9$ μm^2/s for a 17 nm thick film on quartz cover slips with $\tau_{\text{frame}} = 25$ ms [Schu03]. In section 6.3.1 therefore, single molecule trajectories

obtained at different frame times are compared. Furthermore, in section 6.3.2 the time dependence is addressed by analysis of diffusivities for 10 different frame times, ranging from 20 ms to 200 ms.

6.3.1 Mapping of trajectories for two different frame times
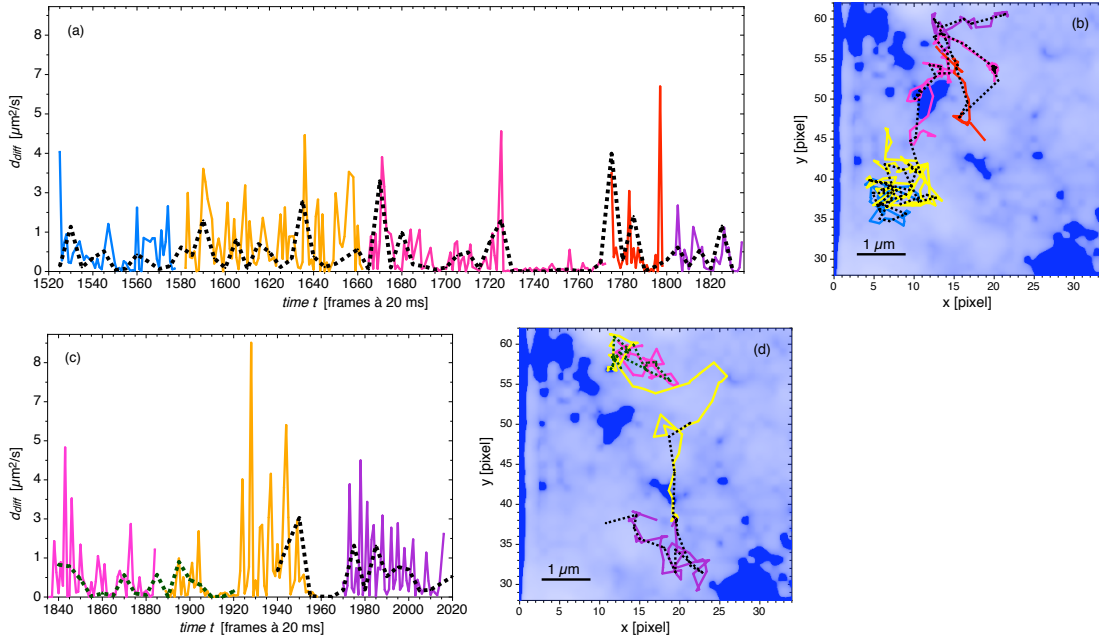
Figure 6.9: Two examples for mapping of trajectories from sequences with (−) $\tau_{\text{frame}} = 20$ ms, and (··) $\tau_{\text{frame}} = 100$ ms (integrated over 5 frames à 20 ms); (a,c) diffusivities along trajectories plotted over the macroscopic time t; (b,d) spatial mapping plotted on intensity distribution from integration of complete video sequence, white corresponds to bright regions.

Due to slightly differing experimental conditions, there are some constraints in comparing video sequences taken at different frame times. This was circumvented by artificially increasing the frame times for a recorded video sequence: Within a sequence taken at $\tau_{\text{frame}} = 20$ ms the recorded intensities were consecutively added up for each pixel from five frames into a new frame, thus increasing τ_{frame} to 100 ms for the artificially created video sequence. Both videos were then analyzed using the package *tracking.sh*. For some trajectories in the original sequence matching trajectories in the integrated video sequence were found. Fig. 6.9 (a,b) shows one trajectory detected in the integrated video sequence together with five trajectories from the original sequence, which each match a part of the former trajectory. Between frames 1730 and 1770 a period of immobilization is recorded within both video sequences. The fluctuations of d_{diff} seen with the trajectory related to $\tau_{\text{frame}} = 20$ ms are due to the position accuracy r_{pa}, which leads to a threshold value for immobile molecules of about 0.08 $\mu m^2/s$. The larger signal at $\tau_{\text{frame}} = 100$ ms, leads to an improved (smaller) r_{pa}, because the snr will increase

with the larger signal and r_{pa} is inversely proportional to snr [Bobr86, Kubi00] (and see section 3.3.1). Scaling by τ_{frame}, further reduces the fluctuations of d_{diff} in case of larger τ_{frame}. As can be seen, the diffusivities along the trajectory found in the sequence with the larger τ_{frame} are mostly averages of the diffusivites obtained along the trajectories with the faster τ_{frame}. However, some fast parts (large diffusivities) of the later are excluded in the former. This is even more pronounced in the second example, see Fig. 6.9 (b,d), where two trajectories from the integrated video sequence were matched by three trajectories from the original sequence. At about frame 1925 the trajectory from the faster sequence shows large diffusivities, up to 6.5 μm^2/s. This fast motion could not be traced within the slower sequence, therefore the detected trajectory from the latter ends at that point. This is in accordance with the observation achieved from the analyzation of simulated video sequences with the software package *tracking.sh*, which show that the diffusion coefficients obtained by *tracking.sh* tend to underestimate the real ones (see section 4.3).

Thus the time dependence of the diffusion coefficients which was observed by the use of different frame times, on the one hand is due to an intrinsic time dependence caused by the diffusion heterogeneity, but on the other hand it is also influenced by the limitation of SMT techniques with respect to the detection of fast diffusion. Nevertheless, the analysis of SMT experiments via msd along trajectories is a strongly averaging method, whereas probability distributions of diffusivites provide more details about diffusion heterogeneity. For this reason, the time dependence can be studied more thoroughly by the use of probability distributions of diffusivites which will be done in the following.

6.3.2 Time dependence of diffusion evaluated from analysis of diffusivities

Theoretical considerations for the time dependence of heterogeneous diffusion explained in this section have been published in [Baue09b]:

M. Bauer, M. Heidernätsch, D. Täuber, C. von Borczyskowski and G. Radons. Investigations of heterogeneous diffusion based on the probability density of scaled squared displacements observed from single molecules in ultra-thin liquid films. *Diffusion Fundamentals Journal*, Vol. 11, p. 104(14), 2009.

Although the anomalous behavior of SM diffusion in ultrathin TEHOS films can be seen within trajectory analysis, the qualitative evaluation of the time dependence using msd along trajectories is limited. For this method trajectories of sufficient length are necessary. However, their number decreases with the increase of the frame time for a given observation length (total time length of the video). On the other hand, the observation time is limited by bleaching events. Furthermore, dye molecules may leave the detection area during acquisition, thus inducing trajectory ends, which is more likely for longer time intervals. Yet, with distributions of diffusivities the effect of lower statistics will be less pronounced, because there the data sets obtained from a given observation time are much larger. Furthermore, probability distributions of diffusivities directly display the heterogeneous diffusion, as was shown in the previous section 6.2 on

film thinning, while the D_{traj} assigned to trajectories only yield time averaged effective diffusion coefficients. Therefore, in the following probability distributions of diffusivities for videos with different frame times will be compared. For this on the one hand videos were obtained at experimentally varied frame times, whereas on the other hand videos with artificially increased frame times were created for the analysis.

As shown in the previous section 6.2 on film thinning, SM dynamics in ultrathin liquid TEHOS films can be described by a three-layer model, where the layers are ascribed to (i) immobile molecules with a diffusion coefficient related to the position accuracy, (ii) near surface diffusion with diffusion coefficient D_{slow}, and (iii) freely diffusing molecules with diffusion coefficient D_{fast}. Whereby D_{fast} is related to bulk diffusion or to some modulation of the latter according to models from continuum hydrodynamics. From the film thinning experiment, two discernible diffusion coefficients D_1 and D_2 were obtained. However, the fast component, D_2 cannot be bulk diffusion, because bulk diffusion is one order of magnitude larger, see section 4.2.3 and [Grab07]. Yet, exchange rates between the corresponding regions on the sample, which are in the range of the video frame time τ_{frame}, will cause non-ergodicity of SM dynamics in that time interval. This will effect diffusion coefficients derived via trajectory analysis as well as via analysis of diffusivities, see section 3.3.6: Depending on the relation between the dwell times within the different regions and the observation time, either the D_{slow} and D_{fast} of the heterogeneous diffusion can be resolved, or time dependent short range diffusion coefficients $D_i(\tau)$ will be observed, or, in the long time limit, effective diffusion coefficient $D_{i,\text{eff}}$ will be obtained. Thereby, the mean dwell times $\tau_{i,\text{dwell}}$ within the different regions are defined by

$$\tau_{i,\text{dwell}} = \left(\sum_j f_{ji} \right)^{-1}, \tag{6.2}$$

where f_{ij} is the exchange rate from region j into region i. This means, the mean dwell time in region i is the inverse of the sum of the exchange rates from i into all the other regions. Yet, the occurring dwell times typically are distributed around the mean dwell time $\tau_{i,\text{dwell}}$. In the experiment, the question, whether the different diffusion components can be separated within experimental error, depends on the one hand on the relation between observation time and the actual distribution of dwell times. For a mathematically exact solution, the observation time has to be shorter than the shortest occurring dwell time. Yet, within the experiment, it may be sufficient, if the observation time is shorter than e.g. 95% of the dwell times or a suitable other quantity of them. On the other hand, the question is influenced by the magnitude of the difference between the involved diffusion coefficients. Thus, for a large difference between the involved diffusion coefficients, already some few shorter dwell times than the observation time, will lead to a notable deviation of the obtained diffusion coefficients from the values of the diffusion coefficients related to the involved regions. However, if the difference between the region-dependent diffusion coefficients is small, these deviations may be below the experimental error, unless a larger amount of the dwell times is shorter than the observation time.

If the observed system is at equilibrium, a stationary distribution of the dye molecules

will be achieved. Thereby, the probability to find a dye molecule in a distinct region is related to the transition rates into the region and out of the region. In case of only two heterogeneous regions, the system can be described by a master equation describing a two-state *Markov* process, for further information see [Baue09b, Risk96]. Then, equilibrium probabilities p_i to find the dye in region i are given as

$$p_i = \frac{f_{ij}}{f_{ij} + f_{ji}} \,. \tag{6.3}$$

Also for systems involving more than two heterogeneous regions, the equilibrium probabilities can be calculated, if the matrix of the transitions between all regions is known. In the long time limit of the observation time, the effective diffusion coefficient D_{eff} of the system can be calculated from the p_i and the corresponding diffusion coefficients D_i:

$$D_{\mathrm{eff}} = \sum_i p_i D_i \,, \tag{6.4}$$

which is a weighted sum of the diffusion coefficients related to the involved heterogeneous regions. However, further theoretical considerations are necessary to clarify, how D_{eff} is approached by the system with increasing observation time. Also it has to be further investigated, how the diffusion coefficients derived from multi-exponential fits to the probability distributions of diffusivities are related to the diffusion coefficients in the heterogeneous regions, and to D_{eff}.

It has been shown above that SM dynamics in ultrathin TEHOS films on 100 nm thick thermally grown SiO_x displays a time dependence within SMT experiments at frame times between 20 ms and 100 ms. However, to fully analyze this time dependence, further theoretical considerations are necessary. Nevertheless, the following study of the time dependence of the three diffusion coefficients D_0, D_1 and D_2 derived from tri-exponential fits to probability distributions of diffusivities can contribute to the understanding: The obtained results can be used to model realistic conditions for the underlying physical process for simulations to test new theoretical considerations. In case of D_1 and D_2 general considerations about the range of the involved diffusion coefficients and the corresponding dwell times and equilibrium probabilities can be derived. In particular, comparisons with results from investigation via FCS (see section 6.4) and from SMT experiments with varied conditions (e.g. changing the hydroxylation of the substrate surface, see section 7.1) will provide insights into the nature of the heterogeneous regions. The interpretation of the slowest component D_0 is more complicated, since in that case the transition between slow motion and immobility is overlaid by the time dependence of the position accuracy r_{pa}. Due to larger sampling time for fluorescence intensities, the snr for immobile molecules increases with increasing τ_{frame}, which leads to a higher r_{pa}. In the section on film thinning, the d_{diff} corresponding to immobile molecules were excluded by use of the average relation between r_{pa} and snr. Whereby r_{pa} was derived from the msd along trajectories related to immobile molecules (see the explanation in section 3.3.1). However, this had a strong influence on the obtained values for D_1. For this reason, probability distributions of all d_{diff} will be investigated in the following.

Experimentally varied frame time
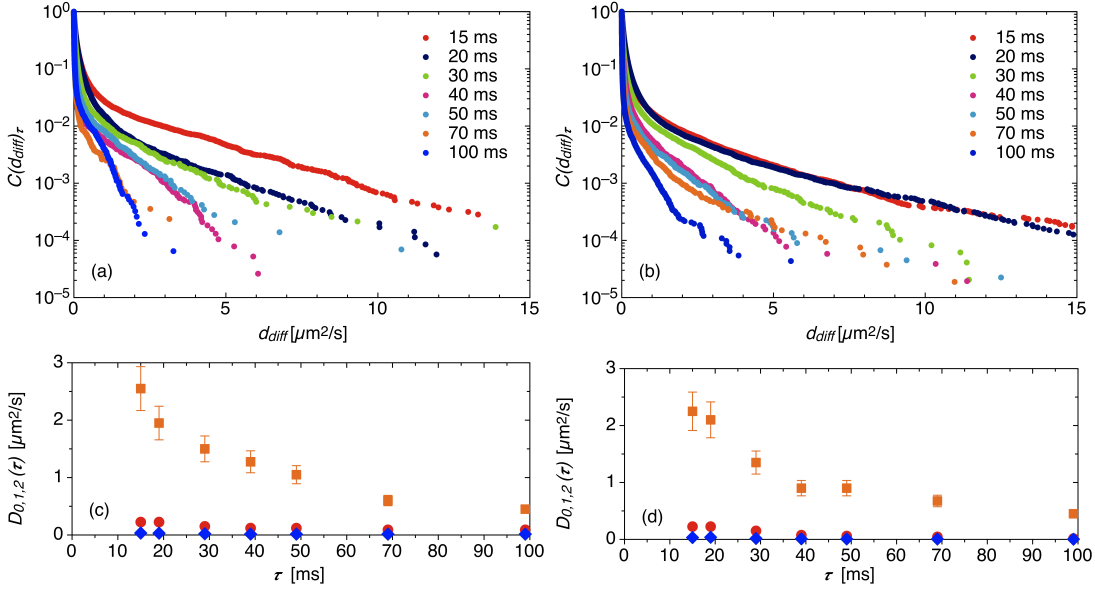
Figure 6.10: Probability distributions of diffusivities obtained from (a) R6G, (b) Oregon Green; in ultrathin TEHOS films with experimentally varied frame times; (c) and (d) time dependent diffusion coefficients obtained from tri-exponential fits to the distributions given in (a) and (b), (♦) D_0 for immobile molecules, (•) D_1 and (■) D_2; fitting uncertainties for D_2 are denoted by error bars, and are smaller than symbols otherwise.

Fig. 6.10 shows the probability distributions of d_{diff} for an ultrathin TEHOS film containing (a) R6G and (b) Oregon Green, obtained at experimentally varied frame times τ_{frame} (from SMT experiments using the PentaMax camera). Within these distributions a trend to smaller probabilities for large d_{diff} at larger τ (i.e. smaller frame rate f) can be seen. However, the experimental conditions for each acquisition are slightly modified by the varying amount of immobile molecules in the detection area and due to sample heterogeneity (see section 7.1 in the following chapter). The former will only change the amplitudes of the respective components within the distribution, while the latter directly affects the values of diffusion coefficients obtained from fits. In Fig. 6.10 (c and d) the diffusion coefficients are shown which were achieved by fitting the probability distributions in (a) and (b) with a tri-exponential function according to eqn. 3.26. The error bars for D_2 denote only fitting uncertainties and not the range of variations due to modifications of experimental conditions. For D_0 and for D_1 these error bars are smaller than the symbols. Interestingly, the two probability distributions derived from Oregon Green at $\tau_{\text{frame}} = 15$ ms and $\tau_{\text{frame}} = 20$ ms almost match each other, while with R6G a strong deviation at the corresponding frame times is seen. This may point to longer mean dwell times in case of Oregon Green. However, the experimental error at $\tau_{\text{frame}} = 15$ ms is quite large, in particular due to the unknown dark time of the CCD camera, which only could be estimated to be 1.5 ms (see section 4.1.1). Furthermore, it

can be seen that all three components decrease with increasing τ_{frame}. The decrease of D_0 is related to improved position accuracy with increasing τ_{frame}. Yet, the decrease of the two other components D_1 and D_2 points to even smaller D_{eff} in the long time limit. As was explained above, the expected time dependence of these diffusion coefficients is not yet clear. In a two-level system, a transition from the two physical diffusion coefficients D_{slow} and D_{fast} to the long time limit D_{eff} will take place, see section 3.3.6. FCS experiments described in the following section 6.4 show that D_{fast} is larger than 10 $\mu\mathrm{m}^2/\mathrm{s}$ for R6G in approximately 10 nm thick TEHOS films on 100 nm $\mathrm{SiO_x}$. The fastest observed D_2 here is about 2.7 $\mu\mathrm{m}^2/\mathrm{s}$. This implies that D_2 is not approaching D_{fast} within the here studied time regime. Moreover, the change of all D_i decreases with increasing τ_{frame}. Yet, at $\tau_{\mathrm{frame}} = 100$ ms there is still no transition to a mono-exponential decay of the probability distributions, as would be expected for the long time limit. This implies that at least some of the dwell times of the dyes in the heterogeneous regions are within the range of the studied τ_{frame}. Yet, the experimental uncertainties together with the sample heterogeneity are quite large. Hence, they conceal assumed differences originating from the different properties of R6G and Oregon Green (which are cationic and anionic, respectively, see section 4.2.1). For this reason, in the following the evolution of $C(d_{\mathrm{diff}})_\tau$ for artificially varied τ_{frame} will be analyzed to reduce contributions to the error from varying experimental conditions.

Artificially varied frame time
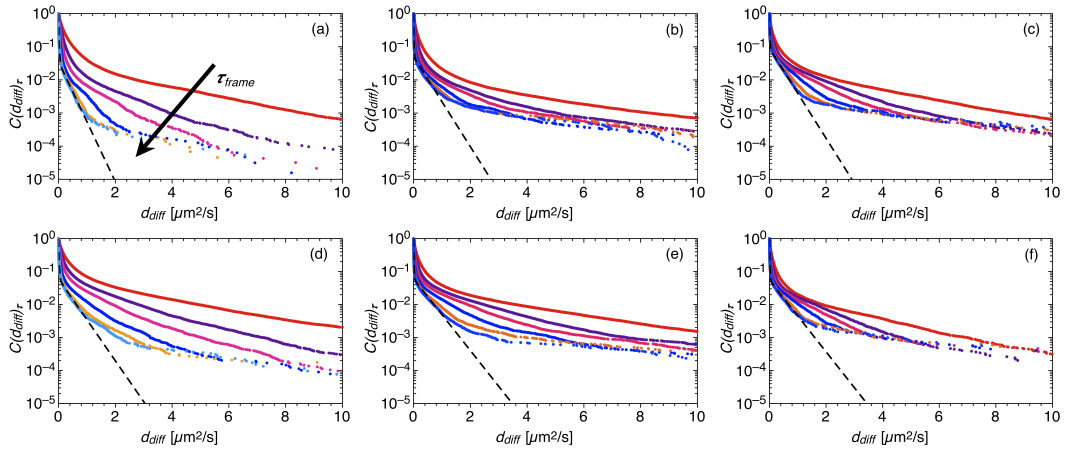
Figure 6.11: Probability distributions of diffusivities obtained from ultrathin TEHOS films containing (a) RhB $d = 6$ nm, (b) R6G $d = 5$ nm, (c) no-PDI $d = 6$ nm, (d) RhB $d = 8$ nm, (e) R6G $d = 10$ nm, and (f) no-PDI $d = 9$ nm; with $\tau_{\mathrm{frame}} = 20$ ms (red) and artificially varied $\tau_{\mathrm{frame}} = 40$ ms, 60 ms, 100 ms, 160 ms, and 200 ms, increasing τ_{frame} marked by arrow in (a) has similar direction in all diagrams; (- -) tri-exponential fits to the $C(d_{\mathrm{diff}})_{\tau=200\,\mathrm{ms}}$, respectively.

Further experiments originally had been conducted on films containing either RhB, R6G or no-PDI to study the dependence of single dye diffusion in ultrathin TEHOS films

on the properties of dyes. Yet with trajectory analysis only minor differences could be seen. The videos obtained from these experiments were suitable for studying the time dependence of SM diffusion within ultrathin TEHOS films by artificially increasing the frame times. For each dye TEHOS films of two different thicknesses had been prepared. All samples were investigated within 2 to 7 h after preparation (to exclude contributions from aging). For all six samples video sequences were acquired at $\tau_{\mathrm{frame}} = 20$ ms (i.e. frame rate $f = 50$ fps). 10 video sequences containing 5 000 frames were obtained from each sample, giving a total of 50 000 frames per sample. For analysis, τ_{frame} was artificially increased in ten steps, by integrating over 2, 3, 4, up to 10 succeeding frames for each experimentally obtained video. Thereby new video sequences with $\tau_{\mathrm{frame}} = 40$, 60, 80, up to 200 ms were created, which all contain the same particular SM motion as the original videos with $\tau_{\mathrm{frame}} = 20$ ms. In that way the total numbers of frames were reduced. However, for $\tau_{\mathrm{frame}} = 200$ ms there was still a total of 5 000 frames per sample, which is sufficient for analysis via probability distributions of d_{diff}. Yet the reduction of the number of frames is not the only restriction of this method. The increase in τ_{frame} also leads to a higher number of single molecules per frame. SMT only works with highly diluted dye molecules. Thus this method is limited to about 10 integration steps, otherwise there will appear too many dye molecules in a single frame. Theoretical considerations suggest the investigation of slower frame rates by a different method, which simply considers displacements not between succeeding frames but between every i^{th} frame. The fortune of this method would be similar numbers of frames for the investigation of all frame rates and no problems with overcrowded frames. However, then *tracking.sh* will no longer be applicable to detect the displacements and also the implications from geometrical averaging will leave the approximation regime of $\tau_{\mathrm{frame}} \approx \tau_{\mathrm{exposure}}$ (see section 3.3.2) rendering the evaluation of diffusion coefficients more complicated and less reliable. Thus, the perviously detailed method had to be used for evaluation of diffusivities at different frame rates from the same experimentally acquired video sequence. Fig. 6.11 shows the obtained probability distributions of d_{diff} for all six samples together with tri-exponential fits (according to eqn. 3.26) to the distributions corresponding to $\tau_{\mathrm{frame}} = 200$ ms (dashed lines). Similar to the distributions from the experimentally varied frame rates, also here the probability for larger d_{diff} decreases with increasing $\tau_{\mathrm{frame}} =$ (see the arrow in Fig. 6.11 (a), a similar relation holds for the other diagrams too). Further results will be discussed in the following using fits to these distributions.

The distributions shown in Fig. 6.11 were fitted with a tri-exponential function according to eqn. 3.26 using *OriginPro8G*™ (*OriginLab Corporation*, MA, USA) where the fits were weighted by the variance. The results are shown in Fig. 6.12. For the $D_i(\tau)$, a semi-log scale was chosen to visualize possible exponential decays. From those fits the following results are derived:

Position accuracy and immobile molecules related to D_0: The slowest component D_0 is strongly related to the position accuracy r_{pa}. For this component a linear relation between $D_i(\tau)$ and $\log(\tau)$ representing an exponential decay of $D_i(\tau)$ can be seen for 20 ms $\leq \tau \leq$ 80 ms (Fig. 6.12 a). The values of r_{pa} decrease with increasing
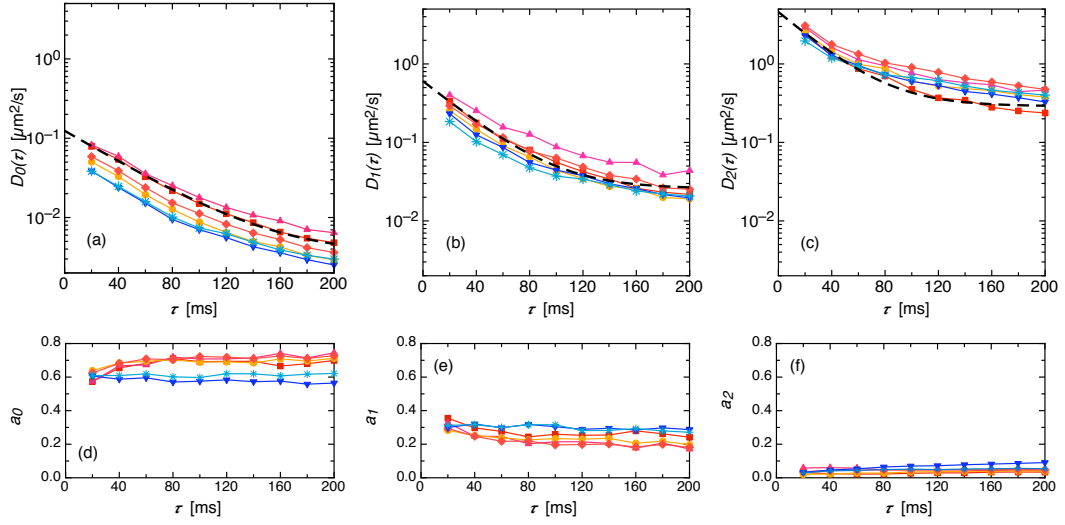
Figure 6.12: Diffusion coefficients (a) $D_0(\tau)$, (b) $D_1(\tau)$, (c) $D_2(\tau)$, and corresponding amplitudes (d) a_0, (f) a_1, (e) a_2, obtained from tri-exponential fits to probability distributions shown in Fig. 6.11. (■) RhB $d = 6$ nm, (▲) RhB $d = 8$ nm, (●) R6G $d = 5$ nm, (♦) R6G $d = 10$ nm, (▼) no-PDI $d = 6$ nm, and (∗) no-PDI $d = 9$ nm, solid lines are for eyes guide, (- -) mono-exponential fit to $D_0(\tau)$ from RhB $d = 6$ nm.

acquisition time (i.e. increasingly improved position accuracy), mainly due to the fact that the snr increases with the increasing signal at longer acquisition. This is related to setup geometry: For larger acquisition time, also adjacent pixels of the CCD chip will be illuminated above the background threshold. This will improve the determination of the center position from the two-dimensional Gaussian fits. Thereby, this effect is stronger, when only few pixels are illuminated, while it will saturate at large numbers of illuminated pixels. For comparison, the position accuracy r_{pa} was evaluated from the msd of immobile and slowly moving dye molecules for the acquisitions from the samples R6G $d = 5$ nm and no-PDI $d = 6$ nm, according to the method described in section 3.3.1. A diffusion coefficient D_0 for immobile molecules can be evaluated from r_{pa} via the *Einstein-Smoluchowski* equation (3.11) for two dimensions leading to

$$D_0(\tau) = \frac{r_{pa}^2}{4\tau} . \tag{6.5}$$

Fig. 6.13 (a) shows a comparison of the $D_0(\tau)$ from the analysis of d_{diff} with the $D_0(\tau)$ derived from r_{pa} via eqn. 6.5 for the 5 nm thin TEHOS film doped with R6G and the 6 nm TEHOS film doped with no-PDI. For $\tau \leq 60$ ms, the values are similar within experimental error and fitting accuracy. The total error for D_0 from the analysis of d_{diff} is approximately 10%. In contrast, for D_0 obtained via analysis of msd the error increases with τ. For the determination of D_0 by the latter method, the snr is averaged over each trajectory. However, the distribution

of snr obtained for detected spots broadens with increasing τ, as can be seen in Fig.6.13 (b,c). Thereby, the distribution of snr obtained from no-PDI is broader than that obtained from R6G, while its mean is smaller for R6G. The reason for this difference is not clear. A higher rotational mobility of adsorbed R6G molecules as well as more frequent fluorescence intermittences (blinking) for R6G are possible causes. Yet, all used dyes have quantum yields close to one and thus should show equally few blinking events.
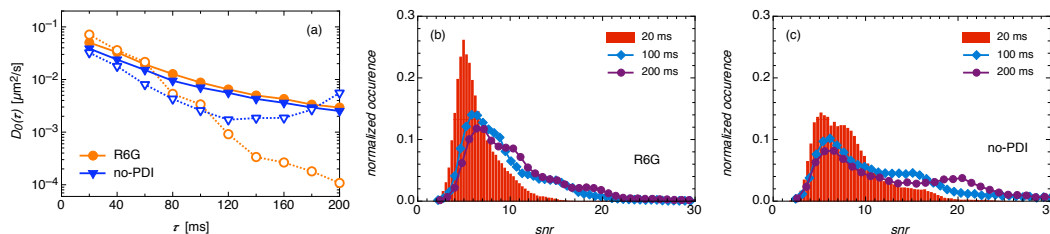
Figure 6.13: (a) Comparison of diffusion coefficients $D_0(\tau)$ obtained from analysis of d_{diff} (solid symbols) and from analysis of msd (open symbols) for R6G $d = 5$ nm and no-PDI $d = 6$ nm, (b,c) corresponding normalized distributions of snr of single detected spots from immobilized dye molecules at $\tau_{\mathrm{frame}} = 20$ ms, 100 ms and 200 ms.

Nevertheless, there may be also an influence on the time dependence of $D_0(\tau)$ from the exchange between mobility and immobility. In particular, short excursions into bulk-like diffusion should contribute to the value of D_0. This agrees with the observation of the smallest D_0 for no-PDI, because the perylene is more than twice the size of the rhodamines, see Fig. 4.3. According to the *Stokes-Einstein* relation eqn. 3.6, the translational diffusion coefficient scales inversely with the hydrodynamic radius of the molecule. Thus, by this relation a bulk diffusion coefficient for no-PDI of about half the magnitude of the one for the rhodamines is expected, i.e. about 20 μm^2/s. Also slow near-surface diffusion may contribute to the temporal evolution of D_0. Similarly to the evaluation of D_0 from analysis of d_{diff}, the evaluation of D_0 via analysis of msd is influenced by mutable periods of diffusion. Periods of mobilization could also explain the broadening of the distributions of snr with τ_{frame}: The snr of truly immobile molecules will increase with τ_{frame}, while their ratio within the distribution will decrease in favor for molecules undergoing one or more periods of mobilization. Thus, the smaller D_0 in case of no-PDI may also be caused by lower desorption-rates (causing larger mean values of adsorption duration).

The curves of $D_0(\tau)$ plottet in Fig. 6.12 (a) for the different samples are almost parallel with only slight vertical shifts, apart from the one obtained from the 8 nm thick film containing RhB, which shows a slightly shallower decay. However, the decays are still similar within the fitting accuracy (error bars are not shown for better visuality. The error from fitting is about 10%). Furthermore, the curves are grouped in respect to the used dyes: For both samples containing no-PDI (blue

curves) the smallest $D_0(\tau)$ are obtained, while those for the samples containing RhB are larger than the others. This agrees with the larger mean snr for no-PDI than for R6G. Since the position accuracy is related to the signal to noise ratio (snr), see 3.3.1. Yet, the total difference here is small, rendering almost similar detection probabilities for the SMT from all three dye molecules (however, the restricted detectability of fast diffusion with SMT will lead to additional differences in detection probabilities, see below).

Fits to $D_0(\tau)$ using a mono-exponential decay to a constant value (see the dashed line in Fig. 6.12) yield characteristic times of about 40 ms for the decay. However, it is not yet clear, whether this characteristic time can be related to a mean adsorption time. For this, more theoretical investigation on the time dependence of the D_i is necessary.

Detection losses: A noticeable result is the time dependence seen in the amplitudes a_0 and a_1: The amplitudes a_0 for the component $D_0(\tau)$ from the tri-exponential fit to the $C(d_{\mathrm{diff}})_\tau$ are constant in case of the no-PDI samples, while the a_0 increase on the first 100 ms from approximately 60% to about 70% for the samples containing rhodamines. This increase in a_0 is accompanied by a decrease in a_1. In case of slowly diffusing molecules, the opposite effect would be expected: As can be seen from the time dependence of $D_0(\tau)$, a molecule diffusing with 0.04 μm^2/s at $\tau = 20$ ms will be considered immobile, while at $\tau = 100$ ms the mobility can be detected. Yet, the amplitudes for each fit are related to each other by the condition $\sum_i a_i = 1$ (see eqn. 3.26). a_2 is one order of magnitude smaller, and therefore does not contribute much to the sum. For this reason, the increase of a_0 is related to the decrease of a_1 observed on the same timescale. Indeed, the decrease of a_1 can be explained by a decrease of detected molecules, which is caused by the loss of fast moving molecules, similar to the example shown in Fig. 6.9 (c and d) between frame numbers 1920 and 1940 (yellow trajectory). This is only seen in SMT experiments containing rhodamines, while for no-PDI the values of a_0 and a_1 remain constant with increasing τ. This discrepancy can be explained by a combination of the slightly superior detection probability for no-PDI (see previous item), and the larger size of no-PDI leading to a smaller diffusion coefficient for the perylene.

Diffusion coefficients $D_1(\tau)$ and $D_2(\tau)$ and dwell times: With $D_1(\tau)$ and $D_2(\tau)$, no linear parts are seen in the semi-log plot within the investigated time regime. This shows that D_1 and D_2 display a strong time dependence, which is not mono-exponential in the studied time regime. In particular, a strong time dependence is seen within 20 ms$\leq \tau \leq$100 ms and within 20 ms$\leq \tau \leq$40 ms for D_1 and D_2, respectively. As was explained in section. 3.3.6, the diffusion coefficients related to heterogeneous regions of the sample can only be separated, if the observation time is shorter than the dwell times within these regions. This is not the case here. Nevertheless, the observed strong time dependence leads to the assumption that at least the mean dwell time for one of the heterogenous regions is in the range of

about 20 ms. However, further theoretical investigations are necessary to clarify the relations between mean dwell times and the observed diffusion coefficients from diffusivity analysis.

From Fig. 6.12 (b and c) it can further be seen that the values of D_1 and D_2 (and also D_0) obtained for no-PDI tend to be smaller than those for the rhodamines, apart from D_2 for the 6 nm thick TEHOS film containing RhB at $\tau > 40$ ms. Thereby the values obtained from both samples containing no-PDI are almost similar, whereas the largest deviation between the two different samples for each dye is observed for RhB. As was explained in the previous item, with the rhodamines the detection of fast diffusion decreases with the increase of τ for $\tau \leq 100$ ms. Hence, the stronger variation observed for the rhodamines can be explained by the in that case larger bulk diffusion coefficient of about 55 μm^2/s, in respect to about 20 μm^2/s for no-PDI. This on the one hand leads to a better detectability of the corresponding SM diffusion. On the other hand, the smaller bulk diffusion coefficient for no-PDI seems to cause the smaller D_1 and D_2 observed for no-PDI. However, the difference between the diffusion coefficients observed for the different dyes is small. For D_2 it is within the estimated error of about 10% from fitting accuracy. For D_1 the difference is slightly larger than this error at least between no-PDI and RhB for 20 ms $\leq \tau \leq 100$ ms. The assumption therefore is that a smaller bulk diffusion coefficient leads to smaller values for D_1 and D_2 (and perhaps also influences D_0, as detailed above), while the total difference is obscured by the decreased detection of fast SM diffusion for increasing τ, and by differences in r_{pac}.

Because of the observed anomalous diffusion in the time regime of tens of ms, the two diffusion coefficients D_{slow} and D_{fast} ascribed to the heterogeneous regions of ultrathin TEHOS films can only be evaluated from experiments gaining access to timescales at least one order of magnitude faster than the SMT experiments. This also affects trajectory analysis. According to Saxton [Saxt97a] the D_{traj} obtained from trajectory analysis by weighted msd represent short range diffusion coefficients with an effective time length of 2.6 time steps [Saxt97a, Schu02b]. For $\tau_{\text{frame}} = 25$ ms this leads to 65 ms. Therefore, a broad distribution of D_{traj} is observed, according to the explanation given in section 3.3.6. This was demonstrated in previous experiments at about that frame time, see section 6.2 and [Schu03]. The diffusion coefficients D_{msd} gained from fitting these distributions of D_{traj} according to a multiple-component version of eqn. 3.18 thus cannot reveal layer dependent diffusion coefficients. Instead, they are short range diffusion coefficients similar to the $D_{i,\text{diff}}$ obtained from probability distributions of diffusivities. However, the analysis via msd uses averages over the trajectory lengths. Hence, the D_{msd} additionally are influenced by the time length (= trajectory length) used for building the averages. Due to the small long time limit D_{eff}, averaging over longer time length will lead to smaller D_{msd}. The reported selection of subsets according to minimum trajectory length [Schu03], demonstrates this time dependence of D_{msd}.

6.3.3 Conclusion

The temporal evolution of probability distributions of diffusivities obtained from a set of measurements on the same sample was studied over one order of magnitude in time. This gives further evidence for the restricted detection of fast diffusing rhodamine molecules, as was already found in section 4.3.2. Moreover, a higher detection efficiency for no-PDI could be seen. The latter may be related to the larger size and thus smaller (bulk) diffusion coefficient of no-PDI, as well as to lower desorption rates for the perylene. Tri-exponential functions were used for fitting the distributions of diffusivities. This reveals a strong dependence on time in particular for 20 ms $\leq \tau \leq$ 100 ms for the medium component D_1. Which points to frequent exchange of dye molecules between the heterogeneous regions of the ultrathin TEHOS films within these time intervals. However, further theoretical considerations are necessary to evaluate interregional exchange rates, and to relate the diffusion coefficients $D_i(\tau)$ derived from tri-exponential fits of the probability distributions of d_{diff} to the diffusion coefficients within these heterogeneous regions as well as to the effective diffusion coefficient in the long time limit.

So far, to evaluate the diffusion coefficients related to the heterogeneous regions, experimental access to timescales at least one order of magnitude shorter is required. This access can be provided by fluorescence correlation spectroscopy (FCS) [Wöll09, Schu10b]. Therefore, in the next section experiments using FCS on ultrathin TEHOS films will be reported.

6.4 Fluorescence correlation spectroscopy

Fluorescence correlation spectroscopy (FCS) allows for the investigation of fluorescent probe molecule diffusion and other processes discernible by fluorescence fluctuations within the focal volume, see section 3.4. The accessible timescale thereby ranges from nanoseconds to seconds [Schw02, Wöll09]. Thus it is suitable to complement the insights on SM diffusion gained from the previously described SMT experiments with respect to faster timescales. In particular, with SMT experiments the diffusion coefficients for near-surface diffusion and free diffusion in the upper film region cannot be resolved, due to anomalous diffusion on the corresponding timescale. For this reason, FCS experiments were accomplished on ultrathin liquid TEHOS films

6.4.1 Experimental
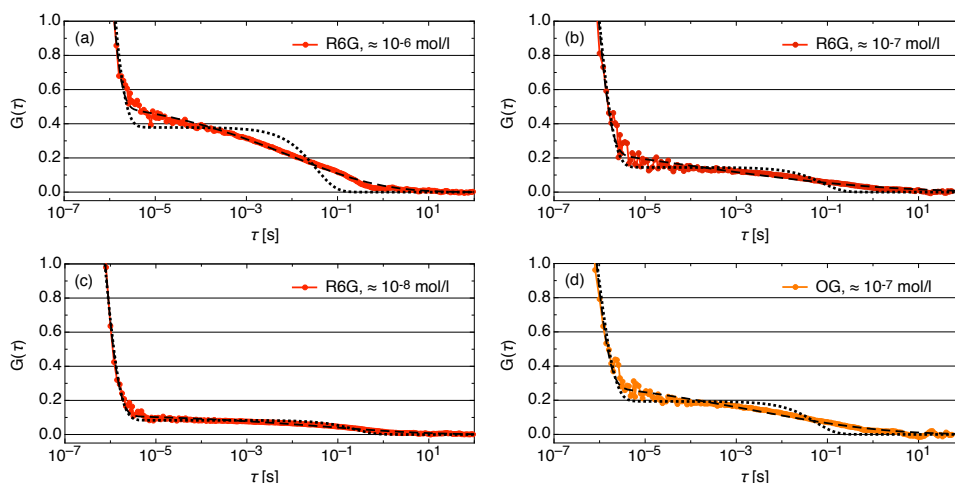
Figure 6.14: Autocorrelation curves and fits for 10 nm TEHOS films: (a - c) R6G, concentrations ranging from (a) $\approx 10^{-6}$ to (c) $\approx 10^{-8}$ mol/l; (d) OG with $c \approx 10^{-7}$ mol/l; (··) bi-exponential fits, (- -) two-component fits containing an exponent and a stretched exponent according to eqn. 6.11.

FCS experiments were conducted on 10 ± 1 nm thick TEHOS films on Si wafers with 100 nm thermally grown oxide. Samples were prepared according to the description in section 4.2.3. The samples were investigated within 1 to 6 hours after preparation. Fluorescent dyes (R6G, RhB, Oregon Green and no-PDI, see 4.2.1) where added to TEHOS in concentrations of about 10^{-6} mol/l to about 10^{-8} mol/l before dissolution in hexane. Excitation power ranged from 0.6 μW to 20 μW at the sample, which due to the small excitation area of about 0.3 μm^2 leads to values of 0.2 kW/cm^2 to 0.7 kW/cm^2. All samples showed initial bleaching after the start of excitation. However, with R6G and with Oregon Green stable count rates could be achieved after excitation of 5 min. Thus, each spot on the sample was excited for 5 min before starting measurements, to avoid bleaching during the measurement. With RhB and with Perylene stable rates hardly could be

achieved. Yet it is not clear why these two dyes behaved so differently, since the photostability is almost similar for all four dyes. For this reason, samples containing RhB and no-PDI were excluded from further considerations. Fluorescence intensities were recorded for 300 s and autocorrelated using the correlator ALV5000, where the shortest time lag is 0.2 μs. To avoid contributions from afterpulsing, the first two to three data points of the autocorrelation curves where excluded from fits [Schw02]. Fig. 6.14 shows autocorrelation curves obtained from four different samples. As was already mentioned, with R6G (Fig. 6.14 a-c) and with OG (Fig. 6.14 d) stable conditions could be achieved. The variation in dye concentration leads to a change in the amplitude of the autocorrelation curve in the range between approximately 1 μs and 1 s, as can be seen from the samples containing R6G in different concentrations in Fig. 6.14 (a-c). The average fraction β of (substrate surface-)binding sites that remain free at equilibrium depends on the total dye concentration. It will decrease with increasing dye concentration. According to Axelrod and Thompson [Thom83], this does affect the reaction rate R_R for surface binding and the bulk diffusion rate R_B, see eqn. 3.42. Also a decrease of the amplitude of $G(\tau)$ related to sorption kinetics is expected, see eqn. 3.44 and [Thom83]. However, in contrary to the setup used by Axelrod et al., with the setup used here the amplitude of $G(\tau)$ is also influenced by lateral transients from diffusing dye molecules. The number of the latter will increase with increasing concentration. Thus, the increase of the amplitude of $G(\tau)$ observed for 1 μs $< \tau < 1$ s is related to an increase of fluctuations due to lateral transients of the focal area by dye molecules. For the lowest concentration $c \approx 10^{-8}$ mol/l, the amplitude gets very low, rendering also low reliability for any fits within the corresponding time interval. Furthermore, from the sample containing OG very similar autocorrelation curves were obtained as from the sample containing R6G in the corresponding concentration. This points to only minor influence of the type of dye charge on diffusion dynamics (R6G is cationic, while OG exists in an anionic and in a neutral state, see section 4.2.1).

6.4.2 Results and discussion

Separation of FCS autocorrelation curves into fast and slow parts

In Fig. 6.14 (a-c) autocorrelation curves for three samples containing R6G in three concentrations differing by about one magnitude each are shown. The curves contain two regions: (i) a fast decay with correlation times in the range below 1 μs, which will be denoted as $G_{\text{fast}}(\tau)$, and (ii) a flat decay reaching over three to four decades into seconds, in the following denoted as $G_{\text{slow}}(\tau)$.

According to the argumentation in section 3.4, $G_{\text{slow}}(\tau)$ should contain the reaction rate R_R (i.e. rate of ad-/desorption at the surface). However, since both adsorbed molecules and diffusing molecules are fluorescent and the diffusing molecules are strongly confined in z-direction by the film thickness, the simplified eqn. 3.47 will give only a rough approximation. On the other hand, it is not possible to determine reaction rates, which would be necessary to be able to use more sophisticated equations, e.g. given in [Liet03]. To calculate reaction rates as suggested by Lieto et al., the dye concentration has to be

known and should then be varied to obtain the reaction rates from the linear dependences on concentration. However, due to the low solubility of the dyes in TEHOS, the dye concentration can only be roughly estimated, e.g. from counting fluorescence spots in wide-field experiments.

In principle there are two possible contributions for correlations in the range below μs (i.e. for $G_{\text{fast}}(\tau)$): (i) rotational diffusion of freely diffusing molecules and (ii) passages of freely diffusing dye molecules between adsorption events (contributions from afterpulsing were excluded by skipping the first two to three data points [Schw02]). The third possibility, triplet lifetimes and other fluorescence intermittences, can be ruled out: As described in section 4.2.1, the quantum yield of the used dyes is close to one, leading to a very small ratio of dye molecules in the triplet state. According to eqn. 3.41 contributions to the correlation curve from triplet blinking therefore are expected to have a very low amplitude. However, the amplitude of $G_{\text{fast}}(\tau)$ is much higher than that of $G_{\text{slow}}(\tau)$, thus it cannot be caused by triplet blinking. Similar considerations apply to other fluorescence intermittences. In the following τ_{FD} (freely diffusing) will denote correlation times corresponding to the fast decay in the range below 1 μs, while τ_D (for lateral diffusion) and τ_R (reacting, i.e. adsorption rate) will be used for the correlation times in the slowly decaying part of the autocorrelation curves.

Rotational diffusion In section 4.2.1 also rotation times of R6G and RhB in various liquids are shown, see Table 4.1. The viscosity of bulk TEHOS is 6.8 mPas and thus well in the range of the viscosities of the liquids listed there. Therefore, rotational correlation times for the rhodamines in TEHOS are expected to be in the range of ns or slightly below. E.g. for R6G in dimethylsulfoxide (DMSO) τ_{rot} is 480 ± 30 ps, while the viscosity is 2.2 mPas. Propanol has a similar viscosity and only slightly smaller τ_{rot}. The indirect proportionality of D_{rot} and η given by the *Debye-Einstein* relation, eqn. 3.7, together with the indirect proportionality of D_{rot} and τ_{rot} yields a linear dependence between τ_{rot} and η. Thus using the R6G/DMSO values and the viscosity of TEHOS renders $\tau_{\text{rot}} \approx 1.5$ ns for R6G in bulk TEHOS. This is two orders of magnitude faster than the fast component τ_{FD} obtained from the FCS experiments described above. However, hydrodynamic considerations (see section 2.2.2) together with estimations of intermolecular forces at solid-liquid interfaces [Isra07] predict an increased viscosity of wetting liquids close to hydrophilic substrates. Nevertheless rotational correlation times in the range of 100 ns will require $\eta \approx 0.5$ Pas, which is two orders of magnitude larger than the value for bulk TEHOS. Since some amount of dye molecules will be in regions far away from the substrate, the calculated viscosity is a mean viscosity for all rotating dye molecules. Therefore, the viscosity close to the substrate had to be even higher, if it really was the cause of the observed fast decay.

Mean first passage times As was shown in section 3.1.1, mean first passage times (mfpt) for molecules diffusing in 10 nm thick TEHOS films with diffusion coefficients between 5 μm^2/s and 70 μm^2/s are in the range of 0.1 μs and below. This matches the observed time scales. Thereby the mfpt corresponds to the width of the decay

of the distribution of passage times. Thus, it might be obtained from an exponential fit to the autocorrelation curve, as long as the first passage process is fast with respect to lateral diffusion (otherwise the change in fluorescence detection throughout the focal area has to be taken into account). However, a slowed down diffusion close to the substrate might increase the mfpt. But, if a substantial slowing down would prolong the mfpt, it similarly would enlarge correlation times stemming from rotational diffusion and thus lead to a change in the fluorescence fluctuations. Therefore the observed fast correlation time might simply be the mfpt for dye molecules re-entering the near-surface region, in case the diffusion outside this region is almost bulk-like. Also, a vertical change of the diffusion coefficient according to continuum hydrodynamic models (see section 6.2.3) agrees with mfpt in the range of 1 μs. Assuming an exponential decay, the mfpt is expected to contribute to the correlation function in a similar way as rotational diffusion does. Thereby the amplitude of the exponential decay is related to the ratio of freely diffusing molecules.

As was mentioned above, both possible processes causing the fast part of the auto-correlation curve will show an exponential decay. However, the timescale of this fast decay is better met by mfpt than by correlation times for rotational diffusion. For this reason, in the following the notation τ_{FD} and A_{FD} corresponding to "freely diffusing" will be used for the fast correlation time and the ratio of freely diffusing molecules, respectively. The contribution from rotational diffusion is given by eqn. 3.40. However, in case of mfpt, not all molecules will contribute to this fast component, because some will be adsorbed at the substrate or will diffuse within the near-surface region. For this reason, the amplitude A of the exponential decay is related to the ratio of freely diffusing molecules A_{FD} by $A = A_{FD}/(1 - A_{FD})$ (in a similar way the correlation function for triplet blinking is scaled by the corresponding ratio A_{Tr} of molecules in the triplet state). Thus the contribution of freely diffusing molecules to the correlation function can be expressed as:

$$G(\tau) = \left(1 + \frac{A_{FD}}{1 - A_{FD}} \exp(-\tau/\tau_{FD})\right) G'(\tau). \tag{6.6}$$

A simple mathematical transformation of eqn. 6.6 yields the following reformulation of eqn. 6.6:

$$G(\tau) = G'(\tau) + \frac{A_{FD}}{1 - A_{FD}} \exp(-\tau/\tau_{FD}) G'(\tau). \tag{6.7}$$

Yet $\exp(-\tau/\tau_{FD})$ with τ_{FD} below 1 μs is a fast decaying function. Thus the second term in eqn. 6.7 can be neglected for $\tau > 1$ μs. Therefore $G_{\text{slow}}(\tau) = G'(\tau)$, while $G_{\text{fast}}(\tau) = A \exp(-\tau/\tau_{FD}) G'(\tau)$. Since G_{slow} is influenced by translational diffusion and ad-/desorption kinetics, either one of the correlation functions G_D (eqn. 3.37), $G_{D,\text{anomal}}$ (eqn. 3.38) or $G_{D,\text{bi}}$ (eqn. 3.39) related to translational diffusion, or an exponential function related to ad-/desorption kinetics according to eqn. 3.47 may be used for approximation (or a combination of both). To understand the influence of adsorption events on

G_{slow} in the following three exemplary fluorescence time traces from the sample containing 10^{-7} mol/l R6G will be shown together with the corresponding correlation functions. Grabowski et al. also investigated SM diffusion in thin TEHOS films by FCS [Grab07] for $\tau \geq 0.1$ ms, for which they used Alexa 488 (a rhodamine derivative). They decided to fit the obtained autocorrelation curves by a function for two components of lateral diffusion. Their results will be compared to the results obtained from fitting the three exemplary autocorrelation curves by the fitting function for two components of lateral diffusion $G_{D,\text{bi}}$ given in eqn. 3.39. The use of other functions for fits to G_{slow} will be discussed afterwards.

Effect of adsorption events
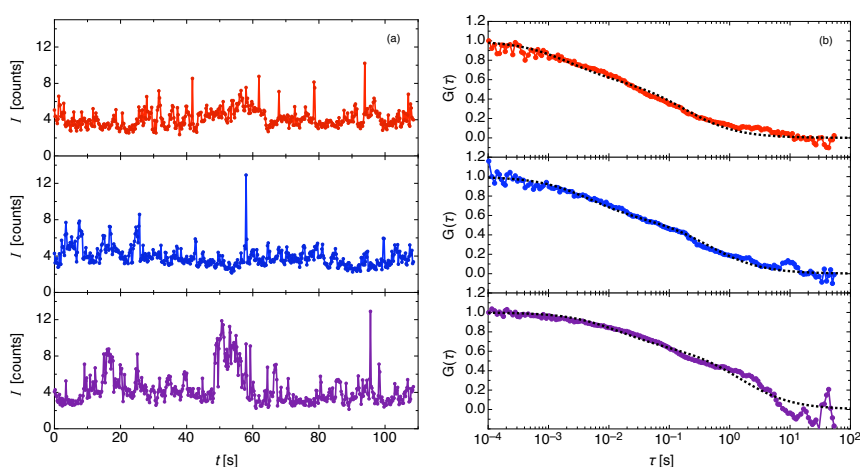
Figure 6.15: (a) Three time traces of fluorescence intensity from a sample containing $\approx 10^{-7}$ mol/l R6G taken at the same spot on the sample, (b) normalized slow parts of corresponding autocorrelation curves, ($\cdots$) fits using the two component function $G_{D,\text{bi}}$ for translational diffusion according to eqn. 3.39.

In Fig. 6.15 (a) three characteristic time traces from a sample containing aproximately 10^{-7} mol/l R6G are shown. The bottom trace displays an interval of higher fluorescence intensity (at 48 s - 58 s), while the other two show either shorter intervals of higher intensity or lower count rates during events of similar duration. Those intervals are most likely due to periods of immobilization of dye molecules. If immobilization occurs in a position favorable for fluorescence excitation and emission, the count rate will be increased. The corresponding autocorrelation curves to fluorescence traces containing such intervals of higher fluorescence intensity show an increased signal at longer times. Fig. 6.15 (b) shows the slow parts ($\tau \geq 0.1$ ms) of the autocorrelation curves corresponding to the three time traces shown in Fig. 6.15 (a). For better comparison these slow parts had been normalized to 1 similar to the curves shown by Grabowski et al. in Fig. 2 [Grab07], who conducted FCS experiments on approximately 15 nm thick TEHOS films doped with Alexa 488 on quartz cover slips (Alexa 488 is a rhodamine derivative,

and thus yields comparable diffusion coefficients to those obtained for R6G and RhB). The bottom curve has a slower decay and a higher amplitude in the range between approximately 0.5 s and 5 s. This can cause problems during fitting, making the fits even impossible. The dotted lines correspond to fits to the plotted slow parts of the autocorrelation curves using the two-component correlation function for translational diffusion in two dimensions, eqn. 3.39 given in section 3.4. As can be seen, the fits match the experimental data for $\tau < 0.1$ s quite well. The top and middle trace show slight deviations for $\tau > 1$ s. However, within the bottom curve, the deviations already start at $\tau < 0.1$ s and lead to a larger miss-match of the fit for $\tau > 1$ s. The data from these fits are collected in Table 6.1 together with mean values for a set of 8 traces obtained from this sample. Two traces displaying intervals of high fluorescence intensity similar to that one shown in Fig. 6.15 (bottom) were excluded from the average. For comparison, diffusion coefficients from similarly fitted FCS curves, obtained by Grabowski et al. on approximately 15 nm thick TEHOS films doped with Alexa 488 on quartz cover slips, are shown [Grab07].

Table 6.1: Fitting parameters to normalized autocorrelation curves from the sample containing 10^{-7} mol/l R6G using eqn. 3.39 for two lateral diffusion components and eqn. 3.36 with $w_{xy} = 0.35$ μm for $D_{1,2}$. For comparison data from Alexa 488 in a TEHOS film ($d \approx 15$ nm) on quartz cover slips by Grabowski et al. [Grab07] are shown.

data set	A_1	τ_{D1} [ms]	D_1 [μm^2/s]	A_2	τ_{D2} [s]	D_2 [μm^2/s]
top[3]	0.57	0.18	0.17 ± 0.04	0.43	2.1	14 ± 5
middle[3]	0.55	0.48	0.06 ± 0.03	0.45	4.7	6.5 ± 2.0
bottom[4]	0.63	1.49	0.02 ± 0.01	0.37	14.4	2.1 ± 0.7
mean[5]	0.54 ± 0.06	0.35 ± 0.15	0.10 ± 0.05	0.46 ± 0.06	5.5 ± 3.1	6.7 ± 3.5
[Grab07]			0.2			13

It is interesting to note that the fast (lateral) diffusion component $D_2 = 4.5 \pm 0.5$ μm^2, obtained from analysis of diffusivities reported in the previous section, is within standard deviation of the mean value $D_2 = 6.7 \pm 3.5$ μm^2 gained from averaging over 8 traces. In contrast, the value obtained for D_1 is one order of magnitude smaller than the one obtained from SMT. In fact, it is of similar range as the threshold value D_0 for immobile molecules related to the position accuracy. The amplitudes A_2 for the fast component is much higher with FCS than with the analysis of diffusivities, which can be explained by the better sensitivity of FCS to faster diffusion.

As can be seen, both D_1 and D_2, vary by one order of magnitude. Two fluorescence time traces out of ten displayed intervals of increased fluorescence intensity similar to

---

[3]trace shown in Fig. 6.15 (top) resp. (middle)

[4]trace shown in Fig. 6.15 (bottom) including interval of high fluorescence intensity. The fit deviates considerably from the autocorrelation curve for $\tau > 0.1$ s.

[5]mean and standard deviations from 8 traces; two traces showing intervals of high fluorescence intensity were excluded from statistics, because of the minor quality of the corresponding fits.

that shown in Fig. 6.15 (bottom). Those two data sets were therefore excluded from averaging. Nevertheless, the standard deviations for both components still remained 50% of the mean values for the remaining 8 data sets, see Table 6.1. The obtained diffusion coefficients are slightly smaller than those obtained by Grabowski et al. Yet, these authors had used a FCS setup for two-photon excitation, which also implies the use of modified correlation functions [Berl95]. Furthermore, they had studied approximately 15 nm thick films instead of the about 10 nm thick ones investigated in this work. And they report that Alexa 488 did not adsorb to the substrate. The diffusion coefficients obtained from fits to the top curve in Fig. 3.39 (b) yield almost similar values as those obtained by Grabowski et al. Since the pronounced adsorption events displayed in the bottom curve result in considerably slower values for D_1 and D_2, it is reasonable that the absence of (major) adsorption events leads to higher diffusion coefficients. Thus the smaller average values obtained from fits to the correlation curves from samples containing R6G can be explained by an effect of adsorption events on diffusion coefficients derived from fitting with the two component function, $G_{D,\mathrm{bi}}$ (eqn. 3.39). Pronounced adsorption events as shown in Fig. 6.15 (bottom) may be excluded from analysis, but shorter and less significant ones will also contribute to the autocorrelation curves. By using a correlation function for translational diffusion (eqn. 3.37 to 3.39) for the fits, thus only effective diffusion coefficients will be obtained.

The ten traces achieved from the sample containing 10^{-7} mol/l R6G were obtained at four different positions on the sample. As mentioned above, two traces displayed pronounced adsorption events by intervals of high fluorescence leading to unreasonable fits. However, they were not taken at the same position on the sample, while other traces at the same positions as those two did not show similar adsorption events. Yet, the focal area has a radius $w_{xy} = 0.35 \pm 0.05\,\mu$m and the dye molecules were highly diluted ($\approx 10^{-7}$ mol/l). Thus, within different traces, taken even at the same position, the dyes will probe different local regions on the sample. Longer total observation times for each trace will eventually lead to averaging over all spatially heterogeneous regions within the focal area. However, suitable correlation functions for fitting the autocorrelation curves from such traces will be needed, since the two component correlation function used here cannot reproduce the adsorption events. Possible other correlation functions for G_{slow} will be discussed below. Afterwards, the discussion is extended to fitting functions for G_{fast} as well.

Fits to G_{slow} using the correlation functions G_D for a single component of translational diffusion and $G_{D,\mathrm{anomal}}$ for anomalous translational diffusion

Above fits to G_{slow} using the two component function $G_{D,\mathrm{bi}}$ for translational diffusion according to eqn. 3.39 were shown. Grabowski et al. had also used a single component function for simplification, although it deviated considerably from their autocorrelation curves. It is also possible to fit the slow parts of the here obtained autocorrelation curves with the function G_D for single component translational diffusion, as can be seen in Fig. 6.16 (dotted line). There the autocorrelation curves shown in Fig. 6.14 (a,b) were plotted with fits to G_{slow} using correlation functions for translational diffusion G_D (dot-
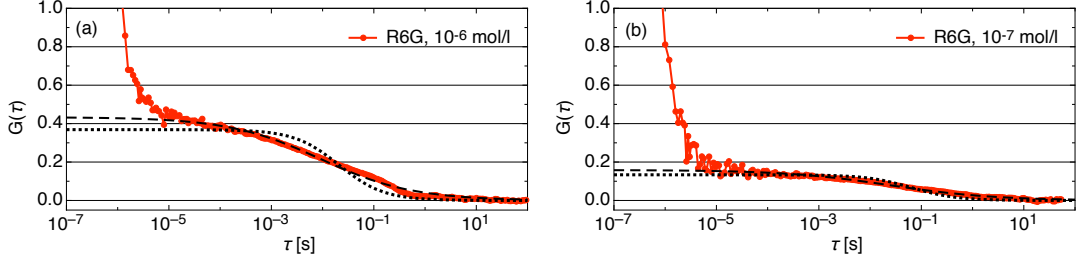
Figure 6.16: The same autocorrelation curves as shown in Fig. 6.14 (a,b) with fits to the slow part: ($\cdots$) fits according to eqn. 3.37 (G_D) for translational diffusion, (- -) fits using the correlation function $G_{D,\mathrm{anomal}}$ for anomalous translational diffusion (eqn. 3.38).

ted lines) and for anomalous translational diffusion $G_{D,\mathrm{anomal}}$ (dashed lines) according to eqn. 3.37 and 3.38, respectively. For the sample containing 10^{-6} mol/l R6G the fit using G_D deviates considerably from the experimentally obtained data. Yet, by using $G_{D,\mathrm{anomal}}$ for anomalous diffusion, the fit could be improved, see Fig. 6.16 dashed lines. The deviation of the fit using G_D is less pronounced in case of the sample containing 10^{-7} mol/l R6G, however, also there the fit was improved by use of $G_{D,\mathrm{anomal}}$. Table 6.2 gives the parameters obtained from fits to G_{slow} using the single component function G_D (according to eqn. 3.37) for the same autocorrelation curves for which Table 6.1 gives the parameters form fits with $G_{D,\mathrm{bi}}$ for two components of lateral diffusion.

Table 6.2: Fitting parameters to G_{slow} from the sample containing 10^{-7} mol/l R6G using the fitting function G_D for a single lateral diffusion component (eqn. 3.37) and eqn. 3.36 with $w_{xy} = 0.35\ \mu$m to obtain D. For comparison the diffusion coefficient obtained from Alexa 488 in a TEHOS film ($d \approx 15$ nm) on quartz cover slips by Grabowski et al. [Grab07] is shown.

data set	τ_D [ms]	$D\ [\mu\mathrm{m}^2/\mathrm{s}]$
top[6]	40	0.8 ± 0.3
middle[6]	84	0.4 ± 0.2
bottom[7]	402	0.08 ± 0.03
mean[8]	55 ± 17	0.6 ± 0.4
[Grab07]		10

Similarly to the fits using $G_{D,\mathrm{bi}}$, also with the single component fitting function G_D the lowest values are obtained for the curve corresponding to a fluorescence intensity trace which contains an interval of high fluorescence intensity. The diffusion coefficient of 10 μm^2/s reported by Grabowski et al. is considerably higher than the here obtained

---

[6] trace shown in Fig. 6.15 (top) resp. (middle)

[7] trace shown in Fig. 6.15 (bottom) including interval of high fluorescence intensity. The fit deviates considerably from the autocorrelation curve for $\tau > 0.1$ s.

[8] mean and standard deviations from 8 traces; two traces showing intervals of high fluorescence intensity were excluded from statistics, because of the minor quality of the corresponding fits.

values. As mentioned above, Grabowski et al. report that Alexa 488 did not adsorb to the substrate [Grab07]. Thus, the much lower diffusion coefficients achieved here are very likely caused by adsorption events. Nevertheless, these diffusion coefficients are comparable to those obtained from SMT experiments using frame rates of 0.1 Hz, see section 6.3.

As was mentioned above, the fits to the autocorrelation curves using the single component function G_D deviate considerably from the curves. The fits are improved by using the fitting function $G_{D,\mathrm{bi}}$ for two components of translational diffusion instead of the single component function G_D. Yet, an improvement of the fits is also achieved by the use of the fitting function $G_{D,\mathrm{anomal}}$ for anomalous translational diffusion according to eqn. 3.38, as can be seen in Fig. 3.38 (dashed lines). In the following FCS curves from the four investigated samples will be compared using $G_{D,\mathrm{anomal}}$ for fitting the autocorrelation curves. The data from these fits are shown in Table 6.3.

Table 6.3: Mean values and standard deviations for fitting parameters to autocorrelation curves obtained from different samples using eqn. 3.38 for anomalous diffusion for G_{slow}:

dye	#	c [mol/l]	A_{slow}	τ_{anomal} [s]	α
R6G	4	$\approx 10^{-6}$	0.37 ± 0.05	6.6 ± 2.3	0.52 ± 0.03
R6G	8	$\approx 10^{-7}$	0.17 ± 0.04	27 ± 8	0.48 ± 0.05
R6G[9]	1	$\approx 10^{-7}$	0.25	238	0.54
R6G	4	$\approx 10^{-8}$	0.06 ± 0.02	68 ± 22	0.42 ± 0.07
OG	5	$\approx 10^{-7}$	0.15 ± 0.04	23 ± 17	0.50 ± 0.06

For R6G at $c = 10^{-8}$ mol/l four fluorescence traces were analyzed. In that case the amplitude of G_{slow} is very low yielding a high fitting uncertainty. For R6G and OG at higher concentrations larger A_{slow} where obtained, while $\alpha \approx 0.5$. This might hint to a concentration dependence of the heterogeneity, but since the α for R6G at $c = 10^{-7}$ and $c = 10^{-6}$ is similar within standard deviation, the low values for α in case of $c = 10^{-8}$, are more likely caused by a larger fitting uncertainty due to the low amplitude. Nevertheless, a comparison of τ_{anomal} obtained for R6G at three different concentrations clearly shows an increase with decrease in concentration. This matches the expectation of a lower fraction of diffusing molecules in case of lower concentration, and thus fewer contributions from diffusion (which contributes at shorter τ). A comparison of the values obtained for OG with those for R6G at similar concentration shows no difference within fitting accuracy. R6G and OG are oppositely charged xanthene derivatives, see section 4.2.1. Thus the near surface diffusion of the dyes seems not to be influenced by the charge of the dye.

In Table 6.3 also the values obtained from a fit to a time trace containing an interval of high fluorescence, (see Fig. 6.15 bottom) are shown. The obtained value for α is only slightly larger than the α obtained from the other time traces. But τ_{anomal} is 238 s and

---

[9]trace shown in Fig. 6.15 (bottom) including interval of high fluorescence.

therefore one order of magnitude larger. As can be seen in Fig. 6.15, the respective interval of increased fluorescence lasts for 10 s only. Interpretation of τ_{anomal} requires deeper insight into the physical processes causing the anomaly [Hac05]. Within the thin TEHOS films investigated here, transients of the focal area as well as adsorption events will contribute to the autocorrelation curve. $G_{D,\text{anomal}}$ is related to translational diffusion. Hence, it will not yield characteristic times for sorption kinetics. Instead the contributions from transients of the focal area will be mixed with the characteristic times for adsorption events to yield τ_{anomal}. Therefore, the simple relation (eqn. 3.36) between τ_D and D cannot be used here to give effective lateral diffusion coefficients. Although the higher contribution from lateral diffusion with increased dye concentration is qualitatively reproduced by $G_{D,\text{anomal}}$, it cannot provide reliable diffusion coefficients nor characteristic times for adsorption events.

The three above applied correlation functions G_D, $G_{D,\text{bi}}$ and $G_{D,\text{anomal}}$ are relied to translational diffusion only. Yet, the slow parts of the FCS curves from the here investigated thin TEHOS films are influenced by transients of the focal area as well as by adsorption events. Hence, different correlation functions are needed, which also can reproduce sorption kinetics. Thompson and Axelrod used an exponential function (see eqn. 3.47) to approximate the sorption kinetics within FCS curves obtained from their TIR setup [Thom83]. This was explained in section 3.4.4. Due to the large area of illumination within their setup in combination with TIR illumination they can neglect contributions from transients of the focal area by diffusing dye molecules. This does not hold true with the here used setup. However, reaction kinetics will nevertheless contribute to the autocorrelation function by some modified exponential function. For this reason, fits to G_{slow} by an exponential function and by a stretched exponential function will be discussed below.

Fits to G_{slow} using exponential functions

As was detailed above, exponential functions may be used to approximate ad-/desorption rates. In case the adsorption events are not caused by a single rate (i.e. the distribution of adsorption events cannot be described by a single exponential function), a stretched exponential function will be more suitable to fit the FCS autocorrelation curve. Thus, the following function may be used for fitting the slow part of the curve:

$$G_{\text{slow}}(\tau) = A_{\text{slow}} \exp(-(\tau/\tau_R)^\alpha), \text{ with } 0 < \alpha < 1 \text{ and } \tau_R = 1/R_R. \qquad (6.8)$$

Instead of fitting G_{slow} separately, this time both parts of the curves were fitted simultaneously, however, the discussion of the fits to G_{fast} will be postponed to the next paragraph. In Fig. 6.14 (see section 6.4.1) fits to the full autocorrelation curves using exponential functions for G_{fast} and for G_{slow} (dotted lines) were shown, as well as fits using a stretched exponential function for G_{slow} (dashed lines) instead of the exponential function, according to eqn. 6.8. For the sample containing 10^{-8} mol/l R6G the amplitude of G_{slow} is very low, rendering fits less reliable. For the other three samples the fits using an exponential function for G_{slow} according to eqn. 3.47 (dotted lines) deviate

considerably from the autocorrelation curves. Nevertheless, the fits can be improved by using a stretched exponential function for G_{slow}, thus using eqn. 6.11 to fit the full autocorrelation curves. Parameters from the latter fits are given in Table 6.4, see next paragraph.

The values for the characteristic time τ_R vary largely over four orders of magnitude for seven FCS traces investigated from the sample containing 10^{-7} mol/l R6G. For three other data sets, unreasonably small values were obtained. For the other two samples only four data sets each were investigated, which explains the smaller variation of τ_R over one and two orders of magnitude only. For the sample containing OG, a fifth data set also rendered unreasonably small τ_R. In Fig. 6.15 three FCS traces from the sample containing 10^{-7} mol/l R6G were shown together with the corresponding autocorrelation curves. As was explained above, they differ very much in respect to recorded adsorption events. This is reflected by the wide range of τ_R. Thereby, the trace shown in Fig. 6.15 (bottom), containing an interval of about 10 s of high fluorescence intensity, renders τ_R of about 0.3 s. In contrast, the top curve in the same figure could not be fitted reasonably by eqn. 6.8. Fits to this curve using $G_{D,\text{bi}}$ had rendered the largest diffusion coefficients, which according to previous considerations can be related to the absence of pronounced adsorption events. Thus, fits using eqn. 6.8 render reasonable values for mean adsorption times, in case of the existence of pronounced adsorption events. The part of G_{slow} caused by transients of diffusing dye molecules cannot be reproduced by eqn. 6.8. Instead, it will shift τ_R to smaller values and increase the stretching exponent α. The latter therefore is unreasonably small, between 0.10 and 0.27, as can be seen in Table 6.4.

From the above considerations it can be concluded that G_{slow} will be best approximated by a fitting function containing two components: G_D for transients of diffusing dyes and a stretched exponential function for the adsorption events. This will be further discussed later on. Before a fitting function for approximation of the full autocorrelation curves can be given, fits to G_{fast} have to be discussed, which will be done in the following paragraph.

Fits to G_{fast}

The initial fast decaying part of the correlation function G_{fast} has not been studied yet. According to eqn. 6.7, G_{fast} can be expressed by

$$G_{\text{fast}}(\tau) = \frac{A_{FD}}{1 - A_{FD}} \exp(-\tau/\tau_{FD}) \, G_{\text{slow}}(\tau) \,, \tag{6.9}$$

with $G'(\tau) = G_{\text{slow}}(\tau)$. For $\tau < 10$ μs, $G_{\text{slow}}(\tau)$ is almost constant (see for example the fits using G_D and $G_{D,\text{anomal}}$ in Fig. 6.16). Thus it can be approximated by a constant A_{slow}, which leads to

$$G_{\text{fast}}(\tau) = A_1 \exp(-\tau/\tau_{FD}) \,, \qquad \text{with} \qquad A_1 = \frac{A_{FD} A_{\text{slow}}}{1 - A_{FD}} \,. \tag{6.10}$$

Together with the use of a stretched exponential function for G_{slow} (as discussed above) this renders:

$$G(\tau) = A_1 \exp(-\tau/\tau_{FD}) + A_{\text{slow}} \exp(-(\tau/\tau_R)^\alpha), \qquad \text{with } 0 < \alpha < 1. \qquad (6.11)$$

The fits using this eqn. were shown in Fig. 6.14 dashed line. The data from the fits are shown in Table 6.4. For each sample 4 to 7 traces were analyzed. The fits match the initial fast decaying part G_{fast} of the autocorrelation curves quite well. The τ_{FD} are about half a microsecond. As was already mentioned, this matches the vertical mfpt of diffusing dye molecules within the ultrathin TEHOS films.

Table 6.4: Parameters with standard deviations from fits to full autocorrelation curves using the two component function eqn. 6.11, which contains an exponent for G_{fast} and a stretched exponent for G_{slow}. The values for τ_R vary strongly for the data sets from the same sample, hence their range is given.

dye	#	c [mol/l]	A_1	τ_{FD} [μs]	A_{slow}	range of τ_R [s]	α
R6G	4	$\approx 10^{-6}$	6.6 ± 0.9	0.48 ± 0.02	0.4 ± 0.2	$10^{-3} ... 0.7$	0.24 ± 0.03
R6G	7	$\approx 10^{-7}$	3.7 ± 0.6	0.63 ± 0.08	0.4 ± 0.1	$10^{-5} ... 0.3$	0.14 ± 0.06
OG	4	$\approx 10^{-7}$	3.0 ± 0.4	0.57 ± 0.03	0.3 ± 0.1	$10^{-3} ... 0.04$	0.17 ± 0.02

The fits to G_{slow} and G_{fast} discussed above can be combined to a tri-component fitting function for the full autocorrelation curves. This will be summarized and further discussed in the following paragraph.

Tri-component fitting function for FCS autocorrelation curves

The above considerations about fitting the autocorrelation curves obtained from single dye diffusion in ultrathin TEHOS films on 100 nm thermally grown SiO$_x$ point to three different processes, which contribute to the autocorrelation:

vertical mfpt with correlation times $\tau_{FD} < 1$ μs. The vertical passage of the dye molecules is enclosed either by short physisorption, or by longer chemisorption events (mainly via H-bonding to surface silanols). When the dye molecule gets in contact to the solid/liquid interface, its rotation is hindered. This will cause a change in fluorescence intensity unless the orientation of the dye molecule towards the optical axis happens to result in the same detected fluorescence intensity as is the case for freely rotating dye molecules. Thus, in most cases, the fluorescence intensity will change at the approach to the interface, which leads to a contribution to the autocorrelation curve in the time regime corresponding to the vertical mfpt. The vertical passage times are distributed: Short passage times related to fast re-adsorption are highly probable, while long passage times are rare. Thereby the mfpt corresponds to the width of the distribution. Due to the small film thickness, most dye molecules will re-adsorb at a position close to the location of

desorption. Thus, no change in detection (and illumination) intensity during the passage can be assumed. For this reason, the vertical passage times contribute to the autocorrelation curve by an exponential function. The amplitude of this exponential function is related to the ratio A_{FD} of freely diffusing molecules. This interpretation of the fast correlation observed in the time range below 1 μs is further evidenced by the influence of the film thickness on this correlation time, which will be reported from FCS experiments on micro-structured substrates in the next chapter, see section 7.1.3.

lateral diffusion – transients of the focal volume. Due to the strong vertical confinement in a liquid film of only few molecular diameters height, the observed lateral diffusion is an effective diffusion influenced by periods of free diffusion, of near-surface diffusion (via gliding on silanol clusters as suggested by Honciuc et al. [Honc08]), and of adsorption. The broad distribution of adsorption events thus also influences the observed lateral diffusion coefficients. For this reason, longer adsorption events lead to slower effective diffusion coefficients, as can be seen from Fig. 6.15 and Table 6.1. Grabowski et al. claim to have seen no adsorption events within their thin TEHOS films on quartz cover slips using Alexa 488 [Grab07]. However, within FCS setups using oil immersion objectives, adsorption events at the substrate typically are recognized by an increased fluorescence signal from the interface region. Yet, to discern an increased fluorescence at the solid-liquid interface, desorption rates have to be slow enough. For very short adsorption events, the minimal increase in fluorescence may not be discriminated from contributions from noise. Thus, the autocorrelation curves invetigated by Grabowski et al. most probably also contain a contribution from very short adsorption events. In the picture of continuum hydrodynamics these very short adsorption events are related to the zero velocity of particles at a solid-liquid interface with no-slip boundary condition. The effective lateral diffusion is related to transients of the focal area. Thus the correlation function G_D for translational diffusion (eqn. 3.37) is implemented into the fitting function to obtain effective lateral diffusion coefficients. Thereby the amplitude of the lateral diffusion is A_D and the related characteristic time is τ_D.

adsorption events. In some cases, intervals of increased fluorescence were visible in the fluorescence time traces. Then the slow part of the autocorrelation curves is shifted to even longer times for τ_R. Thus ad-/desorption kinetics clearly play a role. These intervals of adsorption in the range of some ms to some s are most probably caused by chemisorption of the dye molecules to surface silanols on the substrate. Since thermally grown SiO_x is amorphous and due to the surface treatment contains differently arranged silanol groups on its surface, the dye molecules find a broad variation of adsorption sites. Hence, a broad distribution of interaction energies is expected, leading to a broad distribution of attachment times. Furthermore, the orientation of the molecule at the interface in respect to the direction of excitation/detection also varies. Thus the amplitude of the fluorescence signal depends

on the specific geometry of the binding site, leading to a variation of the amplitude of the corresponding component in the autocorrelation. This also broadens the distribution of correlation times caused by ad-/desorption events. Besides the chemisorption events, the dye molecules also will be slowed to zero at the substrate either by some kind of physisorption (e.g. electrostatic interactions) or simply due to the hydrodynamic interaction with the substrate, which, under the assumption of a no-slip boundary condition, causes a zero velocity at the substrate. The latter will happen, whenever the dye molecule approaches the substrate. Due to the broad distribution of adsorption events, the contribution to the correlation function is approximated by a stretched exponential with stretching exponent α.

Whether gliding of the dye molecules on surface silanols takes place or not, cannot be discerned by the SMT and FCS experiments reported here. In case there is a contribution of near-surface diffusion by this "silanol gliding", this will also contribute to the effective lateral diffusion coefficient. The single steps from one hydrogen bond to the next, however, will appear as single adsorption events, since in general the orientation of the dye molecule (and thus of the optical transition dipole) will change from one step to the next.

The above detailed contributions to the autocorrelation function are summed up in the following tri-component correlation function:

$$G_{\text{tri}}(\tau) = \left[A_B + \frac{A_{FD}}{1 - A_{FD}} \exp\left(\frac{-\tau}{\tau_{FD}} \right) \right] \left\{ \frac{A_D}{1 + \tau/\tau_D} + (1 - A_D) \exp\left[-\left(\frac{\tau}{\tau_R} \right)^\alpha \right] \right\}.$$
(6.12)

Thereby the correlation time τ_{FD} corresponds to the mfpt, the correlation time τ_D is related to the effective lateral diffusion coefficient D_{eff}, and τ_R is related to ad-/desorption kinetics, and for the ratio of adsorbed molecules A_R the following expression holds: $A_R = A_B(1 - A_D)$. The term in the curly brackets represents G_{slow}, which is the sum of the components related to translational diffusion and to sorption kinetics. Yet, as was detailed above, due to the broad distribution of adsorption events, no rate can be derived from the corresponding part of the correlation function. In Fig. 6.17 a tri-component approximation using eqn. 6.12 to the autocorrelation curve shown in Fig. 6.14 (b) is presented. The used parameters are given in Table 6.5. For comparison also a correlation function for lateral diffusion of a rhodamine dye in bulk TEHOS ($D = 55 \ \mu\text{m}^2/\text{s}$) is plotted as well. However, with this tri-component correlation function no stable parameter sets can be found from fitting unless further restrictions are made. This can be understood from the many approximations within this tri-component function. For example, the adsorption events are not really described by an exponential decay, since the here used setup deviates from that used by Thompson and Axelrod [Thom83]. Furthermore, even for their setup, the exponential decay given in eqn. 3.47 is only an approximation. Nevertheless, for $A = A_{FD}/(1 - A_{FD})$ and for τ_{FD} realistic values are obtained from fits using this tri-component function. These values are therefore given in Table 6.5 together with error bars. The other parameters had to be restricted to realistic values.

Experiments using crystalline substrates with restricted bonding geometry for dye adsorption might contribute to further understanding of the effect of adsorption events
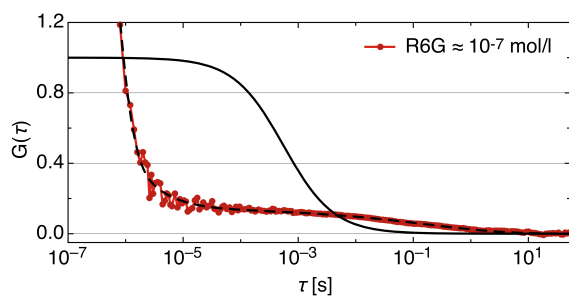
Figure 6.17: FCS autocorrelation curve from 10 nm thick TEHOS film with approximately 10^{-7} mol/l R6G, (- -) tri-component fit using eqn. 6.12, (—) bulk diffusion with $D = 55$ mol/l.

Table 6.5: Parameters used for the approximation of the autocorrelation curve shown in Fig. 6.17 by the tri-component function eqn. 6.12:

A_B	A	τ_{FD} [μs]	A_D	τ_D [ms]	D_{eff} μm^2/s	τ_R [s]	α
0.2	5 ± 3	0.6 ± 0.4	0.5	1.3	24	0.4	0.4

on the FCS autocorrelation curves.

6.4.3 Conclusion

The fast exponential decay of the autocorrelation curves in the range of 0.1 to 1 μs matches the vertical mfpt of the dyes assuming bulk-like diffusion. This hints to the existence of very short periods, where the dye explores the upper regions of the thin film. However, by the here obtained results alone it is not possible to discriminate between possible vertical modulations of the diffusion coefficient according to continuum hydrodynamic models. For the vertical mfpt to appear in the autocorrelation curves, it is sufficient that the free rotation of diffusing molecules is considerably altered, when the dye molecule approaches the solid-liquid interface. Because then a fluctuation of the fluorescence intensity will occur on the timescale related to the vertical mfpt. The relation of the fast decaying part of the autocorrelation curves from the here reported FCS experiments to vertical mfpt is further supported by results from experiments on micro-structured substrates, as will be shown in the following chapter.

Irrespectively to the used fitting function, the slow component of the autocorrelation curve clearly shows a strong heterogeneity. This part cannot be described by simply two characteristic times. Rather there are two broad distributions of characteristic times as can be seen form the distributions of τ_1 and τ_2 in Table 6.1. This strong heterogeneity is caused by a broad distribution of adsorption events due to substrate heterogeneity. Thereby, the characteristic time τ_R related to sorption kinetics is affected. Furthermore, as long as ad-/desorption events to the substrate occur, this also has an effect on transient times, and hence leads to a broadening of the distribution of correlation times related to

lateral diffusion. Due to the small film thickness of only 10 nm, diffusing molecules are forced to approach the solid-liquid interface quite often. Depending on the local surface chemistry, they will either be chemisorbed (mainly via H-bonding to silanol clusters), or they will restart diffusing into the upper regions of the film. Thus transient molecules in the detection volume will show an effective translational diffusion coefficient D_{eff}, which is composed from short intervals of bulk-like diffusion, intervals of adsorption, and possibly also intervals of slowed diffusion in the near-surface region (e.g. by gliding on surface silanol clusters via successive H-bonding). One has to know either the adsorption rate and the diffusion coefficients ascribed to each region and/or the dwell times to deconvolute the contributions of the single components of motion. So far no method has been developed which could solve this on a molecular scale. Though the SMT experiments described in the previous section yield a lower limit for the diffusion in the upper region of the ultrathin film. Also effective diffusion coefficients obtained form fits to FCS autocorrelation curves yield such lower limits for the fast component of diffusion in the upper region of the film (and outside of silanol clusters).

Although in literature equations containing ad-/desorption kinetics as well as diffusion transients can be found, they are far too complicated to be used for fitting without further knowledge of e.g. ad-/desorption rates. Yet, they might only be used with narrow distributions of surface binding energies and cannot be applied to the amorphous and partly hydroxylated substrates used here. Here a tri-component function (eqn. 6.12) is used to approximate the different contributions from vertical mfpt, from lateral diffusion and from adsorption to the autocorrelation curves. Thereby the broad distribution of adsorption events is taken into account by the use of a stretched exponential function. Fits using this function render characteristic times τ_{FD} for the vertical mfpt in the range of few tens of microseconds. Also realistic values for effective lateral diffusion and for the distribution of adsorption events can be achieved.

7 Effect of surface induced spatial heterogeneities on SM dynamics

Spatial heterogeneities of solid substrate surfaces play an important role on structure formation within thin liquid crystal films [Laca04, Jin05, Guo08]. Observations from FCS experiments on ultrathin TEHOS films, reported in the previous chapter, revealed a strong influence of sample heterogeneity on diffusion dynamics. Thereby the sample heterogeneity most probably is caused by an inhomogeneous distribution of adsorption sides at the solid-liquid interface. Here in this chapter, the influence of substrate surface structure on dynamics in ultrathin liquid films will be studied more thoroughly. Furthermore, it will be demonstrated that maps of diffusivities are a suitable tool to reveal structure induced dynamics within thin liquid crystal films. Moreover, also in respect to diffusion anisotropy and LC domain dynamics, probability distributions of diffusivities are superior to msd analysis in revealing fast diffusion components from SMT tracking experiments, as will be shown at the end of this chapter.

7.1 Spatial heterogeneities in ultrathin TEHOS films on SiO_x

Schuster already reported on the observation of heterogeneous diffusion along SM trajectories within ultrathin TEHOS films on quartz cover slips [Schu02b]. There the SMT experiments had been conducted with frame rates of 40 fps. The heterogeneities were visible using spot size analysis [Schu02a] along the trajectories, see section 3.3.8, a method which enables to compare changes along a trajectory between succeeding frames, similar to the distributions of diffusivities developed within this work. From the spotsizes along a trajectory, two segments with slower and faster diffusion were discriminated. Then for those trajectory segments D_{traj} were calculated separately, yielding 0.6 ± 0.1 $\mu\text{m}^2/\text{s}$ and 1 ± 0.2 $\mu\text{m}^2/\text{s}$, respectively. In contrary, the heterogeneities disappeared, when moving averages over 5 succeeding spotsizes were used for calculation of diffusion coefficients. Since the effective segment length (see 3.3.5) for the calculation of D_{traj} is 2.6, Schuster concluded that the heterogeneities have to occur on a timescale between 2.6 and 5 times the frame time, i.e. 65 ms and 125 ms [Schu02b], respectively. Furthermore, from comparison with the corresponding video sequences, he could assign the heterogeneous diffusion to distinct lateral regions on the sample. Similar investigations were reported by Schuster et al. [Schu03], but there it was emphasized that there were no spatial correlations for the heterogeneous diffusion. However, it was not explained how spatial correlations were investigated in that case. Moreover, the adsorption sites within the investigated ultrathin TEHOS films are power-law distributed [Schu03] (see also sec-

tion 7.1.2), leading to anomalous diffusion in the corresponding time regime. Thus, small spatial differences may not be accessible for correlation analysis but disappear within the experimental error due to a combination of position accuracy and temporal resolution. However, to study effects on SM dynamics, the distribution of silanol groups and thus of adsorption sites on the substrate may be manipulated on a larger scale by changing the surface treatment of the substrates before sample preparation (see section 4.2.2).

Thus, in the following part there will be first a report on the observation of discernible effective diffusion coefficients obtained along trajectories for several distinct lateral regions on a sample investigated by SMT experiments. Then the effect of varying substrate treatment on diffusion will be investigated.

7.1.1 Spatial heterogeneities observed from trajectory analysis
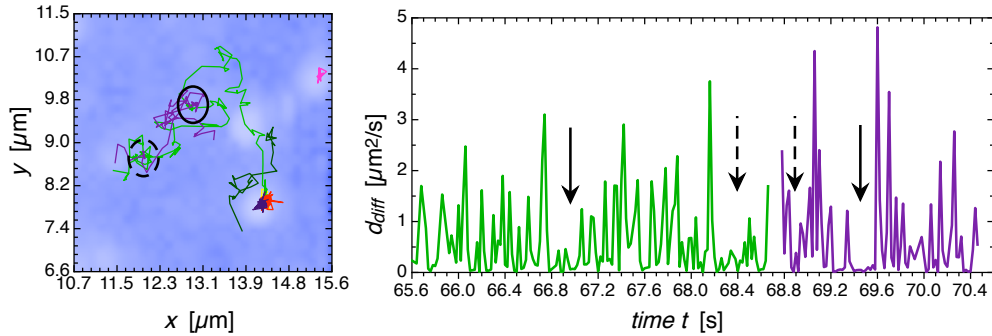
Figure 7.1: (left) Spatial plot of several immobile and three mobile trajectories on integrated intensity plot (white corresponds to bright) obtained from a 10 nm thick TEHOS film on SiO_x doped with RhB; (right) diffusivities d_{diff} over total time t for light green and purple trajectory from left image. The center of the solid and dashed circles in the left image mark locations with repeated periods of immobilization; the corresponding sets of periods are marked by solid and dashed arrows in the right image.

Fig. 7.1 (left) shows integrated intensities (white corresponds to bright) from a region of 30 pixel x 30 pixel (1 pixel $\simeq$ 0.164 μm) over the total video length of 5 000 frames. The video was acquired at a frame time of 20 ms from a 10 nm thick TEHOS film doped with RhB. Detected trajectories (by *tracking.sh*) from that region are plotted onto the plot of integrated intensities. Several immobile trajectories can be seen as bright spots, which are generated by the fluorescence from molecules immobilized at that position over a certain time length during acquisition. Trajectory ends are either caused by blinking or bleaching of the immobile molecule. At the position $x = 14.3$ μm, $y = 7.9$ μm a temporarily immobilized molecule eventually starts to move (light green trajectory starting from the bright spot marked by blue, yellow and red immobile trajectory). The light green and the purple trajectory stem from the same dye molecule, as can be seen from a comparison of the spatial plot in Fig. 7.1 (left) with Fig. 7.1 (right) showing the corresponding diffusivities d_{diff} over total time t. The solid arrows in the right image

mark short periods of immobilization at the same position on the sample ($x = 13.0$ μm, $y = 9.7$ μm, center of solid circle in the left image). There the dye was immobilized within an area of about 0.06 μm^2 (which corresponds to the position accuracy) for the time interval between $t = 66.78$ s and $t = 67.02$ s (light green) and again from $t = 69.22$ s to $t = 69.58$ s (purple, interrupted by a short escape at $t = 69.34$ s). Two other shorter periods of slow motion in a different location ($x = 12.0$ μm, $y = 8.7$ μm, center of dashed circle) occurred from $t = 68.38$ s to $t = 68.64$ s (light green) and from $t = 68.84$ s to $t = 68.92$ s (purple), marked by dashed arrows in Fig. 7.1 (right). The repeated occurrence of slower motion at the same positions on the sample is a strong indication for sample heterogeneities causing diffusion heterogeneities. Thereby the slow motion most probably is caused by a higher adsorption probability within the corresponding region on the sample.

The corresponding msd plots for the light green and for the purple trajectory were shown in Fig. 3.3 (b) in section 3.3.3. For both trajectories the diffusion coefficient obtained via weighted msd D_{traj} is approximately 0.6 μm^2/s (see section 3.3.5). For the dark green trajectory observed in the same region on the sample (see Fig. 7.1 left), also $D_{\text{traj}} \approx 0.6$ μm^2/s was derived. In contrast, for five trajectories within a different region on the sample (not shown here) diffusion coefficients $D_{\text{traj}} \approx 0.3$ μm^2/s were obtained. This points to an influence of substrate heterogeneity on different scales: Within the position accuracy of about 0.06 μm^2 (as above reported from immobilization along trajectories), as well as on larger scales of about 20 μm^2 for total trajectories. To gain more information on the influence of substrate heterogeneities on diffusion dynamics, experiments on samples with different treatment of the substrates will be reported in the following. Furthermore, laser-induced dehydroxylation was used to generate microstructured substrates for additional investigation.

7.1.2 Hydroxylated and dehydroxylated substrates

Here, SMT experiments on samples with different substrate pre-treatment will be reported. First adsorption events along single molecule trajectories will be investigated. As was already mentioned, a power-law distribution of adsorption events from SM trajectories in ultrathin TEHOS films on quartz substrates has been reported in the preliminary work of Schuster et al. [Schu03]. These adsorption events are thought to occur to surface silanols at the substrate [Iler79]. Therefore, an effect of substrate hydropathy on the distribution of adsorption events is expected. This will be investigated in the following.

Adsorption events along single molecule trajectories

Single molecule trajectories from SMT experiments on thin TEHOS films with two different types of substrate pre-treatment were analyzed for the length of adsorption events. A dye molecule was considered to be adsorbed, as long as the corresponding square displacement between successive positions was below a threshold related to the average position accuracy of the acquisition. Thereby, adsorption events at the beginning
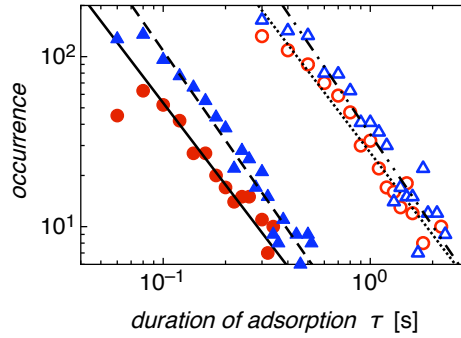
Figure 7.2: Log-log-plot of distributions of durations of adsorption events from SMT tracking on a TEHOS film with RhB on a (●, ○) piranha treated substrate and (▲, △) substrate tempered for 0.5 h at 800°C, observed with (●, ▲) 20 ms and (○, △) 100 ms frame time; lines denote power-law fits.

and at the end of a SM trajectory were excluded from the distributions, because their duration cannot be determined. One substrate was treated by the usual cleaning procedure as described in section 4.2.3, it will be termed "piranha treated," while the other substrate additionally was tempered at 800°C for 0.5 h at ambient atmosphere and will be termed "tempered." SMT experiments were conducted at two different frame rates (50 fps and 10 fps) on both samples. As can be seen in the log-log-plot of the obtained distributions of adsorption events shown in Fig. 7.2, the distributions can be fitted by power-law functions. The power-law exponent derived for the piranha treated sample for both frame rates is -1.6 ± 0.1, while for the tempered sample in both experiments -1.8 ± 0.1 is obtained. The slightly larger absolute value of the power-law exponent in case of the tempered substrate points to a faster decay of the distributions. According to Iler, the dye molecules preferentially adsorb to the silica substrate at sites containing silanol groups [Iler79]. As was explained in section 4.2.2, tempering the substrate at 800°C reduces the amount of silanol groups, while in particular vincinal (grouped by OH-bonding) and geminal (i.e. paired) silanols are removed. Thus, on the tempered substrate the adsorption sites mainly are isolated silanol groups. In contrast, on the piranha treated substrate a certain amount of vincinal and geminal silanols is present. When a dye adsorbs to such kinds of silanols, there is a certain probability for fast re-adsorption within the position accuracy as well as for slow gliding on silanol cluster via successive H-bonding [Honc08]. Both cases will appear as prolonged adsorption events if the re-adsorption occurs within the exposure time or if the gliding is slow enough to occur below the limits for diffusion given by the combination of position accuracy and temporal resolution. Therefore, the slightly faster decay of the distribution of adsorption events in case of the tempered substrate is in accordance with expectations due to reduced interactions with the substrate in that case.

The shift between the distributions corresponding to the 50 fps and the 10 fps experiments is due to experimental conditions, i.e. small adsorption intervals are not accessible for the 10 fps measurements, while a higher number of longer intervals simply stems

from the longer total observation time in case of the 10 fps experiments. In contrast, the slight shift between the measurements conducted on the piranha treated substrate and the tempered substrate observed for both frame rates, can be explained by a slightly higher mobility in the latter case (due to fewer adsorption sites), since this leads to a larger number/increased average length of detected trajectories and therefore also to a higher number of adsorption events in general.

The results from the investigation of adsorption events along trajectories from samples with different degree of hydroxylation further evidence the previous observation of a strong influence of substrate heterogeneity on SM dynamics. However, the threshold for the detection of mobile molecules is about 0.08 $\mu m^2/s$ and about 0.01 $\mu m^2/s$ for SMT experiments with frame rates 50 fps and 10 fps, respectively (derived as slowest component D_0 from tri-exponentail fits to corresponding probability distributions of diffusivities, see section 6.3.2). For this reason, SMT experiments with frame rate 1 fps were accomplished on samples with different substrate pre-treatment to study slow diffusion.

SMT experiment with slow frame rate $f = 1$ fps
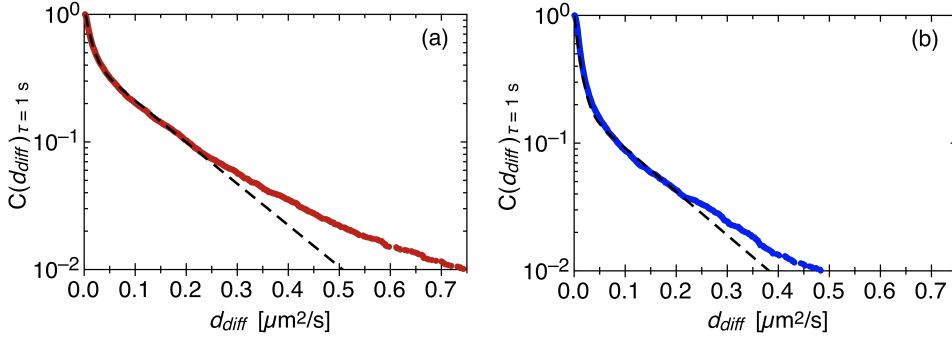
Figure 7.3: Probability distributions of diffusivities from SMT experiments with frame rate $f = 1$ fps on 5 ± 1 nm thick TEHOS films on a SiO_x substrate (a) tempered for 9 h at 800°C in air, and (b) boiled for 20 h in water; (- -) bi-exponential fits.[1]

To investigate the slow near-surface diffusion, SMT experiments with frame rate $f = 1$ fps were performed[1] on two samples with different substrate pre-treatment. Si wafer with 100 nm thick thermally grown SiO_x had been cleaned following the usual procedure. One substrate was tempered for 9 h at 800°C in air, while the other one was boiled for 20 h in water. Afterwards, on the substrates, 5 ± 1 nm thick TEHOS films doped with RhB were prepared as described in section 4.2.3. During tempering the SiO_x layer increased by 20 nm, which was determined by ellipsometry. AFM measurement of a tempered substrate yielded a smaller surface roughness than for a substrate only treated by the cleaning procedure in prianha, see section 4.2.2. However, the main difference

---

[1]Sample preparation and SMT experiments were carried out by Frank Gerlach. He obtained the threshold value for mobility at average snr to be 0.001 $\mu m^2/s$ from the analysis of immobile trajectories.

between the two substrate pre-treatments, is the distribution of surface silanols, see section 4.2.2. For a tempered substrate, a silanol coverage of 46.4% was detected via a R6G adsorption experiment, in respect to 53.5% coverage for a substrate boiled in water. The average silanol cluster size was determined to be 1.42 μm^2 and 1.97 μm^2 respectively [Schu10a]. Since fluorescent dyes preferentially adsorb to silanols [Iler79], the higher coverage and larger cluster size for the boiled substrate should lead to more adsorption events. Furthermore, silanol gliding of the dyes by H-bonding kinetics, as suggested by Honciuc et al. [Honc08], see section 4.2.2, is expected to be more pronounced on larger silanol clusters.

Fig. 7.3 shows probability distributions of diffusivities from SMT experiments with frame rate 1 fps conducted on the ultrathin TEHOS films prepared on the above described substrates. Diffusivities from immobile molecules were excluded from the probability distribution by the method described in section 3.3.1. The probability distributions were fitted bi-exponentially (dashed lines) according to eqn. 3.26. Results are given in Table 7.1.

Table 7.1: Fitting parameters from bi-exponential fits to probability distributions of diffusivities on samples with different substrate pre-treatment shown in Fig. 7.3.

substrate pre-treatment	a_1	D_1 [μm^2/s]	a_2	D_2 [μm^2/s]
tempered	0.61 ± 0.02	0.012 ± 0.002	0.39 ± 0.02	0.13 ± 0.02
boiled	0.80 ± 0.02	0.010 ± 0.002	0.20 ± 0.02	0.13 ± 0.02

As can be seen, for both samples similar diffusion coefficients were obtained within error bars. However, the amplitude a_1 for the slow component is smaller in case of the tempered substrate. Interestingly, the ratio a_1(tempered)$/a_1$(boiled) ≈ 0.75 matches the ratio $1.42/1.97 = 0.72$ of average silanol cluster size determined from the R6G coverage experiment (see section 4.2.2 and [Schu10a]) within experimental error. The slow diffusion coefficient $D_1 = 0.01$ μm^2/s can be ascribed to either gliding of the dyes on silanol clusters as suggested by Honciuc et al. [Honc08], or it is caused by fast re-adsorption events on silanol clusters, or by a combination of both. The obtained faster diffusion coefficient D_2 then contains contributions from lateral excursions into regions, where the dye molecule will diffuse with a higher effective diffusion coefficient, because it will not chemisorb to the substrate (i.e. on regions of the substrate surface consisting of siloxane bridges). Yet, the probability distributions $C(d_{\text{diff}})_{1s}$ deviate from the bi-exponential fits (dashed lines in Fig. 7.3) in favor of higher probabilities for larger d_{diff}. This is more pronounced for the tempered substrate. The distributions can be explained using Fig. 6.7 (right), which depicts the lateral heterogeneity of diffusion caused by the distribution of silanol clusters on the substrate: SM diffusion on and above silanol clusters will yield a slow component of diffusion. Whereby transits between such regions will render larger diffusion coefficients. At the frame rate of 1 fps the exchange between

the different lateral regions can be considered fast. However, the different geometrical extensions of the silanol clusters and the varied distance between such clusters will influence the probability distributions of d_diff. Thus, the higher amplitude a_1 in case of the boiled substrate is caused by the larger average cluster size on that substrate. The component D_2 is related to the occurrence of one lateral passage between two silanol clusters. The deviation of the probability distributions from the bi-exponential fits is caused by diffusivities containing more than one lateral passage between silanol clusters. Due to the smaller cluster size, this will happen with higher probability on the tempered substrate, causing the stronger deviation of the corresponding probability distribution from the fits.

The diffusion coefficients D_1 and D_2 obtained in section 6.3.2 for $\tau_\mathrm{frame} = 200$ ms from the two samples containing RhB are 2 to 4 times the here obtained values. This may point to the extension of anomalous diffusion over two orders of magnitude in time (20 ms to 1 s). However, the restricted sensitivity of SMT tracking for fast diffusion has to be kept in mind (e.g. see section 6.3.1). For larger τ_frame (slower frame rate) this restriction is even more pronounced. Thus, the here reported $C(d_\mathrm{diff})_{1s}$ severely underestimate the occurrence of larger d_diff. For this reason from SMT experiments no reliable effective diffusion coefficients (derived at the long time limit according to the *Einstein-Smoluchowski* eqn. 3.11) will be obtained even for large $\tau_\mathrm{frame} = 200$.

In contrast to SMT experiments, FCS is sensitive to fast diffusion. In the following FCS experiments conducted on micro-structured substrates will be reported, which focus on further evaluation of the fast component observed from FCS experiments in section 6.4.

7.1.3 Ultrathin TEHOS films on micro-structured substrates

Laser-induced dehydroxylation [Hart09, Schu10a] was used to fabricate micro-structured substrates as described in section 4.2.2. The structures were checked with a laser scanning microscope (*Zeiss* LSM 500). Then approximately 10 nm thick TEHOS films doped with R6G ($c \approx 10^{-7}$ mol/l) were coated onto the substrates by the procedure described in section 4.2.3. In such way fabricated samples were investigated via SMT experiments. Yet the results from analysis of probability distributions of diffusivities from micro-structured substrates are very similar to those from hydroxylated and dehydroxylated substrates discussed in the previous section. Therefore, they will not be described here. Furthermore, FCS experiments were conducted on such micro-structured substrates. The results will be reported in the following.

FCS experiment

The maximum size of the overview scans provided by the confocal microscope used for FCS is restricted to 100 μm x 100 μm. Thus, it was rather complicated to find the laser-written structure at this setup. For this reason, the structure was written in close vicinity of a large scratch on the substrate. To further ease the detection of the structure, an envelope of intensely melted lines was generated by locally melting the substrate at high incident laser power (see section 4.2.2). The structure used for the FCS experiments
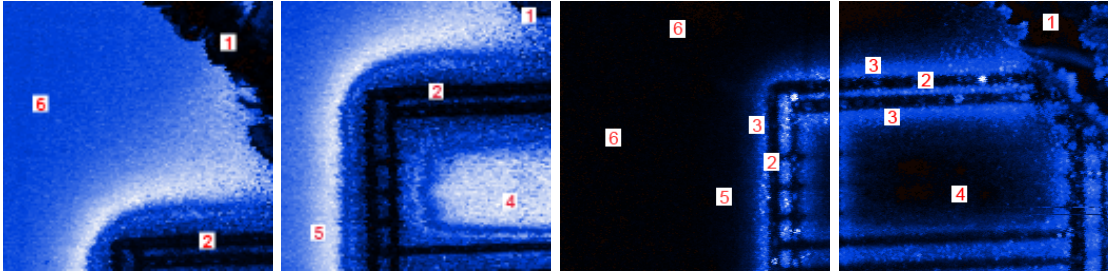
Figure 7.4: Laser-written structure on a hydroxylated SiO_x substrate coated by a 10 nm thick TEHOS film doped with R6G, (left) reflection images, (right) fluorescence images taken at the confocal microscope setup described in section 4.1.2. All images show 100 μm x 100 μm. Part of a scratch (1) can be seen in the top right corner of the structure; (2) melted lines; (3) "halo" i.e. region of increased fluorescence; (4) dehydroxylated region; (5 and 6) hydroxylated region.

is shown in Fig. 7.4. Part of the scratch used to find the structure can be seen in the top right corner of the structure (1). For the two left images the long pass filter (*Omega Optical* 480ALP, $\lambda = 480$ nm, see section 4.1.2) was removed from the detection beam, so the structure appears in reflected excitation light ($\lambda = 465$ nm). Whereas the two right images are taken with implemented long pass filter and therefore show the fluorescence from R6G. The intensely melted lines (2) appear dark in reflection as well as in fluorescence. However, in the fluorescence images, a kind of halo (3) extends approximately 10 μm into each direction from the melted lines. During the dipcoating procedure, R6G preferentially adsorbs in the vicinity of the melted lines, where the substrate is rough. This causes the bright fluorescence from that region. For this reason, this "halo" was excluded from FCS measurements. In the middle of the written structure a dark region (4) with faint horizontal lines can be seen. In contrast to the enveloping lines, the faint inner lines of the structure were melted with much less incident power. The space between the faint lines consists of laser-induced dehydroxylated stripes. Within these stripes a total of 20 FCS measurements was obtained from twelve different positions. The left-hand outside of the structure (5 and 6) shows the hydroxylated substrate. There a total of 19 FCS measurements was conducted on ten different positions. Typical autocorrelation curves from both regions are shown in Fig. 7.5 together with tri-component fits according to eqn. 6.12.

Fluorescence traces from the sample were collected by a single module counting card (*Becker & Hickl* SPC-630) using the program *spcm*. Approximately 300 000 photons were collected for each single measurement, leading to observation times between 40 s and 80 s. Autocorrelation curves on the time interval between 0.1 μs and 10 μs were calculated using the multi-tau correlation of *spcm*. This method is superior to the use of ALV5000 Multiple Tau Digital Correlator for the investigation of the initial exponentially decaying part of the autocorrelation curve, because there the smallest time interval is 0.05 μs, which leads to more data points below 1 μs. But this is achieved on the cost of the investigation of the slower part. The latter thus may be investigated by further
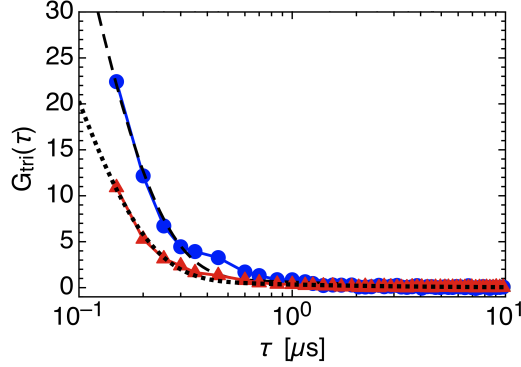
Figure 7.5: Typical autocorrelation curves from (•) a hydroxylated region, and (▲) a dehydroxylated region of a SiO_x substrate coated by a 10 nm thick TEHOS film doped with R6G. Lines denote tri-component fits according to eqn. 6.12.

experiments using the ALV5000 Multiple Tau Digital Correlator. The here investigated fast part appears differently depending on the degree of hydroxylation, as can be seen in Fig. 7.5: The amplitude A of the exponential decay is larger for the autocorrelation obtained from the hydroxylated region. The curves were fitted with the tri-component function G_{tri} according to eqn .6.12. However, due to the fast time interval, the slower components τ_D and τ_R could not be fitted with sufficient accuracy. Yet their variation during fitting showed no effect on the fast component τ_{FD}. The ratio of freely diffusing molecules A_{FD} is related to the amplitude A of the exponential decay by $A = A_{FD}/(1 - A_{FD})$ (see eqn. 6.12). The mean values of A, A_{FD} and τ_{FD} for the two regions are collected in Table 7.2 together with standard deviations.

Table 7.2: Mean values and standard deviations of amplitude A for fast exponential decay, ratio of freely diffusion molecules A_{FD} and corresponding correlation time τ_{FD} from fits to autocorrelation curves using eqn. 6.12 on hydroxylated and dehydroxylated region of a SiO_x substrate coated by a 10 nm thick TEHOS film doped with R6G.

region	#	A	A_{FD}	τ_{FD} $[\mu s]$
hydroxylated	19	121 ± 21	0.992 ± 0.002	0.091 ± 0.007
dehydroxylated	20	74 ± 23	0.987 ± 0.005	0.086 ± 0.008

As can be seen, the correlation times for freely diffusing molecules τ_{FD} averaged over 19 and 20 data sets for the hydroxylated and the dehydroxylated region, respectively, are similar within standard deviation. Though there is a trend to smaller values for τ_{FD} in case of the dehydroxylated substrate. The amplitude A and thus also the calculated ratio of freely diffusing molecules A_{FD} is smaller in case of the dehydroxylated SiO_x. As was explained in section 4.2.2, thermally grown SiO_x will not be fully hydroxylated even after boiling in water for more than 10 h [Duga03, Schu10a]. Therefore, the hydroxylated

substrate is not homogeneously covered by silanols. Instead there exist irregularly sized silanol clusters with siloxane patches in between [Schu10a]. If the dye molecule mainly explores the siloxane patches during the FCS measurement, then there is no difference to the exploration of the surface of the stripes generated by laser-induced dehydroxylation. For this reason, some FCS traces obtained at regions with different degree of hydroxylation may yield similar results.

On dehydroxylated substrates fewer adsorbed molecules and thus a higher A_{FD} would be expected. Yet, a comparison of A_{FD} for different regions is only possible, if the concentration of the dye in the corresponding regions is similar, because the fluctuations $\delta F(\tau)$ of the fluorescence signal also depend on the local concentration $c(\mathbf{r},\tau)$, see eqn. 3.35 in section 3.4. Hence, a different local dye concentration on the dehydroxylated stripes may explain the lower value of A_{FD} in that case.

The trend to shorter correlation times τ_{FD} for the dehydroxylated substrate is more difficult to understand. In section 6.4 it was related to the vertical mean first passage time (mfpt) of the dye molecules in the ultrathin TEHOS film. Since TEHOS dewets on OTS monolayers [Tren09a], it may also dewet on fully dehydroxylated SiO_x leading to a film of minimum thickness (1-2 molecular diameters of TEHOS). On the here studied sample, the dehydroxylated stripes are enclosed by intensely melted lines (Fig. 7.5 2). Therefore, no transition to a hydroxylated region is visible, which could reveal mutable dewetting. However, in Fig 7.4 (middle left), a very bright reflection from the inner region (4) of the laser-written structure can be seen. A similar bright reflection is visible along the outside of the structure, while further away the intensity decreases. This may point to a variation in film thickness. Thus, the observation of shorter τ_{FD} may in fact be explained by short mfpt in regions of minimum film thickness. Minimum film thickness may also explain the bright region (5) on the outside of the written structure. Some FCS traces measured at the hydroxylated substrate were obtained from this outside region (5), since in the fluorescence image it was not discernible from the region (6) further away from the structure. Hence, a variation of τ_{FD} towards shorter values can be explained. Furthermore, the τ_{FD} obtained from the FCS curves investigated in section 6.4 are slightly larger than the values achieved here. This interpretation is also in agreement with the smaller A_{FD} observed for the dehydroxylated region, because minimum film thickness implies a decrease of the ratio of freely diffusing molecules. Therefore, the slight differences observed here for the regions with different degree of hydroxylation are likely not to be caused by different interaction of the dye with the substrate. But they can be explained by difference in film thickness.

To study variations in SM diffusion caused by different degrees of substrate hydroxylation, a combined setup, integrating confocal and wide field microscopy, would be very useful. Then the wide field could be used to find the written structure, rendering intensely melted lines obsolete.

7.1.4 Conclusion

The experiments on substrates with varied degree of hydroxylation further evidence the important influence of substrate surface heterogeneities on SM dynamics in ultrathin

TEHOS films. In particular, the slow diffusion component is related to chemisorption on silanol clusters. However, additional experiments are needed to discriminate between fast re-adsorption and "silanol-gliding" via successive H-bonding to surface silanols. The results from FCS experiments on a sample with a micro-structured substrate can be interpreted by a thinner TEHOS film on the dehydroxylated region. This is further evidenced by brighter reflection from the corresponding region in respect to the untreated sample. The trend to shorter fast correlation times τ_{FD} from this region, together with the obtained lower ratio A_{FD} of freely diffusing molecules from those measurements, support the interpretation of the fast component within FCS autocorrelation as related to vertical mean first passage times.

7.2 Structures in thin liquid crystal 8CB films

The previous chapter and the previous sections in this chapter dealt with translational diffusion in ultrathin liquid films. However, the newly developed method using probability distributions of diffusivities is also suitable to provide additional information to trajectory analysis via msd from SMT experiments on thin liquid crystal films. Furthermore, spatial maps of the diffusivities reveal structure related dynamics within those films. This will be reported in the following. The work presented in this section has contributed to the following publications [Schu10b, Schu11]:

B. Schulz, D. Täuber, F. Friedriszik, H. Graaf, J. Schuster, and C. von Borczyskowski. Optical detection of heterogeneous single molecule diffusion in thin liquid crystal films *Phys. Chem. Chem. Phys.*, Vol. 12, pp. 11555–11562, 2010.

B. Schulz, D. Täuber, J. Schuster, T. Baumgärtel, and C. von Borczyskowski. Influence of mesoscopic structures on single molecule dynamics in thin smectic liquid crystal films. *Soft Matter*, Vol. 7, pp. 7431–7440, 2011.

Liquid crystal 8CB films had been prepared[2] by spin-coating from a solution in toluene as described in section 4.2.5 and [Schu09, Schu10b]. 8CB films with different thickness d were prepared. The here presented results stem from the thickest films with $d \approx 220$ nm. This thickness is known to be at the threshold for the appearance of focal conic domains [Desi06]. Directly after sample preparation the liquid crystal (LC) films displayed a smooth surface when investigated by AFM.[3] However, temperature cycling into the nematic phase induced the appearance of structures, which differed according to the type of substrate: For thin 8CB films on native oxide a smooth LC-air surface with few irregularly distributed several μm size terraced holes was found by AFM measurements. While on the 100 nm thermally grown SiO_x focal conic domains (FCD) with a size distribution between 0.5 μm and 2 μm were observed by optical investigation at a laser scanning microscope (*Zeiss* LSM 500). Fig. 7.6 (middle) shows a reflection image of a

---

[2]Sample preparation, optical investigation at the laser scanning microscope, and SMT and FCS experiments were conducted by Benjamin Schulz.

[3]AFM measurements were conducted by Thomas Baumgärtel.

220 nm 8CB film on 100 nm thick thermally grown oxide after temperature cycling. The FCD can be seen as dumbbells due to the linear polarization of the laser light. In contrast, the steps at the terraced holes represent multiples of the height of an 8CB bi-layer and the film surface besides the holes appeared smooth. This points to a terraced film structure (TF) of 8CB on Si with native oxide.
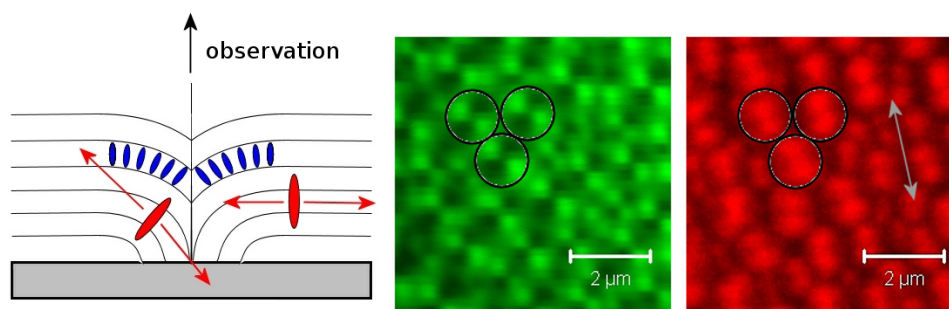
Figure 7.6: (Left) Schematic presentation of a FCD with incorporated o-PDI. Preferred directions of emission of o-PDI molecules in different areas of the FCD are indicated by arrows. (middle) reflection and (right) PDI fluorescence image of o-PDI doped 8CB on Si with 100 nm oxide. FCD are visible as characteristic textures. Open circles highlight the same single FCDs in both images. The arrow marks the direction of linear polarization of incident light. Images taken from [Schu11].

Two different perylene dimides were used to probe the dynamics within the thin frustrated liquid crystal films. One of the dyes, o-PDI, was shown to orient parallel to the liquid crystal director, while the other, no-PDI did not align with the liquid crystal director [Schu10b], see section 4.2.1 for the chemical structures. Fig. 7.6 (left) shows a schematic cut of a FCD with incorporated o-PDI molecules (red). The direction of preferred optical excitation (and emission) of the dye molecules is indicated by red arrows. This preferred emission is perpendicular to the length axis of the molecules. The orientation of o-PDI with the LC director, therefore, is visible within the optical detection: When the preferred (excitation) and emission is parallel to the optical axis of the microscope, the detection of o-PDI is enhanced. In contrast, o-PDI molecules oriented parallel to the incident light (and thus also to the direction of observation) will hardly be excited and thus emit less photons. Furthermore, the reduced emission preferentially occurs perpendicular to the direction of observation and thus will hardly be detected. For this reason, those molecules will not be visible within optical investigation. In contrast, due to their more spherical shape, no-PDI molecules will freely rotate within the LC film on a fast timescale and thus exhibit no preferred direction of detection. The orientation of o-PDI with the LC director can be seen in Fig. 7.6 (right), where the fluorescence of o-PDI from a highly doped 8CB film on 100 nm thermally grown oxide is shown. Since the excitation light was linear polarized (marked by arrow), the FCD appear as two circles interconnected in the center of the FCD [Smal01]. The FCD appear at the same position on the sample as in the reflection image Fig. 7.6 (middle).

The SMT data analysis via msd by Benjamin Schulz was complemented by analysis

of diffusivities. Probability distributions of diffusivities reveal a fast component, which could not be seen from trajectory analysis via msd. Furthermore, spatial maps of diffusivities provide information on spatial structure of the dynamics. Here first spatial maps of diffusivities will be presented, followed by a section on probability distributions of diffusivities from the 8CB films.

7.2.1 Spatial maps of diffusivities
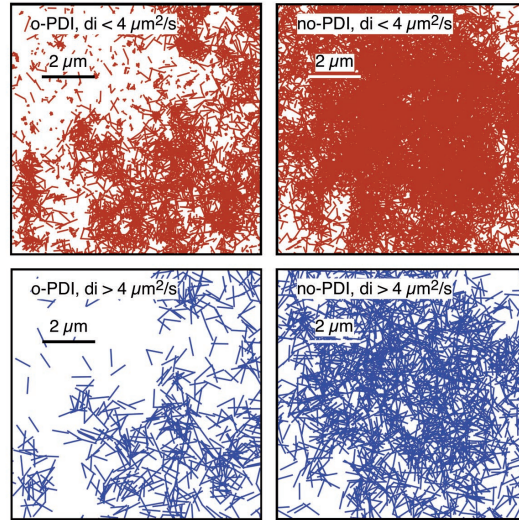
Figure 7.7: Spatial distribution of diffusivities d_{diff} for o-PDI (left) and no-PDI (right) for 225 nm thick 8CB films on 100 nm thermally grown SiO_x (before temperature cycling). For better visualization d_{diff} smaller (larger) than 4 μm^2/s are shown in the two top (bottom) graphs. The size and shape of the laser illuminated spots is the same for both samples. Spatial o-PDI distributions show "holes" in the illuminated area (top left corner). Image presented in [Schu10b].

The diffusivities obtained from tracking experiments can also be used to create spatial maps of mobility. This is in particular of interest, if spatial structures on a scale down to 0.1 μm are expected. Since o-PDI follows the LC director, diffusing o-PDI molecules preferentially will be detected when the LC director is parallel to the substrate (i.e. perpendicular to the direction of observation), see Fig. 7.6 (left). As can be seen in Fig. 7.7 (left), "holes" appear within the map of diffusivities obtained from a sample containing o-PDI. In the top left corner only few diffusivities are visible, and most of them have small values. Thus, this region can be ascribed to LC with director **n** preferentially aligned perpendicular to the substrate. For comparison a similarly obtained map of diffusivities from a sample containing no-PDI is shown (Fig. 7.7 right). Both SMT experiments were conducted on 220 nm thick 8CB films on 100 nm thick SiO_x before temperature cycling. These films exhibit a smooth surface within AFM experiments. However, the map of diffusivities obtained from the sample containing o-PDI reveals

varying LC director orientation on a scale of some μm. This points to the existence of LC-domains within the frustrated 8CB films before temperature cycling.

7.2.2 Probability distributions of diffusivities
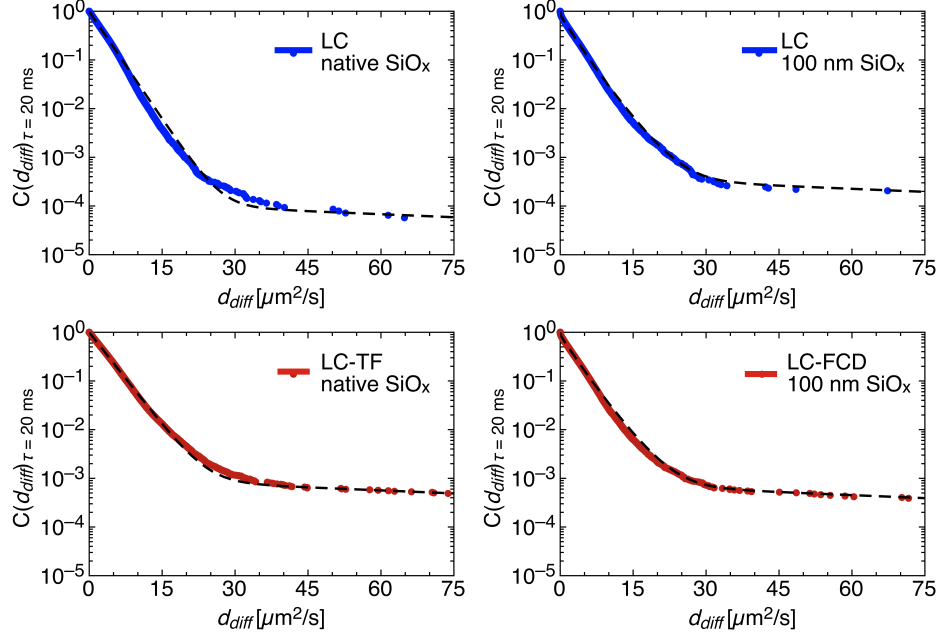
Figure 7.8: Probability distributions of d_{diff} (data points) on two different oxides for no-PDI, together with (dashed lines) multi-exponential fits of LC (top), LC-TF (bottom left) and LC-FCD (bottom right). Image presented in [Schu11] (but there without correction for tracking).

Probability distributions of diffusivities d_{diff} obtained from SMT experiments on thin liquid films reveal a fast component $D_3 = 105 \pm 30$ μm^2/s which cannot be seen by trajectory analysis via msd [Schu09]. This value of D_3 agrees with a fast component obtained from analysis of FCS experiments by a two-component fit according to eqn. 3.39 [Schu10b]. Fig. 7.8 shows probability distributions of diffusivities obtained from no-PDI doped 220 nm 8CB films on native SiO$_x$ (left) as well as on 100 nm thick SiO$_x$ (right) before (top) and after (bottom) temperature cycling in the nematic phase. The dashed lines show multi-component fits according to eqn. 3.26. For the 8CB films on 100 nm oxide two components $D_1 = 2.4 \pm 0.3$ μm^2/s and $D_2 = 3.8 \pm 0.3$ μm^2/s are obtained, which nearly do not change in magnitude upon formation of FCD. According to diffusivity analysis D_2 is a relatively strong component, which shows up only weakly in msd analysis. This is probably caused by the inferior sensitivity of msd analysis to fast components. The amplitude of the faster component D_2 increases from 0.29 ± 0.02 to 0.37 ± 0.02 upon formation of FCD. The absolute range of D_1 and D_2 is in agreement with the anisotropic self-diffusion of 8CB parallel and perpendicular to the LC director **n** in the smectic-A phase [Dvin06]. For this comparison the difference in dye diameter

has been taken into account [Schu10b].

The situation for native oxide is distinct from the one for 100 nm oxide, although also there the temperature cycling leads to faster diffusion. However, in case of terraced films (TF) only one medium component D_2 can be detected, which increases from 2.9 ± 0.2 $\mu\text{m}^2/\text{s}$ to 3.4 ± 0.2 $\mu\text{m}^2/\text{s}$ upon formation of TF. An increase of about 30% in that case can also be seen from distributions of D_{traj} obtained from msd analysis [Schu11].

7.2.3 Conclusion

Spatial maps of diffusivities obtained from o-PDI doped 8CB films provide insight into LC domain structure within those films. In contrast to the strongly confined ultrathin liquid films, no diffusion coefficients below 2 $\mu\text{m}^2/\text{s}$ are expected within 220 nm thick 8CB films. There is a general agreement of the values of D_1 and D_2 observed from analysis of diffusivities with the range of values of D_{traj} from trajectory analysis via msd. However, higher amplitudes for D_2 obtained by diffusivity analysis also in this case reveal a higher sensitivity to fast diffusion than by the analysis via msd. Furthermore, probability distributions of d_{diff} show an even faster component, which cannot be seen within msd analysis, but which is also seen by analysis of FCS experiments.

8 Summary and outlook

Within this work single molecule (SM) dynamics in thin films of soft matter was investigated. For this three different experimental methods were applied: Single molecule tracking (SMT) of translational SM dynamics at a wide field setup, fluorescence correlation spectroscopy (FCS) at a confocal setup, and the acquisition of time traces of SM spectra at a confocal setup.

Due to confinement effects, and in particular due to interactions with the confining interfaces, SM dynamics in thin films of soft matter very often is heterogeneous. For analysis of SMT experiments, evaluation of mean square displacements (msd) along SM trajectories is common usage. However, by this method, diffusion coefficients are derived from temporal averages, which may conceal heterogeneities. For this reason, a different method for analysis of SMT experiments was developed, which evaluates probability distributions of diffusivities (d_{diff}), i.e. time scaled square displacements of SM motion between succeeding frames of SMT videos. This method was used to study SM dynamics in ultrathin films of tetrakis(2-ethylhexoxy)silane (TEHOS) on Si wafer with 100 nm thermally grown oxide. Furthermore, it was applied to complement the analysis via msd of SMT experiments on thin liquid crystal 4-n-octyl-4'-cyanobiphenyl (8CB) films.

For the analysis of spectral diffusion (i.e. energetic displacements of SM spectra within time), the analogy to translational diffusion was used to develop probability distributions of spectral diffusivities (d_{spec}), which are time scaled square energetic displacements of succeeding SM spectra. Furthermore, simulations of two- and three-level systems were used to study the effect of energy gaps on the corresponding probability distributions of d_{spec}, as well as the contributions from noise and fitting uncertainty. Spectral jumps from one energetic position to another may occur during acquisition of a single SM spectrum, thus creating intermediates from the SM spectra corresponding to the involved energetic positions of the spectra. Simulations revealed possible contributions from those intermediates to spectral diffusion, pretending larger spectral diffusion than actually is the case. For the here studied system of Nile Red in poly-n-alkylmethacrylates (PnAMA) and an acquisition time of 1 s, the arbitrary contribution from intermediates is in the range of 10^2 meV^2/s.

Investigation of 25 nm thick PnAMA films via time series of SM spectra

Here, three 25 nm thick PnAMA films, doped with Nile Red in nanomolar concentration, were investigated at different temperatures using time series of SM spectra. At room temperature polymethylmethacrylate (PMMA) and poly-n-propylmethacrylate (PPMA) are in the glassy state. The corresponding probability distributions of d_{spec} reveal two-

level systems with energetic gaps of about 25 meV. This is ascribed to small conformational changes of Nile Red within the free volume. Larger spectral jumps (which are related to an internal charge transfer of Nile Red) were only observed for the poly-n-butylmethacrylate (PBMA) film at about glass transition temperature and in the melt state. In the latter case, due to the higher mobility, the Nile Red molecules will explore different regions of the polymer film. Thereby they monitor the polarity of their local environment by the corresponding energetic position of the emission. For PMMA in the vitreous state, SM spectra were grouped into subsets according to their energetic position, thus creating a subset sensing polar environment and the other one with unpolar environment. The analysis of spectral diffusivities rendered spectral diffusion coefficients of $47 \pm 1\ meV^2/s$ and $31 \pm 1\ meV^2/s$, respectively. This evidences the stronger coupling of energetic fluctuations to conformational changes within the polar environment. Furthermore, the analysis of spectral positions of Nile Red spectra from the three PnAMA films revealed a solvent shift towards higher energies for longer alkyl side chains. This agrees with the idea of nanophase separation for longer alkyl side chains [Bein01].

The analyzed experimental data qualitatively match the predictions from polymer science and previous studies on PnAMA films. Nevertheless more experimental investigations are needed to explore the influence of M_w and temperature, as well as of the side chain length. A comparative investigation of 200 nm thick PnAMA films is under way in cooperation with the argentine collaborators to study the effect of confinement. Further theoretical considerations may even lead to quantitative relations between spectral diffusion and physical properties of the investigated polymers.

Investigation of ultrathin TEHOS films via SMT and FCS

Single molecule diffusion in ultrathin liquid films is known to be anisotropic [Schu03]. However, the cause of this anisotropy was not fully understood yet. Since it is known that liquids may display layering at solid liquid interfaces [Forc93, Yu99], an influence of this layering on SM dynamics was suggested [Schu02b, Schu03, Schu04].

Here, a short literature overview on liquid layering shows the influence from relative humidity, liquid molecule structure, interface roughness and temperature on liquid layering. In contrast, no reports on any impact from the used substrate material were found. However, the well known strong influence of solid-liquid interactions on wetting behavior [Seem01] points to an impact from these interactions on liquid layering as well. A comparative X-ray study of thin TEHOS films on silicon substrate with different SiO_x layer thickness would be suitable, to study the influence from the used substrate material on liquid layering.

In this work, SM dynamics within 2 to 10 nm thick TEHOS films was investigated by FCS and by SMT experiments. The analysis of the latter was done via msd as well as via probability distributions of diffusivities. Film thickness was determined by varying angle ellipsometry. Probability distributions of d_{diff} from SMT experiments with frame times between 20 ms and 100 ms on those films show three components: The slowest component D_0 is related to immobile dye molecules and slowly diffusing ones (below detection threshold). The other two components D_1 and D_2 are related to SM diffusion

and reveal diffusion heterogeneity, which points to contributions from heterogeneous regions within the films.

Long term studies on an ultrathin TEHOS film (via SMT at 20 ms frame time) show that those two components D_1 and D_2 remained stable within experimental error (10%) during evaporative film thinning from 4.9 nm to 3.2 nm. Thus, it can be concluded that there is no noticeable effect from mutable liquid layering in a vertical distance from the substrate between three and five liquid molecules' diameters. However, the amplitude a_2 for the faster component D_2 decreased with decreasing film thickness. This shows that for thinner films there is a higher concentration of dye molecules in the region related to slowed diffusion.

By variation of the frame time τ_{frame} between 20 ms and 100 ms, a time dependence of the evaluated diffusion coefficients from trajectory analysis and from diffusivity analysis was revealed. The SM dynamics in the studied ultrathin TEHOS films is anomalous in the corresponding time regime. This agrees with the observation of power-law distributed adsorption events from trajectory analysis in the time regime between 60 ms and 3 s. It also implies non-ergodicity, i.e. the single dye molecules will not probe all heterogeneous regions of the sample during the observation time. For this reason, the values obtained for D_1 and D_2 are short range diffusion coefficients, depending on τ_{frame}. Therefore, their values are intermediates between the diffusion coefficients related to the different regions of the ultrathin films. These latter diffusion coefficients can be separated in case of frame times faster than the dwell times within these regions. However, the fastest accessible frame time for the here conducted SMT experiments is 15 ms, which is not fast enough.

Furthermore, τ_{frame} was varied between 20 ms and 200 ms in steps of 20 ms, by integrating over 1, 2, up to 10 successive frames from the acquired SMT video. Thus, the same SM dynamics could be studied over one order of magnitude in time, which was applied to SMT measurements from six different samples containing different dyes and film thicknesses. Analysis of the corresponding probability distributions of diffusivities showed a strong time dependence for 20 ms $\leq \tau \leq$ 100 ms. This points to frequent exchange between the heterogeneous regions of the films on that time scale. The probability distributions of diffusivities were fitted by a tri-exponential function, yielding three short range diffusion coefficients $D_{i,\mathrm{diff}}(\tau)$. Thereby for the larger dye molecule, no-PDI, slightly smaller diffusion coefficients were obtained. However, further theoretical considerations are necessary to relate the $D_{i,\mathrm{diff}}(\tau)$ to the diffusion coefficients within the heterogeneous regions and to the effective diffusion coefficient in the long time limit.

Moreover, FCS experiments were conducted on ultrathin TEHOS films. The autocorrelation curves from three samples containing R6G in different concentration, as well as that one from a sample containing Oregon Green (OG) show a fast exponential decay in the range of 0.1 μs and 1 μs. This matches simulated mean first passage times for free diffusion between two adsorption events in the ultrathin films. The slower part of the correlation function shows a strong dependence on adsorption events. This part combines lateral dye transients of the focal volume with contributions from adsorption events and cannot be fitted with a single component. A combination of the function for

two-dimensional translational diffusion G_D with a stretched exponential decay for ad-/desorption kinetics may be used for a rough approximation. Thereby effective lateral diffusion coefficients and mean durations of adsorption are obtained. Grabowski et al. conducted FCS experiments on approximately 15 nm thick TEHOS films on quartz cover slips using the rhodamine derivate Alexa 488 [Grab07]. They used a two-component function for lateral diffusion to fit the obtained autocorrelation curves (for $\tau \geq 0.1$ ms). The two components $D_{slow} = 0.2$ $\mu m^2/s$ and $D_{fast} = 13$ $\mu m^2/s$ are within the range of diffusion coefficients obtained from similar two-component fits to the autocorrelation curves studied in this work. However, they are about one magnitude faster than the diffusion coefficients obtained from FCS traces with pronounced adsorption events. This agrees with the claim from Grabowski et al. not to have seen adsorption of Alexa 488 on quartz cover slips [Grab07].

The substrates with amorphous SiO_x used within this work are known to be covered by heterogeneously distributed surface silanols [Zhur00]. The size of these surface silanol clusters can be modified by different substrate treatment [Schu10a]. For this reason, two differently treated substrates were used within SMT experiments at τ_{frame} to study the effect of substrate hydropathy on SM dynamics. Probability distributions of diffusivities from these SMT experiments, when fitted bi-exponentially, rendered $D_1 = 0.010 \pm 0.02$ $\mu m^2/s$ for the hydroxylated substrate and $D_1 = 0.012 \pm 0.002$ $\mu m^2/s$ for the dehydroxylated substrate (diffusivities related to immobile molecules had been excluded from the distributions). The faster component D_2 in both cases was 0.13 ± 0.02 $\mu m^2/s$. However, also even faster diffusion is visible within the distributions. The amplitude a_1 for the hydroxylated substrate was about 4/3 of the corresponding amplitude for the dehydroxylated substrate. This strongly points to substrate heterogeneity causing the diffusion heterogeneity visible from diffusivity analysis.

Therefore, SM dynamics in ultrathin liquid films on 100 nm thermally grown SiO_x can be described by a vertical three-layer model, which contains (i) immobile molecules adsorbed to the substrate, (ii) a heterogeneous near-surface region with slowly diffusing molecules as suggested by Honciuc et al. [Honc09a], and (iii) freely diffusing molecules in the upper region of the film. Honciuc et al. suggest that probe molecules with the possibility of forming two H-bonds may glide on surface silanol clusters via successive H-bonding steps. However, from the experiments conducted in this work, it cannot be discriminated, whether this "silanol-gliding" exists, or whether simply fast re-adsorption events occur on silanol clusters. The diffusion in the upper film region is bulk-like. Yet it may still follow a vertical modification according to continuum hydrodynamic models. The observed anomalous SM dynamics is caused by the silanol distribution on the substrate.

The suggested explanation of the fast component visible in FCS autocorrelation curves by mean first passage times should be further tested by two-channel FCS (to avoid contributions from afterpulsing) and by variation of film thickness over one order of magnitude. Furthermore, investigation of TEHOS films containing higher dye concentration on structured substrates via video microscopy at a wide field setup,[1] may further evi-

---

[1]This was first suggested by Mario Heidernätsch, TU Chemnitz.

dence the suggested influence of substrate surface heterogeneity on the SM dynamics. Moreover, SM diffusion of dye molecules without side groups suitable for H-bonding may be studied in comparison with SM experiments using dyes with such H-bonding probabilities. By this, discrimination between the suggested "silanol-gliding" and fast re-adsorption on silanol clusters may be achieved.

Analysis of diffusivities applied to SMT experiments on thin 8CB films

Thin smectic-A 8CB films on silicon substrates with different oxide thickness are strongly influenced by the anchoring conditions at the confining interfaces with silicon and with air. For 220 nm thick 8CB films after temperature cycling into the nematic phase structures appear: On silicon substrates with 100 nm grown SiO_x focal conic domains appear, while on silicon substrates with native oxide terraced holes were observed [Schu09, Schu11]. The structure related dynamics in 220 nm thick 8CB films was explored using two different perylene diimide dyes, one of which (o-PDI) orients with the liquid crystal director, while the other one (no-PDI) does not [Schu09, Schu10b].

In this work, FCS and SMT experiments on the above described 8CB films were complemented by analysis of diffusivities from SMT experiments. Maps of diffusivities from SMT experiments on 8CB films doped with o-PDI in nanomolar concentration reveal the existence of differently oriented liquid crystal domains (several micrometer in size) even before temperature cycling, where AFM measurements showed a flat smooth surface of the films on both substrates.

Furthermore, also with the thin 8CB films, analysis of probability distributions of d_{diff} reveals additional information, which cannot be seen from analysis via msd along trajectories: Besides the two diffusion coefficients related to the 8CB anisotropy, a third much faster component was observed, which matched the fast diffusion coefficient obtained from analysis of FCS experiments. Also, for the 8CB films on the 100 nm oxide, the amplitude of the faster component from the diffusion anisotropy was higher than from the corresponding msd analysis. This emphasizes the higher sensitivity of this method to faster diffusion, which was already visible from analysis of diffusivities from SMT experiments on ultrathin TEHOS films.

List of Tables

List of Figures

172

Bibliography

[Abbo61]   A. D. Abbott, J. R. Wright, A. Goldschmidt, W. T. Stewart, and R. O. Bolt. "Silicate Esters and Related Compounds". *Journal of Chemical & Engineering Data*, Vol. 6, pp. 437–442, 1961.

[Adhi11]   S. Adhikari, M. Selmke, and F. Cichos. "Temperature dependent single molecule rotational dynamics in PMA". *Phys. Chem. Chem. Phys.*, Vol. 13, pp. 1849–1856, 2011.

[Ahn09]   S. I. Ahn, J. Kim, J. H. Kim, J. C. Jung, T. Chang, M. Ree, and W. Zin. "Polarity Effect near the Surface and Interface of Thin Supported Polymer Films: X-ray Reflectivity Study". *Langmuir*, Vol. 25, pp. 5667–5673, May 2009.

[Alag99]   M. Alagar and V. Mohan. "Studies on tribological characteristics of alkylalkoxysilanes". *Industrial Lubrication and Tribology*, Vol. 51, pp. 294–300, 1999.

[Arag76]   S. R. Aragon and R. Pecora. "Fluorescence correlation spectroscopy as a probe of molecular dynamics". *The Journal of Chemical Physics*, Vol. 64, pp. 1791–1803, 1976.

[Arci08]   D. Arcizet, B. Meier, E. Sackmann, J. O. Rädler, and D. Heinrich. "Temporal Analysis of Active and Passive Transport in Living Cells". *Phys. Rev. Lett.*, Vol. 101, p. 248103, Dec. 2008.

[Armi69]   C. G. Armistead, A. J. Tyler, F. H. Hambleton, S. A. Mitchell, and J. A. Hockey. "Surface hydroxylation of silica". *The Journal of Physical Chemistry*, Vol. 73, pp. 3947–3953, 1969.

[Atki06]   P. Atkins and J. D. Paula. *Atkins' Physical Chemistry*. Oxford University Press, Oxford, 8 ed. Ed., 2006.

[Baie08]   J. Baier, M. F. Richter, R. J. Cogdell, S. Oellerich, and J. Köhler. "Determination of the Spectral Diffusion Kernel of a Protein by Single-Molecule Spectroscopy". *Phys. Rev. Lett.*, Vol. 100, p. 018108, Jan. 2008.

[Balg06]   T. Balgar, S. Franzka, E. Hasselbrink, and N. Hartmann. "Laser-assisted fabrication of submicron-structured hydrophilic/ hydrophobic templates for the directed self-assembly of alkylsiloxane monolayers into confined domains". *Applied Physics A: Materials Science & Processing*, Vol. 82, pp. 15–18, 2006.

[Baue09a]   M. Bauer, M. Heidernätsch, D. Täuber, J. Schuster, C. von Borczyskowski, and G. Radons. "Investigations of Static and Dynamic Heterogeneities in Ultra-Thin Liquid Films via Scaled Squared Displacements of Single Molecule Diffusion". *Diffusion Fundamentals Journal*, Vol. 11, p. 70(2), 2009.

[Baue09b]   M. Bauer, M. Heidernätsch, D. Täuber, C. von Borczyskowski, and G. Radons. "Investigations of heterogeneous diffusion based on the probability density of scaled squared displacements observed from single molecules in ultra-thin liquid films". *Diffusion Fundamentals Journal*, Vol. 11, p. 104(14), 2009.

[Bein01]   M. Beiner. "Relaxation in Poly(alkyl methacrylate)s: Crossover Region and Nanophase Separation". *Macromolecular Rapid Communications*, Vol. 22, pp. 869–895, 2001.

[Belg10]   C. Belgardt, H. Graaf, T. Baumgärtel, and C. von Borczyskowski. "Self-assembled monolayers on silicon oxide". *physica status solidi (c)*, Vol. 7, pp. 227–231, 2010.

[Bell92]   T. Bellini, N. A. Clark, C. D. Muzny, L. Wu, C. W. Garland, D. W. Schaefer, and B. J. Oliver. "Phase behavior of the liquid crystal 8CB in a silica aerogel". *Phys. Rev. Lett.*, Vol. 69, p. 788–791, Aug. 1992.

[Berl95]   K. Berland, P. So, and E. Gratton. "Two-photon fluorescence correlation spectroscopy: method and application to the intracellular environment". *Biophysical Journal*, Vol. 68, pp. 694–701, Feb. 1995.

[Blos03]   R. Blossey. "Self-cleaning surfaces - virtual realities". *Nature Materials*, Vol. 2, pp. 301–306, May 2003.

[Blow08]   N. Blow. "Cell imaging: New ways to see a smaller world". *Nature*, Vol. 456, pp. 825–828, Dec. 2008.

[Bobr86]   N. Bobroff. "Position measurement with a resolution and noise-limited instrument". *Rev. Sci. Instrum.*, Vol. 57, pp. 1152–1157, June 1986.

[Boir99]   A. Boiron, P. Tamarat, B. Lounis, R. Brown, and M. Orrit. "Are the spectral trails of single molecules consistent with the standard two-level system model of glasses at low temperatures?". *Chemical Physics*, Vol. 247, pp. 119–132, Aug. 1999.

[Bras04]   M. Bras, V. Dugas, F. Bessueille, J. P. Cloarec, J. R. Martin, M. Cabrera, J. P. Chauvet, E. Souteyrand, and M. Garrigues. "Optimisation of a silicon/silicon dioxide substrate for a fluorescence DNA microarray". *Biosensors and Bioelectronics*, Vol. 20, pp. 797–806, Nov. 2004.

[Bril91]   N. V. Brilliantov, V. P. Denisov, and P. L. Krapivsky. "Generalized Stokes-Einstein-Debye relation for charged Brownian particles in solution". *Physica A: Statistical and Theoretical Physics*, Vol. 175, pp. 293–304, July 1991.

[Bron08]   I. Bronstein, K. Semendjajew, G. Musiol, and H. Mühlig. *Taschenbuch der Mathematik*. Verlag Harri Deutsch, Frankfurt am Main, 7th Ed., 2008.

[Brow28]   R. Brown. "Mikroskopische Beobachtungen über die im Pollen der Pflanzen enthaltenen Partikeln, und über das allgemeine Vorkommen activer Molecüle in organischen und unorganischen Körpern". *Poggendorffs Annalen der Physik*, Vol. 14, pp. 294–313, 1828.

[Camp07]   C. G. Campbell and B. D. Vogt. "Examination of the influence of cooperative segmental dynamics on the glass transition and coefficient of thermal expansion in thin films probed using poly(n-alkyl methacrylate)s". *Polymer*, Vol. 48, pp. 7169–7175, Nov. 2007.

[Cauc30]   A. Cauchy. "Sur la réfraction et la réflexion de la lumière". *Bulletin de Férussac*, Vol. 14, pp. 6–10, 1830.

[Chac01]   E. Chacón, M. Reinaldo-Falagán, E. Velasco, and P. Tarazona. "Layering at Free Liquid Surfaces". *Phys. Rev. Lett.*, Vol. 87, p. 166101, Sep. 2001.

[Chak10]   S. Chakraborty and R. Garcia. "Optical-ellipsometric study of the nematic-to-smectic transition in 8CB films adsorbed on silicon". *Phys. Rev. E*, Vol. 81, p. 031702, March 2010.

[Cham74]   R. W. Chambers, T. Kajiwara, and D. R. Kearns. "Effect of dimer formation on the electronic absorption and emission spectra of ionic dyes. Rhodamines and other common dyes". *The Journal of Physical Chemistry*, Vol. 78, pp. 380–387, 1974.

[Cher09]   T. Cherdhirankorn, V. Harmandaris, A. Juhari, P. Voudouris, G. Fytas, K. Kremer, and K. Koynov. "Fluorescence Correlation Spectroscopy Study of Molecular Probe Diffusion in Polymer Melts". *Macromolecules*, Vol. 42, pp. 4858–4866, July 2009.

[Cich00]   F. Cichos and J. Schuster. "Diffusion of Single Molecules Close to Interfaces". *Single Molecules*, Vol. 1, pp. 299–305, 2000.

[Cich07]   F. Cichos, C. von Borczyskowski, and M. Orrit. "Power-law intermittency of single emitters". *Current Opinion in Colloid & Interface Science*, Vol. 12, pp. 272–284, Dec. 2007.

[Dert07]   T. Dertinger, V. Pacheco, I. von der Hocht, R. Hartmann, I. Gregor, and J. Enderlein. "Two-Focus Fluorescence Correlation Spectroscopy: A New Tool for Accurate and Absolute Diffusion Measurements". *ChemPhysChem*, Vol. 8, p. 433–443, 2007.

[Dert10] T. Dertinger, R. Colyer, R. Vogel, J. Enderlein, and S. Weiss. "Achieving increased resolution and more pixels with Superresolution Optical Fluctuation Imaging (SOFI)". *Optics Express*, Vol. 18, p. 18875, 2010.

[Desc02] L. A. Deschenes and D. A. Vanden Bout. "Single molecule photobleaching: increasing photon yield and survival time through suppression of two-step photolysis". *Chemical Physics Letters*, Vol. 365, pp. 387–395, 2002.

[Desi06] V. Designolle, S. Herminghaus, T. Pfohl, and C. Bahr. "AFM Study of Defect-Induced Depressions of the Smectic-A/Air Interface". *Langmuir*, Vol. 22, pp. 363–368, Jan. 2006.

[Diez03] S. Diez, C. Reuther, C. Dinu, R. Seidel, M. Mertig, W. Pompe, and J. Howard. "Stretching and Transporting DNA Molecules Using Motor Proteins". *Nano Letters*, Vol. 3, pp. 1251–1254, 2003.

[Doer00] A. K. Doerr, M. Tolan, J. Schlomka, and W. Press. "Evidence for density anomalies of liquids at the solid/liquid interface". *Europhysics Letters*, Vol. 52, p. 330, 2000.

[Du11]   N. Du, H. B. Park, G. P. Robertson, M. M. Dal-Cin, T. Visser, L. Scoles, and M. D. Guiver. "Polymer nanosieve membranes for CO2-capture applications". *Nature Materials*, Vol. 10, pp. 372–375, May 2011.

[Duga03] V. Dugas and Y. Chevalier. "Surface hydroxylation and silane grafting on fumed and thermal silica". *Journal of Colloid and Interface Science*, Vol. 264, pp. 354–361, 2003.

[Dunm11] D. Dunmur and T. Sluckin. *Soap, science, & flat-screen TVs - A history of liquid crystals*. Oxford University Press, New York, 2011.

[Dutt91] G. B. Dutt, S. Doraiswamy, and N. Periasamy. "Molecular reorientation dynamics of polar dye probes in tertiary-butyl alcohol–water mixtures". *The Journal of Chemical Physics*, Vol. 94, pp. 5360–5368, Apr. 1991.

[Dvin06] S. V. Dvinskikh and I. Furo. "Nuclear magnetic resonance studies of translational diffusion in thermotropic liquid crystals". *Russian Chemical Reviews*, Vol. 75, pp. 497–506, 2006.

[Dyba03] M. Dyba, S. Jakobs, and S. W. Hell. "Immunofluorescence stimulated emission depletion microscopy". *Nat Biotech*, Vol. 21, pp. 1303–1304, Nov. 2003.

[Eins05] A. Einstein. "Über die von der molekularkinetischen Theorie der Wärme geforderte Bewegung von in ruhenden Flüssigkeiten suspendierten Teilchen". *Annalen der Physik*, Vol. 322, p. 549–560, 1905.

[Elso74] E. L. Elson and D. Magde. "Fluorescence correlation spectroscopy. I. Conceptual basis and theory". *Biopolymers*, Vol. 13, p. 1–27, 1974.

[Evme01] G. Evmenenko, S. W. Dugan, J. Kmetko, and P. Dutta. "Molecular Ordering in Thin Liquid Films of Polydimethylsiloxanes". *Langmuir*, Vol. 17, pp. 4021–4024, June 2001.

[Evme02] G. Evmenenko, C. Yu, J. Kmetko, and P. Dutta. "Density Anomalies in Thin Liquid Films of Hydride Functional Siloxanes". *Langmuir*, Vol. 18, pp. 5468–5472, July 2002.

[Evme06] G. Evmenenko, H. Mo, S. Kewalramani, and P. Dutta. "Conformational rearrangements in interfacial region of polydimethylsiloxane melt films". *Polymer*, Vol. 47, pp. 878 – 882, 2006.

[Feng11] L. Feng, Y. Zhang, Y. Cao, X. Ye, and L. Jiang. "The effect of surface microstructures and surface compositions on the wettabilities of flower petals". *Soft Matter*, Vol. 7, pp. 2977–2980, 2011.

[Fick55] A. Fick. "Ueber Diffusion". *Annalen der Physik*, Vol. 170, p. 59–86, 1855.

[Forc93] M. L. Forcada and C. M. Mate. "Molecular layering during evaporation of ultrathin liquid films". *Nature*, Vol. 363, p. 527, 1993.

[Four90] J. B. Fournier, I. Dozov, and G. Durand. "Surface frustration and texture instability in smectic-A liquid crystals". *Phys. Rev. A*, Vol. 41, pp. 2252–2255, Feb. 1990.

[Fran96]   B. Frank, A. P. Gast, T. P. Russell, H. R. Brown, and C. Hawker. "Polymer Mobility in Thin Films". *Macromolecules*, Vol. 29, pp. 6531–6534, Jan. 1996.

[Genn00]   P. G. de Gennes. "Glass transitions in thin polymer films". *The European Physical Journal E: Soft Matter and Biological Physics*, Vol. 2, pp. 201–205, 2000.

[Genn93]   P. G. de Gennes and J. Prost. *The physics of liquid crystals. International series of monographs on physics*, Oxford University Press, Oxford, 2nd Ed., 1993.

[Gens05]   T. Gensch, M. Bohmer, and P. F. Aramendia. "Single Molecule Blinking and Photobleaching Separated by Wide-Field Fluorescence Microscopy". *The Journal of Physical Chemistry A*, Vol. 109, pp. 6652–6658, 2005.

[Gerl11]   F. Gerlach. *Aggregatbildung von Halbleiter-Nanopartikeln und organischen Farbstoffen in Lösung. Diploma Thesis*, TU Chemnitz, Apr. 2011.

[Ghon00]   N. Ghoneim. "Photophysics of Nile red in solution: Steady state spectroscopy". *Spectrochimica Acta Part A: Molecular and Biomolecular Spectroscopy*, Vol. 56, pp. 1003–1010, Apr. 2000.

[Gill04]   J. W. Gilliland, K. Yokoyama, and W. T. Yip. "Effect of Coulombic Interactions on Rotational Mobility of Guests in Sol-Gel Silicate Thin Films". *Chemistry of Materials*, Vol. 16, pp. 3949–3954, 2004.

[Gome92]   J. M. Gomez-Rodriguez, A. M. Baro, L. Vazquez, R. C. Salvarezza, J. M. Vara, and A. J. Arvia. "Fractal surfaces of gold and platinum electrodeposits: dimensionality determination by scanning tunneling microscopy". *The Journal of Physical Chemistry*, Vol. 96, pp. 347–350, 1992.

[Graa07]   H. Graaf, M. Vieluf, and C. v. Borczyskowski. "Selective binding of dye molecules and CdSe nanocrystals on nanostructures generated by AFM lithography of silicon surfaces". *Nanotechnology*, Vol. 18, p. 265306, 2007.

[Grab07]   C. A. Grabowski and A. Mukhopadhyay. "Comparing the activation energy of diffusion in bulk and ultrathin fluid films". *The Journal of Chemical Physics*, Vol. 127, pp. 171101–4, Nov. 2007.

[Guid10]   C. A. Guido, B. Mennucci, D. Jacquemin, and C. Adamo. "Planar vs. twisted intramolecular charge transfer mechanism in Nile Red: new hints from theory.". *Phys. Chem. Chem. Phys.*, Vol. 12, pp. 8016–8023, 2010.

[Guo08]   W. Guo, S. Herminghaus, and C. Bahr. "Controlling Smectic Focal Conic Domains by Substrate Patterning". *Langmuir*, Vol. 24, pp. 8174–8180, 2008.

[Hac05]   A. E. Hac, H. M. Seeger, M. Fidorra, and T. Heimburg. "Diffusion in Two-Component Lipid Membranes - A Fluorescence Correlation Spectroscopy and Monte Carlo Simulation Study". *Biophysical Journal*, Vol. 88, pp. 317–333, Jan. 2005.

[Hall98]   D. B. Hall and J. M. Torkelson. "Small Molecule Probe Diffusion in Thin and Ultrathin Supported Polymer Films". *Macromolecules*, Vol. 31, pp. 8817–8825, Dec. 1998.

[Hart09]   N. Hartmann, B. Klingebiel, T. Balgar, S. Franzka, and E. Hasselbrink. "Laser-induced local dehydroxylation on surface-oxidized silicon substrates: mechanistic aspects and prospects in nanofabrication". *Applied Physics A: Materials Science & Processing*, Vol. 94, pp. 95–103, 2009.

[Heck11]   G. R. V. Hecke. "The Road to Flat TVs". *Science*, Vol. 331, pp. 1388 –1389, March 2011.

[Heid09a]   M. Heidernätsch. *Development of a Computer Program for Simulation and Analysis of Particle Movement in thin Liquid Films. Master Thesis*, TU Chemnitz, Apr. 2009.

[Heid09b]   M. Heidernätsch, M. Bauer, D. Täuber, G. Radons, and C. von Borczyskowski. "An Advanced Method of Tracking Temporarily Invisible Particles in Video Imaging". *Diffusion Fundamentals Journal*, Vol. 11, p. 111(2), 2009.

[Heit05]   P. Heitjans and J. Kärger. *Diffusion in condensed matter, methods, materials, models.* Springer-Verlag, Berlin, Heidelberg, 2005.

[Hell04a]   S. W. Hell. "Strategy for far-field optical imaging and writing without diffraction limit". *Physics Letters A*, Vol. 326, pp. 140–145, May 2004.

[Hell04b]   S. W. Hell, M. Dyba, and S. Jakobs. "Concepts for nanoscale resolution in fluorescence microscopy". *Current Opinion in Neurobiology*, Vol. 14, pp. 599–609, 2004.

[Hell04c]   C. Hellriegel, J. Kirstein, C. Bräuchle, V. Latour, T. Pigot, R. Olivier, S. Lacombe, R. Brown, V. Guieu, C. Payrastre, A. Izquierdo, and P. Mocho. "Diffusion of Single Streptocyanine Molecules in the Nanoporous Network of Sol-Gel Glasses". *Journal of Physical Chemistry B*, Vol. 108, pp. 14699–14709, 2004.

[Hero86]   F. Herold and B. Wolf. "Poly(N-alkylmethacrylate)S: characterization, good and poor solvents, densities and intrisic viscosities". *Materials Chemistry and Physics*, Vol. 14, pp. 311–338, Apr. 1986.

[Hesl89]   F. Heslot, N. Fraysse, and A. M. Cazabat. "Molecular layering in the spreading of wetting liquid drops". *Nature*, Vol. 338, pp. 640–642, 1989.

[Hohl07]   J. Hohlbein, M. Steinhart, C. Schiene-Fischer, A. Benda, M. Hof, and C. G. Hübner. "Confined Diffusion in Ordered Nanoporous Alumina Membranes". *Small*, Vol. 3, p. 380–385, 2007.

[Honc08]   A. Honciuc, A. W. Harant, and D. K. Schwartz. "Single-Molecule Observations of Surfactant Diffusion at the Solution–Solid Interface". *Langmuir*, Vol. 24, pp. 6562–6566, 2008.

[Honc09a]   A. Honciuc, D. J. Baptiste, I. P. Campbell, and D. K. Schwartz. "Solvent Dependence of the Activation Energy of Attachment Determined by Single Molecule Observations of Surfactant Adsorption". *Langmuir*, Vol. 25, pp. 7389–7392, 2009.

[Honc09b]   A. Honciuc and D. K. Schwartz. "Probing Hydrophobic Interactions Using Trajectories of Amphiphilic Molecules at a Hydrophobic/Water Interface". *Journal of the American Chemical Society*, Vol. 131, pp. 5973–5979, 2009.

[Horc07]   I. Horcas, R. Fernandez, J. M. Gomez-Rodriguez, J. Colchero, J. Gomez-Herrero, and A. M. Baro. "WSXM: A software for scanning probe microscopy and a tool for nanotechnology". *Review of Scientific Instruments*, Vol. 78, p. 013705, 2007.

[Hou00]   Y. Hou, A. M. Bardo, C. Martinez, and D. A. Higgins. "Characterization of Molecular Scale Environments in Polymer Films by Single Molecule Spectroscopy". *The Journal of Physical Chemistry B*, Vol. 104, pp. 212–219, Jan. 2000.

[Hou02]   Y. Hou and D. A. Higgins. "Single Molecule Studies of Dynamics in Polymer Thin Films and at Surfaces: Effect of Ambient Relative Humidity". *The Journal of Physical Chemistry B*, Vol. 106, pp. 10306–10315, Oct. 2002.

[Hu11]   X. Hu, Q. He, X. Zhang, and H. Chen. "Fabrication of fluidic chips with 1-D nanochannels on PMMA substrates by photoresist-free UV-lithography and UV-assisted low-temperature bonding". *Microfluidics and Nanofluidics*, Vol. 10, pp. 1223–1232, 2011.

[Höfl06]   F. Höfling, T. Franosch, and E. Frey. "Localization Transition of the Three-Dimensional Lorentz Model and Continuum Percolation". *Phys. Rev. Lett.*, Vol. 96, pp. 165901–4, 2006.

[Iler79]   R. K. Iler. "The Surface Chemistry of Silica". In: *The Chemistry of Silica*, Wiley, New York, 1979.

[Isra07]   J. N. Israelachvili. *Intermolecular and surface forces.* Academic Press, Amsterdam; Heidelberg, 2. ed., repr. Ed., 2007.

[Jabb07]   A. Jabbarzadeh, P. Harrowell, and R. I. Tanner. "Crystal Bridges, Tetratic Order, and Elusive Equilibria: The Role of Structure in Lubrication Films". *Journal of Physical Chemistry B*, Vol. 111, pp. 11354–11365, 2007.

[Jena79]   A. von Jena and H. Lessing. "Rotational-diffusion anomalies in dye solutions from transient-dichroism experiments". *Chemical Physics*, Vol. 40, pp. 245–256, July 1979.

[Jia11]   Y. Jia, A. Cao, X. Bai, Z. Li, L. Zhang, N. Guo, J. Wei, K. Wang, H. Zhu, D. Wu, and P. M. Ajayan. "Achieving High Efficiency Silicon-Carbon Nanotube Heterojunction Solar Cells by Acid Doping". *Nano Letters*, Vol. 11, pp. 1901–1905, May 2011.

[Jin05]   T. Jin, B. Zalar, A. Lebar, M. Vilfan, S. Zumer, and D. Finotello. "Anchoring and structural transitions as a function of molecular length in confined liquid crystals". *The European Physical Journal E: Soft Matter and Biological Physics*, Vol. 16, pp. 159–165, 2005.

[Joly06]   L. Joly, C. Ybert, and L. Bocquet. "Probing the Nanohydrodynamics at Liquid-Solid Interfaces Using Thermal Motion". *Phys. Rev. Lett.*, Vol. 96, p. 046101, Feb. 2006.

[Jung08]   C. Jung, J. Kirstein, B. Platschek, T. Bein, M. Budde, I. Frank, K. Mullen, J. Michaelis, and C. Bräuchle. "Diffusion of Oriented Single Molecules with Switchable Mobility in Networks of Long Unidimensional Nanochannels". *Journal of the American Chemical Society*, Vol. 130, pp. 1638–1648, 2008.

[Kahy04]   N. Kahya, D. Scherfeld, K. Bacia, and P. Schwille. "Lipid domain formation and dynamics in giant unilamellar vesicles explored by fluorescence correlation spectroscopy". *Journal of Structural Biology*, Vol. 147, pp. 77–89, July 2004.

[Kamm08]   A. Kammerer, F. Höfling, and T. Franosch. "Cluster-resolved dynamic scaling theory and universal corrections for transport on percolating systems". *Europhysics Letters*, Vol. 84, p. 66002, 2008.

[Kawa08]   T. Kawai, A. Kubota, K. Kawamura, H. Tsumatori, and T. Nakashima. "Single molecule fluorescence autocorrelation measurement on anisotropic molecular diffusion in nematic liquid crystal". *Thin Solid Films*, Vol. 516, pp. 2666–2669, March 2008.

[Kaws08]   A. Kawski, P. Bojarski, and B. Kuklinski. "Estimation of ground- and excited-state dipole moments of Nile Red dye from solvatochromic effect on absorption and fluorescence spectra". *Chemical Physics Letters*, Vol. 463, pp. 410–412, Oct. 2008.

[Kedd94a]   J. L. Keddie, R. A. L. Jones, and R. A. Cory. "Size-Dependent Depression of the Glass Transition Temperature in Polymer Films". *Europhysics Letters*, Vol. 27, p. 59, 1994.

[Kedd94b]   J. L. Keddie, R. A. L. Jones, and R. A. Cory. "Interface and surface effects on the glass-transition temperature in thin polymer films". *Faraday Discuss.*, Vol. 98, pp. 219–230, 1994.

[Khok07]   A. Khokhlov, R. Valiullin, J. Kärger, F. Steinbach, and A. Feldhoff. "Freezing and melting transitions of liquids in mesopores with ink-bottle geometry". *New Journal of Physics*, Vol. 9, p. 272, 2007.

[Kim06]   H. Kim, N. W. Song, T. S. Park, and M. Yoon. "Laser scanning confocal microscope (LSCM)-fluorescence spectral properties of Nile Red embedded in polystyrene film of different thickness". *Chemical Physics Letters*, Vol. 432, pp. 200–204, Dec. 2006.

[Kirs07]   J. Kirstein. *Diffusion of single molecules in nanoporous mesostructured materials. Dissertation*, LMU München, 2007.

[Kirs75]   R. G. Kirste, W. A. Kruse, and K. Ibel. "Determination of the conformation of polymers in the amorphous solid state and in concentrated solution by neutron diffraction". *Polymer*, Vol. 16, pp. 120–124, Feb. 1975.

[Klei98]   J. Klein and E. Kumacheva. "Simple liquids confined to molecularly thin layers. I. Confinement-induced liquid-to-solid phase transitions". *The Journal of Chemical Physics*, Vol. 108, pp. 6996–7009, Apr. 1998.

[Kowe09]   D. Kowerko, J. Schuster, and C. von Borczyskowski. "Restricted conformation dynamics of single functionalized perylene bisimide molecules on SiO2 surfaces and in thin polymer films". *Molecular Physics*, Vol. 107, pp. 1911–1921, 2009.

[Krau09]   S. Krause. *Aufbau eines Tieftemperaturmessplatzes zur Integration in ein Laserscanning-mikroskop und Messung der spektralen Diffusion von Perylenderivaten. Diploma Thesis*, TU Chemnitz, 2009.

[Krau11a]   S. Krause, P. F. Aramendia, D. Täuber, and C. von Borczyskowski. "Freezing single molecule dynamics on interfaces and in polymers". *Phys. Chem. Chem. Phys.*, Vol. 13, pp. 1754–1761, 2011.

[Krau11b]   S. Krause, D. Kowerko, R. Börner, C. G. Hübner, and C. von Borczyskowski. "Spectral Diffusion of Single Molecules in a Hierarchical Energy Landscape". *ChemPhysChem*, pp. 303–312, 2011.

[Kubi00]   U. Kubitscheck, O. Kückmann, T. Kues, and R. Peters. "Imaging and Tracking of Single GFP Molecules in Solution". *Biophysical Journal*, Vol. 78, pp. 2170–2179, 2000.

[Kukl96]   V. Kukla, J. Kornatowski, D. Demuth, I. Girnus, H. Pfeifer, L. V. C. Rees, S. Schunk, K. K. Unger, and J. Kärger. "NMR Studies of Single-File Diffusion in Unidimensional Channel Zeolites". *Science*, Vol. 272, pp. 702 –704, May 1996.

[Kulz99]   F. Kulzer, F. Koberling, T. Christ, A. Mews, and T. Baschï¿½$\frac{1}{2}$. "Terrylene in p-terphenyl: single-molecule experiments at room temperature". *Chemical Physics*, Vol. 247, pp. 23–34, Aug. 1999.

[Laca04]   E. Lacaze, J. P. Michel, M. Goldmann, M. Gailhanou, M. d. Boissieu, and M. Alba. "Bistable nematic and smectic anchoring in the liquid crystal octylcyanobiphenyl (8CB) adsorbed on a MoS2 single crystal". *Phys. Rev. E*, Vol. 69, p. 041705, Apr. 2004.

[Lang05]   E. Lang, F. Würthner, and J. Köhler. "Photophysical Properties of a Tetraphenoxy-Substituted Perylene Bisimide Derivative Characterized by Single-Molecule Spectroscopy". *ChemPhysChem*, Vol. 6, pp. 935–941, 2005.

[Laug05]   E. Lauga and T. M. Squires. "Brownian motion near a partial-slip boundary: A local probe of the no-slip condition". *Physics of Fluids*, Vol. 17, p. 103102, 2005.

[Lefo08]   R. Lefort, D. Morineau, R. Guegan, M. Guendouz, J. Zanotti, and B. Frick. "Relation between static short-range order and dynamic heterogeneities in a nanoconfined liquid crystal". *Phys. Rev. E (Statistical, Nonlinear, and Soft Matter Physics)*, Vol. 78, pp. 040701–4, Oct. 2008.

[Li04]   J. Li and S. Wu. "Extended Cauchy equations for the refractive indices of liquid crystals". *Journal of Applied Physics*, Vol. 95, pp. 896–901, 2004.

[Li10]   T. Li, S. Kheifets, D. Medellin, and M. G. Raizen. "Measurement of the Instantaneous Velocity of a Brownian Particle". *Science*, Vol. 328, pp. 1673–1675, June 2010.

[Liet03]   A. M. Lieto, R. C. Cush, and N. L. Thompson. "Ligand-Receptor Kinetics Measured by Total Internal Reflection with Fluorescence Correlation Spectroscopy". *Biophysical Journal*, Vol. 85, pp. 3294–3302, Nov. 2003.

[Lin00]   B. Lin, J. Yu, and S. A. Rice. "Direct measurements of constrained Brownian motion of an isolated sphere between two walls". *Phys. Rev. E*, Vol. 62, p. 3909, 2000.

[Lin99]   E. K. Lin, R. Kolb, S. K. Satija, and W. li Wu. "Reduced Polymer Mobility near the Polymer/Solid Interface as Measured by Neutron Reflectivity". *Macromolecules*, Vol. 32, pp. 3753–3757, June 1999.

[Loos08]   M. Loose, E. Fischer-Friedrich, J. Ries, K. Kruse, and P. Schwille. "Spatial Regulators for Bacterial Cell Division Self-Organize into Surface Waves in Vitro". *Science*, Vol. 320, pp. 789 –792, May 2008.

[Lube08]   A. Lubelski, I. M. Sokolov, and J. Klafter. "Nonergodicity Mimics Inhomogeneity in Single Particle Tracking". *Phys. Rev. Lett.*, Vol. 100, p. 250602, June 2008.

[Lópe82]   I. López Arbeloa and P. Ruiz Ojeda. "Dimeric states of rhodamine B". *Chemical Physics Letters*, Vol. 87, pp. 556–560, 1982.

[Manz90]   A. Manz, N. Graber, and H. Widmer. "Miniaturized total chemical analysis systems: A novel concept for chemical sensing". *Sensors and Actuators B: Chemical*, Vol. 1, pp. 244 – 248, 1990.

[McKe09]   H. McKenzie, M. Lewis, and E. Merrill. "First Passage Time Analysis of Animal Movement and Insights into the Functional Response". *Bulletin of Mathematical Biology*, Vol. 71, pp. 107–129, 2009.

[Menz98]   R. Menzel and E. Thiel. "Intersystem crossing rate constants of rhodamine dyes: influence of the amino-group substitution". *Chemical Physics Letters*, Vol. 291, pp. 237–243, July 1998.

[Mial91]   J. C. Mialocq, P. Hébert, X. Armand, R. Bonneau, and J. P. Morand. "Photophysical and photochemical properties of rhodamine 6G in alcoholic and aqueous sodium dodecylsulphate micellar solutions". *Journal of Photochemistry and Photobiology A: Chemistry*, Vol. 56, pp. 323–338, Feb. 1991.

[Mich06]   J. Michel, E. Lacaze, M. Goldmann, M. Gailhanou, M. de Boissieu, and M. Alba. "Structure of Smectic Defect Cores: X-Ray Study of 8CB Liquid Crystal Ultrathin Films". *Phys. Rev. Lett.*, Vol. 96, p. 027803, Jan. 2006.

[Mo06]   H. Mo, G. Evmenenko, S. Kewalramani, K. Kim, S. N. Ehrlich, and P. Dutta. "Observation of Surface Layering in a Nonmetallic Liquid". *Phys. Rev. Lett.*, Vol. 96, p. 096107, March 2006.

[Moer03]   W. E. Moerner and D. P. Fromm. "Methods of single-molecule fluorescence spectroscopy and microscopy". *Review of Scientific Instruments*, Vol. 74, pp. 3597–3619, 2003.

[Moer89]   W. E. Moerner and L. Kador. "Optical Detection and Spectroscopy of Single Molecules in a Solid". *Phys. Rev. Lett.*, Vol. 62, pp. 2535–2538, 1989.

[Mont00]   F. del Monte, J. D. Mackenzie, and D. Levy. "Rhodamine Fluorescent Dimers Adsorbed on the Porous Surface of Silica Gels". *Langmuir*, Vol. 16, pp. 7377–7382, 2000.

[Mont06]   D. Montiel, H. Cang, and H. Yang. "Quantitative Characterization of Changes in Dynamical Behavior for Single-Particle Tracking Studies". *The Journal of Physical Chemistry B*, Vol. 110, pp. 19763–19770, 2006.

[Mori07]   T. Mori, R. D. Vale, and M. Tomishige. "How kinesin waits between steps". *Nature*, Vol. 450, pp. 750–754, Nov. 2007.

[Mukh02]   A. Mukhopadhyay, J. Zhao, S. C. Bae, and S. Granick. "Contrasting Friction and Diffusion in Molecularly Thin Confined Films". *Phys. Rev. Lett.*, Vol. 89, p. 136103, Sep. 2002.

[Munk04]   A. Munkholm and S. Brennan. "Ordering in Thermally Oxidized Silicon". *Phys. Rev. Lett.*, Vol. 93, p. 036106, 2004.

[Neus09]   T. Neusius, I. M. Sokolov, and J. C. Smith. "Subdiffusion in time-averaged, confined random walks". *Phys. Rev. E*, Vol. 80, p. 011109, July 2009.

[Nguy87]   D. C. Nguyen, R. A. Keller, J. H. Jett, and J. C. Martin. "Detection of Single Molecules of Phycoerythrin in Hydrodynamically Focused Flows by Laser-Induced Fluorescence". *Analytical Chemistry*, Vol. 59, pp. 2158–2161, 1987.

[Nunn11]   B. Nunner. *Verhandlungen der Deutschen Physikalischen Gesellschaft*. Vol. 46/1 of *VI*, Deutsche Physikalische Gesellschaft e.V., Bad Honnef, 2011.

[Orri90]   M. Orrit and J. Bernard. "Single Pentacene Molecules Detected by Fluorescence Excitation in a p-Terphenyl Crystal". *Phys. Rev. Lett.*, Vol. 65, pp. 2716–2718, 1990.

[Pati07]   S. Patil, G. Matei, C. A. Grabowski, P. M. Hoffmann, and A. Mukhopadhyay. "Combined Atomic Force Microscopy and Fluorescence Correlation Spectroscopy Measurements to Study the Dynamical Structure of Interfacial Fluids". *Langmuir*, Vol. 23, pp. 4988–4992, 2007.

[Petr08]   E. P. Petrov and P. Schwille. "Translational Diffusion in Lipid Membranes beyond the Saffman-Delbruck Approximation". *Biophysical Journal*, Vol. 94, pp. L41–43, March 2008.

[Post11]   E. B. Postnikov and I. M. Sokolov. "Model of lateral diffusion in ultrathin layered films". *submitted to Phys. Rev. E*, 2011.

[Puse11]   P. N. Pusey. "Brownian Motion Goes Ballistic". *Science*, Vol. 332, pp. 802 –803, May 2011.

[Qian91]   H. Qian, M. P. Sheetz, and E. L. Elson. "Single particle tracking. Analysis of diffusion and flow in two-dimensional systems". *Biophysical Journal*, Vol. 60, pp. 910–921, 1991.

[Risk96]   H. Risken. *The Fokker-Planck Equation. Springer series in synergetics*, Springer, New York Berlin Heidelberg, 2nd edition Ed., 1996.

[Roge57]   S. Rogers and L. Mandelkern. "Glass Transitions of the Poly-(n-Alkyl Methacrylates)". *The Journal of Physical Chemistry*, Vol. 61, pp. 985–991, 1957.

[Ruit97]   A. G. T. Ruiter, J. A. Veerman, M. F. Garcia-Parajo, and N. F. van Hulst. "Single Molecule Rotational and Translational Diffusion Observed by Near-Field Scanning Optical Microscopy". *The Journal of Physical Chemistry A*, Vol. 101, pp. 7318–7323, Oct. 1997.

[Savi05]   T. Savin and P. S. Doyle. "Static and Dynamic Errors in Particle Tracking Microrheology". *Biophysical Journal*, Vol. 88, pp. 623–638, Jan. 2005.

[Saxt96]   M. J. Saxton. "Anomalous diffusion due to binding: a Monte Carlo study". *Biophysical Journal*, Vol. 70, pp. 1250–1262, 1996.

[Saxt97a]   M. J. Saxton. "Single-Particle Tracking: The Distribution of Diffusion Coefficients". *Biophysical Journal*, Vol. 72, pp. 1744–1753, 1997.

[Saxt97b]   M. J. Saxton and K. Jacobson. "SINGLE-PARTICLE TRACKING:Applications to Membrane Dynamics". *Annual Review of Biophysics and Biomolecular Structure*, Vol. 26, pp. 373–399, 1997.

[Sbal05]   I. Sbalzarini and P. Koumoutsakos. "Feature point tracking and trajectory analysis for video imaging in cell biology". *Journal of Structural Biology*, Vol. 151, pp. 182 – 195, 2005.

[Scha96]   M. Schadt, H. Seiberle, and A. Schuster. "Optical patterning of multi-domain liquid-crystal displays with wide viewing angles". *Nature*, Vol. 381, pp. 212–215, May 1996.

[Schl02]   S. Schlagowski, K. Jacobs, and S. Herminghaus. "Nucleation-induced undulative instability in thin films of n CB liquid crystals". *Europhysics Letters*, Vol. 57, p. 519, 2002.

[Schm10]   R. Schmidt. *Zeitaufgelöste Konfokalmikroskopie an einzelnen CdSe/ZnS-Halbleiternano-kristallen. Diploma Thesis*, TU Chemnitz, 2010.

[Schm95]   T. Schmidt, G. J. Schuetz, W. Baumgartner, H. J. Gruber, and H. Schindler. "Characterization of Photophysics and Mobility of Single Molecules in a Fluid Lipid Membrane". *The Journal of Physical Chemistry*, Vol. 99, pp. 17662–17668, 1995.

[Schm96]   T. Schmidt, G. J. Schütz, W. Baumgartner, H. J. Gruber, and H. Schindler. "Imaging of single molecule diffusion". *Proceedings of the National Academy of Sciences of the United States of America*, Vol. 93, pp. 2926–2929, Apr. 1996.

[Scho04]   A. Schob, F. Cichos, J. Schuster, and C. von Borczyskowski. "Reorientation and translation of individual dye molecules in a polymer matrix". *European Polymer Journal,*, Vol. 40, pp. 1019–1026, 2004.

[Schu02a]   J. Schuster, F. Cichos, and C. von Borczyskowski. "Diffusion Measurements by Single-Molecule Spot-Size Analysis". *The Journal of Physical Chemistry A*, Vol. 106, pp. 5403–5406, June 2002.

[Schu02b]   J. Schuster. *Untersuchung der Diffusion in dünnen Flüssigkeitsfilmen mit Methoden der Einzelmoleküldetektion. Dissertation*, TU Chemnitz, 2002.

[Schu03]   J. Schuster, F. Cichos, and C. von Borczyskowski. "Anisotropic diffusion of single molecules in thin liquid films". *The European Physical Journal E: Soft Matter and Biological Physics*, Vol. 12, pp. 75–80, 2003.

[Schu04]   J. Schuster, F. Cichos, and C. von Borzcyskowski. "Diffusion in ultrathin liquid films". *European Polymer Journal*, Vol. 40, pp. 993–999, 2004.

[Schu05]   J. Schuster, F. Cichos, and C. von Borczyskowski. "Blinking of single molecules in various environments". *Optics and Spectroscopy*, Vol. 98, pp. 712–717, 2005.

[Schu07]   J. Schuster, J. Brabandt, and C. von Borczyskowski. "Discrimination of photoblinking and photobleaching on the single molecule level". *Journal of Luminescence*, Vol. 127, pp. 224–229, Nov. 2007.

[Schu09]   B. Schulz. *Untersuchung der Diffusion von Farbstoffmolekülen in dünnen smektischen Flüssigkristallfilmen. Diploma Thesis*, TU Chemnitz, June 2009.

[Schu10a]   S. Schubert. *Untersuchung der Diffusion und der Anbindung von Farbstoffen an nanostrukturierten Grenzflächen. Diploma Thesis*, TU Chemnitz, March 2010.

[Schu10b]   B. Schulz, D. Täuber, F. Friedriszik, H. Graaf, J. Schuster, and C. von Borczyskowski. "Optical detection of heterogeneous single molecule diffusion in thin liquid crystal films". *Phys. Chem. Chem. Phys.*, Vol. 12, pp. 11555–11564, 2010.

[Schu11]   B. Schulz, D. Täuber, J. Schuster, T. Baumgärtel, and C. von Borczyskowski. "Influence of mesoscopic structures on single molecule dynamics in thin smectic liquid crystal films.". *Soft Matter*, Vol. 7, pp. 7431–7440, 2011.

[Schw02]   P. Schwille and E. Haustein. "Fluorescence correlation spectroscopy, an introduction to its concepts and applications.". In: *Single Molecule Techniques*, Biophysical Society, Bethesda, MD, 2002.

[Schü97]   G. Schütz, H. Schindler, and T. Schmidt. "Single-molecule microscopy on model membranes reveals anomalous diffusion". *Biophysical Journal*, Vol. 73, pp. 1073–1080, Aug. 1997.

[Seem01]   R. Seemann, S. Herminghaus, and K. Jacobs. "Dewetting Patterns and Molecular Forces: A Reconciliation". *Phys. Rev. Lett.*, Vol. 86, p. 5534–5537, June 2001.

[Seem05]   R. Seemann, S. Herminghaus, C. Neto, S. Schlagowski, D. Podzimek, R. Konrad, H. Mantz, and K. Jacobs. "Dynamics and structure formation in thin polymer melt films". *Journal of Physics: Condensed Matter*, Vol. 17, p. S267, 2005.

[Shir76]   H. Shiraki. "Suppression of Stacking Fault Generation in Silicon Wafer by HCl Added to Dry O_2 Oxidation". *Japanese journal of applied physics*, Vol. 15, pp. 83–86, 1976.

[Shle07]   M. F. Shlesinger. "Mathematical physics: First encounters". *Nature*, Vol. 450, pp. 40–41, Nov. 2007.

[Skai00]   J. J. Skaife and N. L. Abbott. "Quantitative Interpretation of the Optical Textures of Liquid Crystals Caused by Specific Binding of Immunoglobulins to Surface-Bound Antigens". *Langmuir*, Vol. 16, pp. 3529–3536, Apr. 2000.

[Smal01]   I. I. Smalyukh, S. V. Shiyanovskii, and O. D. Lavrentovich. "Three-dimensional imaging of orientational order by fluorescence confocal polarizing microscopy". *Chemical Physics Letters*, Vol. 336, pp. 88–96, March 2001.

[Smol06]   M. von Smoluchowski. "Zur kinetischen Theorie der Brownschen Molekularbewegung und der Suspensionen". *Annalen der Physik*, Vol. 326, p. 756–780, 1906.

[Sper06]   L. H. Sperling. *Introduction to Physical Polymer Science*. Wiley, 4 Ed., 2006.

[Stei09]   M. Steiner, D. Rueda, and R. K. O. Sigel. "Ca2+ Induces the Formation of Two Distinct Subpopulations of Group II Intron Molecules". *Angewandte Chemie International Edition*, Vol. 48, p. 9739–9742, 2009.

[Stru00]   C. W. Struijk, A. B. Sieval, J. E. J. Dakhorst, M. van Dijk, P. Kimkes, R. B. M. Koehorst, H. Donker, T. J. Schaafsma, S. J. Picken, A. M. van de Craats, J. M. Warman, H. Zuilhof, and E. J. R. Sudhölter. "Liquid Crystalline Perylene Diimides: Architecture and Charge Carrier Mobilities". *Journal of the American Chemical Society*, Vol. 122, pp. 11057–11066, Nov. 2000.

[Tani90]   K. Taniguchi, M. Tanaka, C. Hamaguchi, and K. Imai. "Density relaxation of silicon dioxide on (100) silicon during thermal annealing". *J. Appl. Phys.*, Vol. 67, pp. 2195–2198, March 1990.

[Tats04]   K. Tatsumura, T. Watanabe, D. Yamasaki, T. Shimura, M. Umeno, and I. Ohdomari. "Residual order within thermally grown amorphous SiO2 on crystalline silicon". *Phys. Rev. B*, Vol. 69, p. 085212, 2004.

[Tats05]   K. Tatsumura, T. Shimura, E. Mishima, K. Kawamura, D. Yamasaki, H. Yamamoto, T. Watanabe, M. Umeno, and I. Ohdomari. "Reactions and diffusion of atomic and molecular oxygen in the Si O2 network". *Phys. Rev. B*, Vol. 72, p. 045205, 2005.

[Thom83]   N. Thompson and D. Axelrod. "Immunoglobulin surface-binding kinetics studied by total internal reflection with fluorescence correlation spectroscopy". *Biophysical Journal*, Vol. 43, pp. 103–114, July 1983.

[Tren09a]   I. Trenkmann. *Untersuchung der Sondendiffusion von Nanopartikeln in ultra-dünnen Flüssigkeitsfilmen mittels Einzelteilchenmikroskopie. Diploma Thesis*, TU Chemnitz, Aug. 2009.

[Tren09b]   I. Trenkmann, D. Täuber, M. Bauer, J. Schuster, S. Bok, S. Gangopadhyhay, and C. von Borczyskowski. "Investigations of solid liquid interfaces in ultra-thin liquid films via single particle tracking of silica nanoparticles". *Diffusion Fundamentals Journal*, Vol. 11, p. 108(12), 2009.

[Täub09a]   D. Täuber, M. Heidernätsch, M. Bauer, G. Radons, J. Schuster, and C. von Borczyskowski. "Single molecule tracking of the molecular mobility in thinning liquid films on thermally grown SiO2". *Diffusion Fundamentals Journal*, Vol. 11, p. 107(10), 2009.

[Täub09b]   D. Täuber, J. Schuster, M. Heidernätsch, M. Bauer, G. Radons, and C. von Borczyskowski. "Discriminination between static and dynamic heterogeneities in single dye diffusion in ultrathin liquid films". *Diffusion Fundamentals Journal*, Vol. 11, p. 76(2), 2009.

[Vale05]   B. Valeur. *Molecular fluorescence - principles and applications*. Wiley-VCH Verlag GmbH, 1st, 2nd repr. Ed., 2005.

[Vali07]   R. Valiullin. "Diffusion and phase transitions in compartmented nanochannels". oral communication at symposium of DPG-FOR 877, Leipzig, 2007.

[Vall04]   R. A. L. Vallée, M. Cotlet, M. Van Der Auweraer, J. Hofkens, K. Müllen, and F. C. De Schryver. "Single-Molecule Conformations Probe Free Volume in Polymers". *Journal of the American Chemical Society*, Vol. 126, pp. 2296–2297, March 2004.

[Veni99]   A. V. Veniaminov and H. Sillescu. "Polymer and Dye Probe Diffusion in Poly(methyl methacrylate) below the Glass Transition Studied by Forced Rayleigh Scattering". *Macromolecules*, Vol. 32, pp. 1828–1837, March 1999.

[Vilf07]   M. Vilfan, T. Apih, P. J. Sebastiao, G. Lahajnar, and S. Zumer. "Liquid crystal 8CB in random porous glass: NMR relaxometry study of molecular diffusion and director fluctuations". *Phys. Rev. E (Statistical, Nonlinear, and Soft Matter Physics)*, Vol. 76, pp. 051708–15, Nov. 2007.

[Vill96]   S. Villette, M. P. Valignat, A. M. Cazabat, L. Jullien, and F. Tiberg. "Wetting on the Molecular Scale and the Role of Water. A Case Study of Wetting of Hydrophilic Silica Surfaces". *Langmuir*, Vol. 12, pp. 825–830, 1996.

[Voge95]   M. Vogel, A. Gruber, J. Wrachtrup, and C. von Borczyskowski. "Determination of Intersystem Crossing Parameters via Observation of Quantum Jumps on Single Molecules". *The Journal of Physical Chemistry*, Vol. 99, pp. 14915–14917, 1995.

[Wide94]   J. Widengren, R. Rigler, and Ülo Mets. "Triplet-state monitoring by fluorescence correlation spectroscopy". *Journal of Fluorescence*, Vol. 4, pp. 255–258, 1994.

BIBLIOGRAPHY

[Wide99]   J. Widengren, Ülo Mets, and R. Rigler. "Photodynamic properties of green fluorescent proteins investigated by fluorescence correlation spectroscopy". *Chemical Physics*, Vol. 250, pp. 171–186, Dec. 1999.

[Wöll09]   D. Wöll, E. Braeken, A. Deres, F. C. D. DeSchryver, H. Uji-i, and J. Hofkens. "Polymers and single molecule fluorescence spectroscopy, what can we learn?". *Chemical Society Reviews*, Vol. 38, pp. 313–328, 2009.

[Xu00]   L. Xu, M. Salmeron, and S. Bardon. "Wetting and Molecular Orientation of 8CB on Silicon Substrates". *Phys. Rev. Lett.*, Vol. 84, p. 1519–1522, Feb. 2000.

[Yang06]   C. Yang, U. Tartaglino, and B. N. J. Persson. "Influence of Surface Roughness on Superhydrophobicity". *Phys. Rev. Lett.*, Vol. 97, p. 116103, Sep. 2006.

[Yosh02]   Z. Yoshimitsu, A. Nakajima, T. Watanabe, and K. Hashimoto. "Effects of Surface Structure on the Hydrophobicity and Sliding Behavior of Water Droplets". *Langmuir*, Vol. 18, pp. 5818–5822, July 2002.

[Yu00]   C. J. Yu, A. G. Richter, A. Datta, M. K. Durbin, and P. Dutta. "Molecular layering in a liquid on a solid substrate: an X-ray reflectivity study". *Physica B: Condensed Matter*, Vol. 283, pp. 27–31, June 2000.

[Yu99]   C. J. Yu, A. G. Richter, A. Datta, M. K. Durbin, and P. Dutta. "Observation of Molecular Layering in Thin Liquid Films Using X-Ray Reflectivity". *Phys. Rev. Lett.*, Vol. 82, p. 2326, March 1999.

[Zakh08]   A. Zakharov, D. Taguchi, and M. Iwamoto. "Rotational self-diffusion coefficients in dipolar organic liquid crystal film on the solid surfaces". *Chemical Physics Letters*, Vol. 458, pp. 143–146, June 2008.

[Zapp11]   B. Zappone, E. Lacaze, H. Hayeb, M. Goldmann, N. Boudet, P. Barois, and M. Alba. "Self-ordered arrays of linear defects and virtual singularities in thin smectic-A films". *Soft Matter*, Vol. 7, pp. 1161–1167, 2011.

[Zhan07]   B. Zhang, J. Zerubia, and J. Olivo-Marin. "Gaussian approximations of fluorescence microscope point-spread function models". *Appl. Opt.*, Vol. 46, pp. 1819–1829, Apr. 2007.

[Zhur00]   L. T. Zhuravlev. "The surface chemistry of amorphous silica. Zhuravlev model". *Colloids and Surfaces A: Physicochemical and Engineering Aspects*, Vol. 173, pp. 1–38, 2000.

[Zihe03]   P. Ziherl and S. Zumer. "Morphology and structure of thin liquid-crystalline films at nematic-isotropic transition". *The European Physical Journal E: Soft Matter and Biological Physics*, Vol. 12, pp. 361–365, 2003.

[Zond04]   R. Zondervan, F. Kulzer, M. A. Kol'chenk, and M. Orrit. "Photobleaching of Rhodamine 6G in Poly(vinyl alcohol) at the Ensemble and Single-Molecule Levels". *The Journal of Physical Chemistry A*, Vol. 108, pp. 1657–1665, 2004.

[Zürn07]   A. Zürner, J. Kirstein, M. Doblinger, C. Bräuchle, and T. Bein. "Visualizing single-molecule diffusion in mesoporous materials". *Nature*, Vol. 450, pp. 705–708, 2007.

Published work and contributions to conferences and meetings

Publications

B. Schulz, D. Täuber, J. Schuster, T. Baumgärtel, and C. von Borczyskowski. Influence of mesoscopic structures on single molecule dynamics in thin smectic liquid crystal films. *Soft Matter*, 7(16), pp. 7431-7440, 2011.

S. Krause, P.F. Aramendía, D. Täuber and C. von Borczyskowski. Freezing Single Molecule Dynamics on Interfaces and in Polymers. *PhysChemChemPhys*, 13(5), pp. 1754-1761, 2011.

B. Schulz, D. Täuber, F. Friedriszik, H. Graaf, J. Schuster and C. von Borczyskowski. Optical Detection of Heterogeneous Single Molecule Diffusion in Thin Liquid Crystal Films. *PhysChemChemPhys*, 12(37), pp. 11555-11564, 2010.

D. Täuber, M. Heidernätsch, M. Bauer, G. Radons, J. Schuster and C. von Borczyskowski. Single molecule tracking of the molecular mobility in thinning liquid films on thermally grown SiO_2. *Diffusion Fundamentals Journal*, Vol. 11, p. 107(11), 2009.

M. Bauer, M. Heidernätsch, D. Täuber, C. von Borczyskowski and G. Radons. Investigations of heterogeneous diffusion based on the probability density of scaled squared displacements observed from single molecules in ultra-thin liquid films. *Diffusion Fundamentals Journal*, Vol. 11, p. 104(14), 2009.

I. Trenkmann, D. Täuber, M. Bauer, J. Schuster, S. Bok, S. Gangopadhyay, C. von Borczyskowski. Investigations of solid liquid interfaces in ultra-thin liquid films via single particle tracking of silica nanoparticles. *Diffusion Fundamentals Journal*, Vol. 11, p. 108(12), 2009

D. Täuber, M. Heidernätsch, M. Bauer, G. Radons, J. Schuster and C. von Borczyskowski. Disciminination between static and dynamic heterogeneities in single dye diffusion in ultrathin liquid films. *Diffusion Fundamentals Journal*, Vol. 11, p. 76(2), 2009.

M. Heidernätsch, M. Bauer, D. Täuber, G. Radons and C. von Borczyskowski. An advanced method of tracking temporarily invisible particles in video imaging. *Diffusion Fundamentals Journal*, Vol. 11, p. 111(2), 2009.

M. Bauer, M. Heidernätsch, D. Täuber, J. Schuster, C. von Borczyskowski, G. Radons Investigations of Static and Dynamic Heterogeneities in Ultra-Thin Liquid Films via Scaled Squared Displacements of Single Molecule Diffusion. *Diffusion Fundamentals Journal*, Vol. 11, p. 70(2), 2009.

Poster Presentations

D. Täuber*, and C. von Borczyskowski. Characterization of dynamics in ultrathin liquid films using fluorescence correlation spectroscopy and single molecule tracking. *WEH Seminar 488 on Single Molecule Spectroscopy: Current Status and Perspectives*, July 2011.

B. Schulz, D. Täuber*, and C. von Borczyskowski. Structure formation and dynamics of thin liquid crystal (8CB) films depending on the type of substrate. *DPG spring meeting*, CPP 19.5, Dresden, March 2011.

F. Gerlach*, D. Täuber, and C. von Borczyskowski. Competition between diffusion and aggregate formation on a single molecule level. *DPG spring meeting*, CPP 36.17, Dresden, March 2011.

B. Aráoz*, D. Täuber, J. Faust, C. von Borczyskowski, and P.F. Aramendía. Local Movements in thin polymer films around T_g. *CONICET conference*, Santiago/Chile, October 2010.

D. Täuber*, F. Gerlach, S. Schubert, and C. von Borczyskowski. Interfacial effects on single dye diffusion in ultrathin liquid films. *DPG spring meeting*, CPP 14.12, Regensburg, March 2010.

F. Gerlach*, D. Täuber, D. Kowerko, and C. von Borczyskowski. Investigation of assembly formation of quantum dots and dyes on a single molecule particle level in thin liquid films. *DPG spring meeting*, CPP 36.6, Regensburg, March 2010.

S. Krause*, D. Täuber, and C. von Borczyskowski. Spectral diffusion probing nanoscale fluctuations. *DPG spring meeting*, CPP 31.10, Regensburg, March 2010.

D. Täuber*, M. Heidernätsch, M. Bauer, G. Radons, J. Schuster and C. von Borczyskowski *13. Physikerinnentagung der DPG*, Sa5.24, Frankfurt, November 2009.

D. Täuber*, M. Heidernätsch, M. Bauer, G. Radons, J. Schuster and C. von Borczyskowski. Discrimination between static and dynamic heterogeneities in single dye diffusion in ultrathin liquid films. *Diffusion Fundamentals III Conference*, Athens/Greece, August 2009.

S. Schubert*, D. Täuber, D. Kowerko, J. Schuster, and C. von Borczyskowski. Orientation and spatial distribution of dyes binding to SiO2 surfaces. *DPG spring meeting*, CPP 28.12, Dresden, March 2009.

* contributing author

Oral Presentations

D. Täuber, S. Krause, B. Aráoz, P.F. Aramendía, and C. von Borczyskowski. Characterization of spectral diffusion and its application to probe thin polymer films. *DPG spring meeting*, CPP 7.8, Dresden, March 2011.

D. Täuber, B. Schulz, and C. von Borczyskowski. Anomalous diffusion in frustrated liquid crystal films. 11th *European conference on liquid crystals*, Maribor/Slovenien, February 2011.

D. Täuber, B. Schulz, and C. von Borczyskowski. Structure related dynamics of single molecules in frustrated liquid crystal films. *2nd European Workshop on Advanced Fluorescence Imaging and Dynamics, LMU München*, München, December 2010.

D. Täuber, B. Aráoz, P.F. Aramendía, and C. von Borczyskowski. Characterization of spectral diffusion and its application to Nile Red in polyalkylmethacrylates. *Symposium DFG-For 877*, Leipzig, 2010/10/29.

D. Täuber, S. Schubert. and C. von Borczyskowski. Rhodamine Spectra and hydropathically modified SiO_2 Surfaces. *Universidad de Buenos Aires*, Buenos Aires/Argentina, 2010/03/26.

I. Trenkmann*, D. Täuber, M. Bauer, and C. von Borczyskowski. Analysis of heterogeneous diffusion in ultra-thin liquid films via single particle tracking. *DPG spring meeting*, CPP 17.11, Regensburg, March 2010.

D. Täuber, and C. von Borczyskowski. Characterisation of diffusion by various analytical methods. *Symposium DFG-For 877*, Leipzig, 2009/09/22.

D. Täuber, J. Schuster, and C. von Borczyskowski. Diffusion in ultrathin liquid films. *Universidad de Buenos Aires*, Buenos Aires/Argentina, 2009/06/26.

D. Täuber, J. Schuster, and C. von Borczyskowski. Tracing physio-chemical changes at the solid liquid interface with single molecule microscopy. *DPG spring meeting*, CPP 5.1, Dresden, March 2009.

D. Täuber, and M. Bauer. Diffusion in ultrathin liquid films. *Symposium DFG-For 877*, Eibenstock, 2009/03/11-13.

D. Täuber, J. Schuster, and C. von Borczyskowski. Binding and Diffusion of individual dye molecules in ultrathin liquid films. *DPG spring meeting*, CPP 37.6, Berlin, February 2008.

D. Täuber, J. Schuster, and C. von Borczyskowski. Single molecule microscopy of ultrathin liquid films - Control of film thickness by diffusion measurements. *Symposium DFG-For 877*, Leipzig, 2007/11/27.

* contributing author. The first named author always gave the presentation.

Theses

- Analysis of probability distributions of diffusivities (i.e. time scaled square displacements from SMT experiments) is a powerful tool to study diffusion heterogeneity within ultrathin liquid films. In particular, this method is superior to trajectory analysis via msd in respect to the capture of fast diffusion.

- Spatial maps of diffusivities are suitable tools to reveal structure related dynamics within thin smectic liquid crystal films.

- Single dye dynamics in ultrathin liquid films can be explained by a three-layer model containing (i) immobile molecules adsorbed at the solid-liquid interface, (ii) a laterally heterogeneous near-surface region within 1-2 liquid molecular diameters from the solid-liquid interface, and (iii) an upper layer with freely diffusing molecules.

- Vertical diffusion within the upper layer is fast, with vertical mean first passage times in the range of 0.1 μs. This mfpt is related to the initial fast decay of the FCS autocorrelation curves.

- Due to the vertical confinement within few molecular diameters, for lateral diffusion effective diffusion coefficients D_{eff} are observed from SMT and from FCS experiments. These are strongly influenced by the lateral heterogeneity of the solid-liquid interface. The diffusion coefficients obtained from SMT, thereby, underestimate the D_{eff} due to the reduced sensitivity of SMT for fast diffusion.

- All used dye molecules possess at least two end groups (amino- and/or ketone-) for H-bonding. Thus near-surface diffusion may be caused by successive H-bonding steps on silanol clusters as suggested by Honciuc et al. [Honc08].

- FCS autocorrelation curves in the range of 0.01 ms $\leq \tau \leq$ 10 s contain contributions from diffusion transients of the focal area and from sorption kinetics. An approximation by the sum of the function G_D for translational diffusion and a stretched exponential function yields realistic values for the translational diffusion coefficient and mean adsorption duration.

- For decreasing film thickness, narrowing distributions of diffusion coefficients D_{traj}, (obtained from trajectory analysis via weighted msd) are observed, while their mean shifts towards smaller values. This is caused by a higher concentration of the dye molecules within the near-surface region in case of thinner films.

- Probability distributions of diffusivities from SMT experiments reveal anomalous diffusion behavior of probe molecules over one order of magnitude in the time regime between 20 ms and 200 ms. This is caused by the lateral heterogeneity of the solid-liquid interface.

- In analogy to translational diffusion, probability distributions of spectral diffusivities (i.e. time scaled square energetic displacements between succeeding spectra) are a suitable tool to study spectral diffusion.

- Within spectral diffusion (at acquisition time 1 s), contributions from noise and fitting uncertainty are expected to range between 2 meV^2/s and 5 meV^2/s. Furthermore intermediates obtained form spectral jumps during acquisition may lead to arbitrary diffusion coefficients in the range of 10^2 meV^2/s.

- Within 25 nm thick polyalkylmethacrylate (PnAMA) films, below glass transition T_g, probability distributions of spectral diffusivities obtained from incorporated Nile Red molecules, resemble two-level systems with energy gaps (between the two levels of transition energies) in the range of 25 ± 3 meV. These energy gaps are related to small conformational changes. The change in local polarity is too small to trigger internal charge transfer of Nile Red.

- Within 25 nm thick PBMA films close to glass transition and in the melt state, the Nile Red molecules also undergo translational diffusion, thus sensing regions with different polarity.

- Larger alkyl side chains of PnAMA lead to a solvent shift of SM spectra of Nile Red towards higher energies. This agrees with the idea of nanophase separation for alkyl chain C numbers larger than two, as suggested by Beiner [Bein01].

Acknowledgement

Selbstständigkeitserklärung

Hiermit erkläre ich, daß ich die vorliegende Arbeit selbstständig angefertigt, nicht anderweitig zu Prüfungszwecken vorgelegt und keine anderen als die angegebenen Hilfsmittel verwendet habe. Sämtliche wissentlich verwendete Textausschnitte, Zitate oder Inhalte anderer Verfasser wurden ausdrücklich als solche gekennzeichnet.

Chemnitz, den 18. August 2011

_____

Daniela Täuber

Curriculum Vita

Name:	Daniela Täuber (birth name: März)
date of birth:	08.05.1967
place of birth:	Nürnberg
family status:	married, four children
09/1977 – 06/1986	Emil-von-Behring Gymnasium, Spardorf near Erlangen
27.06.1986	Abitur at the Emil-von-Behring Gymnasium in Spardorf
10/1986 – 12/1991	Studies of Physics and Mathematics at the Friedrich Alexander Universität Erlangen-Nürnberg
09.12.1991	First State Examination in Mathematics and Physics Zulassungsarbeit: "Die Akzeptanz der Newtonschen Gesetze der Bewegungslehre"
02/1992 – 02/1994	Trainee Teaching, Second State Examination title: "Lehramtsassessorin"
1994 – 2006	Births and Child Care (children born 1994, 1996, 1998, 2000), honorary work in support of talented Primary School Students
10/2006 – 02/2007	Studies of Computational Science, TU Chemnitz
since 11/2006	PhD Student, TU Chemnitz, Institute of Physics, OSMP
since 3/2007	Research Assistant, TU Chemnitz, Institute of Physics, OSMP
11/2007 – 12/2010	Co-worker in DFG-FOR 877 "From Local Constraints to Macroscopic Transport"
06-07/2009 and 03-04/2010	Research at the Universidad de Buenos Aires, Argentina, department of photochemistry, within DAAD-PROALAR-cooperation project PK2D/08/11702 "Controlling Dynamic Properties of Ultra-thin Polymer Films via Photoactive Molecules"
since 2011	Co-worker in DFG-FOR 877 extension "Driven Diffusion in Nanoscaled Materials"